DOCTORAL DISSERTATION

博 士 論 文

INTERPRETATION OF COMPACTION BEHAVIOR THROUGH THE MECHANICS OF UNSATURATED SOIL

（不飽和土の力学に基づく締固め現象の解釈）

CHORTHAM SRINIL

チョーサム　スリ二ル

Yokohama National University

Graduate School of Urban Innovation

国立大学法人　横浜国立大学大学院都市イノベーション学府

September 2020

令和 2 年 9 月

INTERPRETATION OF COMPACTION BEHAVIOR THROUGH THE MECHANICS OF UNSATURATED SOIL

(不飽和土の力学に基づく締固め現象の解釈)

by

CHORTHAM SRINIL

チョーサム　スリ二ル

A Dissertation Submitted to the Graduate School of Urban Innovation, Yokohama National University in Partial Fulfillment of the Requirement for the Degree of

Doctor of Engineering

Yokohama National University, Graduate School of Urban Innovation

国立大学法人　横浜国立大学大学院都市イノベーション学府

Examination Committee

Associate Professor, Dr. Mamoru KIKUMOTO (Chair)

Professor, Dr. Kimitoshi HAYANO

Associate Professor, Dr. Ying CUI

Professor, Dr. Koichi MAEKAWA

Associate Professor, Dr. Hiroshi TAMURA

September 2020

令和 2 年 9 月

ABSTRACT

Compaction is an important phenomenon that is related to the construction of soil structures. Regarding the concept of compaction, the compaction mechanisms and compacted soil behaviors shall be investigated through the mechanics of unsaturated soil which volume change and strength are varied by degree of saturation at a current packing density. Variations of compaction water content and compaction effort in the compaction control cause the difference of compacted soil behavior due to the variation of dry density and degree of saturation along the compaction curve. Especially, at a given dry density, the variation of degree of saturation are observed regarding the typical convex-upward compaction curve. By these reasons, the behaviors of compacted soils are also different through the compaction curve for each compaction effort, even at the same dry density. Since the behavior of compacted soil is influenced by mechanism of compaction from the beginning, therefore the heterogeneity of substance soil in the real condition of geotechnical work, which is able to trigger the strain localization failure may affect the behavior of compacted soil from compaction. Consequently, interpretation of compacted soil behavior shall be considered from its origin as the compaction process to its failure considering the heterogeneity of soil at the initial state.

From the literature reviews, the behavior of soil during compaction and the strength of the compacted soil at the given prescribed initial states under long term shearing, heavy rainfall and fully undrained cyclic shearing have been study by many researchers in the framework of unsaturated soil both in experiments and simulations by constitutive models. However, the progressive life of the compacted soil with the variations of initial compaction control parameter from its origin through its failure has not been widely study yet. Moreover, some researchers utilized the Finite Element Method as the tool to imitate the real condition of compaction mechanism while at the same time the heterogeneity of soil at the initial state of compaction has not been considered yet.

In this study, the critical state constitutive model for unsaturated compacted soil was proposed and validated. It is fabricated by incorporates: Bishop's effective stress; soil water characteristic curve considering the effect of hydraulic hysteresis and packing density; and state boundary surface that moves in volumetric direction due to variation in the degree of saturation. Subloading surface concept has also been applied to the model to consider the effect of packing density on the stress-strain characteristics. By the proposed model, a series of simulation starting from the beginning of compaction process through its failure was produced. The effect of compaction water content and compaction effort on the characteristic behavior of unsaturated compacted soil were investigated. Then, the responses of unsaturated compacted soil against

long term shearing, heavy rainfall and fully undrained cyclic shearing which rely on its characteristic after compaction were also interpreted. Regarding the simulation results, the proposed model is capable to generate the typical convex-upward compaction curves with maximum dry density at the optimum water content with the variation of the compaction control parameter. It is also able to predict the tendency of shear strength, volumetric behavior of compacted soil against considered loads through the compaction curve.

In addition, the proposed model was utilized for the soil-water-air three-phases seepage-deformation coupled FEM for the unsaturated porous media. By this tool, we could extend the capability of the model to investigate the compaction process from its origin considering the heterogeneity of substance soil which certainly find in the real condition of geotechnical work. In this study, the numerical investigations of 1-D static compaction mechanisms considering the effect of heterogeneities of dry density and degree of saturation at the initial state in unsaturated porous media were performed by the in-house coupled FEM program for unsaturated soil. The simulation results show that the material heterogeneities at the initial state including dry density and degree of saturation affect the average dry density at any considering stage of compaction excluding in the saturated state and it could be alleviated by the appropriate compaction control parameter specification.

All in all, from the simulation results, we recommend that soil compacted at the optimum water content is suitable for the soil structures that confront with heavy rainfall and subjected to static monotonic shearing for strength and serviceability purposes. In case of the optimum water content could not be reached, the soil shall be compacted on the wet side of optimum to prevent the highly collapse compression due to soaking. In addition, aiming to achieve the optimum water content is also the rational way to increase the liquefaction resistance of the unsaturated compacted soil. Regarding the real condition of geotechnical works, using the appropriate compaction control parameter specification including high compaction effort or compaction water content on the wet side or at the optimum, the effect of heterogeneity after compaction to the localized failure of compacted soil when subjected to loadings could be alleviated. Importantly, engineer can specify the behavior of soil structure from compaction through a numerical method incorporating the proposed constitutive model for compaction.

ACKNOWLEDGEMENT

I would like to express my deepest gratitude to Assoc. Prof. Mamoru KIKUMOTO, my research supervisor, for his profound belief in my ability doing the research. He always supports, educates, gives the valuable advice in every directions of my interested research and encourages me through the study. Not only the research work, he always takes care and supports the livelihood and sense of every students. It is a great honor to work under his supervision.

I would also like to extend my deepest gratitude to the committee members: Prof. Kimitoshi HAYANO, Assoc. Prof. Ying CUI, Prof. Koichi MAEKAWA and Assoc. Prof. Hiroshi TAMURA for their valuable advices and practical suggestions in improving the content of the dissertation and research's implementation in the engineering works.

I would like to extend my sincere thanks to Dr. Veerayut KOMOLVILAS, for his research consulting, clearly explanation of queries relating with the constitutive modeling and computer programming. Thanks should also go to Dr. Keita NAKAMURA and Dr. Nguyen Pham Quang Vu who introduced and provided the guidelines of generating the programming of Finite Element Method which is one of the important part in this dissertation.

I very much appreciate to all the colleagues and my good friend in Yokohama National University for their encouragement and all supports for everything. We shared all the memories of living, traveling and study life in Japan along this time.

I would like to take this opportunity to express my sincere gratitude to Yokohama National University and Ministry of Education, Culture and Sports, Science and Technology, Japan for providing me the great opportunity and a full financial support to fulfill my PhD degree.

Finally, I would like to thank my family and my friend in Thailand for all their encouragement, understanding and support throughout my study.

TABLE OF CONTENTS

LIST OF TABLES

LIST OF FIGURES

CHAPTER 1

INTRODUCTION

1.1 RESEARCH BACKGROUND

Compaction is an important phenomenon that is related to the construction of soil structures, including dams, levees, dikes, and barriers. Recently, a number of soil structures failed due to the severe rainstorms, e.g., failure of Sanyo Expressway embankment due to Typhoon No.14 (Nabi) in Japan (2005), and earthquakes, e.g., Dateshita landslide due to Sanriku Minami earthquake in Japan (2003). Low collapse resistance of compacted soil due to the inappropriate specification of compaction control parameter is one of the reasons of the failures. Therefore, trying to understand the compacted soil behaviors is necessary for the design and construction of the soil structures.

Regarding the typical convex-upward compaction curve, the characteristics of the soils compacted on the dry side of optimum and the wet side of optimum are different. This is because the variations of compaction water content and compaction effort affect the particle reorientation degrees. They cause the variations of dry density and degree of saturation of the compacted soils through the compaction curve (Marwick, 1945; Lambe, 1958; Seed & Chan, 1959; Lambe & Whitman, 1969 and Koga, 1991), especially the variation of degree of saturation at a given dry density. As the kernel concept of soil compaction is to repel the void air for increasing the dry density without changing the water content, therefore the compaction mechanisms and the compacted soil behaviors shall be investigated through the mechanics of unsaturated soils. In the unsaturated soil framework, volume change and strength of unsaturated soil are provided through the bonds between particles maintained by capillary tension owning to the variations of degree of saturation at a current packing density (Fredlund, 2006). Therefore, the behaviors of compacted soils such as the shear strength before soaking (Seed & Monismith, 1954; Leonard, 1955; Bell, 1956; Yoder & Witezak, 1975; Essigman, 1976 and Koga, 1991), the shear strength after soaking (Wilson, 1952 and Tatsuoka & Shibuya, 2014), the volumetric change due to soaking (Holtz & Gibbs, 1956; Yoder & Witezak, 1975; Alonso et al., 1987; Alonso et al., 2013 and Tatsuoka & Shibuya, 2014) and the liquefaction resistance (Zhang et al., 2016 and Komolvilas & Kikumoto, 2017) are also different through the compaction curve for each compaction effort, even at the same dry density. Consequently, we can see from the studies of many researchers that the behaviors of compacted soils are dominantly influenced by compaction mechanism from the beginning. Moreover, the heterogeneity of substance soil at the beginning in the real condition of geotechnical work,

which is caused by either naturally occurring (e.g., typical soil deposit and seasoning ground water level) or man-made (e.g., variation of soil preparation for the fill work and effect of compaction quality), could trigger the strain localization failure under the loadings (Song, et al., 2017). That means the heterogeneity at the initial state of soil may affect the behavior of compacted soil from compaction. Consequently, interpretation of compacted soil behaviors shall be considered from the origin as the compaction process and heterogeneity of soil to the strengths and the failures against the considered loadings.

From the literature reviews, the soil mechanism during compaction has been studied by many researchers through both experiments and numerical simulations in order to develop the constitutive models for the compaction of unsaturated soils (Tarantino & De Col, 2008; Kikumoto et al., 2010 and Alonso et al., 2013). In addition, the strengths and the failures of compacted soils under the various loadings, including the long term shearing (Sivakumar & Wheeler, 2000; Gallipoli et al., 2003a; Gallipoli et al., 2003b; Sun et al., 2007b; Marinho et al., 2013 and Zhou & Sheng, 2015), the hydraulic collapse due to the heavy rainfall (Wheeler & Sivakumar, 2000; Gallipoli et al., 2003a; Gallipoli et al., 2003b and Sun et al., 2007b and Zhou & Sheng, 2015) and the liquefaction due to the fully undrained cyclic shearing (Zhang et al., 2016 and Komolvilas & Kikumoto, 2017), have also been studied through the combination of experiments and simulations. However, the progressive life of the compacted soil with the variations of initial compaction control parameter from its origin through its failure has not been widely studied yet. This is because the long duration of conducting the experiment in the unsaturated state and the complexity of the unsaturated constitutive model.

Moreover, some researchers have utilized the Finite Element Method or FEM as a tool to imitate the real condition of soil. For the compaction mechanism, using coupled FEM for unsaturated soil, one-dimensional (1-D) static compaction mechanisms (Kawai, et al., 2012 and Kawai, et al., 2014) and the distributions of dry density and degree of saturation after compaction (Kawai, et al., 2016) were numerically investigated. However, the heterogeneity of soil at the initial state of compaction has not been considered yet. In another way, using coupled FEM for unsaturated soil, many researchers have found that the material heterogeneities, such as density and degree of saturation, play the important role in triggering strain localization in unsaturated porous media (Song, et al., 2012; Borja & Song, 2014; Song, 2014; Song, et al., 2017 and Likos, et al., 2019). However, their main purpose is to interpret the inception of strain localization in unsaturated soils only.

In this study, the critical state constitutive model for unsaturated compacted soil is proposed and validated. It is fabricated by incorporating: Bishop's effective stress; soil water characteristic curve considering the effects of hydraulic hysteresis and packing density; and

state boundary surface that moves in volumetric direction due to variation in the degree of saturation. Subloading surface concept has also been applied to the model to consider the effect of packing density on the stress-strain characteristics. By the proposed model, series of simulations starting from the beginning of compaction process through the failures of compacted soils are produced. The effects of compaction water content and compaction effort on the characteristic behavior of unsaturated compacted soil are investigated. Then, the responses of unsaturated compacted soils against long term shearing, heavy rainfall and fully undrained cyclic shearing which rely on its characteristic after compaction are also interpreted.

In addition, in this study, the proposed model is utilized for the soil-water-air three-phases seepage-deformation coupled FEM for the unsaturated porous media. By this tool, we could extend the capability of the model to investigate the effect of heterogeneity of substance soil in compaction which certainly find in the real condition of geotechnical work. In this study, the numerical investigations of 1-D static compaction mechanisms considering the effect of heterogeneities of dry density and degree of saturation at the initial state in unsaturated porous media is performed by the in-house coupled FEM program for unsaturated soil.

Finally, with the proposed constitutive model for unsaturated soil and soil-water-air three-phases seepage-deformation coupled FEM for the unsaturated porous media, we aim to predict the behavior of soil structure from compaction considering the heterogeneity of the initial state of soil for imitating the real condition of soils. Afterwards, we would like to recommend the optimum compaction control parameter specifications through the compaction curve for the soil structures under the service and the catastrophic (e.g., heavy rainfall and liquefaction) situations and the heterogeneity alleviation after compaction. The quality control of soil preparation for compaction test is also recommended.

1.2 RESEARCH OBJECTIVES.

The main objective of this research is to predict the behavior of soil structure from compaction through a numerical method incorporating the proposed constitutive model for compaction.

Sub-objectives are indicated below in order to response the main research objective.

1) To propose the coupled hydro-mechanical constitutive model for the unsaturated compacted soils and the simulation algorithm through the lifetime of compacted soil.
2) To predict the compaction mechanism and characteristic behaviors of compacted soil through the lifetime of compacted soil by the proposed constitutive model.
    a. To study the effects of compaction water content and compaction effort on the characteristic behaviors of compacted soils.

b. To study the characteristic behavior of unsaturated compacted soils under i) fully drained monotonic static loading, ii) hydraulic collapse and iii) fully undrained cyclic static loading.

3) To propose a soil-water-air three-phases seepage-deformation coupled FEM incorporated the proposed constitutive model for compaction.
4) To predict the behaviors of soil structure from compaction by incorporating the heterogeneity of substance soil for imitating the real condition of geotechnical work using the proposed coupled FEM.
5) To recommend the optimal specification of compaction control parameter for each construction purpose of the soil structure, including static shearing, cyclic shearing and heavy rainfall resistances, and for heterogeneity alleviation.

The main objective could be achieved by the accomplishment of the sub-objectives as summarized in the framework of dissertation (Section 1.3).

1.3 FRAMEWORK OF THE DISSERTATION

The synopsis of the research work in each chapter is summarized here in order to illustrate the framework of this study.

Chapter 1 Introduction

This chapter describes the background, objectives and framework of this research.

Chapter 2 An elastoplastic constitutive model for unsaturated soils

In this chapter, concept of the proposed elastoplastic constitutive model for unsaturated soil (Kikumoto et al. (2010) and Komolvilas & Kikumoto (2017)) used in this study is thoroughly explained. In addition, the constitutive relationship for each considering testing condition, including adjusting water content, compaction, monotonic shearing, fully undrained cyclic loading and hydraulic collapse, which is the combination between the rate form of elastoplastic stress-strain relationship of unsaturated soil and the drainage conditions are also presented.

Chapter 3 Parameter calibration and model validation of constitutive model for unsaturated soils

In this chapter, the series of experimental tests conducted by Koike (2010) on the 5:5 mixed Toyoura sand and Fujinomori clay by weight which is related to the compaction, shearing and soaking processes are briefly described. The calibrated constitutive model parameters and soil water characteristic curve parameters of the considered soil are used in the model validation through the experiments that was conducted by Koike (2010). The ability of

the constitutive model for unsaturated soils on the prediction of the compaction, the shearing and the soaking process of unsaturated compacted soils are presented.

Chapter 4 Interpretation of compacted soil behaviors through the constitutive model for unsaturated soils

In this chapter, recent studies of many researchers about the characteristics of compacted soil at the origin, the strength and the failure of compacted soils under the various loadings, including the long term shearing, the hydraulic collapse due to the heavy rainfall, the shear strength after soaking and the liquefaction due to the fully undrained cyclic shearing are summarized. Then, by the proposed model, the compaction mechanisms and the compacted soil behaviors under the considered various loads are investigated and discussed under the proposed simulation algorithm through its lifetime of compacted soil. The ability of the proposed model for the predicting the progressive life of compacted soil is illustrated. The characteristic of compacted soil behaviors along the compaction curve are also interpreted and recommended as the optimal specification of compaction control parameter for the considering loading case in the continuum mechanics.

Chapter 5 Finite element analysis for unsaturated soils

In this chapter, general steps of Galerkin's FEM are briefly described. Follow the general steps of FEM, we generate the in-house FEM programs by the assumption of 2-D plain strain condition starting from the simple algorithm of saturated soil through the complicated algorithm of unsaturated soil (passive air pressure). By this assumption, the applications of the program are limited for the loading conditions, oedometer compression and biaxial shearing, and drainage conditions, fully drained and exhausted air – undrained water. Then, the in-house FEM programs are validated through the exact solution or the proposed constitutive model in order to ensure their algorithm and accuracy for predicting the behavior of saturated and unsaturated soils.

Chapter 6 Effect of heterogeneity in 1-D static compaction

In this chapter, recent studies of many researchers about the investigations of the compaction mechanism and heterogeneity effect at the initial state of unsaturated soil by coupled FEM algorithms for unsaturated soil are summarized. Then, in the scope of this study, the numerical investigations considering the heterogeneity effects of unsaturated soil at the initial state, including dry density and degree of saturation, on 1-D static compaction mechanism are performed using 2-D soil-water-air three-phases seepage-deformation coupled FEM (passive pore air pressure) as proposed in Chapter 5. The effects of heterogeneity at the initial state, including the arrangement of initial element dry density and the variation of initial

element dry density, on the characteristic behavior of compacted soil are investigated. Moreover, the effects of compaction water content and compaction effort along the compaction curve on the variation of heterogeneity during compaction are also illustrated. Finally, the optimum specification of compaction control parameter for the considering soil structure construction purpose and heterogeneity alleviation are recommended. The implementation to the quality control of soil preparation for compaction test in the laboratory are also explained.

Chapter 7 Concluding remarks and future research

In this chapter, overall activities, result and discussing of the study are summarized. Lastly, we would like to point out the gained benefits from the study and the improvement of the current study for the future research.

CHAPTER 2

ELASTOPLASTIC CONSTITUTIVE MODEL FOR UNSATURATED SOILS

Since the compaction shall be discussed through the mechanics of unsaturated soil, the concept of coupled hydro-mechanical elastoplastic constitutive model for unsaturated soils (Kikumoto et al., 2010 and Komolvilas and Kikumoto, 2017) is proposed in this study. In addition to the model's capability for the prediction of unsaturated soil behaviors, the extension concept of soil water characteristic curve by incorporating the effects of density and hysteresis (Section 2.2), is also proper to predict the unique mechanism of compaction, e.g., the effect of density on the post compaction suction (Tarantino and Tombolato, 2005 and Tarantino and De col, 2008) and the imitation of the realistic behavior of compaction by compaction and unloading process.

In the big picture (Figure 2-1), the proposed coupled hydro-mechanical elastoplastic constitutive model for unsaturated soils is fabricated by incorporating: Bishop's effective stress; soil water characteristic curve considering the effects of hydraulic hysteresis and packing density; and state boundary surface that moves in volumetric direction due to variation in the degree of saturation. Subloading surface concept has also been applied to the model to consider the effect of packing density on the stress-strain characteristics. The proposed model assumes associated flow rule and employs a conventional nonlinear elastic relationship with a swelling index κ and Poisson's ratio ν_e in the same way as modified Cam-clay.

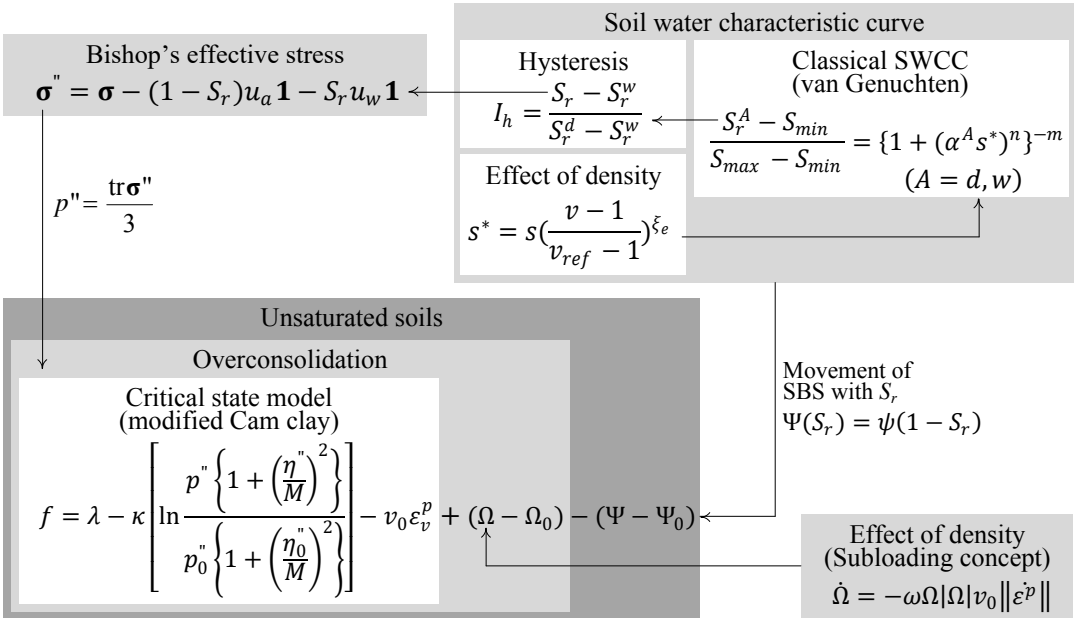

Figure 2-1 Basic concept of constitutive model for unsaturated soils.

2.1 EFFECTIVE STRESS

In unsaturated soils, the porous media filled with two fluid phases (water and air), the single effective stress $\boldsymbol{\sigma}''$ is defined as:

$$\boldsymbol{\sigma}'' = \boldsymbol{\sigma} - \{\beta_{u_a} u_a + \beta_{u_w} u_w\}\mathbf{1} \tag{2-1}$$

where $\boldsymbol{\sigma}$ denotes the Cauchy's total stress tensor; β_{u_a} and β_{u_w} are the scaling effects of pore air pressure u_a and pore water pressure u_w, respectively, on the overall behavior (Khalili et al., 2005).

The Bishop's effective stress tensor $\boldsymbol{\sigma}''$ (Bishop, 1959) which the scaling effects of water and air phases are represented by effective stress parameter χ (lying in the width range of 0 for fully–dried and 1 for fully–saturated) and $1-\chi$, respectively, is given as:

$$\boldsymbol{\sigma}'' = \boldsymbol{\sigma} - \{(1-\chi)u_a + \chi u_w\}\mathbf{1} = \underbrace{(\boldsymbol{\sigma} - u_a\mathbf{1})}_{\boldsymbol{\sigma}_{net}} + \chi \underbrace{(u_a - u_w)}_{s}\mathbf{1} \tag{2-2}$$

where s represents suction $(u_a - u_w)$; $\boldsymbol{\sigma}_{net}$ is net stress tensor; and $\boldsymbol{\sigma}''$ reduces to Terzaghi's effective stress $\boldsymbol{\sigma}'(= \boldsymbol{\sigma} - u_w\mathbf{1})$ at the saturated state.

Regarding the experimental results using volume change and shear strength processes, measured effective stress parameter χ evidences a trend that follows the variation of degree of saturation S_r as shown in Figure 2-2 (Bishop and Donald, 1961; Bishop et al., 1960; Jennings and Burland, 1962). Consequently, a uniqueness of the relationship between χ and S_r which was suggested by Schrefler (1984) as shown in Equation (2-3) is incorporated to the Bishop's effective stress in this study for the sake of simplicity.

$$\chi = S_r \tag{2-3}$$

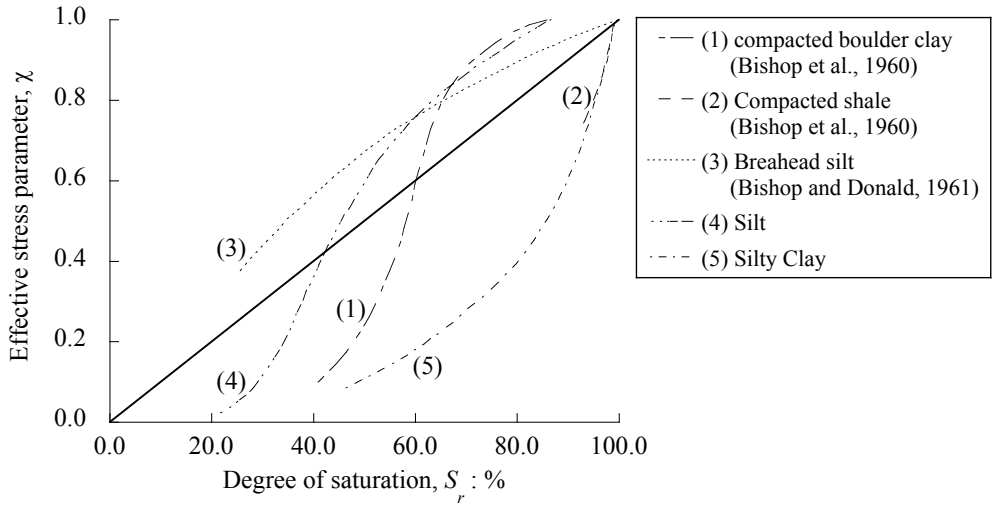

Figure 2-2 The relations of effective stress parameter and degree of saturation for various soil type (Jennings and Burland, 1962)

Substitute Equation (2-3) into Equation (2-2), Bishop's effective stress can be written as:

$$\boldsymbol{\sigma}'' = \boldsymbol{\sigma} - (1 - S_r)u_a\mathbf{1} - S_r u_w\mathbf{1} = \underbrace{(\boldsymbol{\sigma} - u_a\mathbf{1})}_{\boldsymbol{\sigma}_{net}} + S_r \underbrace{(u_a - u_w)}_{s}\mathbf{1} \tag{2-4}$$

By the incorporation, the interpretations of effective stress for critical state line or CSL highlight a uniqueness of CSLs regardless of the degree of saturation as reported by Nuth and Laloui (2008). They observed the uniqueness of CSL by the reinterpretation of the experiment data conducting by Sivakumar (1993) and Geiser et al. (2006) using the invariants of Bishop's effective stress $p''\left(=\frac{\mathrm{tr}\boldsymbol{\sigma}''}{3}\right)$ and $q\left(=\sqrt{\frac{3}{2}}\|\mathbf{s}\| = \sqrt{\frac{3}{2}}\left\|\boldsymbol{\sigma} - \frac{\mathrm{tr}\boldsymbol{\sigma}}{3}\mathbf{1}\right\|\right)$ with $\chi = S_r$. This encourages simplification of parameter determination, assuming that critical state stress ratio M for saturated parameters are sufficient to describe both saturated and unsaturated critical state behaviors.

In conclusion, the Bishop's effective stress is selected as a single effective stress for the proposed model of unsaturated soil in this study due to the following reasons;

- Averaging the stresses over a representative elementary volume containing all constituents: air, water and solid grains.
- Simple transition from the unsaturated state to the fully saturated state by the function of effective stress parameter that lies in the range of 0 to 1.
- The simplification of parameter determination due to a uniqueness of CSLs regardless of the degree of saturation.

2.2 SOIL WATER CHARACTERISTIC CURVE (SWCC)

In this study, a rational soil water characteristic curve or SWCC, which is extended from a classical SWCC (van Genuchten, 1980) to incorporate the effects of density and hysteresis, is applied into the proposed model for predicting the hydraulic behavior of unsaturated soils.

First, the effective degree of saturation S_e is defined for the possible S_r ranging from 0 to 1 as:

$$S_e = \frac{S_r - S_{min}}{S_{max} - S_{min}} \tag{2-5}$$

where S_{max} and S_{min} are the maximum and minimum degrees of saturation, respectively. In this study, using the classical SWCC model which was proposed by van Genuchten (1980), S_e in the single-value function of suction can be written as:

$$S_e = S_e(s) = \{1 + (\alpha s)^n\}^{-m} \tag{2-6}$$

where α, n, and $m(= 1 - \frac{1}{n})$ are the material parameters.

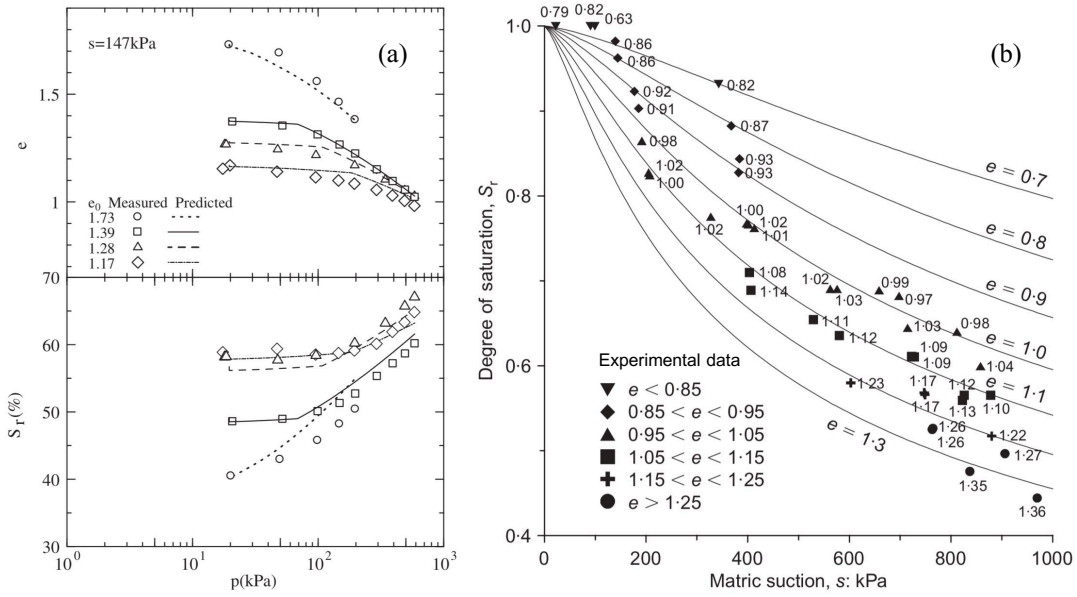

Figure 2-3 Effect of density on SWCCs : the experimental data during (a) the compression test under constant suction (Sun et al. 2007b) and (b) the compaction test (Tarantino and Tombolato, 2005)

Regarding the experimental results which were conducted by many researchers, they indicated that the specific volume affects the locations of main SWCCs where the denser soils tend to retain higher S_r as illustrated in Figure 2-3(a) for the constant suction case during fully drained compression test (Sun et al., 2007b) and Figure 2-3(b) for the suction reduction during compaction (Tarantino and Tombolato, 2005 and Tarantino and De col, 2008). Therefore, the classical SWCC model is extended using a modified suction s^*, where the effect of density is scaled by the volume of voids as shown by:

$$s^* = s\left(\frac{v-1}{v_{ref}-1}\right)^{\xi_e} \tag{2-7}$$

where v is the specific volume, v_{ref} is a reference specific volume at which s^* is equal to the matric suction s, and ξ_e is a parameter controlling the effect of specific volume. Thus, using s^*, Equation (2-6) is rewritten as:

$$S_e = S_e(s^*) = \{1 + (\alpha s^*)^n\}^{-m} \tag{2-8}$$

Combining the Equations (2-5) and (2-8), the general equation for SWCCs which is the value of degree of saturation as the function of modified suction can be written as:

$$S_r = S_{min} + (S_{max} - S_{min})\{1 + (\alpha s^*)^n\}^{-m} \tag{2-9}$$

Regarding the experimental results and interpretation of many researchers (e.g., Sun et al., 2007a; Tsiampousi et al., 2013 and Lu and Khorshidi, 2015), they have indicated the trace

hysteric paths of SWCCs according to drying and wetting cycles. Therefore, using Equation (2-9), the main drying and wetting curves are defined, which gives the maximum and minimum bounding values of the degree of saturation, $S_{\mathrm{r}}^{\mathrm{d}}$ and $S_{\mathrm{r}}^{\mathrm{w}}$, respectively, as:

$$S_r^A = S_{min} + (S_{max} - S_{min})\{1 + (\alpha^A s^*)^n\}^{-m};\ \ A = d \vee w \tag{2-10}$$

where d and w denote the main drying and wetting curves, respectively. The main drying and wetting curves are schematically illustrated in Figure 2-4. A unified set of parameters is applied for n and m, while α^d and α^w are the parameters for the main drying and wetting curves, respectively. Regarding the typical SWCCs as observed in the experiments a value of α^d is defined as the smaller value than α^w which results in $S_r^d(s^*) \geq S_r^w(s^*)$.

In order to indicate the current state of degree of saturation in the boundary of main SWCCs, Figure 2-4, a ratio I_h of internal division ranging from 0 ($S_r = S_r^w$) to 1 ($S_r = S_r^d$) can be defined as a state parameter by:

$$I_h = \frac{S_r - S_r^w}{S_r^d - S_r^w} \tag{2-11}$$

Therefore, the current state of degree of saturation in the function of modified suction in the boundary of main SWCCs can be written as:

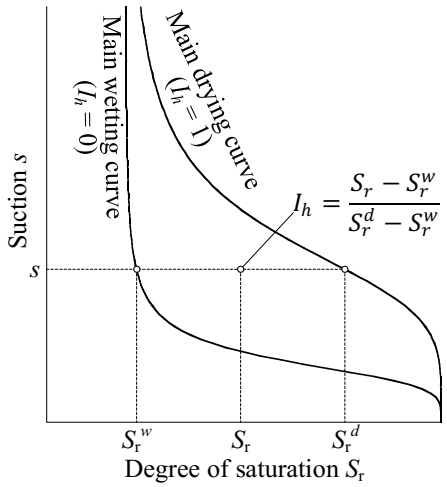

Figure 2-4 Main wetting and drying curves, and definition of state parameter I_h for the hysteresis effect.

$$S_r = I_h S_r^d + (1 - I_h) S_r^w \tag{2-12}$$

The time derivative of degree of saturation in the function of I_h, s and v $\dot{S}_{\mathrm{r}}(I_h, s, v)$ is given as follows:

$$\dot{S_r} = \frac{\partial S_r}{\partial I_h}\dot{I_h} + \frac{\partial S_r}{\partial s}\dot{s} + \frac{\partial S_r}{\partial v}\dot{v} \tag{2-13}$$

In Equation (2-13), the time derivatives of suction $\dot{s}$ and specific volume $\dot{v}$ are directly evaluated by the stress-strain relationship of the unsaturated model. While the time derivative of I_h is depend on the current state of SWCCs. I_h monotonically increases to 1 (decreasing S_r or drying) tills the current state approaches the main drying curve, and it monotonically decreases to 0 (increasing S_r or wetting) tills the current state approaches the main wetting curve. Thus, an evolution law for I_h needs to satisfy the following requirements.

$$\dot{I_h}\begin{cases} > 0 \;\; when \;\; \dot{S_r} < 0 \; and \; 0 \le I_h < 1 \\ < 0 \;\; when \;\; \dot{S_r} > 0 \; and \; 0 < I_h \le 1 \\ = 0 \quad else \end{cases} \tag{2-14}$$

A simple, third–order evolution law which satisfies this requirement is employed herein:

$$\dot{I_h} = \frac{dI_h}{dS_r}\dot{S_r} \;\; where \;\; \frac{dI_h}{dS_r} = \begin{cases} -\xi_h(1-I_h)^3 & when \;\; \dot{S_r} \le 0 \\ -\xi_h {I_h}^3 & when \;\; \dot{S_r} > 0 \end{cases} \tag{2-15}$$

where ξ_h is the material constant controlling the rate of evolution of I_h.

Finally, substitution (2-15) into Equations (2-13), the time derivative of degree of saturation $\dot{S}_\mathrm{r}$ is rewritten by:

$$\dot{S_r} = \frac{\frac{\partial S_r}{\partial s}\dot{s} + \frac{\partial S_r}{\partial v}\dot{v}}{1 - \frac{\partial S_r}{\partial I_h}\frac{dI_h}{dS_r}} \tag{2-16}$$

In the simulation, from Equation (2-10) and Equation (2-12), the gradients of S_r with the control parameter I_h, s and v in Equation (2-13) are written by Equations (2-17), (2-18) and (2-19), respectively, using the chain rule as:

$$\frac{\partial S_r}{\partial I_h} = S_r^d - S_r^w \tag{2-17}$$

$$\frac{\partial S_r}{\partial s} = \frac{\partial S_r}{\partial s^*}\frac{\partial s^*}{\partial s} = \left(\frac{\partial S_r}{\partial S_r^d}\frac{dS_r^d}{ds^*} + \frac{\partial S_r}{\partial S_r^w}\frac{dS_r^w}{ds^*}\right)\frac{\partial s^*}{\partial s} \tag{2-18}$$

$$\frac{\partial S_r}{\partial v} = \frac{\partial S_r}{\partial s^*}\frac{\partial s^*}{\partial v} = \left(\frac{\partial S_r}{\partial S_r^d}\frac{dS_r^d}{ds^*} + \frac{\partial S_r}{\partial S_r^w}\frac{dS_r^w}{ds^*}\right)\frac{\partial s^*}{\partial v} \tag{2-19}$$

where

$$\frac{\partial S_r}{\partial S_r^d}\frac{dS_r^d}{ds^*} = I_h(S_{max} - S_{min})(-m)\left\{1 + \left(\alpha^d s^*\right)^n\right\}^{-m-1}{\alpha^d}^n n{s^*}^{n-1} \tag{2-20}$$

$$\frac{\partial S_r}{\partial S_r^w}\frac{dS_r^w}{ds^*} = (1 - I_h)(S_{max} - S_{min})(-m)\{1 + (\alpha^w s^*)^n\}^{-m-1}{\alpha^w}^n n{s^*}^{n-1} \tag{2-21}$$

$$\frac{\partial s^*}{\partial s} = \left(\frac{v-1}{v_{ref}-1}\right)^{\xi_e} \tag{2-22}$$

$$\frac{\partial s^*}{\partial v} = \frac{s\xi_e}{(v-1)}\frac{\partial s^*}{\partial s} \tag{2-23}$$

2.3 STRESS–STRAIN RELATIONSHIP OF ELASTOPLASTIC UNSATURATED SOIL

In this study, the proposed elastoplastic stress–strain relationship for unsaturated soils is thoroughly described. Considering the small strain level, an additive decomposition of the total strain rate tensor is assumed in this study as written by:

$$\dot{\boldsymbol{\varepsilon}} = \dot{\boldsymbol{\varepsilon}}^e + \dot{\boldsymbol{\varepsilon}}^p \tag{2-24}$$

where $\dot{\boldsymbol{\varepsilon}}^e$ and $\dot{\boldsymbol{\varepsilon}}^p$ are elastic and plastic strain rate tensors, respectively.

2.3.1 Elasticity

In critical state theory, the elastic volumetric behavior is assumed as the linear relationship in $v - \ln p''$ plane. For a very small increment of effective mean stress, using the Taylor's expression, the variation of specific volume in elastic region dv^e can be written as:

$$dv^e = -\kappa\frac{dp''}{p''} \tag{2-25}$$

where κ is the slope of the swelling line in $v - \ln p''$ plane. Regarding the relation between specific volume and volumetric strain, from Equation (2-25), a nonlinear elastic bulk modulus K is given by:

$$K = \frac{v_0}{\kappa}p'' \tag{2-26}$$

Assuming Poisson's ratio ν_e is constant, the shear modulus G is given by

$$G = \frac{3K(1-2\nu_e)}{2(1+\nu_e)} \tag{2-27}$$

Thus, the isotropic elastic stress-strain relationship can be written by

$$\dot{\boldsymbol{\sigma}}'' = \underbrace{\left\{K\mathbf{1}\otimes\mathbf{1} + 2G\left(\boldsymbol{I} - \frac{1}{3}\mathbf{1}\otimes\mathbf{1}\right)\right\}}_{\boldsymbol{D}^e} : \dot{\boldsymbol{\varepsilon}}^e \tag{2-28}$$

where $\dot{\boldsymbol{\sigma}}''$ is the rate of Bishop's effective stress tensor and $\boldsymbol{D}^{\mathrm{e}}$ is the elastic stiffness tensor.

2.3.2 State boundary surface

In the critical state theory, for the saturated normal consolidated (NC) soil, the isotropic normal consolidation line or NCL which is caused by the isotropic compression and the critical

state line or CSL which is caused by the shearing to the critical state (no change in imposed stresses or volume of the soil) are assumed as the linear relationship in $v - \ln p'$ plane with the compression index λ as the slope. The equations of NCL and CSL can be written by Equation (2-29) and Equation (2-30), respectively:

$$v = N - \lambda ln\,(\frac{p'}{P_a}) \tag{2-29}$$

$$v = \Gamma - \lambda ln\,(\frac{p'}{P_a}) \tag{2-30}$$

where $p'\left(=\frac{\mathrm{tr}\boldsymbol{\sigma}'}{3}\right)$ and $\eta'\left(=\frac{q}{p'}\right)$ are the mean effective stress and the effective stress ratio given by Cauchy's effective stress tensor $\boldsymbol{\sigma}'(=\boldsymbol{\sigma} - u_{\mathrm{w}}\mathbf{1})$ at the saturated state, respectively. At the saturated state under atmospheric pressure ($p' = P_a$) in Figure 2-5, N and Γ are the reference specific volumes on the NCL at isotropic stress ($\eta' = 0$) and on the CSL at critical state ($\eta' = M$), respectively.

The loosest specific volume surface along and on the NCL and CSL which is known as the State Boundary Surface or SBS is uniquely defined and linearized in the $lnp' - \zeta(\eta')$– v plane (Figure 2-5). When the current state of soil is a point below the SBS, then soil behavior is elastic. While, soil states on the SBS indicate yielding, and it is impossible for the states equivalent to points above the SBS. The reference specific volume ($p' = P_a$) on SBS could be linearly interpolated between N ($\eta' = 0$ on NCL) and Γ ($\eta' = M$ on CSL). Then, the specific volume on SBS at any η' for saturated soil v_{sbs}^{sat} can be written by:

$$v \le v_{sbs}^{sat} = N - \lambda\, ln\frac{p'}{p_a} - (N - \Gamma)\zeta(\eta') \tag{2-31}$$

where $\zeta(\eta')$ is a monotonic increasing function of η' that satisfies 0 at the isotropic stress state ($\eta' = 0$) and 1 at the critical state ($\eta' = M$). The simplest form of $\zeta(\eta')$ is a linear function $\frac{\eta'}{M}$, which was employed in the original Cam clay model (Roscoe et al. 1958). In this study, we use a nonlinear function based on modified Cam-clay (Roscoe & Burland, 1968) as written by:

$$\zeta(\eta') = \frac{ln\left\{1 + \left(\frac{\eta'}{M}\right)^2\right\}}{ln\,2} \tag{2-32}$$

Capturing the behavior of unsaturated soils, in addition to defining the SBS using the Bishop's effective stress $\boldsymbol{\sigma}''$ as explained in Section 2.1, assuming the movement of specific volume of unsaturated NC soils in the volumetric direction by the variation of degree saturation is basically applied for the constitutive model of unsaturated soil. This assumption relies on the experimental evidences that (i) the current loosest state of specific volume of unsaturated soils

tend to retain larger volume than the saturated soil at the same stress (Jennings and Burland, 1962), (ii) the critical state specific volume of unsaturated soils tend to be larger than the saturated soil (Sivakumar 1993), (iii) the variation of degree of saturation (wetting) affects the volumetric response of unsaturated soil (Jennings and Burland, 1962; Sun et al., 2007c and Tadepalli and Fredlund, 1991) and (iv) the collapsed sample follows the stress-strain path of the initially saturated sample in compression once it wet (Jennings and Burland, 1962 and Sun et al, 2007c). For this assumption, we assume that the specific volume of unsaturated NC soils increases by $\Psi(S_r)$ with decreasing the degree of saturation in the volumetric directions and also in the reverse direction.

Therefore, using $\Psi(S_{\mathrm{r}})$, the specific volume on the state boundary surface v_{sbs} of unsaturated soils is defined as:

$$v \le v_{sbs} = \underbrace{N - \lambda \ln\frac{p''}{p_a} - (N-\Gamma)\zeta(\eta'')}_{v_{sbs}^{sat}} + \Psi(S_r) \tag{2-33}$$

where η'' is the Bishop's effective stress ratio and $\Psi(S_r)$ is a non–negative simplest linear function of the degree of saturation S_{r}, which monotonically decreases to 0 as S_{r} approaches 1 (fully saturated state) which is introduced as:

$$\Psi = \psi(1 - S_r) \tag{2-34}$$

where ψ is a material parameter representing the volumetric distance between the SBSs of fully–dried and fully–saturated states in the v direction. Using this function, in the fully saturated state ($S_{\mathrm{r}} = 1$), Equation (2-33) for unsaturated state can simply transit to Equation (2-31) for the saturated stated.

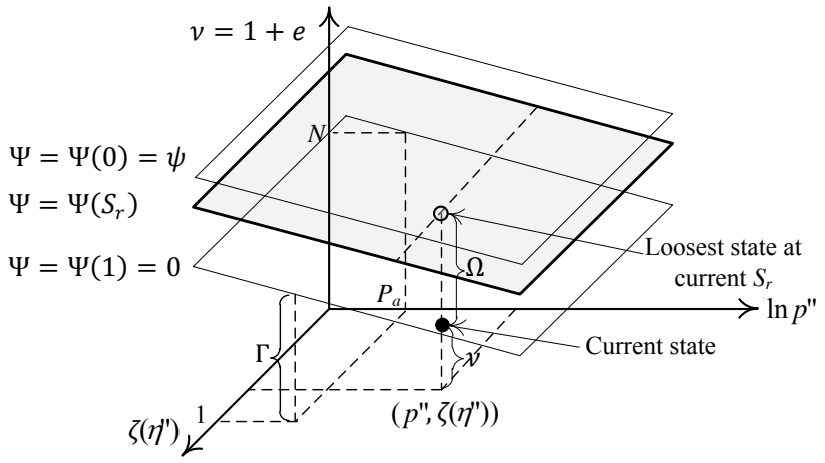

Figure 2-5 State boundary surface for unsaturated soils: loosest specific volume defined by p'', q and S_r.

In the next section, the yield function *f* for unsaturated soil is given considering this movement of the proposed state boundary surface.

2.3.3 Yield function, plastic potential, and flow rule.

Since the soil states on the SBS and below the SBS indicate the pure plastic and elastic behaviors, respectively. The difference Ω between the specific volume on the SBS and the current specific volume under the current mean effective stress p'', deviator stress q, and degree of saturation S_r (Figure 2-5) is applied as a measure of density (Kikumoto et al. 2010). A non-negative Ω can be written by:

$$\Omega = v_{sbs} - v(\geq 0) \tag{2-35}$$

Below the SBS, although the classical critical state models predict purely elastic behavior while at the same time the actual soils exhibit elastoplastic irreversible deformation. Thus, a subloading (bounding) surface (Hashiguchi and Ueno 1977; Dafalias and Popov 1975) is used to describe a smooth transition from elastic to plastic behavior. The normal yield (bounding) surface, $\tilde{f}$ is defined by:

$$\tilde{f} = v - v_{sbs}(\leq 0) \tag{2-36}$$

where the parameter, Ω, given by equation (2-35) is used as a state variable to scale the distance from the current state to the normal yield (bounding) surface. From Equations (2-35) and (2-36), the yield function for unsaturated soils is derived:

$$f = v - v_{sbs} + \Omega \equiv 0 \tag{2-37}$$

where the function f is identically equal to zero from Equation (2-35).

The variables $(v, p'', \eta'', S_r, \Omega)$ at the initial state and the current state are hereafter denoted by $(v_0, p_0'', \eta_0'', S_{r0}, \Omega_0)$ and $(v, p'', \eta'', S_r, \Omega)$, respectively. The variation in the specific volume from the initial to the current state, $\Delta v(= v - v_0)$, can be decomposed into the elastic and plastic variations in the specific volume, Δv^e and Δv^p when $\varepsilon_{v0}^p(= 0)$:

$$\Delta v(= v - v_0) = \underbrace{\left(-\kappa \, ln\frac{p''}{p_0''}\right)}_{\Delta v^e} + \underbrace{\left(-v_0 \varepsilon_v^p\right)}_{\Delta v^p} \tag{2-38}$$

where $\varepsilon_v^p(= \mathrm{tr}\boldsymbol{\varepsilon}^{\mathbf{p}})$ denotes plastic volumetric strain. From Equation (2-33) and (2-35), the initial specific volume v_0 on the left hand side in Equation (2-38) can be written as:

$$v_0 = N - \lambda \, ln\frac{p_0''}{p_a} - (N - \Gamma)\zeta(\eta_0'') + \Psi_0 - \Omega_0 \tag{2-39}$$

Substituting Equations (2-33), (2-38) and (2-39) into the Equation (2-37), the yield function for unsaturated soil can be rewritten as:

$$f\left(p'', \eta'', \varepsilon_v^p, \Psi, \Omega\right) = \underbrace{(\lambda - \kappa)\, ln \frac{p''}{p_0''} + (N - \Gamma)\{\zeta(\eta'') - \zeta(\eta_0'')\}}_{F(\boldsymbol{\sigma})} - \underbrace{\left\{v_0 \varepsilon_v^p + (\Psi - \Psi_0) - (\Omega - \Omega_0)\right\}}_{H\left(\varepsilon_v^p, \Psi, \Omega\right)} \tag{2-40}$$

Unsaturated soils are assumed to obey associated flow (normality condition) so that the plastic potential, g, is given by the same function, f, in the stress space. Then the direction of the plastic strain rate, $\dot{\boldsymbol{\varepsilon}}^p$, is given by $\frac{\partial f}{\partial \boldsymbol{\sigma}''}$.:

$$\dot{\boldsymbol{\varepsilon}}^p = \langle \dot{\Lambda} \rangle \frac{\partial f}{\partial \boldsymbol{\sigma}''} \tag{2-41}$$

As the soil does not exhibit any dilation at the critical state ($\eta = M$), following condition is obtained:

$$\left.\frac{\partial f(p'', q)}{\partial p''}\right|_{\eta = M} = 0 \tag{2-42}$$

From Equations (2-32) and (2-40), Equation (2-42) reduces to:

$$N - \Gamma = ln\, 2\, (\lambda - \kappa) \tag{2-43}$$

and the yield function (and plastic potential function) is as follows.

$$f\left(p'', \eta'', \varepsilon_v^p, \Psi, \Omega\right)(= g) = \underbrace{(\lambda - \kappa)\, ln \frac{p''\left\{1 + \left(\frac{\eta''}{M}\right)^2\right\}}{p_0'\left\{1 + \left(\frac{\eta_0''}{M}\right)^2\right\}}}_{F(\boldsymbol{\sigma})} - \underbrace{\left\{v_0 \varepsilon_v^p + (\Psi - \Psi_0) - (\Omega - \Omega_0)\right\}}_{H\left(\varepsilon_v^p, \Psi, \Omega\right)} \equiv 0 \tag{2-44}$$

Here, $F(\boldsymbol{\sigma})$ is the yield stress function and $H\left(\varepsilon_{\mathrm{v}}^p, \Psi, \Omega\right)$ is the isotropic hardening function. Note that the function *f* identically equals zero regardless of plastic deformation volumetric strain. The function *f* satisfies the necessary condition that the yield function is a non–positive, convex function of stress $\boldsymbol{\sigma}''$ and hardening parameters $\varepsilon_{\mathrm{v}}^p$, Ψ, and Ω.

2.3.4 Loading / unloading conditions

In any loading path, the Kuhn–Tucker conditions (Kuhn and Tucker, 1951) as shown in Equation (2-45) must be satisfied.

$$f \leq 0;\ \dot{\Lambda} \geq 0;\ \dot{\Lambda} f = 0 \tag{2-45}$$

As the yield function applied in the proposed model (Equation (2-44)) is identically equal to zero, the loading conditions can be simplified to:

$$\dot{\Lambda} \geq 0 \tag{2-46}$$

where $\dot{\Lambda} = 0$ corresponds to elastic behavior (neutral; unloading) and plastic deformation is exhibited for $\dot{\Lambda} > 0$ (loading).

2.3.5 Consistency condition and hardening laws

When soil exhibits elastoplastic deformation, the consistency condition that the time derivative of the yield function $f\left(\boldsymbol{\sigma}'', \varepsilon_{\mathrm{v}}^{\mathrm{p}}, \Psi, \Omega\right)$ is zero needs to be satisfied.

$$\dot{f} = \frac{\partial f}{\partial \boldsymbol{\sigma}''} : \dot{\boldsymbol{\sigma}}'' + \frac{\partial f}{\partial \varepsilon_v^p} \dot{\varepsilon_v^p} + \frac{\partial f}{\partial \Psi} \dot{\Psi} + \frac{\partial f}{\partial \Omega} \dot{\Omega} = 0 \tag{2-47}$$

Hardening rule for the plastic volumetric strain, ε_v^p, is given as follows.

$$\frac{\partial f}{\partial \varepsilon_v^p} \dot{\varepsilon_v^p} = -v_0 \langle \dot{\Lambda} \rangle tr \frac{\partial f}{\partial \boldsymbol{\sigma}''} \tag{2-48}$$

Hardening and softening also occur due to the decrease and increase in the degree of saturation, respectively, from Equation (2-34).

$$\frac{\partial f}{\partial \Psi} \dot{\Psi} = \psi \dot{S_r} \tag{2-49}$$

As Ω is the parameter scaling the volumetric distance from the current state to the normal yield (bounding) surface, it must decrease with the development of plastic deformation and converge to 0. So, in case a soil exhibits plastic deformation (loading), a simple law enabling such evolution of Ω is given as:

$$\frac{\partial f}{\partial \Omega} \dot{\Omega} = -\omega \Omega |\Omega| v_0 \left\| \dot{\boldsymbol{\varepsilon}^p} \right\| \quad \left(\dot{\Lambda} > 0\right) \tag{2-50}$$

where ω is a parameter controlling the rate of the evolution of Ω.

In case the soil exhibits purely elastic deformation (unloading or neutral), the consistency condition (Equation (2-47)) still needs to be satisfied because the yield function, f, is identically equal to zero (equation (2-37)). Consequently, the evolution law of Ω during unloading or neutral conditions is obtained:

$$\dot{\Omega} = -\frac{\partial f}{\partial \boldsymbol{\sigma}''} : \dot{\boldsymbol{\sigma}}'' - \psi \dot{S_r} \quad \left(\dot{\Lambda} = 0\right) \tag{2-51}$$

2.3.6 Elastoplastic tensor

From Equations (2-24), (2-28) and (2-41) the stress rate tensor is given as:

$$\dot{\boldsymbol{\sigma}}'' = \boldsymbol{D}^e : (\dot{\boldsymbol{\varepsilon}} - \dot{\boldsymbol{\varepsilon}}^p) = \boldsymbol{D}^e : \left(\dot{\boldsymbol{\varepsilon}} - \langle \dot{\Lambda} \rangle \frac{\partial f}{\partial \boldsymbol{\sigma}''}\right) \tag{2-52}$$

Substituting Equation (2-52) and the evolution laws of the hardening parameters given by Equations (2-48), (2-49) and (2-50) in to the consistency condition given by Equation (2-47), the magnitude of the plastic strain rate, $\langle \dot{\Lambda} \rangle$ is given as:

$$\langle \dot{\Lambda} \rangle = \langle \frac{\frac{\partial f}{\partial \boldsymbol{\sigma}''} : \boldsymbol{D}^e : \dot{\boldsymbol{\varepsilon}} + \psi \dot{S}_r}{\underbrace{v_0 tr \frac{\partial f}{\partial \boldsymbol{\sigma}''} + \omega \Omega |\Omega| v_0 \left\| \frac{\partial f}{\partial \boldsymbol{\sigma}''} \right\| + \frac{\partial f}{\partial \boldsymbol{\sigma}''} : \boldsymbol{D}^e : \frac{\partial f}{\partial \boldsymbol{\sigma}''}}_{M^p}} \rangle \tag{2-53}$$

where M^p is the plastic modulus. Finally, the rate form of the elastoplastic stress–strain relationship is given.

$$\dot{\boldsymbol{\sigma}}'' = \boldsymbol{D}^e : \dot{\boldsymbol{\varepsilon}} - \langle \frac{\frac{\partial f}{\partial \boldsymbol{\sigma}''} : \boldsymbol{D}^e : \dot{\boldsymbol{\varepsilon}} + \psi \dot{S}_r}{M^p + \frac{\partial f}{\partial \boldsymbol{\sigma}''} : \boldsymbol{D}^e : \frac{\partial f}{\partial \boldsymbol{\sigma}''}} \rangle \boldsymbol{D}^e : \frac{\partial f}{\partial \boldsymbol{\sigma}''} \tag{2-54}$$

When the rate of the plastic multiplier $\dot{\Lambda}$ is positive, the rate form of the elastoplastic stress–strain relationship Equation (2-54) can be converted to Equation (2-55) as:

$$\dot{\boldsymbol{\sigma}}'' = \underbrace{\left(\boldsymbol{D}^e - \frac{\boldsymbol{D}^e : \frac{\partial f}{\partial \boldsymbol{\sigma}''} \otimes \frac{\partial f}{\partial \boldsymbol{\sigma}''} : \boldsymbol{D}^e}{M^p + \frac{\partial f}{\partial \boldsymbol{\sigma}''} : \boldsymbol{D}^e : \frac{\partial f}{\partial \boldsymbol{\sigma}''}} \right)}_{\boldsymbol{D}^{ep}} : \dot{\boldsymbol{\varepsilon}} - \underbrace{\left(\frac{\boldsymbol{D}^e : \frac{\partial f}{\partial \boldsymbol{\sigma}''} \psi}{M^p + \frac{\partial f}{\partial \boldsymbol{\sigma}''} : \boldsymbol{D}^e : \frac{\partial f}{\partial \boldsymbol{\sigma}''}} \right)}_{\boldsymbol{D}^{Sr}} \dot{S}_r \tag{2-55}$$

In addition, the rate form of elastoplastic Bishop's effective stress – strain relationship for unsaturated soil Equation (2-55) which is generated by the yield function is utilized for conducting the elementary analysis under the specified drainage condition for each testing conditions in Appendix A.

CHAPTER 3

PARAMETER CALIBRATION AND MODEL VALIDATION OF CONSTITUTIVE MODEL FOR UNSATURATED SOILS

In this study, simulating the mechanics of unsaturated soils in regard to the compaction, shearing and soaking processes, first, the proposed constitutive model is validated through the series of experimental results conducted by Koike (2010) using the calibrated constitutive model parameters for unsaturated soil and soil water characteristic curve parameter of the 5:5 mixed Toyoura sand and Fujinomori clay by weight. The series of experiments consist of the mechanisms of soil compaction, the volumetric change of compacted soil due to soaking and the monotonic shearing of unsoaked and soaked compacted soil as briefly explained in Section 3.1. In addition, the capabilities of the proposed constitutive model for predicting the soaking behavior (Komolvilas, 2017) and the liquefaction behavior (Komolvilas & Kikumoto, 2017) of unsaturated soil were previously described. Therefore, the model's applications for predicting the behaviors the compaction, the monotonic shearing, the hydraulic collapse and the liquefaction of unsaturated soils could be applied in this study.

3.1 SERIES OF EXPERIMENTAL TESTS

In order to simulate the mechanics of unsaturated soils in regard to the compaction, the shearing and the soaking processes, three experimental series were conducted for the parameter calibration and model validation. The experimental procedures are briefly explained in this section. Mixed Toyoura sand and Fujinomori clay with the ratio of 5:5 by weight was used as the specimens through the series of experiments. The specific gravity G_s was 2.673. Consistency characteristic of the soil including liquid limit *LL*, plastic limit *PL* and plasticity index I_p were 24.13 %, 15.18 % and 8.95, respectively.

3.1.1 One-dimensional static compaction test

The compaction mechanisms of unsaturated soils were investigated through 1-D static compression test under exhausted-air and undrained-water condition. The standard oedometer testing apparatus was used with the water-impermeable plastic sheets to apply exhausted-air, undrained-water condition. The air-dried specimens were first prepared, and distilled water was added to achieve the prescribed water contents. For each specimen, it was compacted to the vertical compaction stress σ_v from the series of 9.8, 19.6, 39.2, 78.5, 157.0, 314.0, 628.0 and 1256.0 kPa, respectively. Figure 3-4 shows the compression behavior during compaction to the compaction stress 1256.0 kPa of the 3 prescribed water contents. For clear illustration, only

compaction curves of the applied vertical compaction stress 19.6, 157.0, 314.0, 628.0 and 1256.0 kPa are presented in Figure 3-5. Figure 3-5 illustrates that compaction curves only on the dry side could be conducted in the experiments. The compaction curve on the wet side could not be achieved, since the undrained-water condition of the specimens could not be maintained during the compaction. If they could be maintained, the specimens shall be compressed up to the limit of the saturated line as shown by line AA' and BB' in Figure 3-5. Take the shading area as shown in Figure 3-5, for instance of range of expected testing results on the wet side for the compaction stress 1256 kPa.

3.1.2 One-dimensional compression soaking test

The compression and soaking mechanisms of the unsaturated soil were investigated through the series of 1-D compression soaking test (Figure 3-3). The standard consolidation testing machine which normally uses for the fully saturated soils was applied in the experiment without the suction control. The air-dried specimens and the slurry specimens were prepared in the experiments to study the behaviors of unsaturated soils and fully saturated soils, respectively. The air-dried specimens were set under the initial vertical net stress 1.2 kPa with the average initial specific volume v_o 2.323 in the consolidation testing machine. Each specimen was compressed in the fully drained condition to the vertical net stress from the series of 10.7, 20.5, 40.1, 79.4, 157.9, 314.9, 628.9 and 1256.9 kPa, respectively. Then, at the vertical net stress 1.2, 20.5, 157.9 and 1256.9 kPa, the specimens were soaked to fully saturated condition. Regarding the soil saturation with water, Carbon Dioxide (CO_2) was injected from the lower part of the specimen during the soaking process. Finally, the soaked specimens were compressed under the fully drained condition to vertical net stress 1256.9 kPa. While, the slurry specimens with average initial specific volume v_o 2.18 were compressed under fully drained condition from the initial vertical total stress 0.8 kPa to 1256.9 kPa (Figure 3-1). The experimental results (Figure 3-1and Figure 3-3) are used in the parameter calibration (Section 3.2).

For the parameter calibration, 1-D compression soaking test of air-dried specimens were imitated by the simulation in the framework of unsaturated soils. Since the suction was not controlled in the experiments the following assumptions were defined in the simulation. The minimum degree of saturation (S_{min}) was assumed to be 10%. For air-dried state, initial degree of saturation was defined to be 11% in the simulation. In the main wetting path of SWCC (I_h = 0), initial suction s_0 10.68 kPa was calculated by Equation (2-10). Assuming that air pressure u_a 98 kPa (at atmospheric pressure), initial water pressure u_{w0} 87.32 kPa at vertical net stress 1.2 kPa.

3.1.3 Triaxial soaking compression test

The soaking mechanism under anisotropic stress condition of unsaturated soil was investigated through the series of mean stress constant (*p*-constant) compression soaking test. The triaxial testing machine for unsaturated soil was used. Mechanism of testing machine was particularly set to perform the compression soaking test without suction control. For the unsaturated condition, both air and water were allowed to drain by the porous stone embedded with the pedestal at the bottom of the specimen. The volume change of unsaturated specimen was measured by the double cell method. Two set of unsaturated specimens, dense soil (Md) and loose soil (Ml), were prepared. Both of their initial states are summarized in Table 3-1. While, the series of experiments under fully drained condition are listed as shown in Table 3-2. The definitions of the experiment are indicated as follows; UnsatC denotes the monotonic shearing of unsaturated soil in compression, S denotes soaking for the fully saturated state, SatC denotes monotonic shearing of saturated soil in compression and R denotes the amplitude of principle stress ratio. Start with the initial state of unsaturated soil specimens (Table 3-1), three mechanisms were conducted using the triaxial testing machine for unsaturated soil as follows.

3.1.3.1 Monotonic shearing of unsaturated soil (UnsatC)

The monotonic *p*-constant shearing was applied to the specimens till they were approached the critical state of soil by the strain control under fully drained condition. The experimental results of monotonic shearing behavior of specimens Md-UnsatC and Ml-UnsatC are shown in Figure 3-6 and Figure 3-7, respectively.

3.1.3.2 Monotonic shearing of saturated soil after soaking (S-SatC)

The specimens were soaked under *p*-constant to saturated condition by allowing water flow and facilitate the saturation by applying CO_2 from the bottom part to the upper part of the specimen. Then, the monotonic *p*-constant shearing was applied to the saturated specimens until approaching the critical state of soil by strain control under fully drained condition. The experimental results of monotonic shearing behavior of specimens Md-S-SatC and Ml-S-SatC are shown in Figure 3-2.

3.1.3.3 The compression soaking test of unsaturated soil under anisotropic condition. (UnsatC-Ri-S)

The monotonic p-constant shearing was applied to the specimens by stress control under fully drained condition to the prescribed deviatoric stress q. The specimens were soaked with the same method as stated in Section 3.1.3.2 afterwards. The experimental results of monotonic

shearing behavior of specimens Md-UnsatC-Ri-S and Ml-UnsatC-Ri-S are shown in Figure 3-6 and Figure 3-7, respectively.

For parameter calibration and model validation, the experimental results of monotonic shearing of saturated soil after soaking (S-SatC) is used in the parameter calibration section (Section 3.2). While monotonic shearing of unsaturated soil (UnsatC) and compression soaking test of unsaturated soil under anisotropic condition (UnsatC-Ri-S) are used to validate the model described mechanism of monotonic shearing of unsaturated soil (Section 3.3.2). In the simulation of unsaturated soil, using main wetting path Equation (2-10), the calculated initial suctions of Md and Ml were 2.54 kPa and 0.77 kPa respectively. Assuming that u_a is 98 kPa (at atmospheric pressure), u_w is 95.46 kPa for Md and 97.23 kPa for Ml.

Table 3-1 Initial state of unsaturated soil specimens for triaxial compression soaking test series.

Material	Symbol	Void ratio, e	Water content, w_n [%]	Degree of saturation, S_r [%]	Mean net stress, p_{net} [kPa]
Dense	Md	0.693	20.44	78.85	49.0
Loose	Ml	1.010	21.12	55.86	49.0

Table 3-2 Details of triaxial compression soaking test series under fully drained condition.

Material	Experiment name	Details of experiments		
		Stage	Test	Control path
Dense	Md-UnsatC	A	Shearing	strain
	Md-S-SatC	A	Soaking	stress
		B	Shearing	strain
	Md-UnsatC-R3S	A	Shearing	stress (Δq = 58.8 kPa)
		B	Soaking	stress
	Md-UnsatC-R6S	A	Shearing	stress (Δq = 91.9 kPa)
		B	Soaking	stress
Loose	Ml-UnsatC	A	Shearing	strain
	Ml-S-SatC	A	Soaking	stress
		B	Shearing	strain
	Ml-UnsatC-R2S	A	Shearing	stress (Δq = 36.8 kPa)
		B	Soaking	stress
	Ml-UnsatC-R3S	A	Shearing	stress (Δq = 58.8 kPa)
		B	Soaking	stress

3.2 PARAMETER CALIBRATION

A set of constitutive model parameters for unsaturated soil and soil water characteristic curve of 5:5 mixed Toyoura sand and Fujinomori clay by weight (Table 3-3 and Table 3-4) were finally calibrated through the three experimental series conducted by Koike (2010) .

The set of parameters for soil water characteristic curve (SWCC) which extended from the classical SWCC described by van Genuchten (1980) consists of S_{max}, S_{min}, α_d, α_w, n, m, ξ_e and ξ_h. It could be calibrated with the water characteristic curve experiment. The set of parameters for constitutive model for unsaturated soil could be calibrated with 2 main saturation conditions through the experiments. The first group of the parameter is λ, κ, M, ν_e, N and ω which could be obtained from the elementary test of compression and shear in the context of fully - saturated condition. The experimental results of the 1-D consolidation test of slurry sample and triaxial p-constant shearing test after soaking could be predicted well by the simulations obtained from the defined set of parameters as illustrated in Figure 3-1 and Figure 3-2, respectively. The second group of the parameter is ψ that could be obtained from soaking test of the dried soil related to the context of unsaturated condition (Figure 3-3). Since it controls the movement proportion of state boundary surface of soil varying with degree of saturation, so we could determine ψ by the different of the specific volume of soil in the dried state or unsaturated state at the minimum degree of saturation and fully - saturated state. At last, however, the set of parameters in this study was finalized by fitting the simulation to a series of 1-D compression soaking test (Figure 3-3).

Table 3-3 Constitutive model parameters of 5:5 mixed Toyoura sand and Fujinomori clay by weight.

λ	0.12	Compression index
κ	0.01	Swelling index
M	1.30	Critical state stress ratio
ν_e	0.25	Poisson's ratio
N	1.78	Reference ν at saturated state under p" = 98.0 and q = 0.0 kPa
ω	100	Effect of density
ψ	0.35	Volumetric distance between SBSs for fully dried and fully saturated states

Table 3-4 Parameters for soil water characteristic curve.

S_{max}	1.00	Parameters for main wetting and drying curves (van Genuchten's equation)	Maximum degree of saturation
S_{min}	0.10		Minimum degree of saturation
α_d	0.01		Parameter for main drying curve (1/kPa)
α_w	0.60		Parameter for main wetting curve (1/kPa)
n	2.00		Parameters for the shape of main curves
m	0.50		
ξ_h	100	Parameter for hysteresis	
ξ_e	5.00	Parameter for effect of void ratio	

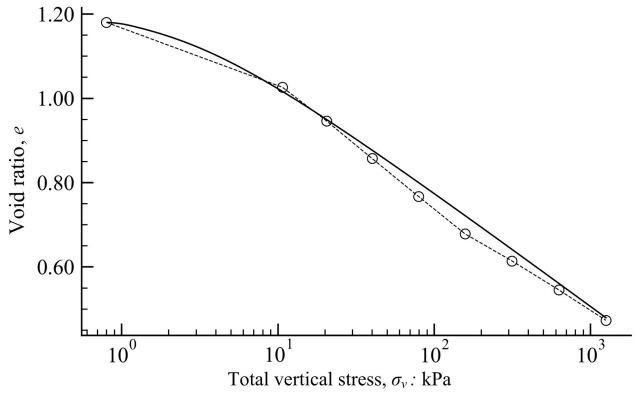

Figure 3-1 Parameter calibration of 1-D compression test of the slurry specimen.

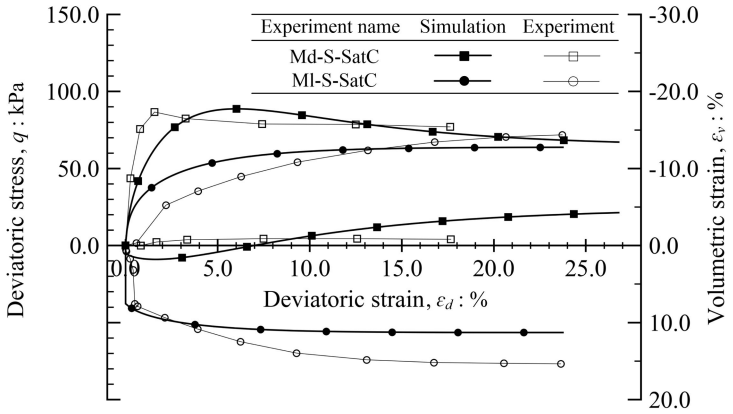

Figure 3-2 Parameter calibration of monotonic shearing of the saturated specimens due to soaking (S-SatC).

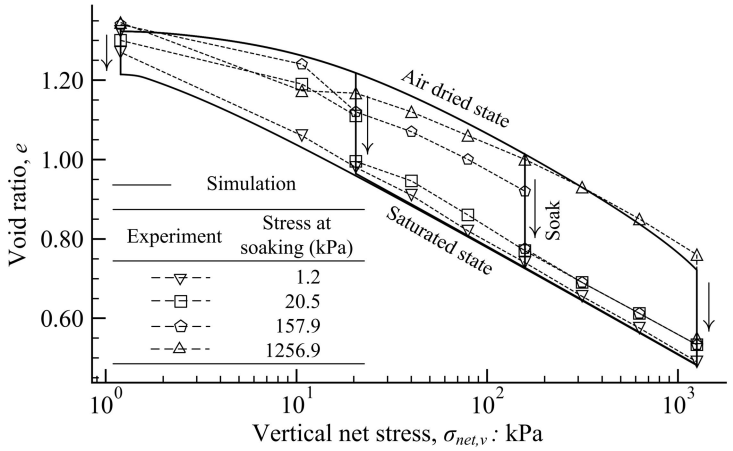

Figure 3-3 Parameter calibration of 1-D compression and compression soaking tests of the air-dried specimens.

3.3 MODEL VALIDATION THROUGH THE EXPERIMENT INVESTIGATION OF UNSATURATED SOIL MECHANISM

In order to simulate the mechanisms of unsaturated soils, including soil compaction, the volumetric change of compacted soil due to soaking and shearing of compacted soil, the proposed constitutive modeling of unsaturated soil was validated through the experiment investigations explained in Section 3.1 using the calibrated constitutive model parameters for unsaturated soil and soil water characteristic curve (Table 3-3 and Table 3-4) of 5:5 mixed Toyoura sand and Fujinomori clay by weight (Section 3.2). The applications of the proposed constitutive model in regard to the soaking and the liquefaction behaviors of unsaturated soils could be implemented in this study since they have been validated by Komolvilas (2017) and Komolvilas & Kikumoto (2017), respectively.

In the following simulations, the initial state of soil specimens, including the water content w_n, void ratio e and specific gravity of soil G_s, were observed from the experimental results. Thus, in the simulation, initial suction s_0 of each specimen was calculated by Equation 2-10 in the assumption of $I_h = 0$ for wetting path.

3.3.1 Mechanism of static compaction

The experimental results of 1-D static compaction test (Section 3.1.1) were used to validate the proposed model for describing the mechanism of the static compaction.

Compression behaviors and compaction curves obtained from the experiments and simulations are compared in Figure 3-4 and Figure 3-5, respectively. We can see from Figure 3-4 that the proposed model could imitate the compression behaviors which soils having lower water content and degree of saturation exhibited the higher stiffness and the smaller change of void ratio in compression. In addition, the proposed model could generate convex-upward compaction curves with maximum dry densities and optimum water content as shown in Figure 3-5. The shape of the curves on the dry side of the optimum water contents observed in the experiments could be predicted well by the proposed model.

3.3.2 Mechanism of monotonic shearing of unsaturated soil

The experimental results of uncontrolled suction triaxial compression test (Section 3.1.3) are used to validate the proposed model for describing the mechanism of monotonic shearing of compacted soil before and after soaking. The shearing behavior obtained from the experiments and simulations are compared in Figure 3-2 for the compacted soil after soaking and Figure 3-6 and Figure 3-7 for the compacted soils before soaking. From the experimental results, the dense soil (Md) exhibited strain softening with volumetric dilation. While the loose soil (Ml) exhibited strain hardening with volumetric contraction. We can see that the proposed

model could predict well the shearing behavior of unsaturated soil including the effect of density.

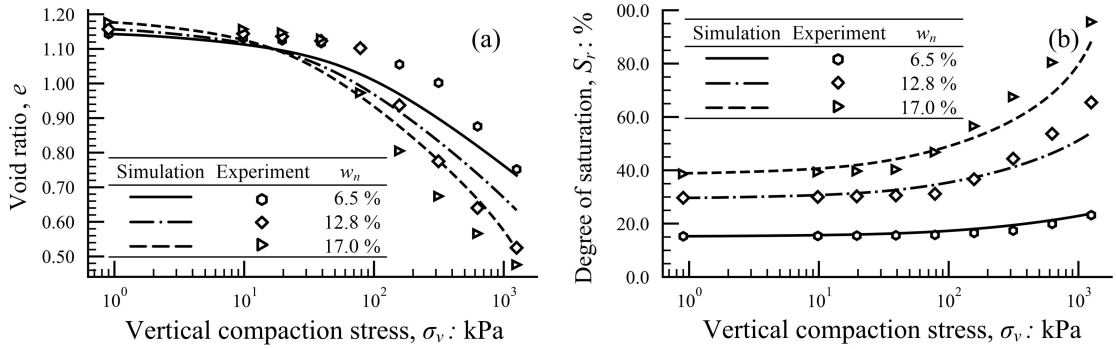

Figure 3-4 Model validation of compression behavior compaction stress 1256.0 kPa in the relationship of vertical compaction stress vs. (a) void ratio and (b) degree of saturation.

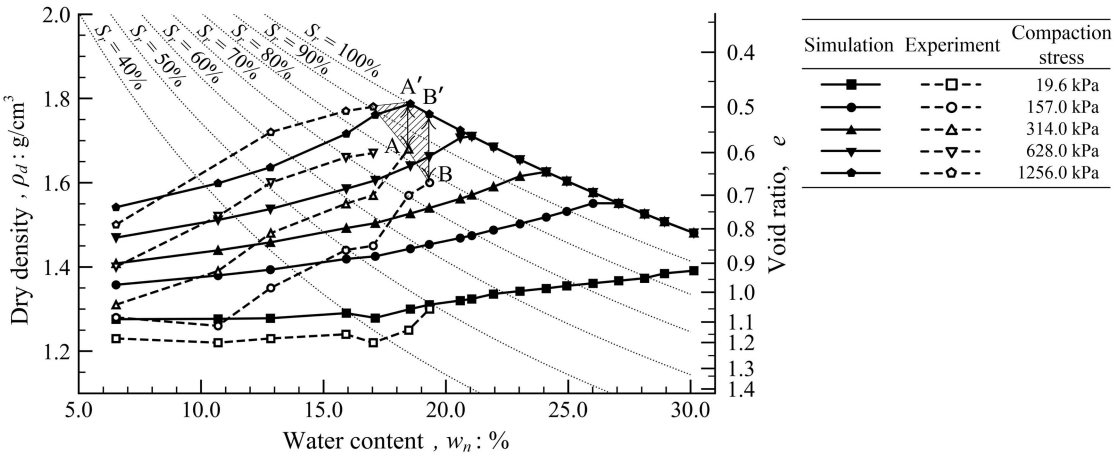

Figure 3-5 Model validation of compaction curve simulation for different compaction stress σ_v 19.6, 157.0, 314.0, 628.0 and 1256.0 kPa

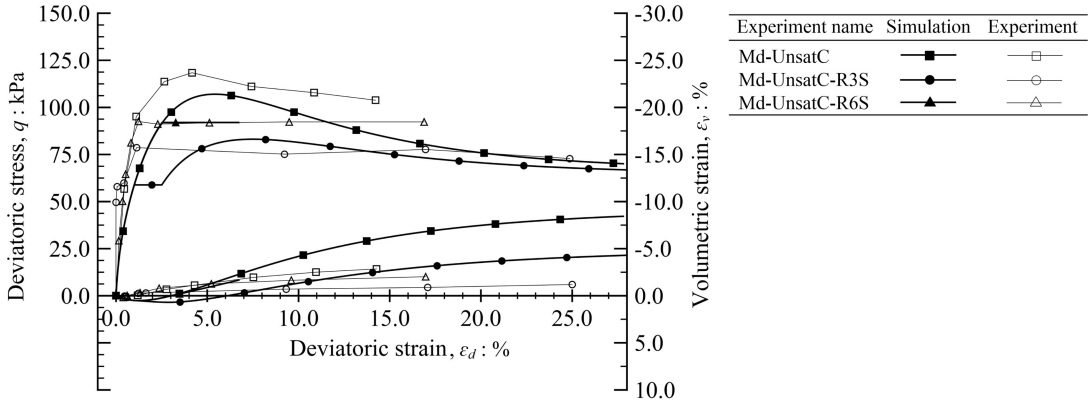

Figure 3-6 Model validation of monotonic shearing on dense mixed unsaturated soil (Md)

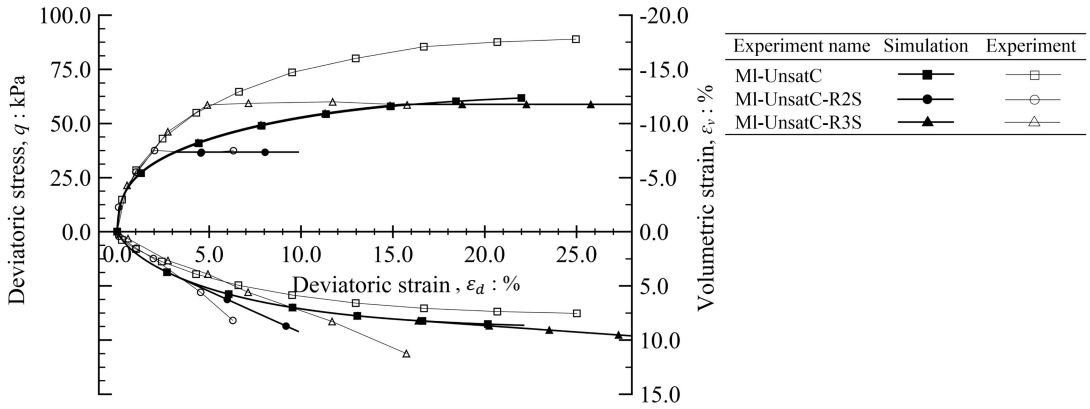

Figure 3-7 Model validation of monotonic shearing on loose mixed unsaturated soil (Ml)

3.3.3 Volumetric change of compacted soil due to wetting

Beside the validation results relating with the soaking process as shown in Figure 3-2, Figure 3-3, Figure 3-6 and Figure 3-7, Komolvilas (2017) was validated the proposed model and discussed the applicability of the proposed model described the hydraulic collapse behavior of unsaturated soils under isotropic and anisotropic conditions. The model was validated through a series of soaking tests on Pearl clay under isotropic and anisotropic condition (Sun et al., 2007). Consequently, we can conclude that soaking induced collapse phenomena of unsaturated soils under isotropic and anisotropic conditions are suitable described by the proposed model.

3.3.4 Liquefaction in unsaturated soils under fully undrained cyclic shearing

To confirm the capability of model for the fully undrained cyclic shearing simulation, the proposed model has been validated by Komolvilas & Kikumoto (2017) through the experimental results of cyclic triaxial tests on saturated and unsaturated soil under fully undrained condition at the constant pressure of Tsukidate volcanic sand (Unno et al., 2013). Therefore, the proposed model is also able to predict the fully undrained cyclic behavior of unsaturated soils, such as liquefaction.

3.4 CONCLUSIONS

The proposed constitutive model was validated through the series of experimental results conducted by Koike (2010) using the calibrated constitutive model parameters for unsaturated soil and soil water characteristic curve of the 5:5 mixed Toyoura sand and Fujinomori clay by weight (Table 3-3 and Table 3-4). The capabilities of the proposed model to predict the behavior of unsaturated soil against the compaction, the soaking, the fully drained shearing and the fully undrained shearing are illustrated. This set of constitutive model parameters will be used through the simulations in this study unless otherwise specified.

CHAPTER 4

INTERPRETATION OF COMPACTED SOIL BEHAVIORS THROUGH THE CONSTITUTIVE MODEL FOR UNSATURATED SOILS

In this study, the simulations of compacted soil behaviors will be performed from the origin as the compaction process to the strengths and the failures against loadings using the proposed constitutive model for unsaturated soils.

From the literature reviews, the soil mechanisms during compaction have been studied by many researchers through both experiments and numerical simulations in order to develop the constitutive models for the compaction of unsaturated soils. Tarantino & De Col (2008) observed the positive slope of post-compaction suction contours in the compaction plane at high water contents by conducting 1-D static compaction test. They found that a coupled mechanical water retention model is required for the simulation of compaction. Kikumoto et al. (2010) proposed the simplify 1-D coupled hydro-mechanical critical state constitutive model for unsaturated soils which is capable to generate the proper typical compaction curves for various soil types. Alonso et al. (2013) proposed the model for predicting the compaction behavior incorporating the effect of microstructure on the soils compacted on the dry side and the wet side of optimum. Zhou & Sheng (2015) proposed the model which is capable to model the hydro-mechanical behavior of unsaturated compacted soils with the different initial densities.

In addition, the strengths and the failures of compacted soils under the various loadings, including long term shearing, hydraulic collapse due to the heavy rainfall and liquefaction due to the fully undrained cyclic shearing, have also been studied by many researchers through the combination of experiments and simulations. Sivakumar and Wheeler examined the soil modelling considering the effects of compaction effort and compaction water content through the experimental results of soaking, isotropic loading (Wheeler & Sivakumar, 2000) and shearing (Sivakumar & Wheeler, 2000). They found that compaction effort and compaction water content affect initial position of yield surface and initial suction, respectively. Gallipoli et al. (2003a) and Gallipoli et al. (2003b) improved the elastoplastic constitutive model by incorporating the variation of degree of saturation and effect of suction, respectively. Their proposed model succeeds in predicting the mechanical behavior of unsaturated soil under isotropic compression, soaking and shearing. Sun et al. (2007b) proposed the 3-D elastoplastic constitutive model for coupled hydro-mechanical behaviors of unsaturated compacted soils with different initial densities using the same material constant. The experimental results with

different initial densities under isotropic compression, triaxial compression and collapse behavior could be predicted well by their proposed model. Marinho et al. (2013) examined the influence of soil structure associated with the initial compaction water contents and the initial stress on the shear strength of compacted soil. They found that the shear strength behavior is significantly influenced by the different initial compaction water contents. An empirical model was proposed to estimate the 3-D failure envelope of the tested compacted residual soil for any condition of the initial stress state. Zhou & Sheng (2015) proposed the hydro-mechanical model for unsaturated compacted soil which is capable to predict the dependence of loading–collapse volume on initial void ratio and density effect on the shearing-induced saturation change. Komolvilas (2017) proposed the 3-D simplify critical state constitutive model for unsaturated soil that could describe the hydraulic collapse behavior of unsaturated soils under isotropic and anisotropic conditions. Zhang et al. (2016) proposed the couple hydromechanical elastoplastic constitutive model for unsaturated sands to investigate the effects of initial degree of saturation, relative density and mean effective stress on the liquefaction resistance of unsaturated sands. Komolvilas & Kikumoto (2017) proposed the 3-D simplify critical state constitutive model for unsaturated soil to investigate the effects of initial degree of saturation, relative density and mean effective stress on the liquefaction behavior in unsaturated clay.

Based on the previous studies, the behaviors of compacted soils at the origin, the services and the failures with some prescribed initial states under the long term shearing, the heavy rainfall and the fully undrained cyclic shearing have been studied by many researchers in the framework of unsaturated soils both in experiments and elementary simulations. However, the progressive life of the compacted soil with the variations of initial compaction control parameter from the origin through the failure has not been widely studied yet.

In this chapter, by the proposed model that suitable for the unsaturated compacted soils (Chapter 2), the series of simulations that beginning with the compaction process through the failures will be produced. We further explore the mechanisms of the soil compaction, the compacted soils during soaking, the compacted soils before and after soaking under the monotonic shearing and the compacted soils under fully undrained static cyclic shearing through the series of elementary simulations. The effects of compaction water content and compaction effort on the characteristic behaviors of unsaturated compacted soils are investigated. Then, the responses of unsaturated compacted soil under the considered loads which rely on its characteristic after compaction are also interpreted. The set of validated parameters for 5:5 mixed Toyoura sand and Fujinomori clay by weight (Table 3-3 and 3-4) is used through the series of simulation.

4.1 SOIL COMPACTION

4.1.1 Compaction simulation procedure

4.1.1.1 Specimen preparation stage

First of all, the initial state of unsaturated soil was assumed to be identical: void ratio e_0 0.95, water content w_n 6.37 % and degree of saturation S_{r0} 17.94 % under mean net stress p_{net} 20.0 kPa where pore air pressure u_a 98.0 kPa (assumed atmospheric pressure) and pore water pressure u_w 62.50 kPa. Then, the initial water content was increased to the prescribed water contents by increasing u_w (or decreasing suction s) under the constant mean net stress. The prescribed water content specimens in the range of 7.6% and 32.3% were prepared in the simulations. Prepared specimens A through E were selected by the prescribed degree of compaction or D.C. as the substitute specimens for the explanation of mechanism of soil compaction and the behaviors of compacted soils in the study. Table 4-1 shows the details of specimens A through E before compaction. From the simulation results, Figure 4-1 reveals that degree of saturation increased as the decrease of suction under constant mean net stress during the water content adjustment. Consequently, for the simulation using the proposed model, the degree of saturation could be varied by the suction control.

Table 4-1 Details of specimens A through E before and after compactions.

Specimen	w_n [%]	D.C. [%]	Before compaction (A ~ E)			After compaction (A2 ~ E2) (Compaction case 1)		
			e	S_r [%]	s [kPa]	e	S_r [%]	s [kPa]
A → A2	10.51	90.0	0.948	29.61	4.39	0.787	35.69	7.12
B → B2	18.44	95.0	0.931	52.96	1.43	0.692	71.21	3.48
C → C2	22.69	100.0	0.917	66.10	1.00	0.608	99.78	0.42
D → D2	25.91	95.0	0.904	76.59	0.76	0.692	99.99	0.00
E → E2	29.46	90.0	0.886	88.91	0.50	0.787	99.99	0.00

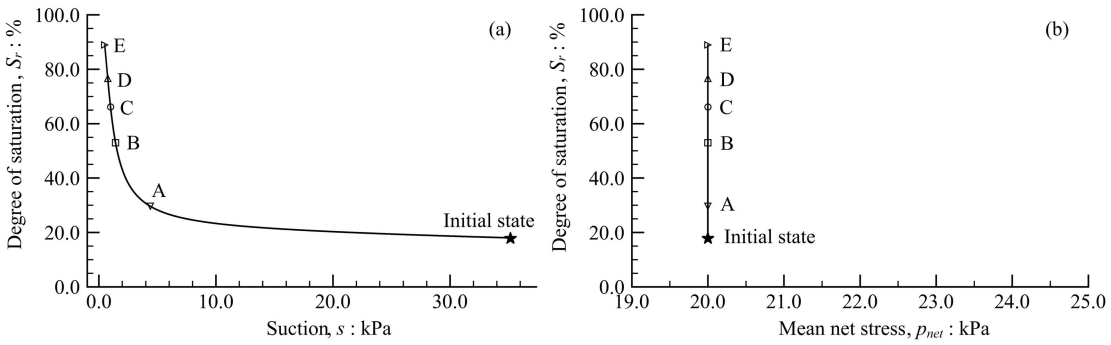

Figure 4-1 Variation of degree of saturation due to suction control in the specimen preparation stage.

4.1.1.2 Compaction stage

The sequence of compaction process significantly affects the behaviors of the compacted soils before and after soakings. It is important to closely duplicate the field condition (Gibbs et al., 1960), especially the effect of remained confining pressure to the volumetric behavior during soaking and the shear strength of compacted soils that have been experimentally investigated by many researchers (Holtz & Gibbs, 1956; Turnbull & Foster, 1956; Seed et al.,1960; Lambe, 1960 and Sun et al., 2007b). Therefore, two cases of the compaction process considering the effect of confining pressure were simulated in this study as follows.

- Compaction case 1 is named for compaction without unloading to the initial state. It represents the compacted specimen under high confining pressure after compaction.
- Compaction case 2 is named for compaction with unloading to the initial state. It represents the compacted specimen under low confining pressure after compaction.

However, in this section, only compaction case 1 is thoroughly described in this section for the explanation of compaction curve generation through the simulations.

For compaction case 1, the prescribed water content specimens were isotopically compressed to the defined compaction stress under exhausted air - undrained water condition. During the compaction, the compaction water contents were kept constant by the balancing of the increase of degree of saturation and the decrease of void ratio. The defined compaction stresses were 78.5, 314.0 and 1256.0 kPa which were substituted by compaction stress index i equal to 1, 2 and 3, respectively. For the substitute specimens A through E with the variation number of compaction stress i (Ai through Ei), the compression behaviors are illustrated in Figure 4-2. For each prescribed water content specimen, the final void ratio, degree of saturation and suction for each compacted stress were observed after the compaction. Then, the dry density ρ_d was calculated by the observed void ratio e by:

$$\rho_d = \frac{\rho_w G_s}{1 + e} \tag{4-1}$$

where ρ_w is the density of water and G_s is the specific gravity of soil. After compaction, the dry density, void ratio and post compaction suction are plotted against compaction water contents as shown in Figure 4-3. The final states of the compacted specimens A2 through E2 of compaction case 1 are also summarized in Table 4-1. Then, we consecutively performed the same simulation process under varied prescribed water content and compaction stress. The compaction curves of compaction case 1 and case 2 were numerically generated as shown in Figure 4-4 and Figure 4-5, respectively. With the variations of water content w_n, contours of

prescribed post compaction degree of saturation S_r can be drawn in the compaction plane by calculated void ratio *e* using basic volume mass relationship as given by:

$$e = \frac{w_n G_s}{S_r} \tag{4-2}$$

The contours are increased with dry density and water content and they are limited by the zero-air void curve. Last, post compaction suctions contours are also plotted in Figure 4-4 and Figure 4-5. The suction contour had the positive slope which is consistence with the study of Tanrantino & De col (2008). We can see from the contours that suction increased as the increasing of degree of saturation at constant water content. It implies that the density affects the post compaction suctions during compaction could be predicted well by the proposed coupled hydro-mechanical model for unsaturated soils.

4.1.2 Characteristics of compacted soil

The typical behavior of compacted soils along the compaction curve have been studied by many researchers from time to time. The convex-upwards curve with maximum dry density and optimum water content is the typical compaction curve that was firstly published by Proctor (1933). Due to the increasing of compaction effort, the compaction curve is observed to shift upward left-hand side (Johnson and Sallberg, 1960). The characteristics of compacted soils along the compaction curve have been continuously studied by many researchers through the experiments (see for instance, Marwick, 1945; Lambe, 1958; Seed & Chan, 1959; Lambe & Whitman, 1969; and Koga, 1991). Most of the studies have explained the characteristics of compacted soils along the compaction curve by the different of particle reorientation as the result of compaction water content and compaction effort. They found that these parameters reflect the characteristics of compacted soils in the form of density and degree of saturation. As the proposed model is fabricated by the stress-strain relationship of unsaturated soil, including the effects of density and the state boundary surface that moves in volumetric direction due to variation of the degree of saturation. Therefore, the following parametric study results demonstrate the capability of the proposed model to simulate the compaction mechanism.

In the parametric study, the characteristics of compacted soil are explained in this study through the compression behaviors (Figure 4-2); specimens A2 through E2 of compaction case 1 for instance. Figure 4-2 reveals that soils having lower water content and degree of saturation exhibited higher stiffness and smaller change of void ratio in compression. At a given compaction stress 314.0 kPa, starting with the specimen A2 in Figure 4-6, water content increased, thereby increasing the dry density and degree of saturation as represented by the specimen B2. The tendency of compacted soil thereof continued until the highest packing

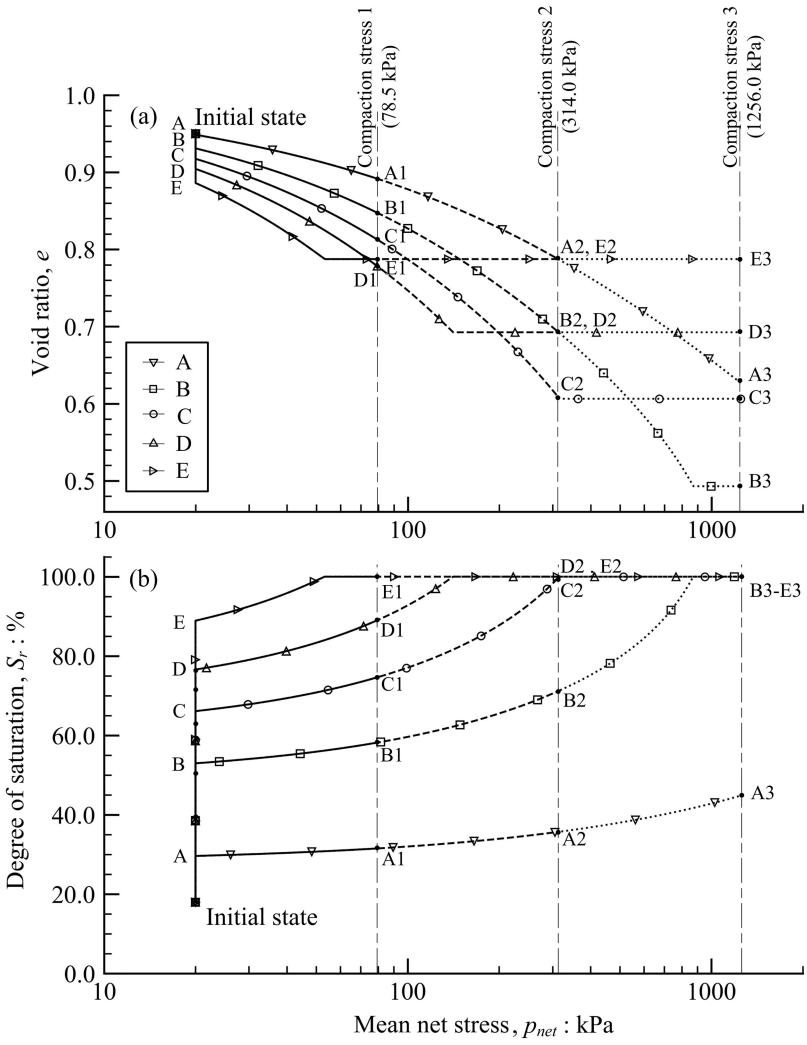

Figure 4-2 Simulation of isotropic compaction test of specimens Ai through Ei where i = 1, 2, 3 in the relationship of mean net stress against a) void ratio and b) degree of saturation. (Compaction case 1)

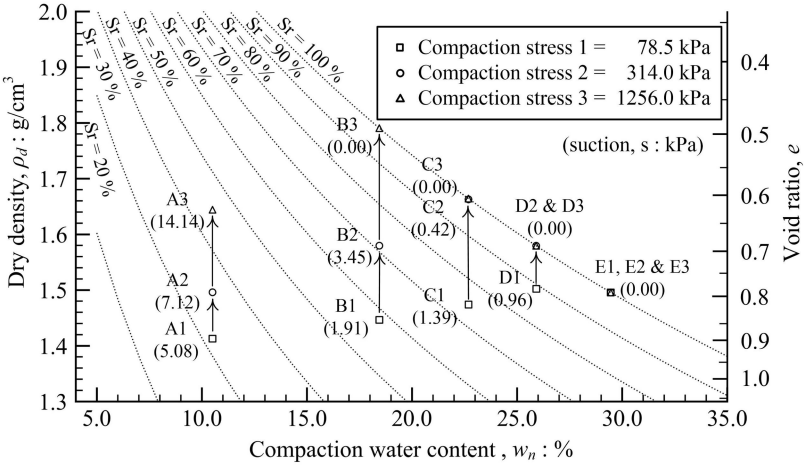

Figure 4-3 Final state of specimens Ai through Ei where i = 1, 2, 3 after compaction (Compaction case 1).

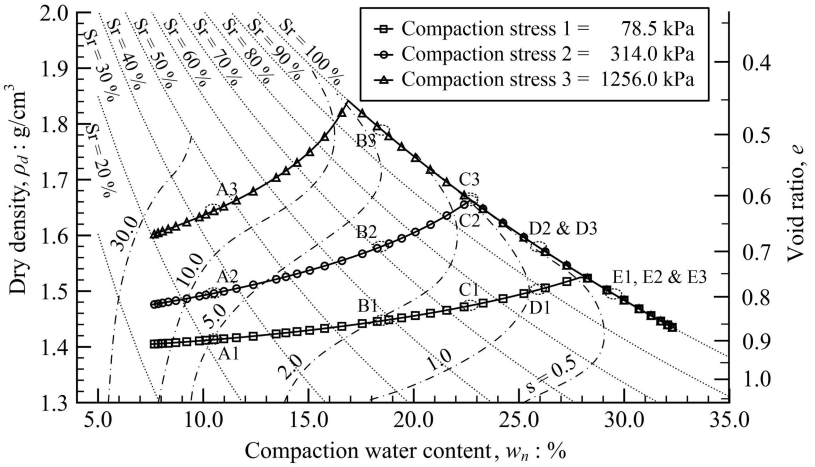

Figure 4-4 Simulation of compaction curve for different compaction stresses 78.5, 314.0 and 1256.0 kPa of compaction case 1.

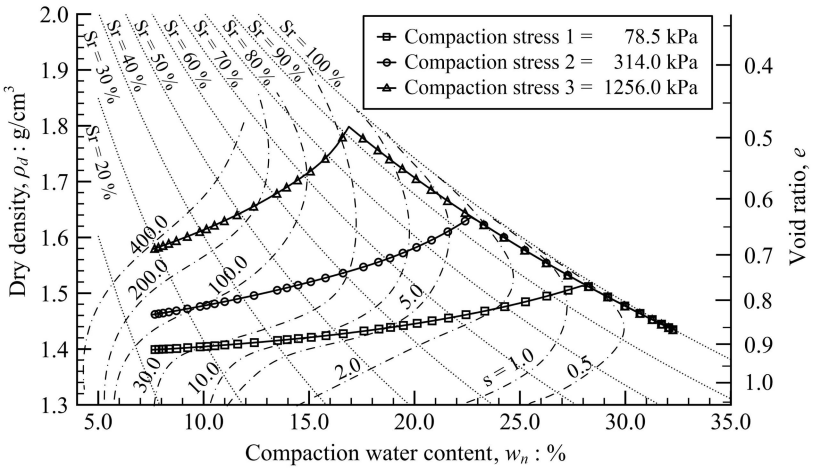

Figure 4-5 Simulation of compaction curve for different compaction stresses 78.5, 314.0 and 1256.0 kPa of compaction case 2.

density (or maximum dry density) which was observed at the optimum water content (specimen C2); thereafter, increasing of water content resulted in lowering the dry density with high degree of saturation as represented by specimens D2 and E2. This is because, meanwhile, the larger water content specimens are more compressible in the beginning stage of the compaction, but further compression hardly occurs once the soil approached the saturated state without drainage of water since the water is not allowed to flow out in the compaction process (Figure 4-2). Consequently, the typical compaction curve which is the convex-upwards curve with maximum dry density and optimum water content could be observed as shown in Figure 4-4 and Figure 4-5 for compaction case 1 and case 2, respectively. Through a compaction curve, Figure 4-6, compacted soils are categorized as the dry side of optimum water content, the wet side of optimum water content and the optimum water content. They are categorized by the

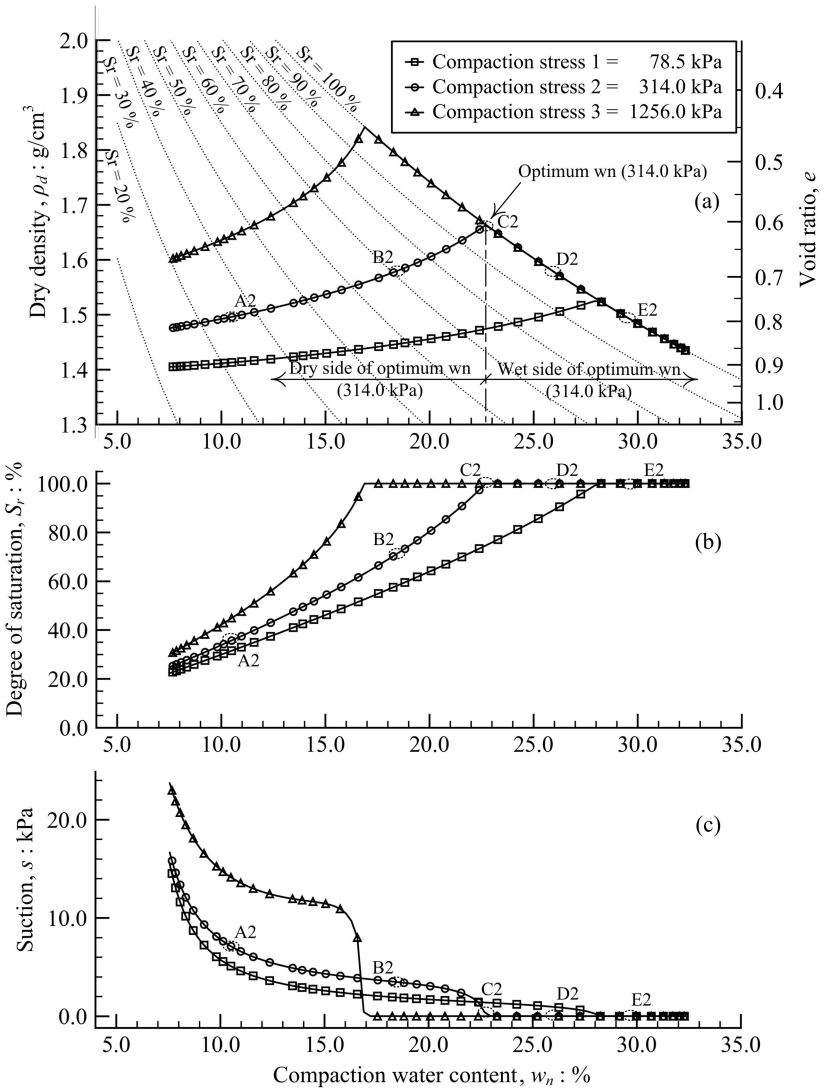

Figure 4-6 Compaction curve and the tendencies of degree of saturation and suction against compaction water content (compaction case 1).

characteristic of compaction water content that affects dry density and degree of saturation during compaction as explained through the substitute specimens A2 through E2. Moreover, Figure 4-6 also shows the effect of compaction effort to the characteristics of compacted soil. At a given water content, compaction effort hardly influenced to the dry density of soils compacted wet of optimum while significantly affected to the soils compacted dry of optimum. Since there is no substantial change in volume while approaching the saturated state as stated above. Increasing the compaction effort by keeping constant water content, the specimen changed from dry of optimum to be wet of optimum. The optimum water content decreased with the increasing of compaction effort, so the compaction curves shifted upward left-hand side. In addition, the proposed model could generate the typical compaction curve which

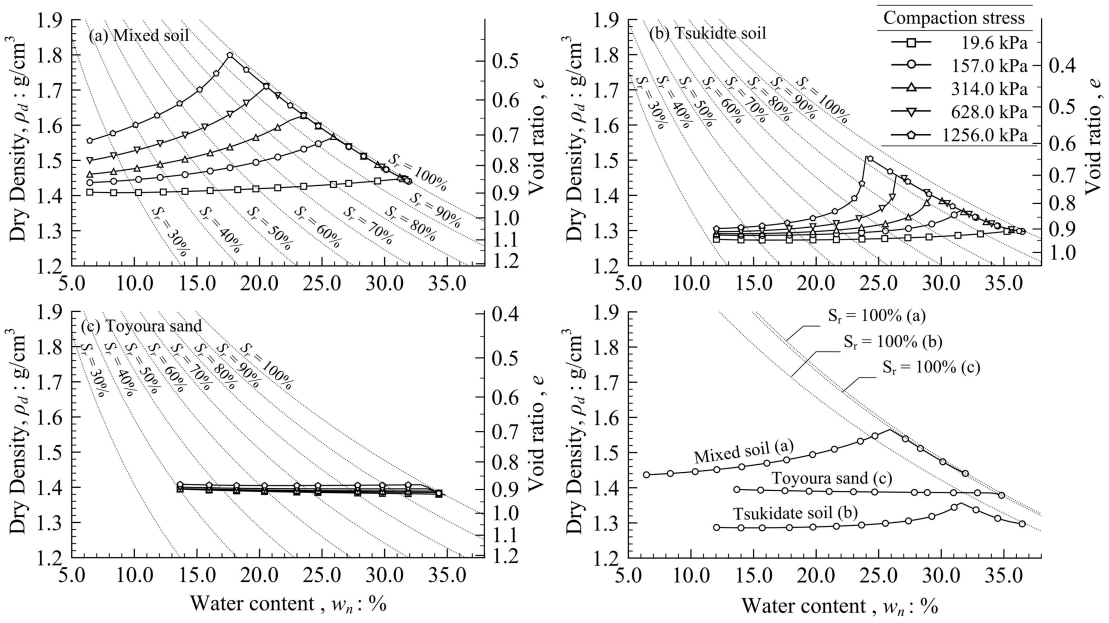

Figure 4-7 Typical compaction curve of various soil types

reflects the characteristic of each soil type by using the specific constitutive model parameter as shown in Figure 4-7.

Coefficient of permeability (k) of unsaturated compacted soil is able to calculate by the function of the void ratio and the degree of saturation (Appendix D) which they were generated by the compaction simulation using the proposed model. The calculated k of compaction case 1 and case 2 are plotted with respect to the compaction water content as shown in Figure 4-17(c) and Figure 4-18(c), respectively. From the simulations, the characteristics of the simulated dry density and degree of saturation provided the typical characteristic of k that increases with the increasing of compaction water content as shown in the experimental result of Barden & Pavlakis (1971) (Figure 4-8(a)). In addition, at a given compaction water content, increasing of degree of saturation due to the increasing of compaction effort resulted in the increasing of k.

To summarize, the proposed model is able to generate the typical convex-upward compaction curves with maximum dry densities and optimum water contents for various soil types. It also could generate the transition of the compaction curve due to the compaction stress. The simulation results of compaction using the proposed model could be used to provide the typical characteristic of coefficient of permeability. We found that the realistic compaction curve as in the experimental results could be generated by considering the over consolidated (OC) compacted soil.

4.2 BEHAVIORS OF COMPACTED SOILS

The effect of initial compaction control parameter, including compaction water content, compaction effort and field condition, to the serviceability of the embankment through the

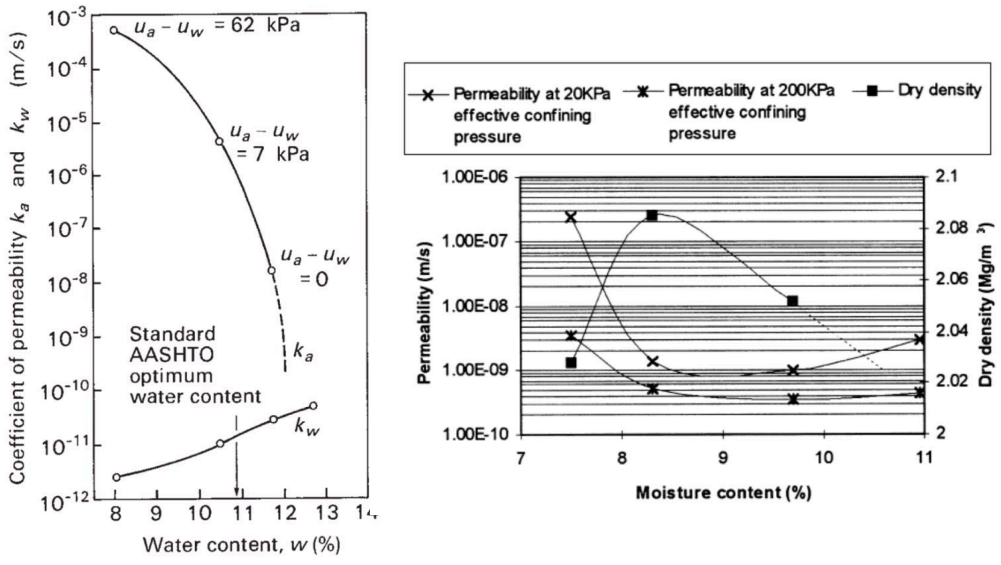

(a) (b)

Figure 4-8 Effect of compaction water content on (a) coefficient of permeability before soaking (Barden & Pavlakis, 1971) and (b) coefficient of permeability after soaking (Smith et al., 1999) of compacted soils

serviced life of compacted soil under soaking (heavy rainfall), monotonic shearing (long term structural load) and fully undrained cyclic loading (earthquake) is considered in the parametric study for the interpretation of compacted soil behavior using the proposed constitutive model for unsaturated soils.

4.2.1 Behaviors of unsaturated compacted soils under soaking process

Soaking process was applied in the simulation to imitate the compacted soils under the heavy rainfall. Compacted specimens of compaction case 1 and case 2 in Section 4.1 were continuously soaked to the fully saturated state by increasing pore water pressure u_w from the current state until the suction value approaching zero under constant mean net stress of each specimen.

For compaction case 1, the compacted specimens were soaked under constant confining pressure equal to their compaction stress 78.5, 314.0 and 1256 kPa. Figure 4-9(a) shows the collapse compression behaviors during soaking of compacted specimens A2 through E2 as the representative. Tendencies of dry density, changes of total volumetric strain after soaking and coefficient of permeability are plotted against the compaction water content for all compacted specimens and compaction efforts as shown in Figure 4-17(a) through Figure 4-17(c), respectively. In the simulation, after soaking, degree of saturation of soil compacted dry side of optimum extremely increased from their lower current state while it insignificantly changed in wet side of optimum. Consequently, the soil compacted dry side of optimum showed large

compression collapse during soaking and it decreased with the increasing of compaction water content. The compression collapse resulted in the significant increase of dry density. While k after soaking to the saturated state significantly increased from before soaking state due to the extreme increasing of degree of saturation after soaking. As opposed to k before soaking, at a given compaction water content, increasing of compaction effort resulted in the decreasing of saturated k since packing density of soil controls k at the fully saturated state. In contrast, soil compacted wet side of optimum, the volumetric behavior and degree of saturation were not affected by compaction water content and compaction effort since they were approached saturated state before soaking as the result of high remained confining pressure.

For compaction case 2, the compacted specimens were soaked under a constant confining pressure after unloading to the initial state of compaction. For this case, Figure 4-9(b) and Figure 4-18(a) through Figure 4-18(c) are plotted with the same relations as Figure 4-9(a) and Figure 4-17(a) through Figure 4-17(c) of compaction case 1, respectively. Tendencies of dry density, changes of total volumetric strain after soaking and k showed the similar trend as the compaction case 1. However, due to the low remained confining pressures during soaking, the small amount of compression collapse behavior and some of the swelling behavior were observed in this compaction case. Furthermore, at a given compaction water content, the higher compaction effort or higher over consolidation ratio reduced the magnitude of collapse. This behavior resulted in the variation of k after soaking with the packing density of compacted soil along the compaction curve and compaction effort. k after soaking of soil compacted dry side of optimum decreased with increasing of compaction water content and slightly increased on the wet side of optimum.

All in all, refer to the simulation results, the remained confining pressure and the initial compaction control parameter affect the volumetric behavior of compacted soil upon soaking. First, lower compaction water content exhibits higher magnitude of compression collapse due to soaking, especially volumetric strain of the specimens compacted dry of optimum. Thus, in term of volumetric behavior of compacted soil after soaking, the compaction at larger water content especially wet side of optimum is proper for subsequent soaking. This is consistent with the typical volumetric behavior of compacted soil upon soaking that have been investigated by many researchers (Turnbull & Foster, 1956; Yoder & Witezak, 1975; Alonso, 1987; Taibi et al., 2011; Alonso et al., 2013; Tatsuoka & Shibuya, 2014 and Mountassir et al., 2014). Second, at a given compaction water content and a compaction stress, normal consolidated (NC) soil which is generated by the case of without unloading after compaction shows higher magnitude of compression collapse than over consolidated (OC) soil which is generated by the case of

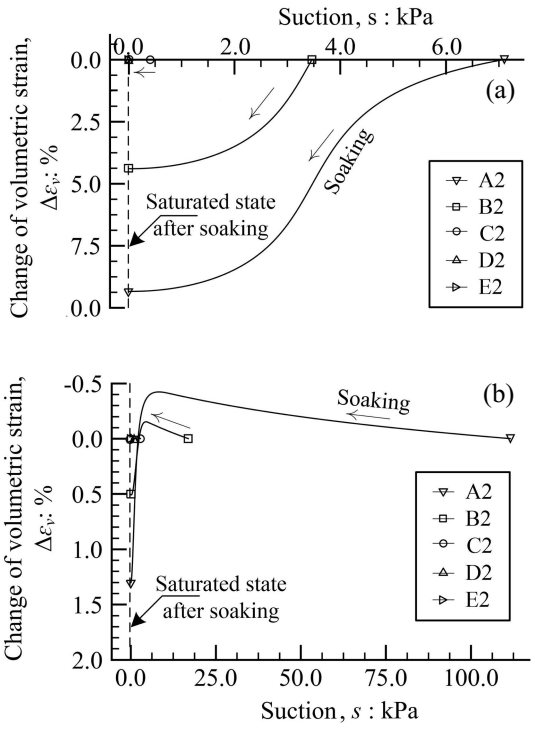

Figure 4-9 Change of total volumetric strain against suction of specimens A2 through E2 a) compaction case 1 and b) compaction case 2

unloading after compaction. Highly over consolidated (HOC) specimen which is compacted under high compaction effort and unloaded to the low confining pressure is able to expand. This behavior corresponds with the investigation reported by Cox (1978), Rampino et al. (2000), Sun et al. (2007c) and Komolvilas (2017). Last, at a given confining pressure during soaking of compacted OC soils, the greater compaction effort (or HOC soil) reduces the magnitude of compression collapse (Sivakumar and Wheeler, 2000). In addition, after soaking to saturated state, final packing density as the result of compaction process and compression collapse due to soaking controls the characteristic of k in the compaction. This is consistent with the typical characteristic of $k$after soaking of compacted soil with the compaction water content and compaction effort (Figure 4-8(b)).

We can see that the proposed model is able to predict the volumetric behavior upon soaking of compacted soil considering the initial compaction control parameter and the remained confining pressure (effect of OCR). In addition, characteristic of k at the saturated state along the compaction curve could be consequently investigated from the hydraulic and volumetric behaviors after soaking. The results conform with the experiments that have been investigated by many researchers.

4.2.2 Behaviors of unsaturated compacted soils under fully drained static monotonic shearing

The typical strength of compacted soil along the compaction curve has been study by many researchers. Generally, shear strength of compacted soil is a function of both density and water content. The strength of soils compacted on dry side of optimum are significantly higher than soil compacted on wet side of optimum. At a given water content, it increases with the density and degree of saturation. (Seed & Monismith, 1954; Leonard, 1955; Bell, 1956; Seed & Chan, 1961; Yoder & Witezak, 1975; Essigman, 1976 and Koga, 1991). In addition, after soaking, the typical tendency of the strength is convex-upwards curve with the maximum peak strength and optimum water content of compaction. The strength of soil compacted at the optimum water content and over are slightly dropped upon soaking. However, the strengths significantly decrease on the dry side of optimum (Holtz and Gibbs, 1956; Seed & Chan, 1961; Yoder & Witezak, 1975; Wilson, 1977 and Tatsuoka & Shibuya, 2014). Figure 4-10 shows the examples of previous experimental studies about the strength of compacted soils before and after soaking using California Bearing Ratio (CBR) test.

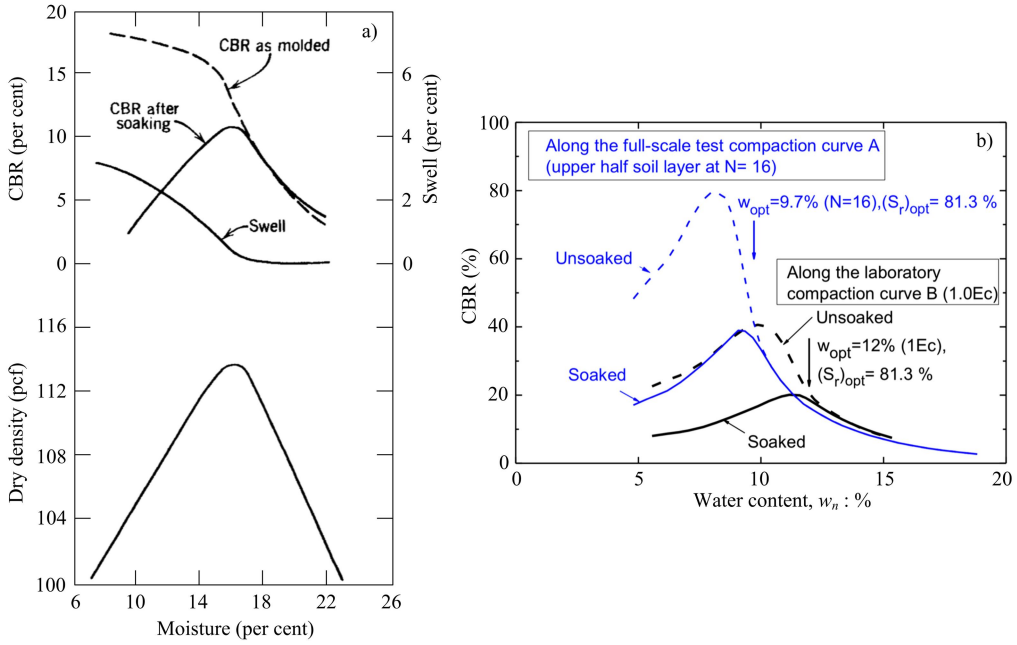

Figure 4-10 Tendencies of CBR values before and after soaking from the previous experimental studies of a) Yoder and Witezak (1975) and b) Tatsuoka et al. (2016)

In this study, the behaviors of unsaturated compacted soils under fully drained static monotonic shearing considering the effects of compaction control parameter and soaking were simulated using the proposed model in order to represent its capability.

In the parametric study, simulations of the mean stress constant triaxial shearing test under unsaturated condition were performed on all of the compacted specimens before soaking

(Section 4.1.1) and the compacted specimens after soaking (Section 4.2.1) for both compaction case 1 and case 2. By the strain control, the specimens were continuously sheared to the critical state under fully drained condition. Shear behaviors and the comparison between peak strength of compacted soil before and after soaking are discussed in this section.

4.2.2.1 Shear behaviors of unsaturated compacted soils before soaking

First, the effect of overconsolidation ratio (OCR), which is caused by the different compaction procedure (compaction case 1 (NC soil) and compaction case 2 (OC soil)), to the shearing behaviors is discussed. For compacted specimens A2 through E2, the shearing behaviors of NC compacted soil (compaction case 1) exhibited strain hardening and volumetric contraction behaviors (Figure 4-11). While the shearing behaviors of OC compacted soil (compaction case 2) exhibited strain softening and dilation behaviors (Figure 4-13).

Second, the effect of constant confining pressure during shearing process; high confining pressure (compaction case 1) and low confining pressure (compaction case 2); to the amplitude of peak strength is discussed. For all specimens and compaction efforts, the peak strength of compaction case 1 and case 2 are plotted against the compaction water content as shown in Figure 4-12 and Figure 4-14, respectively. We can see that both compaction cases exhibited the similar tendency of the peak strength against compaction water content. However, the peak strength of compaction case 1 is greater than compaction case 2 due to the high confining pressure.

Last, the tendency of peak strength against compaction water content is discussed according to the simulation results. From Figure 4-12 and Figure 4-14, the peak strength of soils compacted dry of optimum is significantly higher than the soils compacted wet of optimum. For soils compacted dry of optimum, with larger compaction water content, the significant decrease of peak strength corresponded to the increase of post compaction density and degree of saturation. On the other hand, on the wet side of optimum, the decrease of peak strength corresponded to the decrease of post compaction density while the post compaction degree of saturation was approximately the same along the wet side (nearly saturated state). Consequently, we can imply that post compaction degree of saturation significantly controls the peak strength of compacted soils. If degree of saturation is approximately the same, peak strength increases with increased density. In addition, at a given water content, compaction effort did not influence to the peak strength of soils compacted wet of optimum while significantly affected to soils compacted dry of optimum. This is because the density and degree of saturation are insignificantly changed at the nearly saturated state. By these reasons, we can

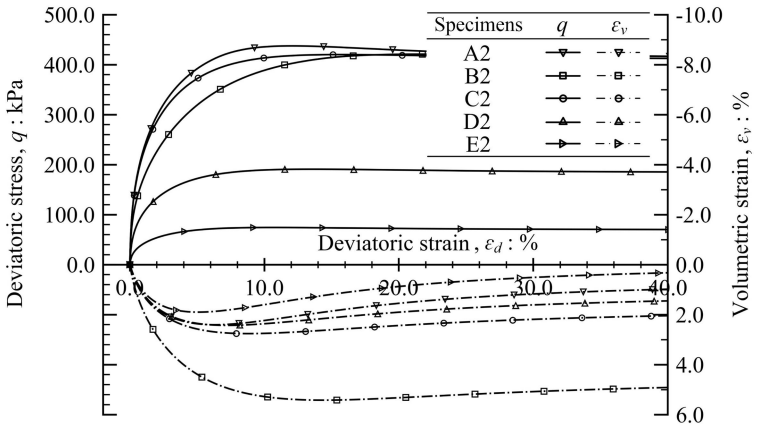

Figure 4-11 Relations of deviatoric stress and total volumetric strain against deviatoric strain of compacted specimens during shear before soaking (compaction case 1).

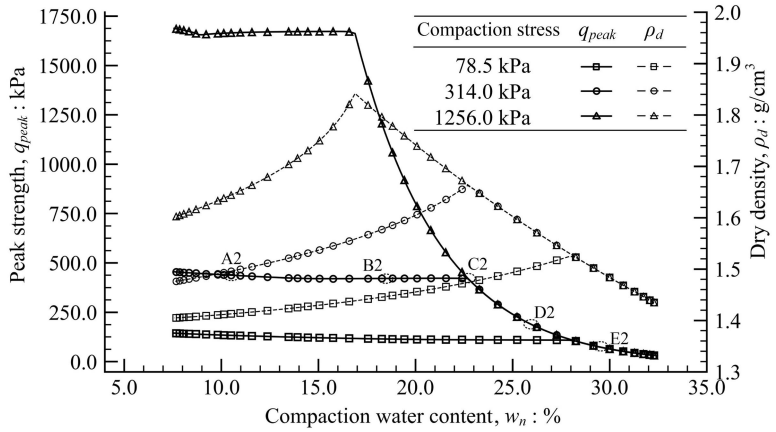

Figure 4-12 Tendency of peak strength before soaking with compaction water content. (compaction case 1).

conclude that variations of density and degree of saturation in the compaction plane affect the strength of compacted soil.

In conclusion, the peak strength of compacted soils before soaking are consistent with the typical tendency of shear strength along the compaction curve. Therefore, the proposed model is able to predict the peak strength varied with compaction water content and compaction effort.

4.2.2.2 Shear behaviors of unsaturated compacted soil after soaking

After the compacted soils were soaked, Figure 4-15 and Figure 4-16 show the similar tendency of shearing behaviors as discussed in Section 4.2.2.1 considering the effect of OCR of compacted specimens A2 through E2 for compaction case 1 and case 2, respectively. In addition, the comparisons between peak strength of compacted soils before and after soaking against compaction water content of compaction case 1 and case 2 are generated as shown in Figure 4-17 and Figure 4-18, respectively. Change of volumetric strain of soil after soaking is

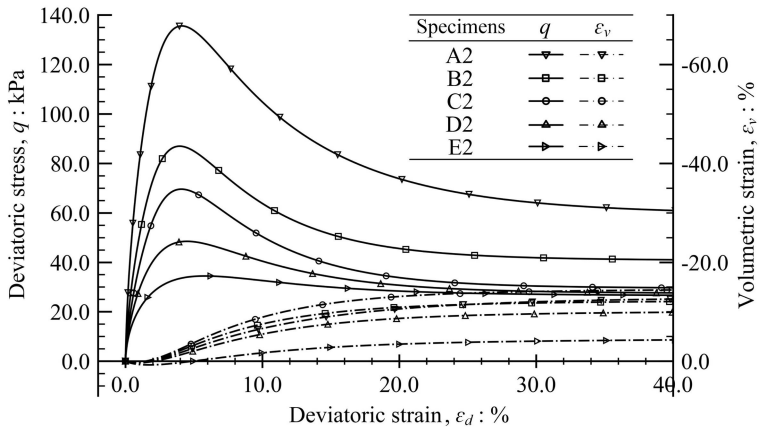

Figure 4-13 Relations of deviatoric stress and total volumetric strain against deviatoric strain of compacted specimens during shear before soaking (compaction case 2).

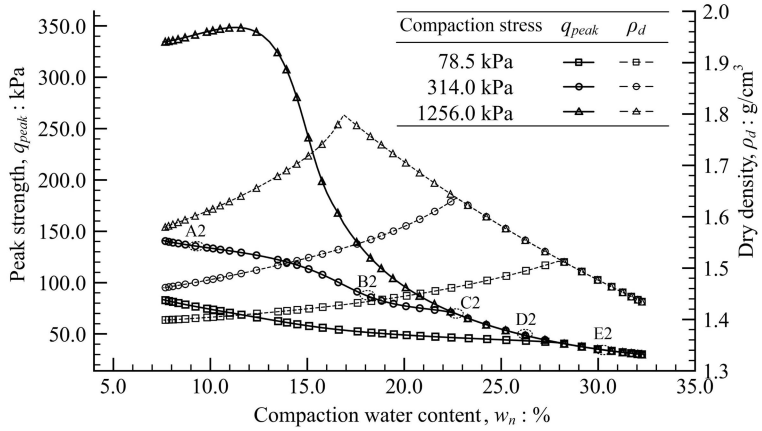

Figure 4-14 Tendency of peak strength before soaking with compaction water content. (compaction case 2).

also taken into consideration for the discussion of its effect to the variation of the peak strength.

For compaction case 1, specimens A2 through E2 exhibited strain hardening and volumetric contraction behaviors (Figure 4-15) for NC compacted soils. For soils compacted dry of optimum, Figure 4-17(d), the peak strength insignificantly reduced after soaking. This is because the balancing between the influence of the density and the degree of saturation after soaking. The compression collapse behavior induced the significant denser state of soils (Figure 4-17(b)) while the strength of soil was also deduced by the increasing of the degree of saturation which was approached to 100% during soaking from the drier state. For soils compacted wet of optimum, the peak strength after soaking was similarly the same (Figure 4-17(d)) since there was no change of density (Figure 4-17(b)) and degree of saturation during soaking of the fully saturated specimens.

For compaction case 2, specimens A2 through E2 exhibited strain softening and dilation behaviors (Figure 4-16) for OC compacted soils. Figure 4-18(d) shows the reduction of peak

strength after soaking of compacted soils through the compaction curve. We observed the significant reduction of peak strength on the dry side of optimum. This is because, as the discussion in Section 4.2.1, the small amount of compression collapse occurred (Figure 4-18(b)) therefore the extreme increasing of degree of saturation dominantly affected the reduction of peak strength after soaking. While the specimens compacted wet of optimum, less peak strength reduction were observed as the result of lowering both collapse behavior (Figure 4-18(b)) and variation of degree of saturation due to high initial degree of saturation before soaking (nearly saturated soil). Thus, the relation of peak strength of compacted soil after soaking against the compaction water content demonstrated the convex-upward curves with the maximum peak strength and the optimum water content similar to the tendency of compaction curve. Moreover, the soils which were compacted with higher compaction effort exhibited greater reduction of peak strength and lower collapse compression. However, it remained the higher peak strength (Figure 4-18).

From both compaction cases, the initial compaction control parameter and the remained confining pressure during soaking affect the variations of degree of saturation and dry density of the compacted soil after soaking. Their variations also significantly affect the peak strength of compacted soil after soaking. During soaking, the peak strength increases with the denser state of compacted soil meanwhile it dominantly decreases with the increase of degree of saturation. However, for all specimens along the compaction curve, most of the peak strength after fully soaking is reduced. Although, remaining high confining pressure during soaking is able to alleviate the reduction of peak strength after soaking. However, it results in high magnitude of compression collapse which is not proper for the serviceability of the embankment. The maximum peak strength of the soaked soil is at the optimum water content with the small amount of collapse compression. In addition, the soil compacted with higher compaction effort exhibit greater peak strength after soaking.

In conclusion, the proposed model properly predicts the tendency of peak strength of compacted soils after soaking through the compaction curve. The simulation results of the peak strength of compacted soils after soaking, especially for the OC soils, are consistent with the typical tendency of shear strength after soaking of compacted soil.

By the proposed model, the dry density, peak strength before soaking and peak strength after soaking in the relations of compaction water content and compaction effort were generated as the 3-D surfaces in Figure 4-19 (compaction case 1) and Figure 4-20 (compaction case 2). Regarding the 3-D surfaces, the engineers could specify the optimum compaction control parameters in the construction for the considered range by the simulations. The solid lines in

Figure 4-19 and Figure 4-20 illustrate the simulation results that we already discussed in this Chapter for compaction stress 1256.0 kPa.

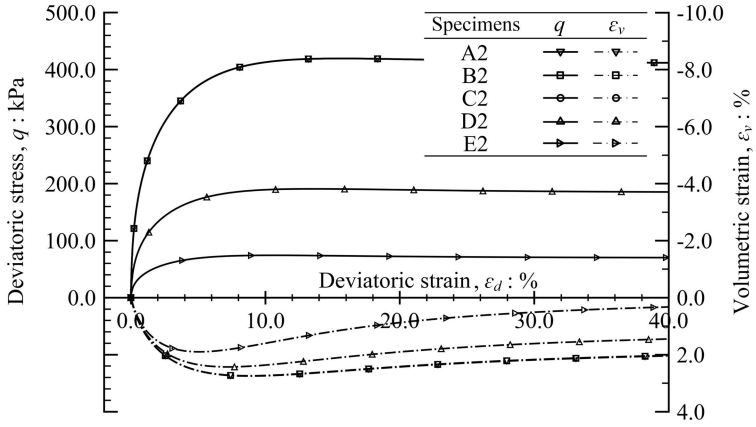

Figure 4-15 Relations of deviatoric stress and total volumetric strain against deviatoric strain of compacted specimens during shear after soaking (compaction case 1).

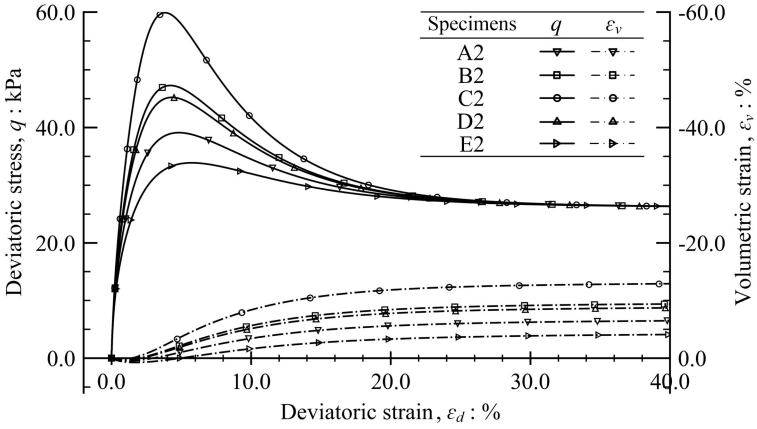

Figure 4-16 Relations of deviatoric stress and total volumetric strain against deviatoric strain of compacted specimens during shear after soaking (compaction case 2).

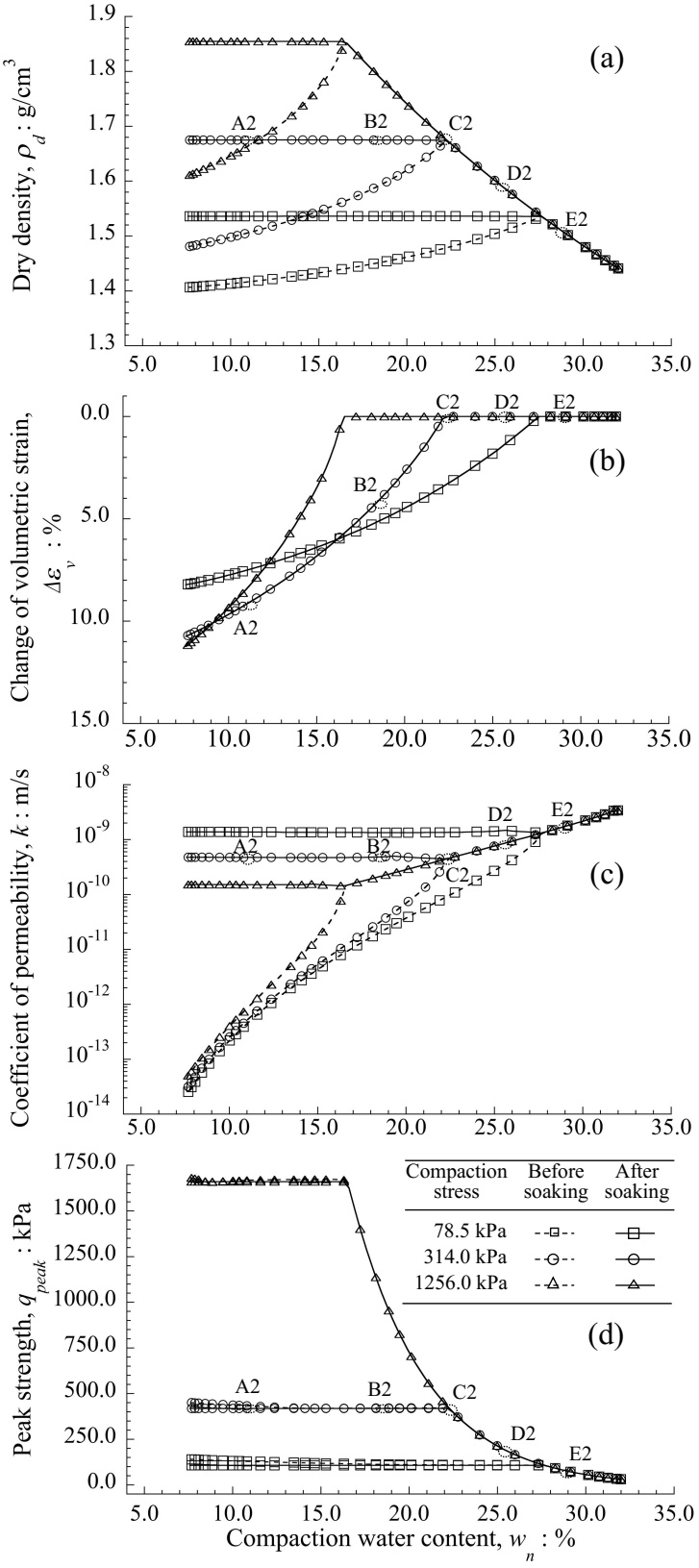

Figure 4-17 Relations of a) dry density, b) changes of volumetric strain, c) coefficient of permeability and d) peak strength of compacted soil against compaction water content due to soaking after compaction (compaction case 1).

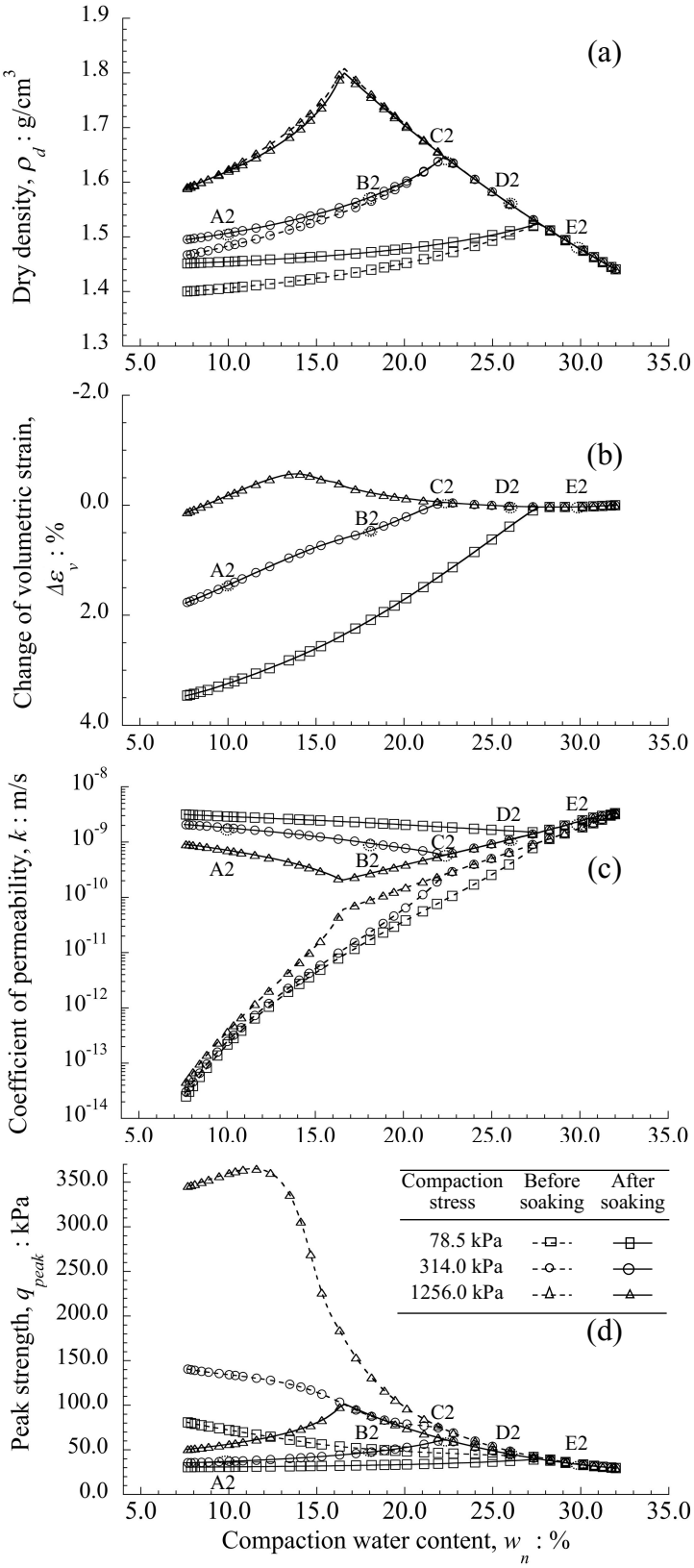

Figure 4-18 Relations of a) dry density, b) changes of volumetric strain, c) coefficient of permeability and d) peak strength of compacted soil against compaction water content due to soaking after compaction (compaction case 2).

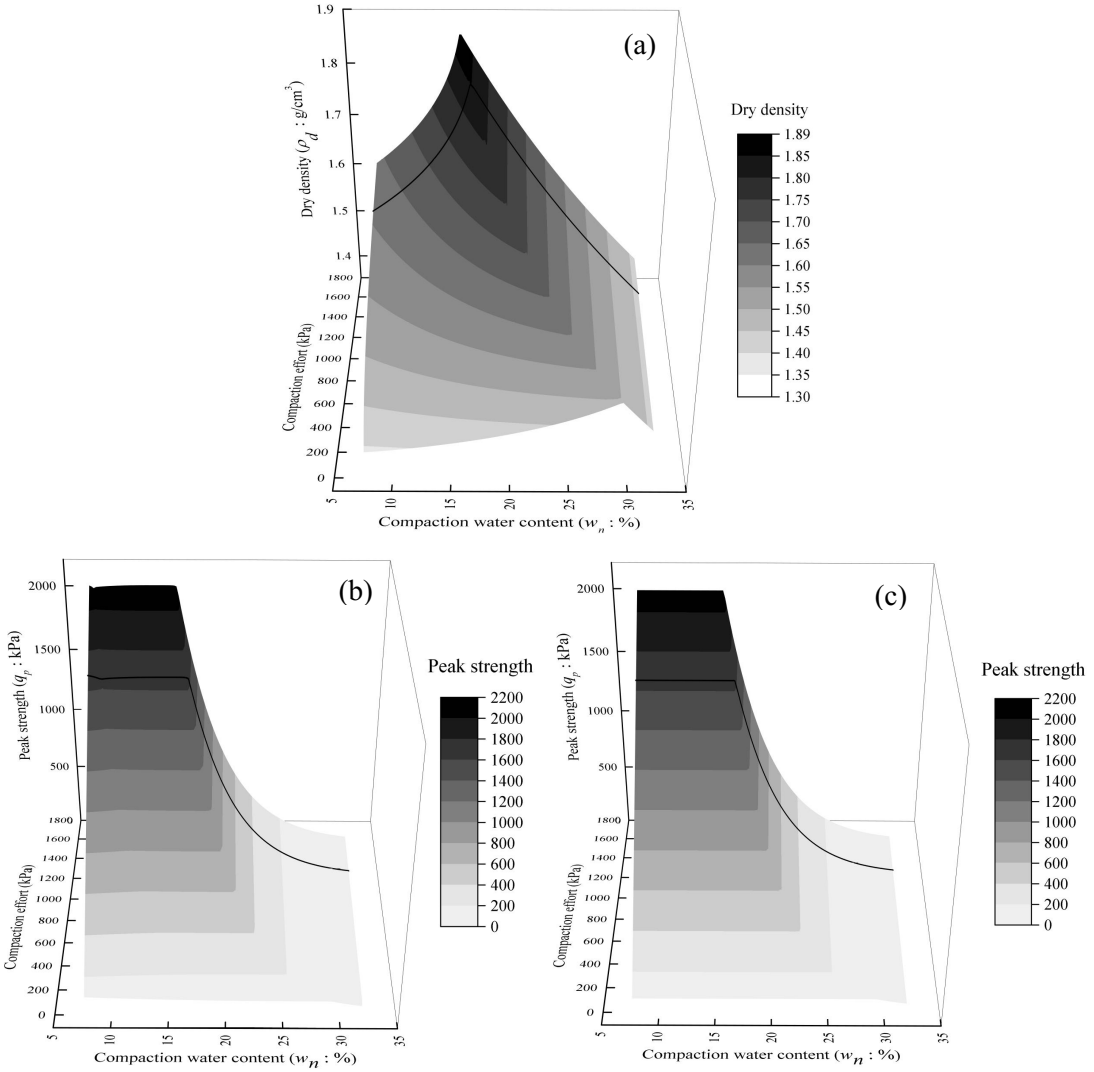

Figure 4-19 Simulation of compaction case 1; a) compaction surface, b) peak strength surface before soaking and c) peak strength surface after soaking

4.2.3 Behaviors of unsaturated compacted soils under fully undrained static cyclic shearing

In the parametric study, using the similar simulation algorithm of compaction process (Section 4.1), initial state of unsaturated soil (5:5 mixed Toyoura sand and Fujinomori clay by weight) for compaction process was newly set for the clear explanation of liquefaction behavior of unsaturated compacted soil when subjected to fully undrained cyclic loading.

For this series of compaction simulation, initial state of soil was assumed to be identical: void ratio e_0 1.143, water content w_n 6.52 % and degree of saturation S_{r0} 15.25 % under mean total stress p 0.9 kPa, pore air pressure u_a 0.0 kPa and pore water pressure u_w -4.22 kPa. Water content was first increased to the prescribed water contents by increasing u_w. Each specimen was isotopically compressed to the prescribed compaction stress of 78.5, 314.0 and 1256.0 kPa, respectively, and unloaded to the initial stress level of 0.9 kPa under exhausted air and

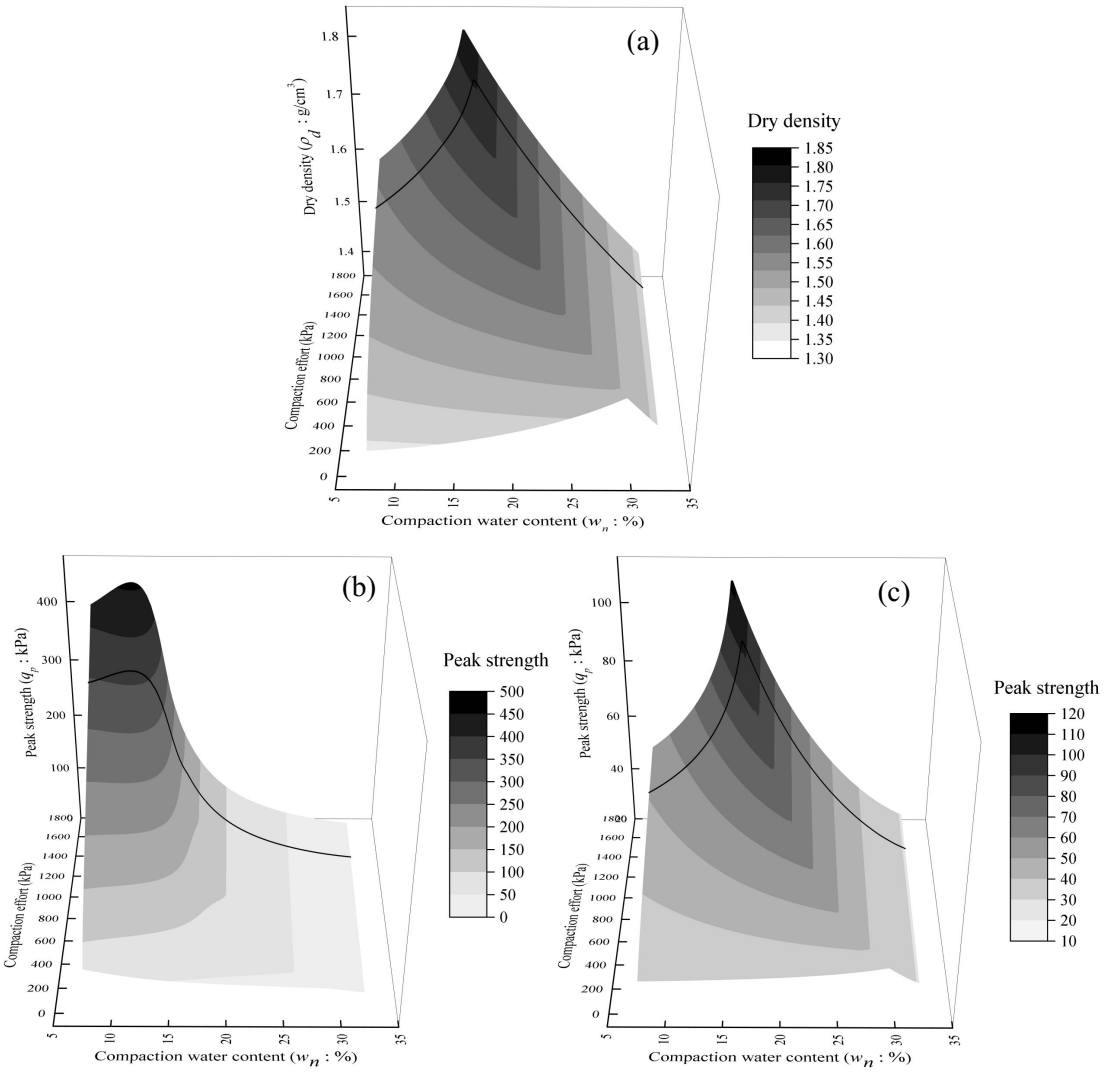

Figure 4-20 Simulation of compaction case 2; a) compaction surface, b) peak strength surface before soaking and c) peak strength surface after soaking

undrained water condition. Compaction behaviors of five specimens having different water contents are compared in Figure 4-21. Final states of the compaction simulation are summarized in Table 4-2. We consecutively performed the similar simulation under varied water contents and compaction stresses and plotted final values of water content and dry density (or void ratio). By the series of simulations, the convex- upward compaction curves are shown in Figure 4-22. The specimens A to E in Figure 4-21 and Table 4-2 are also indicated in this figure.

According to the mechanism of liquefaction, the liquefaction resistance could be considered by the number of cycles causing liquefaction which initial mean effective stress gradually reduces to almost zero. Therefore, 0.10 % of initial mean effective stress $p_o^{"}$ is selected as judgment criteria of liquefaction in this study for simulation effort reduction. In addition, in the case of the soil is unable to liquefy with the limit number of cycles, the tendency of liquefaction resistance is also showed in the relationship of water content and mean effective

stress reduction ratio at the proper cycles of loading. Mean effective stress reduction ratio, Equation (4-3), is the rate of decrease in the mean effective stress of unsaturated soil after they are subjected to cyclic shear loading (Unno et al., 2008).

$$Mean\ effective\ stress\ reduction\ ratio = 1 - \frac{p''}{p''_0} \tag{4-3}$$

The higher the mean effective stress reduction ratio, the lower is the liquefaction resistance of unsaturated soil. By this definition, the apparent tendency of liquefaction resistance could be clearly presented.

Liquefaction behaviors and the comparison between liquefaction resistance of compacted soil along the compaction curve are discussed in this section.

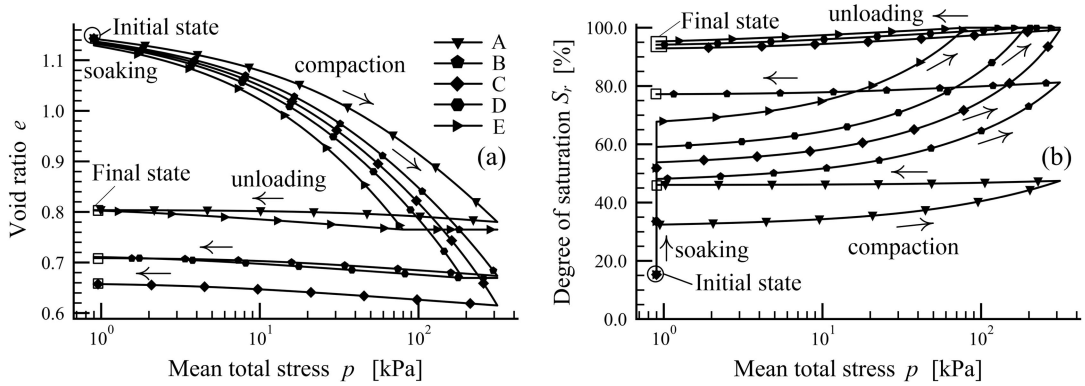

Figure 4-21 Simulation of isotropic compaction test of specimens A, B, C, D and E when compaction stress 314.0 kPa in the relationship of mean total stress vs. (a) void ratio and (b) degree of saturation.

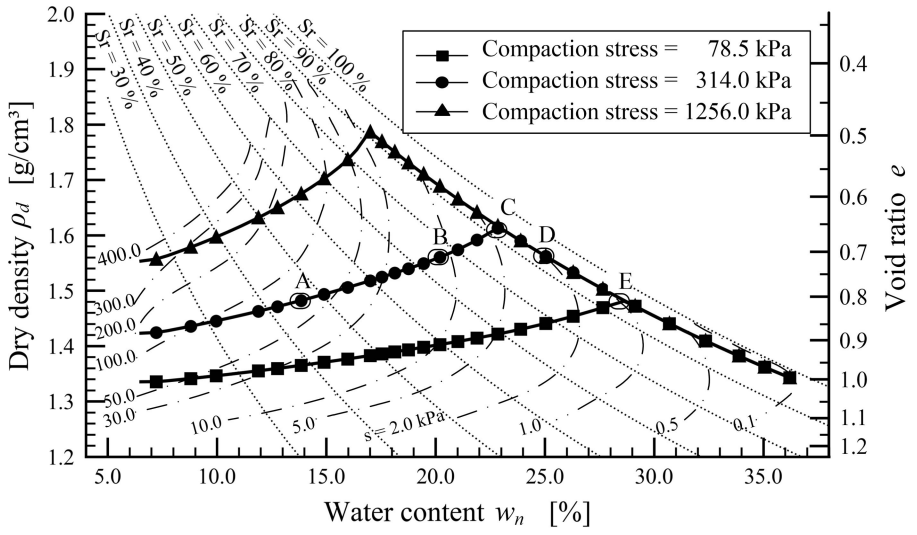

Figure 4-22 Simulation of compaction curve for different compaction stresses 78.5, 314.0 and 1256.0 kPa at the final state of compaction (after unloading).

Table 4-2 Description of the variables of specimens A, B, C, D and E.

Sample	Water content (%)	Degree of compaction (%)	Degree of saturation (%)	Number of cycles causing liquefaction	Remarks
A	13.84	92.0	63.97	49	$w_n < w_{opt}$ (dry side)
B	20.46	97.0	77.18	36	$w_n < w_{opt}$ (dry side)
C	22.85	100.0	92.90	39	$w_n = w_{opt}$ (optimum)
D	25.04	97.0	94.15	38	$w_n > w_{opt}$ (wet side)
E	28.62	92.0	95.29	35	$w_n > w_{opt}$ (wet side)

4.2.3.1 Liquefaction behaviors of unsaturated compacted soils after compaction

Fully undrained (unexhausted-air, undrained-water) cyclic radial constant triaxial shearing with 100 cycles of ± 0.3 % axial strain amplitude (Figure 4-23), was applied to the compacted soils that were numerically generated in the section.

Cyclic behaviors of the compacted samples A to E (Figure 4-22) are illustrated in Figure 4-24. From Figure 4-24(e), all the specimens experienced a significant reduction in mean effective stress after several cycles of fully undrained cyclic shearing. The number of cycles causing liquefaction of samples A to E are shown in Table 4-2. From the table, it reveals that samples A and E demonstrated the highest and lowest liquefaction resistance in the considered range, respectively. However, specimen C which was at optimum water content demonstrated the highest liquefaction resistance in the range of water content between specimens B and D. Both pore water pressure and pore air pressure of all the specimens gradually increased and became constant when the soil were liquified, as shown in Figure 4-24(a) and Figure 4-24(b), respectively. With the increase in pore air pressure, the void ratio was decreased as shown in Figure 4-24(d), which highlights the liquefaction characteristic of unsaturated soils. However, specimens C, D, and E did not exhibit evident variation in the void ratio as they were compacted on the wet side of optimum and they were in nearly saturated state after compaction. Lastly, the degree of saturation of all specimens increased and became constant when the soils were liquified. The increasing of the degree of saturation of specimens A and B is higher than C, D, and E due to the lower of initial degree of saturation (Figure 4-24(c)).

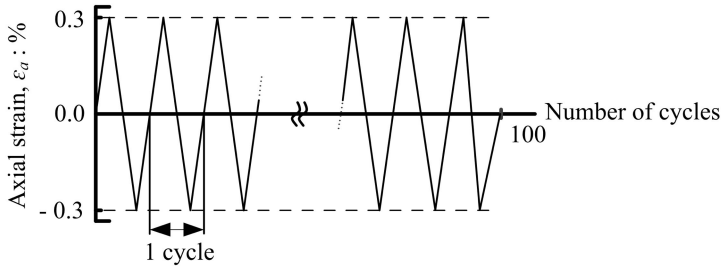

Figure 4-23 Fully undrained (unexhausted-air, undrained-water) cyclic radial constant triaxial shearing with 100 cycles of ± 0.3 % axial strain amplitude

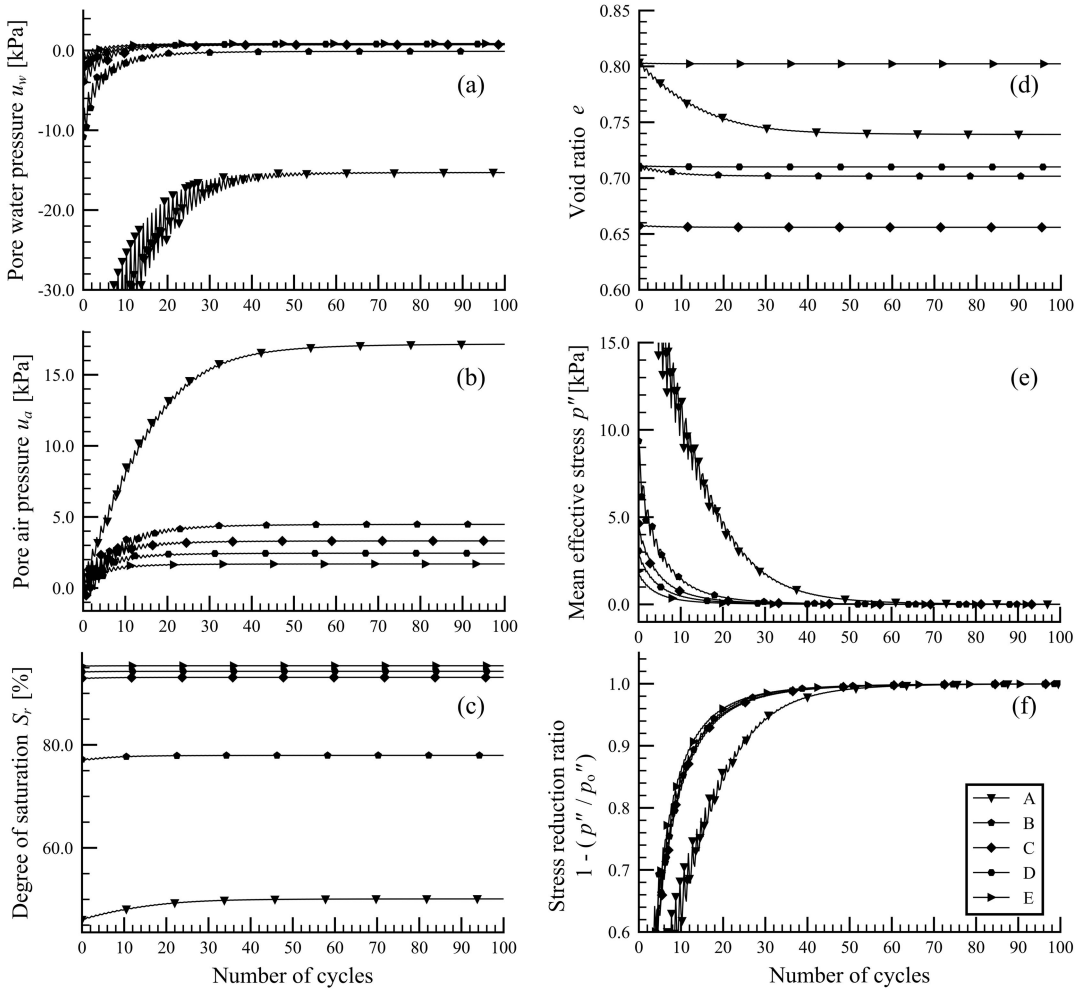

Figure 4-24 Simulation of fully undrained cyclic loading of Points A, B, C, D and E when compaction stress 314.0 kPa in the relationship of number of cycles vs. (a) pore water pressure, (b) pore air pressure, (c) degree of saturation, (d) void ratio, (e) mean effective stress and (f) mean effective stress reduction ratio.

Moreover, the liquefaction resistance of compacted soil was further interpreted as shown in Figure 4-25. The specimens A to E in Figure 4-24 and Table 4-2 are indicated in the figure. As shown in Figure 4-25, the tendency of liquefaction resistance is separately discussed into three main groups. Group 1, low degree of saturation, the liquefaction resistance is very high. It is dominantly affected by the degree of saturation (Komolvilas & Kikumoto 2017). Group 2, high degree of saturation in the dry side of the compaction curve, the liquefaction resistance is quite consistent. It is affected by the combined effects of degree of saturation and dry density. Group 3, the specimens compacted in the wet side of the compaction curve, the liquefaction resistance is low at larger water content. In this group, the liquefaction resistance is dominantly affected by the dry density while the degree of saturation is quite steady. Hence, the simulation results indicate that the water content of compaction affects the liquefaction resistance of the compacted soil through degree of saturation and dry density. Aiming to achieve the optimum

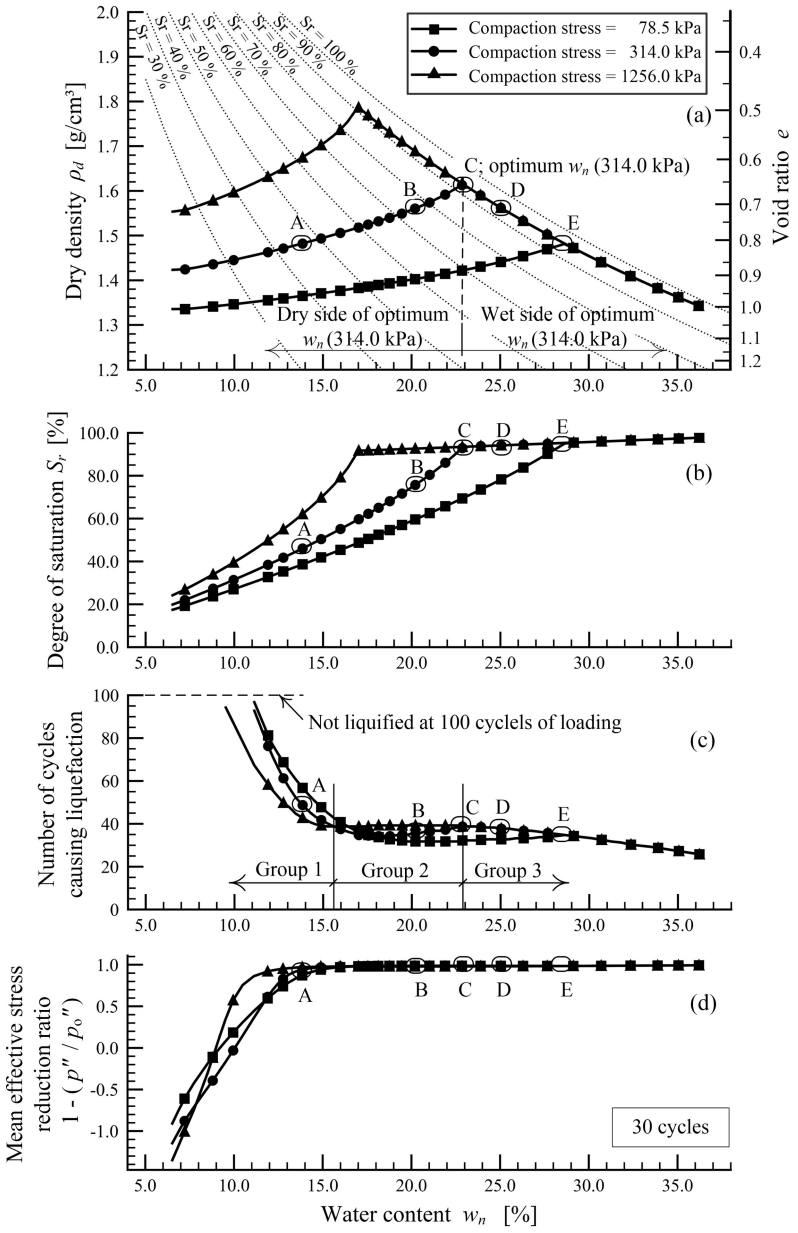

Figure 4-25 Simulation of the tendency of liquefaction potential varied with water content associated with the simulated compaction curve.

water content is rational way to increase liquefaction resistance. The ranges of water content in the compaction curve which is defined as Group 1 through Group 3 are illustrated in Figure 4-25(c), take the compaction stress 314.0 kPa for instance. Besides, we can see from Figure 4-25(c) and Figure 4-25(d) that the compaction effort significantly affects the liquefaction resistance of compacted soils at low water content and the effect gradually decreases when water content increases.

In the simulation, compacted soil with water content approximately less than 10.0% could not be liquefied with 100 cycles of shearing (Figure 4-25(c)). So, the tendency of liquefaction

resistance is also illustrated in the relationship of water content and mean effective stress reduction ratio at 30 cycles of shearing which the apparent tendency is presented (from Figure 4-25(d)). Figure 4-25(d) shows a similar tendency as the relation between the number of cycles causing liquefaction and water content (Figure 4-25(c)).

4.3 CONCLUSIONS

Through the simulations using proposed constitutive model for unsaturated soils, they confirm that the compaction water content affects the behavior of compacted soils including characteristic of compaction curve, hydraulic collapse, shear strength and liquefaction resistance through the degree of saturation and dry density. First, the proposed model could predict well the mechanism of compaction. By the proposed model, the typical convex-upward curves with maximum dry density and optimum water content could be numerically generated for various soil types and their transition due to compaction stress is properly simulated. The typical characteristic of coefficient of permeability before and after soaking against compaction water content are properly calculated from the unique characteristic of degree of saturation and dry density from the compaction and soaking simulations. Second, regarding the shearing behaviors under fully drained static monotonic shearing, the proposed model could demonstrate the different between the strength of compacted soil before and after soaking of the compacted specimens along the compaction curve. Initial compaction control parameter and remained confining pressure affect the peak strength of the compacted soil both before and after soakings. After soaking, the convex-upward peak strength curves which the maximum peak strengths are observed at the optimum water content with the small amount of volumetric change. Last, regarding the liquefaction behavior of compacted soil, the liquefaction resistance is very high in the dry side of compaction curve which is dominantly affected by degree of saturation. When the water contents are approached the optimum water content or higher, combined effect of degree of saturation and dry density on liquefaction resistance could be seen. In addition, the compaction effort significantly affects the liquefaction resistance at low water content and the effect gradually decrease when water content increase. All the tendencies simulated by the proposed model are correspondence with the experimental results reported by many researchers.

For the considering condition, we recommend that soil compacted at the optimum water content is suitable for the compacted soil confronted with the heavy rainfall and subjected to the static monotonic shearing. This is because the highest peak strength, the minimum volumetric changes and low coefficient of permeability after soaking are observed. In case of the optimum water content could not be reached in the compaction process, the soil shall be

compacted on the wet side of optimum to prevent the highly collapse compression due to soaking for the serviceability of the embankment. In addition, aiming to achieve the optimum water content is also the rational way to increase the liquefaction resistance of the unsaturated compacted soil. Importantly, engineer can specify the optimum compaction control parameters in the construction for the considered range by the simulation of the proposed model.

Exploring the real geotechnical engineering which the soil shall be considered in the heterogeneity condition, with the validity and capability of the proposed model as described in Chapters 3 and 4, the proposed constitutive model for unsaturated soil is implemented to the algorithm of soil-water-air three-phases seepage-deformation coupled finite element method (Chapter 5). Afterward, the interpretation of the mechanics of unsaturated soil in the heterogenous problems is discussed in Chapter 6.

CHAPTER 5

FINITE ELEMENT ANALYSIS FOR UNSATURATED SOILS

In the continuum mechanics, the elementary behaviors of unsaturated compacted soil are interpreted and explained by the elastoplastic constitutive model for unsaturated soils (Chapter 4). However, the interpretation based on the basic soil properties does not allow the solution of the real condition of geotechnical work which the stress-strain distribution in the considered domain system is non-uniform. The variation of stress-strain distribution can be caused by the heterogeneities of typical soil deposit and man-made soil structure, the seasoning ground water level and the non-uniform pressure load on the space. Therefore, in this study, the heterogeneity at the initial state of density and degree of saturation of the unsaturated media on the soil structure is taken into account in the geotechnical engineering design. Finite element method or FEM is a calculation procedure which keeps track of the variation of stress-strain distribution of many small elements of soil in the domain system. At the same time, it ensures compatibility and equilibrium of the stress-strain state for each small element with its neighbors.

To interpret the real condition of geotechnical work and achieve the purpose of the research, in-house coupled FEM program for unsaturated soils are generated. In this chapter, the general steps of Galerkin's FEM are briefly described. For clearly explanation and programming algorithm checking, finite element equations for in-house FEM programs are formulated staring from the simple algorithm of saturated soil through the complicated algorithm of unsaturated soil. The in-house FEM programs are simply generated by the assumption of two-dimensional or 2-D plane strain condition. Therefore, application of the programs is limited for the oedometer compression test and the biaxial shearing test only. In addition, for the scope of this study, the soil-water-air three-phase seepage-deformation coupled FEM for unsaturated soil is based on the assumption of constant air pressure. However, by the low loading rate, this assumption is still applicable in many practical situations and sufficiently response to the purpose of this study including the interpretation of the soil compaction and the fully drained shearing behaviors. Finally, the in-house FEM programs for saturated and unsaturated soils are validated through the exact solution or the proposed elastoplastic constitutive model in order to ensure their algorithm and accuracy.

Afterwards, in the Chapter 6, the parametric study through FEM will be performed using the validated soil-water-air three-phase seepage-deformation coupled FEM in order to interpret the mechanism of unsaturated soil in the heterogenous problems.

5.1 GENERAL STEP OF FINITE ELEMENT METHOD

The development process for FEM is generally performed by the following 5 main steps:

1) Subdividing the problem domain into finite elements
2) Selecting the element geometry and the element interpolation function
3) Formulation of FEM equation (using weighted residuals Galerkin's method)
4) Solving the assembled global equation
5) Boundary condition application and determination of the approximate solution

Further details of each main steps are explained by the followings.

5.1.1 Subdividing the problem domain into finite elements

The problem domain system $\boldsymbol{\Omega}$ and the boundary of the domain system $\boldsymbol{\Gamma}$ are discretized into the finite element domain Ω^{ele} and the boundary of the finite element domain Γ^{ele}, respectively. The superscription *ele* denotes number of elements n_{el} in the domain system where $1 \leq ele \leq n_{el}$ (Figure 5-1).

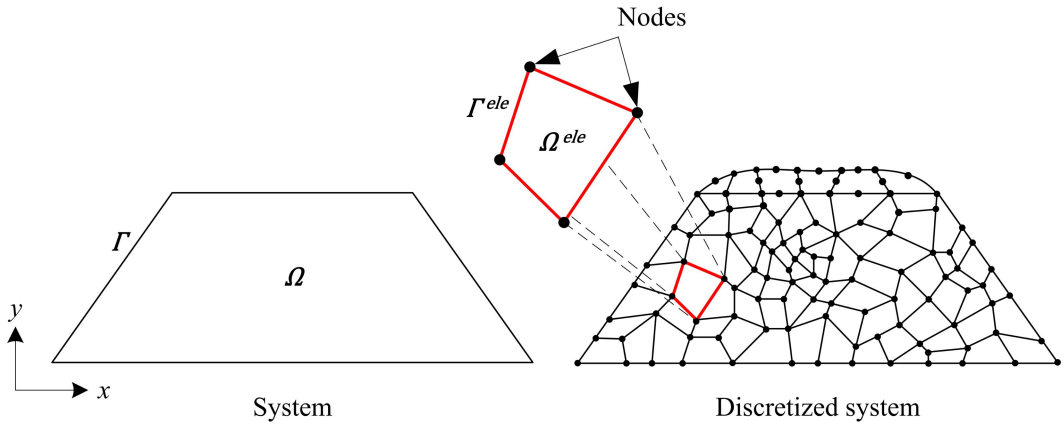

Figure 5-1 Subdividing the problem domain into finite elements

5.1.2 Selecting the element geometry and element interpolation function

FEM is a numerical method to find the approximate solution of the governing equation which is applicable to the complex shape or its original shape of the problem. The infinite value will be approximated by replacing the problem with the shaped finite elements. Because of this, the accuracy of the approximate solution and the numerical stability due to the locking problem are depend on mesh size, amount of element, element geometry and interpolation function.

Keeping the accuracy of the approximate solution and the robustness of the in-house FEM program, in this section, the appropriate element geometry, interpolation functions and alternative FEM formulation (locking remediation options) are together specified for the in-house FEM program based on the characteristic of each interested problem. Although the size

and amount of element could improve the accuracy and delay the locking problem, but they will not be discussed in this section. This is because, they would take the high price of computational and could not completely eliminate the problem.

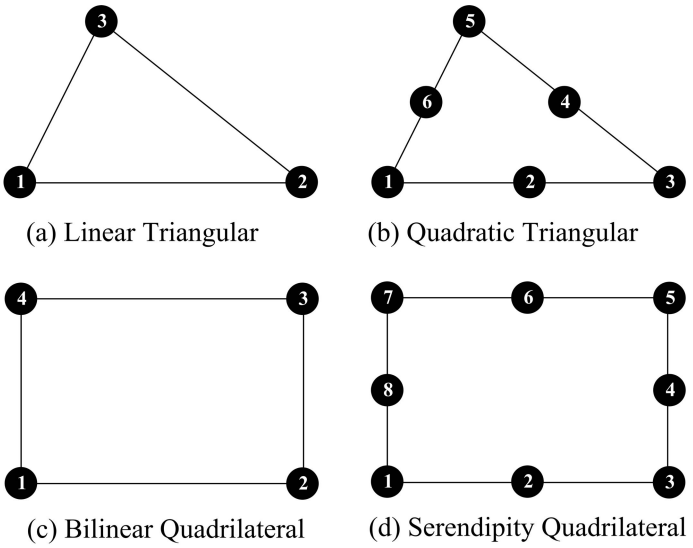

Figure 5-2 Basic type of elements in 2-D FEM

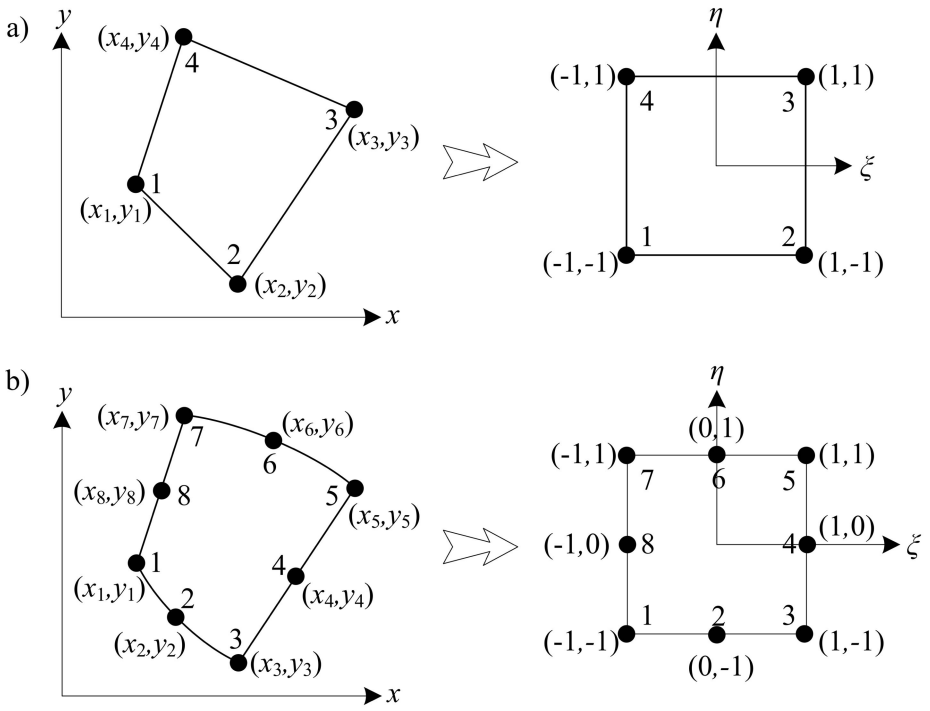

Figure 5-3 Transformation of a) trapezium (4 nodes or 8 nodes) and b) curved surfaces (8 nodes) elements to the natural coordinate (ξ - η) square element

5.1.2.1 Element geometry and interpolation function

For 2-D problems in the plane strain condition, the quadrilateral (rectangular) element which is the basic type of element in 2-D FEM (Figure 5-2(c) and Figure 5-2(d)) shall be applied into the in-house FEM program in this study. Since it could provide a better solution due to the curved plane of bilinear or serendipity interpolation function with a less computational price compare to the triangular element (Figure 5-2(a) and Figure 5-2(b)). In the incompressible case, although, the quadrilateral may face the locking problems, but they could be eliminated by selecting the appropriate element interpolation function and alternative FEM formulation (See further discussion in Section 5.1.2.2).

In the practical, however, the linear or curved surfaces trapezium element shall be used instead of the rectangular element in order to exactly generate the complex shape of the problem. By this condition, the numerical integration over the trapezium element for element matrix generation is much more complicated. Solving this, the Gauss-Legendre integration formulas (See Appendix B-4) which is the simple integration method is implemented into the program. However, for the integrating by the Gauss-Legendre formulas, the local coordinate (x-y) of trapezium element must be transformed into the natural coordinate (ξ - η) square element with the distance from -1 to 1 in each direction (Figure 5-3). Doing this, any x-y coordinates in the trapezium element can be written in the relation of local trapezium element node (x_i, y_i) and the shape function in term of natural coordinates, $\widehat{N}_i(\xi,\eta)$ by:

$$\begin{aligned} x(\xi,\eta) &= \sum_{i=1}^{n} \widehat{N}_i(\xi,\eta)x_i = \left[\widehat{\boldsymbol{N}}(\xi,\eta)\right]_{1\times n}\{\boldsymbol{x}\}_{n\times 1} \\ y(\xi,\eta) &= \sum_{i=1}^{n} \widehat{N}_i(\xi,\eta)y_i = \left[\widehat{\boldsymbol{N}}(\xi,\eta)\right]_{1\times n}\{\boldsymbol{y}\}_{n\times 1} \end{aligned} \tag{5-1}$$

where i (= 1, 2,…, n) denotes node number of the n-nodes element, x_i and y_i represent x and y coordinates at node i of trapezium element, and $\widehat{N}(\xi_i,\eta_i)$ is the shape function that is used to transform the shape of the element. The selected shape function for the in-house FEM in term of natural coordinate (Zienkiewicz et al., 2005), including bilinear quadratic lateral (4 nodes) and serendipity quadrilateral element (8 nodes), are illustrated in Appendix B-1.

Moreover, for the determination of approximate solution distribution which is generally written by:

$$\tilde{\phi} = \sum_{i=1}^{n} N_i\phi_i = [\boldsymbol{N}]_{1\times n}\{\boldsymbol{\phi}\}_{n\times 1} \tag{5-2}$$

where i (= 1, 2,…, n) denotes node number of the n-nodes element, ϕ_i or $\{\boldsymbol{\phi}\}$ is the approximate solution of any element and N_i or $[\boldsymbol{N}]$ is the element interpolation function. In order to simplify the approximate solution determination, the assumption of isoparametric element is applied. Therefore, the selected shape function is also used as the interpolation function of the element as expressed by:

$$N_i = \widehat{N}_i(\xi, \eta) \tag{5-3}$$

The isoparametric element, which is widely used for solving general problem in FEM (Zienkiewicz et al., 2005), will be applied to the FEM equation formulation in Section 5.1.3.

In summary, for the in-house FEM program, the FEM equation is generated for the trapezium elements using the shape function of quadrilateral element in term of natural coordination, the approximate solution of an element could be determined by integrating on the square isoparametric element by the Gauss-Legendre integration.

5.1.2.2 Alternative FEM formulation for locking remediation

In fact, for the problems that is solved by standard FEM (or deformation-only analysis uncoupled FEM) the best approximated solution of Galerkin's FEM (Section 5.1.3) is precisely accommodated by selecting a suitable quadrature rule in order to maintain the full rate of convergence of the exactly integrated formulation using Gauss-Legendre integration. The proper quadrature rule including the optimal number of gauss point, weight of gauss integration and gauss point location for numerical integration of the specified shape function are illustrated in Table B-1 in Appendix B-4. However, the poor approximation could have happened if there is no any function in trial solution which is able to accurately predict the exact solution. This case refers to the constrained media problem which includes incompressible or nearly incompressible behavior and the constant volumetric plastic strain at the critical state of the elastoplastic constitutive model or known as the locking problem. The alternative finite element formulations, including the reduced integration techniques and the mixed finite element method, have been suggested to accommodate the successful approximation (Hughes, 1987 and Zienkiewicz et al., 2005).

5.1.2.2.1 Mixed Finite Element Method

Mixed Finite Element Method (or Mixed FEM) is applicable for generating the coupled FEM, displacement and pressure variable capturing the seepage – deformation behavior of soil in fully saturated and unsaturated conditions. Besides, it effectively improves the locking problem.

Due to the fact that the incompressible or nearly incompressible problems analysis using the standard FEM, the pressure value could be determined only up to an arbitrary constant due to the locking behavior. This is because solving a single governing equation in the standard matric problem is not valid for all behaviors. Therefore, the way of the improvement using Mixed FEM is establishing the "constrained variational problem" which is modified from the original governing equation in order to capture all the possible behaviors. The additional governing equation or constraints shall be added and combined with the original condition.

However, using this method, the matrix equation is different from the standard FEM. The eigen value of coefficient matrix is not always positive. In the severe case, especially when the improper interpolation function combination of the mixed element is used, the eigen value may lead to be zero (or singular coefficient matrix) in the incompressible case which the solution is impossible. Since the combination of interpolations may lead to poor numerical performance and even nonconvergence, so selecting the proper element geometry and interpolation function is the first important step for generation the mixed FEM.

Selecting the proper interpolation function for mixed FEM requires two necessary coefficient matrix singularity assessment methods which are the constrain count and the Babuska-Brezzi (LBB) stability condition.

Constraint count (Hughes, 1987) is the first simple criterion, in order to determine the ability of an element performing in the constrained media. Constraint ratio, r, by:

$$r = \frac{n_{eq}}{n_c} \tag{5-4}$$

where n_{eq} is the total number of equilibrium equations after boundary conditions have been imposed and n_c is the total number of incompressibility constraints (or number of incompressibility equation in linear pressure equation). The interpretation of r-value, for 2-D element about the locking problems and accuracy of approximation result are summarized in Table 5-1.

Even though the constraint count is able to alleviate the locking (r-value is more than or equal to optimal value as shown in Table 5-1) but the element may exhibit spurious pressure modes due to the non-convergence of FEM. Therefore, Babuska-Brezzi (LBB) stability condition (Babuska, 1971; Babuska, 1973 and Brezzi, 1974) which is the mathematical convergence theory for mixed FEM shall be additionally taken into account in order to control the stability (or singularity) of the element equation solving.

Regarding to the singularity assessment on the coefficient matrix, serendipity deformation quadrilateral (8 nodes) and the bilinear pore water pressure quadrilateral (4 nodes) are widely used in the incompressible analysis (Hughes, 1987). Since this element could alleviate the

locking problem by satisfying the Babuska-Brezzi condition and constraint count with the lowest possible constraint ratio.

In conclusion, the proper set of elements, serendipity deformation quadrilateral (8 nodes) and the bilinear pressure quadrilateral (4 nodes), is used in this study for coupled pressure – deformation analysis (Figure 5-4). Mixed FEM which is the arbitrary combinations of displacement and pressure alternative finite element formulation is implemented and described in Sections 5.2.3 and 5.2.4 for saturated and unsaturated soils, respectively.

5.1.2.2.2 Reduced integration technique

The standard FEM for deformation – only analysis is the simple way to evaluate the compressibility (load – deflection) problem. For incompressible application, however, this element frequently exhibits a tendency of lock since the element interpolation function could not represent the field approximation distribution as mention before. By this reason, the approximate solution calculated by the numerical integration (Gauss's Integration) on the surface of each Gauss point will give some erroneous. For standard FEM, the simple modification to alleviate the locking is reducing the order of Gauss's integration lower than normally used for the coefficient matrix generation. This modification is called reduced integration (Zienkiewicz et al., 1971). However, the reduced integration causes unwanted behavior of the element (or spurious mode) since it reduces the rank of the stiffness matrix, especially in the lower order element.

Regarding this study, the performance of the quadrilateral element type in order to alleviate locking problem is discussed. Bilinear quadrilateral (4 nodes) element is one of the lower-order elements that has the high tendency of locking. It is troubled with both 2 kinds of locking, volumetric locking and shearing locking (Macneal, 1994). Due to the lower order element, eliminating both kinds of locking using fully reduced integration severely lead to the spurious mode. Recently, many researchers have developed the solutions for locking problem in lower order element which is sophisticated and out of scope in this study such as selective reduced integration (Hughes et al., 1978), B-bar method (Hughes, 1980), mixed assumed strain method (Simo & Rifai, 1990) and etc.

Table 5-1 Constraint ratio r-value interpretation for 2-D problem (Hughes, 1987)

Constraint ratio	Interpretation
$r > 2$	too few incompressibility constraint
$r = 2$	optimal
$r < 2$	too many incompressibility constraints
$r \leq 1$	locking

In the other hand, serendipity quadrilateral (8 nodes) which is the higher order element that can exactly interpolate field properties is used in this study. Although, it is only troubled with the shearing locking (Macneal, 1994), fully reduced integration could solve the issue without the spurious mode. Therefore, the in-house FEM for deformation – only analysis uncoupled FEM in this study for solving 2-D problems is based on the serendipity quadrilateral element (8-nodes), together with fully reduced integration (four Gauss points per element). This particular combination is chosen for its simplicity, and also its well-known ability to compute collapse loads accurately (e.g., Zienkiewicz et al., 1975; Griffiths, 1980 and Griffiths, 1982).

In conclusion, the element geometry, element interpolation function and alternative formulation for locking remediation are summarized as follows;

- For uncoupled FEM deformation-only analysis, the standard FEM serendipity quadrilateral (8 nodes) deformation element is used to perform the numerical simulation with the full reduced integration (four Gauss points per element) (Figure 5-4(a)).
- For uncoupled FEM pressure-only analysis, no locking problem, the standard FEM bilinear quadrilateral (4 nodes) pressure element is used to perform the numerical simulation without any reduced integration (four Gauss points per element) (Figure 5-4(b)).
- For coupled FEM seepage (2 and 3 phases) – deformation analysis, the mixed FEM serendipity deformation quadrilateral (8 nodes) and the bilinear pressure quadrilateral (4 nodes)", is used to perform the numerical simulation for saturated and unsaturated conditions (Figure 5-4(c)).

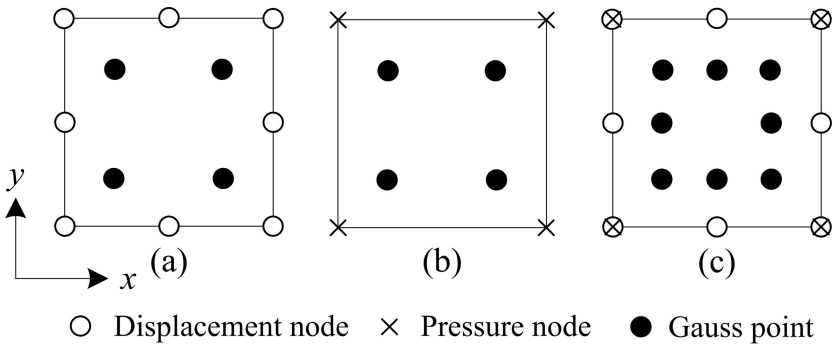

Figure 5-4 The element geometry, location of node and its gauss point using in the in-house FEM programs a) uncoupled FEM deformation-only analysis, b) uncoupled FEM pressure-only analysis, c) coupled FEM seepage (2 and 3 phases) – deformation analysis

5.1.3 Formulation of FEM equation by weighted residuals Galerkin's method

Most of the engineering problems could be explained by the conventional differential equation that the solution is always truth on every single point in the domain as known as the governing equation (or strong form). However, determining the exact solution of governing equation using analytic solution is tough or impossible.

FEM is the numerical method for determining the approximate solution of the governing equation. In the FEM development process, the governing equation will be relaxed all requirements on solutions to a certain extent, the weak form is formulated. Weak form is the integral equation containing the differentiate equation states that the conditions need to be satisfied in an average sense. Although all solutions of the weak form will not satisfy the governing equation, but the weak form implies the governing equation. Thus, we could obtain the approximate solution of the governing equation by solving the weak form afterward.

In this study, the well-known weighted residuals Galerkin's method is implemented to the in-house FEM program in order to generate the weak form of the governing equation, since this method provides the simple calculation, low computation price and the symmetric finite element matric which is good for the large problem computational. So, in this section, following is step by step explanation of the important procedure in order to formulate FEM equation by the weighted residuals Galerkin's method.

Step 1: Determination of the differential equation corresponding to the considered problem

General differential equation can be written by Equation (5-5) , where *L* is the differential operator and $\bar{\phi}$ is the exact solution.

$$L(\bar{\phi}) = 0 \tag{5-5}$$

Step 2: Determination of distribution of approximate solution on the element (spatial discretization)

By the assumption of isoparametric element, general distribution of approximate solution (Equation (5-2)) can be written as the distribution of approximation in local x-axis and y-axis for n-nodes 2-D element by:

$$\begin{aligned} &\text{In x-axis:} && \widetilde{\phi}_{\mathrm{x}} = \mathrm{N}_1\phi_{\mathrm{x}_1} + \mathrm{N}_2\phi_{\mathrm{x}_2} + \cdots + \mathrm{N}_{\mathrm{n}}\phi_{\mathrm{x}_{\mathrm{n}}} \\ &\text{In y-axis:} && \widetilde{\phi}_{\mathrm{y}} = \mathrm{N}_1\phi_{\mathrm{y}_1} + \mathrm{N}_2\phi_{\mathrm{y}_2} + \cdots + \mathrm{N}_{\mathrm{n}}\phi_{\mathrm{y}_{\mathrm{n}}} \end{aligned} \tag{5-6}$$

where n is number of nodes of an element and N_i is the isoparametric element interpolation function in term of natural coordinate (Appendix B-1). Equation (5-6) can be written in the matrix form as expressed by:

$$\begin{Bmatrix}\phi_x\\ \phi_y\end{Bmatrix}_{2\times1} = \begin{bmatrix}N_1 & 0 & N_2 & 0 & \dots & \dots & N_n & 0\\ 0 & N_1 & 0 & N_2 & \dots & \dots & 0 & N_n\end{bmatrix}_{2\times2n} \begin{Bmatrix}\phi_{x_1}\\ \phi_{y_1}\\ \phi_{x_2}\\ \phi_{y_2}\\ \vdots\\ \phi_{x_n}\\ \phi_{y_n}\end{Bmatrix}_{2n\times1} \tag{5-7}$$

or we can write in the compacted form as:

$$\{\tilde{\boldsymbol{\phi}}\} = [\boldsymbol{N}]\{\boldsymbol{\phi}\} \tag{5-8}$$

where $\{\tilde{\boldsymbol{\phi}}\}$ denotes the vector of approximated solution distribution, $[\boldsymbol{N}]$ denotes the row matrix of isoparametric interpolation function and $\{\boldsymbol{\phi}\}$ denotes the nodal vector of approximate solation or unknown of each node in the element.

Step 3: Formulation the finite element equation by weighted residuals Galerkin's method

From Equation (5-5), if the exact solution $\bar{\phi}$ is substituted by the approximate solution $\tilde{\phi}$ (Equation (5-2)), some errors or residual (R) may be occurred as shown in Equation (5-9).

$$R = L(\tilde{\phi}) = L([\boldsymbol{N}]_{1\times n}\{\boldsymbol{\phi}\}_{n\times1}) = L(\sum_{i=1}^{n} N_i\phi_i) \tag{5-9}$$

Using the Galerkin's method, the residual is weighted by multiplying with weighting function (W_i), then we integrate the multiplied equation on all the domain of element and set the result to be zero as shown in Equation (5-10).

$$\int_{-1}^{1} W_i R d\boldsymbol{\Omega} = 0 \tag{5-10}$$

Step 4: Integration by parts

Substitute the residual (Equation (5-9)) into Equation (5-10), we will get:

$$\int_{-1}^{1} W_i R d\boldsymbol{\Omega} = \int_{\Omega^{ele}} W_i L(\sum_{i=1}^{n} N_i\phi_i) d\boldsymbol{\Omega} = 0 \tag{5-11}$$

For a body of arbitrary shape, we usually consider the points inside the body as the domain denoted by Ω^{ele} and the boundary of the domain in denoted by Γ^{ele} (Figure 5-1). In any conservation law, a weak form of the differential equations (Equation (5-11)) could be written in the combinations of domain and boundary of the element based on the divergence theorem which is the surface integral of a vector field over a closed surface is equal to the volume integral of the divergence over the region inside the surface as written by:

$$\int_{\Omega^{ele}} W_i L\left(\sum_{i=1}^{n} N_i \phi_i\right) d\boldsymbol{\Omega} = \int_{\Omega^{ele}} (W_i, N_i, \phi_i) d\boldsymbol{\Omega} + \int_{\Gamma^{ele}} (W_i, N_i, \phi_i) d\boldsymbol{\Gamma} = 0 \quad (5\text{-}12)$$

For 2-D problem as considering in this study, the second derivative part in Equation (5-12) would cause them to vanish (Smith, Griffiths, & Margetts, 2014), this difficulty is resolved by applying Green's theorem (Zienkiewicz et al., 2005) which is equivalent to divergence theorem in 2-D. In addition, the element interpolation function is normally selected as the weighting function in the calculation which is called Buvnov-Galerkin ($W_i = N_i$). Therefore, the final element equation can be generally written by:

$$\int_{\Omega^{ele}} N_i L\left(\sum_{i=1}^{n} N_i \phi_i\right) d\boldsymbol{\Omega} = \int_{\Omega^{ele}} (N_i, \phi_i) d\boldsymbol{\Omega} + \int_{\Gamma^{ele}} (N_i, \phi_i) d\boldsymbol{\Gamma} = 0 \quad (5\text{-}13)$$

The general procedure for finite element equation formulation described here will be applied for the considering problems in Section 5.2.

5.1.4 Solving the assembled FEM global equation

The matrix forms of element equations are generated and summed up into the global equation in the domain. In this study, a typical global equation system is normally expressed in the form of first-order time dependent problems as:

$$[\boldsymbol{K_c}]\{\boldsymbol{\phi}\} + [\boldsymbol{M_c}]\{\dot{\boldsymbol{\phi}}\} = \{\boldsymbol{Q_c}\} \quad (5\text{-}14)$$

where $\{\boldsymbol{\phi}\}$ represents the approximate dependent variable nodal vector, $[\boldsymbol{K_c}]$ and $[\boldsymbol{M_c}]$ represent the general coefficient matrices and $\{\boldsymbol{Q_c}\}$ represents the general load vector.

From Equation (5-14), the Euler's method (Figure 5-5) is the computational method in order to approximate the solution of the ordinary differential equation as typically shown in Equation (5-15).

$$\dot{\phi} = f(t, \phi) \quad (5\text{-}15)$$

Defining the initial condition $\phi(t_0) = \phi_0$, for any step of time $t_{n_t} = t_{n_t-1} + h_t$, the dependent variable of any time step n_t (or ϕ_{n_t}) is determined by:

$$\phi_{n_t} = \phi_{n_t-1} + h_t f(t_{n_t-1}, \phi_{n_t-1}) \quad (5\text{-}16)$$

for all considering time range $t_0 \leq t \leq t_0 + \Delta t$ and h_t is the constant sub-increment of Δt.

In addition, for the nonlinear elastoplastic problems, the incremental method is applied. This method approximates the nonlinear problem by using a piecewise linear step. If the discretized time h_t is very small, the nonlinear problem is able to approximate by the linear interpolation. For the n_t^{th} time step ranging from t_{n_t-1} to $t_{n_t} = t_{n_t-1} + h_t$, the interpolated dependent variable $\phi_{n-1+\theta}$ is linearly interpolated by:

$$\phi_{n_t-1+\theta} = \theta\phi_{n_t} + (1-\theta)\phi_{n_t-1} \tag{5-17}$$

where interpolation parameter $\theta = [0,1]$ for sub-incremental interpolated time is in the range of range $t_{n_t-1} \leq t_{n_t-1+\theta} \leq t_{n_t}$ (Figure 5-5).

With the time discretization and the Euler's method, the dependent variable ϕ and $\dot{\phi}$ for non-linear problem can be written as Equations (5-18) and (5-19), respectively.

$$\phi = \theta\phi_{|t+h_t} + (1-\theta)\phi_{|t} \tag{5-18}$$

$$\dot{\phi} = \frac{\Delta\phi}{h_t} = \frac{\phi_{|t+h_t} - \phi_{|t}}{h_t} \tag{5-19}$$

where $\phi_{|t}$, $\phi_{|t+h_t}$ is the dependent variable at current time t and the next step time $t + h_t$. Substituting Equations (5-18) and (5-19) into the Equation (5-14), the approximate solution could be solved form the global equation system.

In this study, choosing the value of $\theta = 0$ together with the small discretized time h_t, gives the forward Euler's method which is accurate and robust in solving the systems of ordinary differential equations for nonlinear problems. It is closely related to the large family of explicit methods which are used for solving systems of ordinary differential equations. This property makes them attractive for geomechanics studies which frequently employ very complex constitutive laws. Therefore, the explicit Euler's is implemented to the in-house FEM program in order to solve the finite element equation.

The general procedure for solving the finite element equation described here will be applied for the considering problems in Section 5.2.

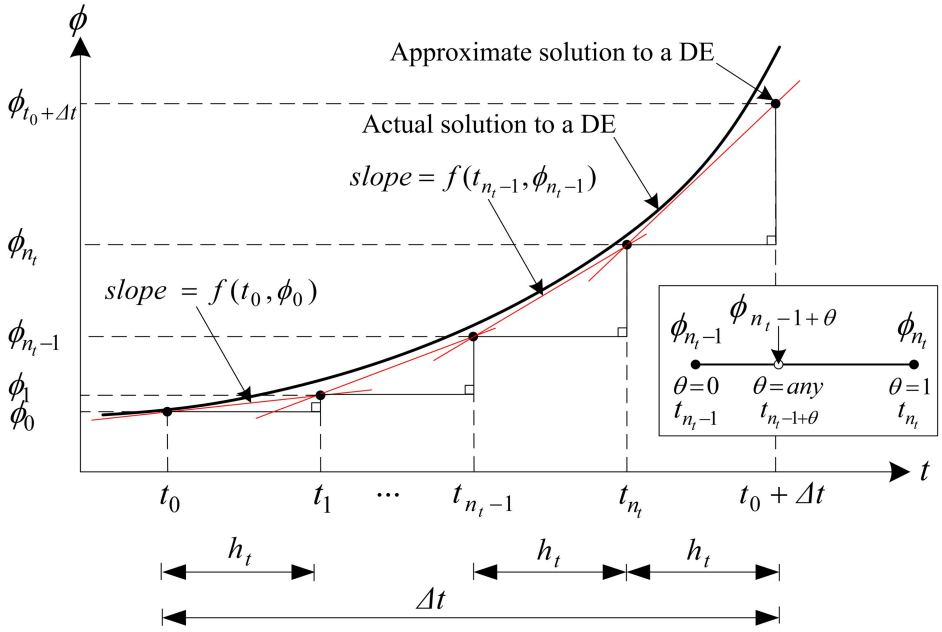

Figure 5-5 Euler's method and sub-incremental time step

5.1.5 Boundary condition application and determination of the approximate solution

After the global FEM equation was discretized by time for solving ordinary differential equation, then the boundary conditions are applied in order to determine the interested approximated solution.

In this study, the boundary conditions shall be applied to the nodal variable vectors of the global equation, including the incremental of displacement $\{\boldsymbol{\Delta U}\}$, the pore water pressure at time t $\{\boldsymbol{U_{w|t}}\}$, the pore water pressure at time $t + h_t$ $\{\boldsymbol{U_{w|t+h_t}}\}$, increment of external force $\{\boldsymbol{\Delta F_{ext}}\}$ and inflows-outflows of water $\{\boldsymbol{Q}\}$.

The stated variables need to be control at the boundary of the domain for setting the drainage condition and loading condition for solving the finite element equation of each experiments.

5.1.5.1 Displacement boundary condition

The displacement in the specified direction at the boundary could be constrained by the following conditions at constrained nodal points of the boundary.

- Compression or shearing by the displacement control in the specific direction;

$$\Delta U = \frac{Total\ displacement}{number\ of\ discritizing\ step} \tag{5-20}$$

- The boundary is not allowed to be deformed in the specific direction;

$$\Delta U = 0 \tag{5-21}$$

5.1.5.2 External force boundary condition

The external force in the specified direction at the boundary could be constrained by setting the following conditions at constrained nodal points of the boundary.

- Compression or shearing by the force control in the specific direction;

$$\Delta F_{ext} = \frac{\text{Total external force}}{\text{number of discritizing step}} \tag{5-22}$$

- The external force at the boundary is kept constant in the specific direction;

$$\Delta F_{ext} = 0 \tag{5-23}$$

5.1.5.3 Seepage boundary condition

Disallowing the inflows or outflows of water through the surface boundary or undrained water condition could be constrained by setting the following condition at constrained nodal points of the boundary.

$$Q = 0 \tag{5-24}$$

Allowing the inflows or outflows of water through the surface boundary or drained water condition could be constrained by setting the following condition at constrained nodal points of the boundary.

$$\Delta U_w = 0 \; or U_{w|t+h_t} = U_{w|t} \tag{5-25}$$

Remarks: In this study, u_a is assumed to be constant in order to allow the air flow in and out freely along the surface and in the domain.

Boundary conditions for the considering experiments are presented by the illustration of 3x3 rectangular elements figures as shown in Figure 5-6.

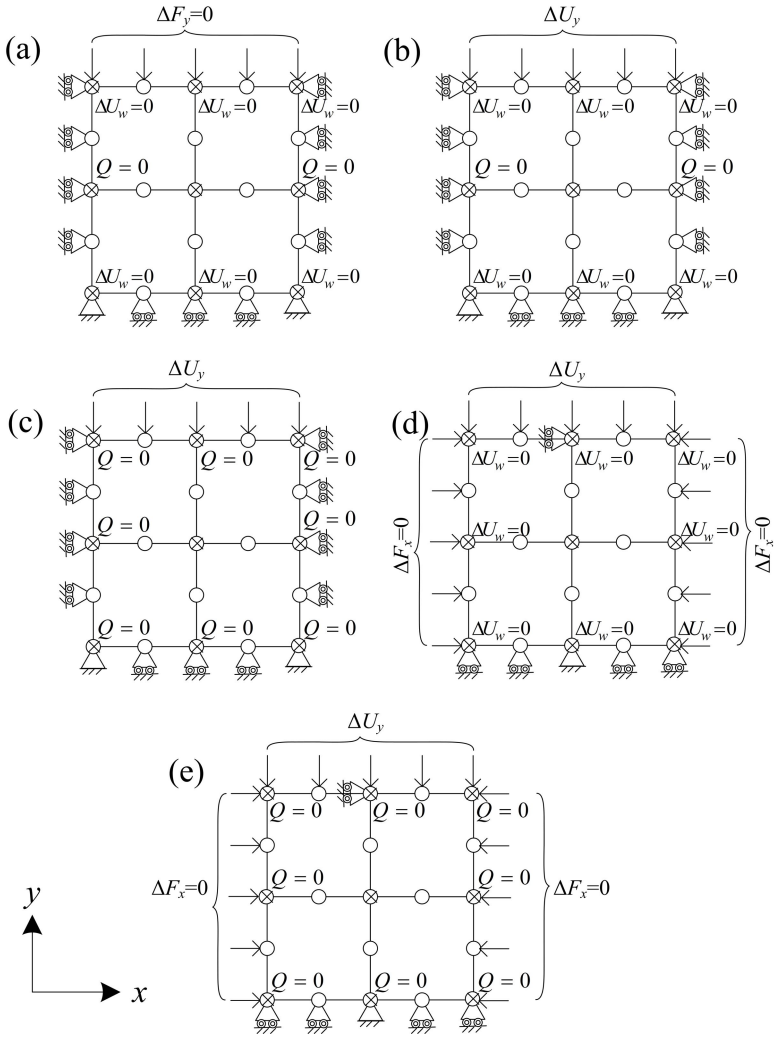

Figure 5-6 Boundary conditions of the considering experiments: (a) oedometer consolidation test of saturated soil (open layer), (b) oedometer fully drained compression test , (c) oedometer compaction test, (d) biaxial radial constant fully drained shearing test and (e) biaxial radial constant exhausted air – undrained water shearing test

5.2 FORMULATION AND SOLUTION OF FINITE ELEMENT EQUATIONS FOR CONSIDERING PROBLEMS

This section illustrates the development process of FEM for considering problems starting from the simple algorithm of saturated soil through the complicated algorithm of unsaturated soil. Followings are the considered formulation list of finite element equation in this study:

1) Formulation of solid deformation uncoupled FEM for saturated soils
2) Formulation of transient state of water seepage uncoupled FEM for saturated soils
3) Formulation of soil – water two – phase seepage – deformation coupled FEM for saturated soils
4) Formulation of soil – water – air three – phase seepage – deformation coupled FEM for unsaturated soils (constant air pressure)

5.2.1 Formulation of solid deformation uncoupled FEM for saturated soils

The formulation of solid deformation uncoupled FEM for saturated soils is represented by the governing load – deflection equation. It is established from 3 mains governing equations as listed below:

1) Principal of static equilibrium for 2 – D in a plane stress state
2) Principal of effective stress when excess pore water pressure $\dot{u}_w = 0$
3) Constitutive model for saturated soil for 2 -D plane strain condition $\dot{\varepsilon_{zz}} = 0$

The principal of static equilibrium in 2-D plane stress condition (x-y plane, $\dot{\sigma_{zz}} = 0$) can be written in the differential equations by:

$$\begin{aligned} &\text{In x-axis:} && \frac{\partial \dot{\sigma}_{xx}}{\partial x} + \frac{\partial \dot{\tau}_{xy}}{\partial y} + \dot{b}_x = 0 \\ &\text{In y-axis:} && \frac{\partial \dot{\sigma}_{yy}}{\partial y} + \frac{\partial \dot{\tau}_{xy}}{\partial x} + \dot{b}_y = 0 \end{aligned} \tag{5-26}$$

where $\dot{\sigma}_{xx}$ and $\dot{\sigma}_{yy}$ are the incremental total stresses along the *x*-axis and *y*-axis, respectively. $\dot{\tau}_{xy}$ is the incremental shear stress on the *x*-*y* plane and $\dot{b}_x$, $\dot{b}_y$ are the incremental body forces (units of force/length^2) along the *x*-axis, *y*-axis, respectively. The Equation (5-26) could be written in the matrix form as:

$$\begin{bmatrix} \frac{\partial}{\partial x} & 0 & \frac{\partial}{\partial y} \\ 0 & \frac{\partial}{\partial y} & \frac{\partial}{\partial x} \end{bmatrix} \begin{Bmatrix} \dot{\sigma}_{xx} \\ \dot{\sigma}_{yy} \\ \dot{\tau}_{xy} \end{Bmatrix} + \begin{Bmatrix} \dot{b_x} \\ \dot{b_y} \end{Bmatrix} = \begin{Bmatrix} 0 \\ 0 \end{Bmatrix} \tag{5-27}$$

or we can write in the compacted form as:

$$[\boldsymbol{\nabla}]^T \{\dot{\boldsymbol{\sigma}}\} + \{\dot{\boldsymbol{b}}\} = \{\mathbf{0}\} \tag{5-28}$$

where $[\boldsymbol{\nabla}]^T$ denotes the transpose matrix of differential operator $[\boldsymbol{\nabla}]$ that can be expressed by:

$$[\boldsymbol{\nabla}]^T = \begin{bmatrix} \frac{\partial}{\partial x} & 0 & \frac{\partial}{\partial y} \\ 0 & \frac{\partial}{\partial y} & \frac{\partial}{\partial x} \end{bmatrix} \text{ and } [\boldsymbol{\nabla}] = \begin{bmatrix} \frac{\partial}{\partial x} & 0 \\ 0 & \frac{\partial}{\partial y} \\ \frac{\partial}{\partial y} & \frac{\partial}{\partial x} \end{bmatrix} \tag{5-29}$$

The increment of total stress vector $\{\dot{\boldsymbol{\sigma}}\}$ which denotes $\{\dot{\sigma}_{xx}, \dot{\sigma}_{yy}, \dot{\tau}_{xy}\}$ are specifically defined for all plane strain analysis in this chapter, the increment of body force $\{\dot{\boldsymbol{b}}\}$ denotes $\{\dot{b_x}, \dot{b_y}\}$ and $\{\mathbf{0}\}$ is the zero vector.

In this study, assuming that there is no change of the body force ($\{\dot{\boldsymbol{b}}\} = \{\mathbf{0}\}$), therefore the Equation (5-28) can be shorten as written by:

$$[\boldsymbol{\nabla}]^T\{\dot{\boldsymbol{\sigma}}\} = \{\mathbf{0}\} \tag{5-30}$$

From Equation (5-30), the weak form is generated using the weighted residuals Galerkin's method with the matrix of weighting function $[\boldsymbol{W_u}]$ for the displacement approximation. Considering a body, the domain Ω^{ele} and boundary of the domain Γ^{ele}, the weak form can be written by:

$$\int_{\Omega^{ele}} [\boldsymbol{W_u}]\,[\boldsymbol{\nabla}]^T\{\dot{\boldsymbol{\sigma}}\} d\boldsymbol{\Omega} = \{\mathbf{0}\} \tag{5-31}$$

Integrating Equation (5-31) by parts using the Green theorem for 2-D problem in the second derivative part results in the weak form as:

$$\int_{\Gamma^{ele}} [\boldsymbol{W_u}](\{\dot{\boldsymbol{\sigma}}\} \cdot \{\hat{\boldsymbol{n}}\}) d\boldsymbol{\Gamma} - \int_{\Omega^{ele}} [\boldsymbol{W_\varepsilon}]\{\dot{\boldsymbol{\sigma}}\} d\boldsymbol{\Omega} = \{\mathbf{0}\} \tag{5-32}$$

where $(\{\dot{\boldsymbol{\sigma}}\} \cdot \{\hat{\boldsymbol{n}}\}) = \begin{bmatrix} \dot{\sigma_{xx}} & \dot{\tau_{xy}} \\ \dot{\tau_{xy}} & \dot{\sigma_{yy}} \end{bmatrix} \cdot \begin{Bmatrix} n_x \\ n_y \end{Bmatrix} = \begin{Bmatrix} \dot{\sigma_{xx}} n_x + \dot{\tau_{xy}} n_y \\ \dot{\tau_{xy}} n_x + \dot{\sigma_{yy}} n_y \end{Bmatrix}$ is the vector of surface traction forces acting on the surface boundary $\boldsymbol{\Gamma}$. Since the direction of unit vector $\{\hat{\boldsymbol{n}}\}$ is always positive (+) orthogonal to the surface, so the compressive stress vector which is in the opposite direction will be implicitly negative (-). Since the compressive force is always defined as the positive value in the world of soil mechanics, the negative sign (-) shall be applied to the stress with resulting in the positive traction force in the compression case as:

$$\{\dot{\boldsymbol{t}}\} = -\{\dot{\boldsymbol{\sigma}}\} \cdot \{\hat{\boldsymbol{n}}\} \tag{5-33}$$

In addition, refer to Equation (5-32), the total stress $\{\dot{\boldsymbol{\sigma}}\}$ is always positive (+) for the compression case in soil mechanics. However, the compression produces the negative sign (-) on the displacement increment which resulting in the negative strain (compatibility) or matrix of weighting function $[\boldsymbol{W_\varepsilon}]$ for the strain approximation is negative. Hence, in order to keep

the positive internal stress-strain in compression case, the negative sign shall multiply to the weighting function for the strain approximation $[\boldsymbol{\nabla W_u}]$ as shown in Equation (5-34).

$$[\boldsymbol{W_\varepsilon}]\{\dot{\boldsymbol{\sigma}}\} = -[\boldsymbol{\nabla W_u}]\{\dot{\boldsymbol{\sigma}}\} \tag{5-34}$$

Substitute Equations (5-33) and (5-34) into Equation (5-32), we will get:

$$-\int_{\Gamma^{ele}} [\boldsymbol{W_u}]\{\dot{\boldsymbol{t}}\} d\boldsymbol{\Gamma} + \int_{\Omega^{ele}} [\boldsymbol{\nabla W_u}]\{\dot{\boldsymbol{\sigma}}\} d\boldsymbol{\Omega} = \{\boldsymbol{0}\} \tag{5-35}$$

The matrix of weighting function $[\boldsymbol{W}]$ is assumed to be equal to the matrix of isoparametric interpolation function $[N]$ using Buffnode's Galerkin. Then, Equation (5-35) can be written by:

$$-\int_{\Gamma^{ele}} [\boldsymbol{N_u}]^{\mathrm{T}}\{\dot{\boldsymbol{t}}\} d\boldsymbol{\Gamma} + \int_{\Omega^{ele}} [\boldsymbol{\nabla N_u}]^{\mathrm{T}}\{\dot{\boldsymbol{\sigma}}\} d\boldsymbol{\Omega} = \{\boldsymbol{0}\} \tag{5-36}$$

where the matrix forms of $[\boldsymbol{N_u}]^{\mathrm{T}}$ and $[\boldsymbol{\nabla N_u}]^{\mathrm{T}}$ are illustrated in Appendix B-2.

The total stress increment $\dot{\boldsymbol{\sigma}}$ in Equation (5-36), using the principal of Terzaghi's effective stress for dried soils or fully drained condition of saturated soils, is equal to the Terzaghi's effective stress increment $\dot{\boldsymbol{\sigma}}'$ as expressed by:

$$\{\dot{\boldsymbol{\sigma}}\} = \{\dot{\boldsymbol{\sigma}}'\} \tag{5-37}$$

Considering the load – displacement problem in FEM for solid mechanics, for the saturated soil, constitutive model plays the important role to relate the increment of internal effective stress in the loading part and the increment of internal total strain in the displacement part by:

$$\dot{\boldsymbol{\sigma}}' = \boldsymbol{D^{ep}} : \dot{\boldsymbol{\varepsilon}} \tag{5-38}$$

where $\dot{\boldsymbol{\sigma}}'$, $\dot{\boldsymbol{\varepsilon}}$, $\boldsymbol{D^{ep}}$ are specifically defined for the Terzaghi's effective stress vector, strain vector and elastoplastic stiffness tensor of the proposed constitutive model for fully saturation case (Chapter 2).

In plane strain condition, the increment of normal strain in *z*-axis is zero or $\dot{\varepsilon}_{zz} = 0$, the reduced form of constitutive equation can be re-written as shown in the matrix form by:

$$\begin{Bmatrix} \dot{\sigma}'_{xx} \\ \dot{\sigma}'_{yy} \\ \dot{\tau}'_{xy} \end{Bmatrix} = \begin{bmatrix} D_{11}^{ep} & D_{12}^{ep} & D_{14}^{ep} \\ D_{21}^{ep} & D_{22}^{ep} & D_{24}^{ep} \\ D_{41}^{ep} & D_{42}^{ep} & D_{44}^{ep} \end{bmatrix} \begin{Bmatrix} \dot{\varepsilon}_{xx} \\ \dot{\varepsilon}_{yy} \\ \dot{\gamma}_{xy} \end{Bmatrix} \tag{5-39}$$

or we can write in the compacted form as:

$$\{\dot{\boldsymbol{\sigma}}'\} = \left[\boldsymbol{D_{ij}^{ep}}\right]\{\dot{\boldsymbol{\varepsilon}}\} = [\boldsymbol{D}]\{\dot{\boldsymbol{\varepsilon}}\} \tag{5-40}$$

where $\{\dot{\boldsymbol{\sigma}}'\}$ and $\{\dot{\boldsymbol{\varepsilon}}\}$ are specifically defined for this chapter for the Terzaghi's effective stress vector and strain vector in *x-y* plane for plane strain condition. The subscription orders *i* and *j* of the elastoplastic stiffness matrix $\left[\boldsymbol{D}_{\boldsymbol{ij}}^{\boldsymbol{ep}}\right]$ refer to the stress part and the strain part, respectively. In addition to Equation (5-39), the subscription indices, including 1, 2 and 4, denote the normal stress (σ_{xx}) or strain (ε_{xx}) in x-axis, the normal stress (σ_{yy}) or strain (ε_{yy}) in y-axis and shear stress (τ_{xy}) or strain (γ_{xy}) on the x-y plane, respectively.

The strain increment vector $\{\dot{\boldsymbol{\varepsilon}}\}$ in Equation (5-40) could be written in term of nodal displacement increment vector $\{\dot{\boldsymbol{U}}\}$ by:

$$\{\dot{\boldsymbol{\varepsilon}}\} = [\boldsymbol{B_u}]\{\dot{\boldsymbol{U}}\} \tag{5-41}$$

where $[\boldsymbol{B_u}]$ denotes the element strain – displacement matrix. See Appendix B-2 for further details of vector and matrix calculation for this equation.

Substituting the combination of Equations (5-40) and (5-41) into Equation (5-36), we will get the element equation for the solid deformation uncoupled FEM for saturated soils as:

$$-\int_{\Gamma^{ele}}[\boldsymbol{N_u}]^{\mathrm{T}}\{\dot{\boldsymbol{t}}\}d\boldsymbol{\Gamma} + \int_{\Omega^{ele}}[\boldsymbol{\nabla N_u}]^{\mathrm{T}}[\boldsymbol{D}][\mathbf{B_u}]d\boldsymbol{\Omega}\{\dot{\boldsymbol{U}}\} = \{\mathbf{0}\} \tag{5-42}$$

As proved in Appendix B-2, we could replace $[\boldsymbol{\nabla N_u}]$ in the Equation (5-42) by $[\boldsymbol{B_u}]$ matrix and rearrange the equation as shown below:

$$\int_{\Omega^{ele}}[\boldsymbol{B_u}]^{\mathrm{T}}[\boldsymbol{D}][\boldsymbol{B_u}]d\boldsymbol{\Omega}\{\dot{\boldsymbol{U}}\} = \int_{\Gamma^{ele}}[\boldsymbol{N_u}]^{\mathrm{T}}\{\dot{\boldsymbol{t}}\}d\boldsymbol{\Gamma} \tag{5-43}$$

From Equation (5-43), the system equation is combined from many elements and it can be written in the compacting matrix form as expressed by:

$$\left[\boldsymbol{K_{ep}^{sat}}\right]\{\dot{\boldsymbol{U}}\} = \{\dot{\boldsymbol{F}}_{\boldsymbol{ext}}\} \tag{5-44}$$

where the summary of integration equation of the coefficient matrices and the nodal load vectors is shown in Table 5-2

Table 5-2 Summary of integration equation for the formulation of solid deformation uncoupled FEM for saturated condition

No.	Coefficient matrices or Nodal load vectors	Integration equation
1	Elastoplastic element stiffness matrix (saturated soil)	$\left[\boldsymbol{K_{ep}^{sat}}\right] = \int_{\Omega}[\mathbf{B_u}]^{\mathrm{T}}[\mathbf{D}][\mathbf{B_u}]d\boldsymbol{\Omega}$
2	Nodal external force vector	$\{\dot{\boldsymbol{F}}_{\boldsymbol{ext}}\} = \int_{\Gamma}[\boldsymbol{N_u}]^{\mathrm{T}}\{\dot{\mathbf{t}}\}d\boldsymbol{\Gamma}$

Remarks: See Appendix B-5 for further details and formulas of the numerical integration.

5.2.2 Formulation of transient state of water seepage uncoupled FEM for saturated soils

The purpose of establishing the formulation of transient state of water seepage uncoupled FEM for saturated soils in this study is to validate the FEM with the Terzaghi's theory of consolidation (one dimensional flow) in the part of pore water pressure distribution with time.

Assuming that water and soil particle are the incompressible materials, therefore the FEM's formulation is generated based on the assumption that the net volume of water flow through the soil ΔV_w is equal to the volume change of soil ΔV as written by:

$$\Delta V_w = \Delta V \tag{5-45}$$

In the transient condition, the volume changes are considered with small increment of time t, Equation (5-45) can be re-written as:

$$\frac{\partial V_w}{\partial t} = \frac{\partial V}{\partial t} \tag{5-46}$$

With regards to the equilibrium Equation (5-46), the FEM formulation is established from 3 mains governing equations as listed below:

1) Darcy's law
2) Continuity of flow
3) Volumetric behavior of soil in 1-D

First, the transient net volume of water flow through the soil is equivalent to the net flow rate q_{net} which can be written as:

$$\frac{\partial V_w}{\partial t} = q_{net} \tag{5-47}$$

$$q_{net} = q_{out} - q_{in} \tag{5-48}$$

where q_{out} and q_{in} are outflow rate and inflow rate, respectively. For 2-D element in the *x-y* plane (Figure 5-7), considering a unit thickness of soil element $dz = 1$ and there is no flow in z-direction ($q_z = 0, \frac{\partial q_z}{\partial z} = 0$), q_{out} and q_{in} can be written as the Equations (5-49) and (5-50), respectively.

$$q_{out} = q_x + \frac{\partial q_x}{\partial x} dx + q_y + \frac{\partial q_y}{\partial y} dy \tag{5-49}$$

$$q_{in} = q_x + q_y \tag{5-50}$$

Substituting Equations (5-48), (5-49) and (5-50) into Equation (5-47), we will get:

$$\frac{\partial V_w}{\partial t} = (q_x + \frac{\partial q_x}{\partial x} dx + q_y + \frac{\partial q_y}{\partial y} dy) - q_x - q_y = \frac{\partial q_x}{\partial x} dx + \frac{\partial q_y}{\partial y} dy \tag{5-51}$$

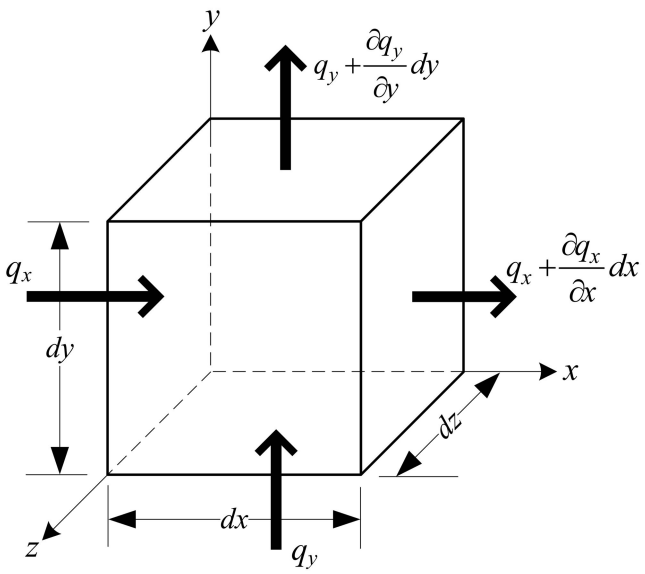

Figure 5-7 Water flow through a soil element

Since the flow rate in the specified direction q_{dir} can be written in term of velocity of water flow in the specified direction v_{dir} and the cross-section area A_c that orthogonal with the direction of flow as:

$$q_{dir} = v_{dir} A_c \tag{5-52}$$

Considering the velocity of water flows in or out in *x*-direction v_x and y-direction v_y, from the Darcy's law which is in the assumption of the saturated soil in a slow range of velocity and there is no change of the body force, v_x and v_y can be written as:

$$v_x = -k_x \frac{\partial h}{\partial x} \ , \qquad v_y = -k_y \frac{\partial h}{\partial y} \tag{5-53}$$

where h is the total head pressure (considering only the pressure head) and k_x, k_y are the saturated coefficients of permeability in *x*-direction and *y*-direction, respectively. Therefore, the flow rate in *x*-direction and *y*-direction can be written by Equations (5-54) and (5-55), respectively.

$$q_x = -k_x \frac{\partial h}{\partial x} A_{y-z} = -k_x \frac{\partial h}{\partial x} dydz \tag{5-54}$$

$$q_y = -k_y \frac{\partial h}{\partial y} A_{x-z} = -k_y \frac{\partial h}{\partial y} dxdz \tag{5-55}$$

Substituting Equations (5-54) and (5-55) into Equation (5-51), we will get the form of Laplace's equation for 2-D steady state flow as:

$$\frac{\partial V_w}{\partial t} = -k_x \frac{\partial^2 h}{\partial x^2} dydzdx - k_y \frac{\partial^2 h}{\partial y^2} dxdzdy \tag{5-56}$$

Second, in the side of the volume change of soil ΔV, the coefficient of volume compressibility m_v ,which is the ratio of volumetric strain of soil and increment of vertical effective stress ($\Delta\sigma_y'$), is used. It is also the reciprocal of the constrained modulus (M_{con}) or the modulus of the oedometer compression as shown below:

$$m_v = \frac{\frac{\Delta V}{V}}{\Delta\sigma_y'} = \frac{1}{M_{con}} \tag{5-57}$$

where V is the total volume of soil. Therefore, the volume change of soil (ΔV) in the oedometer compression test which is equivalent to the Terzaghi's theory of consolidation can be calculated by:

$$\Delta V = m_v \Delta\sigma_y' V \tag{5-58}$$

In the transient condition, the volume change of soil is considered with small increment of time t, Equation (5-58) can be re-written as:

$$\frac{\partial V}{\partial t} = m_v \frac{\partial \sigma_y'}{\partial t} dxdzdy \tag{5-59}$$

For the consolidation in the saturated soil, the increment of total vertical stress is zero, the increment of effective stress with time can be written by:

$$\frac{\partial \sigma_y'}{\partial t} = -\frac{\partial u_w}{\partial t} \tag{5-60}$$

where u_w is pore water pressure. Substituting Equation (5-60) into Equation (5-59), we get:

$$\frac{\partial V}{\partial t} = -m_v \frac{\partial u_w}{\partial t} dxdzdy \tag{5-61}$$

Finally, substituting Equations (5-56) and (5-61) into the equilibrium equation (Equation (5-46)), the differential equation for the formulation of transient state of water seepage uncoupled FEM for saturated soils can be written as:

$$-k_x \frac{\partial^2 h}{\partial x^2} dydzdx - k_y \frac{\partial^2 h}{\partial y^2} dxdzdy = -m_v \frac{\partial u_w}{\partial t} dxdzdy \tag{5-62}$$

Then, we will get:

$$-k_x \frac{\partial^2 h}{\partial x^2} - k_y \frac{\partial^2 h}{\partial y^2} = -m_v \frac{\partial u_w}{\partial t} \tag{5-63}$$

Substituting the pressure head h in Equation (5-63) by the following equation:

$$h = u_w / \gamma_w \tag{5-64}$$

Equation (5-63) can be re-written in term of pore water pressure u_w as:

$$-\frac{k_x}{m_v \gamma_w} \frac{\partial^2 u_w}{\partial x^2} - \frac{k_y}{m_v \gamma_w} \frac{\partial^2 u_w}{\partial y^2} = -\frac{\partial u_w}{\partial t} \tag{5-65}$$

As the characteristics of the oedometer compression test, that water cannot flow in and flow out in the x-direction (lateral is constrained by the steel proving ring), the flow rate q_x at the boundary is zero ($\frac{\partial^2 h}{\partial x^2} = 0$). Therefore, Equation (5-63) satisfies the formula of coefficient of volume compressibility for 1-D consolidation. However, for simplicity and uniqueness of coding in the coupled pressure – deformation FEM, 2-D flow is described herein.

The compacted form of Equation (5-65) is written and rearranged by:

$$-\{\boldsymbol{\nabla}\}^{\mathrm{T}}[\boldsymbol{K_w}]\{\boldsymbol{\nabla}u_w\} + \frac{\partial u_w}{\partial t} = 0 \tag{5-66}$$

where the conductivity matrix $[\boldsymbol{K_w}]$ denotes $\frac{\begin{bmatrix} k_x & 0 \\ 0 & k_y \end{bmatrix}}{m_v \gamma_w}$, γ_w is unit weight of water and $\{\boldsymbol{\nabla}\}^{\mathrm{T}}$ denotes the transpose matrix of differential operator $\{\boldsymbol{\nabla}\}$ as shown below:

$$\{\boldsymbol{\nabla}\}^{\mathrm{T}} = \begin{bmatrix} \frac{\partial}{\partial x} & \frac{\partial}{\partial y} \end{bmatrix}, \{\boldsymbol{\nabla}\} = \begin{Bmatrix} \frac{\partial}{\partial x} \\ \frac{\partial}{\partial y} \end{Bmatrix} \tag{5-67}$$

From Equation (5-66), the weak form is generated using the weighted residuals Galerkin's method with the matrix of weighting function $\left[\boldsymbol{W_{u_w}}\right]$ for pore water pressure approximation. Considering a body, the domain Ω^{ele} and boundary of the domain Γ^{ele}, the weak form can be written by:

$$-\int_{\Omega^{ele}} \left[\boldsymbol{W_{u_w}}\right]\{\boldsymbol{\nabla}\}^{\mathrm{T}}[\boldsymbol{K_w}]\,\{\boldsymbol{\nabla}u_w\}d\boldsymbol{\Omega} + \int_{\Omega^{ele}} \left[\boldsymbol{W_{u_w}}\right]\dot{u_w}d\boldsymbol{\Omega} = \{\mathbf{0}\} \tag{5-68}$$

Integrating Equation (5-68) by parts using the Green theorem for 2-D problem in the second derivative part results in the weak form as:

$$\begin{aligned} &\int_{\Omega^{ele}} \left[\boldsymbol{W_{u_w}}\right]\{\boldsymbol{\nabla}\}^{\mathrm{T}}[\boldsymbol{K_w}]\{\boldsymbol{\nabla}u_w\}d\boldsymbol{\Omega} + \int_{\Omega^{ele}} \left[\boldsymbol{W_{u_w}}\right]\dot{u_w}d\boldsymbol{\Omega} \\ &\qquad = \int_{\Gamma^{ele}} \left[\boldsymbol{W_{u_w}}\right]\{\boldsymbol{\nabla}\}^{\mathrm{T}}[\boldsymbol{K_w}](u_w \cdot \{\hat{\boldsymbol{n}}\})d\boldsymbol{\Gamma} \end{aligned} \tag{5-69}$$

The matrix of weighting function $[\boldsymbol{W}]$ is assumed to be equal to the matrix of isoparametric interpolation function $[\boldsymbol{N}]$ using Buffnode's Galerkin. Then, Equation (5-69) can be written by:

$$\begin{aligned} &\int_{\Omega^{ele}} \left[\boldsymbol{N_{u_w}}\right]^{\mathrm{T}}\{\boldsymbol{\nabla}\}^{\mathrm{T}}[\mathbf{K_w}]\{\boldsymbol{\nabla}u_w\}d\boldsymbol{\Omega} + \int_{\Omega^{ele}} \left[\boldsymbol{N_{u_w}}\right]^{\mathrm{T}}\dot{u_w}d\boldsymbol{\Omega} \\ &\qquad = \int_{\Gamma^{ele}} \left[\boldsymbol{N_{u_w}}\right]^{\mathrm{T}}\{\boldsymbol{\nabla}\}^{\mathrm{T}}[\boldsymbol{K_w}](u_w \cdot \{\hat{\boldsymbol{n}}\})d\boldsymbol{\Gamma} \end{aligned} \tag{5-70}$$

where the matrix forms of $\left[\boldsymbol{N_{u_w}}\right]^{\mathrm{T}}$ are illustrated in Appendix B-2.

The approximation of the pore water pressure u_w and the transient pore water pressure with time $\dot{u_w}$ can be written as Equations (5-71) and (5-72), respectively, as proved in Appendix B-2.

$$u_w = [\boldsymbol{N_{u_w}}]\{\boldsymbol{U_w}\} \tag{5-71}$$

$$\dot{u_w} = [\boldsymbol{N_{u_w}}]\{\dot{\boldsymbol{U_w}}\} \tag{5-72}$$

where $[\boldsymbol{N_{u_w}}]$ is the matrix of isoparametric interpolation function $[\boldsymbol{N}]$, $\{\boldsymbol{U_w}\}$ is the nodal pore water pressure vector and $\{\dot{\boldsymbol{U_w}}\}$ is the nodal transient pore water pressure with time vector. See Appendix B-2 for further details of vector and matrix calculation for these equations.

Substituting Equations (5-71) and (5-72) into Equation (5-70), we will get the element equation for the transient state of water seepage uncoupled FEM for saturated soils as:

$$\begin{aligned}\int_{\Omega^{ele}} [\boldsymbol{\nabla N_{u_w}}]^{\mathrm{T}} [\boldsymbol{K_w}] [\boldsymbol{\nabla N_{u_w}}] d\boldsymbol{\Omega}\{\boldsymbol{U_w}\} + \int_{\Omega^{ele}} [\boldsymbol{N_{u_w}}]^{\mathrm{T}} [\boldsymbol{N_{u_w}}] d\boldsymbol{\Omega}\{\dot{\boldsymbol{U_w}}\} \\ = \int_{\Gamma^{ele}} [\boldsymbol{N_{u_w}}]^{\mathrm{T}} \{\boldsymbol{\nabla}\}^{\mathrm{T}} [\boldsymbol{K_w}] (u_w \cdot \{\hat{\boldsymbol{n}}\}) d\boldsymbol{\Gamma}\end{aligned} \tag{5-73}$$

As proved in Appendix B-2, we could replace $[\boldsymbol{\nabla N_{u_w}}]$ in the Equation (5-73) by $[\boldsymbol{B_{u_w}}]$ as:

$$\begin{aligned}\int_{\Omega^{ele}} [\boldsymbol{B_{u_w}}]^{\mathrm{T}} [\boldsymbol{K_w}] [\boldsymbol{B_{u_w}}] d\boldsymbol{\Omega}\{\boldsymbol{U_w}\} + \int_{\Omega^{ele}} [\boldsymbol{N_{u_w}}]^{\mathrm{T}} [\boldsymbol{N_{u_w}}] d\boldsymbol{\Omega}\{\dot{\boldsymbol{U_w}}\} \\ = \int_{\Gamma^{ele}} [\boldsymbol{N_{u_w}}]^{\mathrm{T}} \{\boldsymbol{\nabla}\}^{\mathrm{T}} [\boldsymbol{K_w}] (u_w \cdot \{\hat{\boldsymbol{n}}\}) d\boldsymbol{\Gamma}\end{aligned} \tag{5-74}$$

From Equation (5-74), the system equation is combined from many elements and it can be written in the compacting matrix form as expressed by:

$$[\boldsymbol{K_h}]\{\boldsymbol{U_w}\} + [\boldsymbol{M_m}]\{\dot{\boldsymbol{U_w}}\} = \{\boldsymbol{Q}\} \tag{5-75}$$

For solving the nonlinear first order differential equation, discretizing Equation (5-75) with time (see Appendix B-6), we will get:

$$(\theta h_t [\boldsymbol{K_h}] + [\boldsymbol{M_m}])\{\boldsymbol{U_{w|t+h_t}}\} = h_t\{\boldsymbol{Q}\} + ([\boldsymbol{M_m}] - (1-\theta) h_t [\boldsymbol{K_h}])\{\boldsymbol{U_{w|t}}\} \tag{5-76}$$

where the summary of integration equation of the coefficient matrices and the nodal load vectors is shown in Table 5-3

Table 5-3 Summary of integration equation for the formulation of transient state of water seepage uncoupled FEM for saturated condition

No.	Coefficient matrices or Nodal load vectors	Integration equation
1	Suction independent permeability element matrix	$[\boldsymbol{K_h}] = \int_{\Omega} \left[\boldsymbol{B_{u_w}}\right]^{\mathrm{T}} [\boldsymbol{K_w}] \left[\boldsymbol{B_{u_w}}\right] d\boldsymbol{\Omega}$
2	Mass matrix	$[\boldsymbol{M_m}] = \int_{\Omega} \left[\boldsymbol{N_{u_w}}\right]^{\mathrm{T}} \left[\boldsymbol{N_{u_w}}\right] d\boldsymbol{\Omega}$
3	Nodal inflows/outflows vector	$\{\boldsymbol{Q}\} = \int_{\Gamma} \left[\boldsymbol{N_{u_w}}\right]^{\mathrm{T}} \{\boldsymbol{\nabla}\}^{\mathrm{T}} [\mathbf{K_w}] (u_w \cdot \{\hat{\mathbf{n}}\}) d\boldsymbol{\Gamma}$

Remarks: See Appendix B-5 for further details and formulas of the numerical integration.

5.2.3 Formulation of soil – water two – phase seepage – deformation coupled FEM for saturated soils

The mixed FEM formulation which incorporates displacement and pore water pressure freedoms is used to generate the formulation of soil-water two-phase seepage-deformation coupled FEM for saturated soil. The coupled element equation of the seepage – deformation analysis combines 2 parts of the governing equation as follows;

- The combination of the principal of static equilibrium in 2 – D and principal of effective stress for saturated soils
- The combination of the volume change of soil relating with the inflows/outflows of water through the soil elements

The detail of each part is further explained in this section.

5.2.3.1 The combination of the principal of static equilibrium in 2-D and principal of effective stress for saturated soils

In this part, the element equation is established from the combinations of 3 main governing equations which are shown in the following list:

1) Principal of static equilibrium for 2 – D plane stress condition
2) Principal of effective stress for saturated condition
3) Constitutive model for saturated soil for 2 -D plane strain condition $\dot{\varepsilon_{zz}} = 0$

The governing load – deflection equation for the solid deformation uncoupled FEM for saturated soil (Section 5.2.1) is the basic element for proving the element equation in this section. The element equation could be continuously proved by replacing the total stress with the effective stress and pore water pressure based on the principle of Terzaghi's effective stress.

Starting from the weak form Equation (5-36) of governing load – deflection equation for the solid deformation uncoupled FEM for saturated soil (Section 5.2.1), it is rewritten in this section in term of total stress vector $\{\dot{\boldsymbol{\sigma}}\}$ as:

$$-\int_{\Gamma^{ele}}[\boldsymbol{N_u}]^{\mathrm{T}}\{\dot{\boldsymbol{t}}\}d\boldsymbol{\Gamma}+\int_{\Omega^{ele}}[\boldsymbol{\nabla N_u}]^{\mathrm{T}}\{\dot{\boldsymbol{\sigma}}\}d\boldsymbol{\Omega}=\{\boldsymbol{0}\} \tag{5-77}$$

where the matrix forms of $[\boldsymbol{N_u}]^{\mathrm{T}}$ and $[\boldsymbol{\nabla N_u}]^{\mathrm{T}}$are illustrated in Appendix B-2.

In order to couple the excess pore water pressure with the deformation analysis, the total stress vector $\{\dot{\boldsymbol{\sigma}}\}$ in Equation (5-77) will be substituted by Equation (5-78) which is the principal of effective stress for saturated soil or the Terzaghi's effective stress.

$$\{\dot{\boldsymbol{\sigma}}\}=\{\dot{\boldsymbol{\sigma}}'\}+\{\boldsymbol{m}\}\dot{u}_w \tag{5-78}$$

where $\{\boldsymbol{m}\}$ which denotes $\{1,1,0\}$ is multiplied to the excess pore water pressure for plane strain condition since the shearing stress is not affected by excess pore water pressure. Then, we get:

$$-\int_{\Gamma^{ele}}[\boldsymbol{N_u}]^{\mathrm{T}}\{\dot{\boldsymbol{t}}\}d\boldsymbol{\Gamma}+\int_{\Omega^{ele}}[\boldsymbol{\nabla N_u}]^{\mathrm{T}}\{\dot{\boldsymbol{\sigma}}'\}d\boldsymbol{\Omega}+\int_{\Omega^{ele}}[\boldsymbol{\nabla N_u}]^{\mathrm{T}}\{\boldsymbol{m}\}\dot{u}_w d\boldsymbol{\Omega}=\{\boldsymbol{0}\} \tag{5-79}$$

Substituting $\dot{\boldsymbol{\sigma}}'$ by the combination of Equation (5-40) and Equation (5-41) of Section 5.2.1) and discretization of $\dot{u}_w$ Equation (5-72) of Section 5.2.2 into Equation (5-79), we get:

$$\begin{aligned}&-\int_{\Gamma^{ele}}[\boldsymbol{N_u}]^{\mathrm{T}}\{\dot{\boldsymbol{t}}\}d\boldsymbol{\Gamma}+\int_{\Omega^{ele}}[\boldsymbol{\nabla N_u}]^{\mathrm{T}}[\boldsymbol{D}][\boldsymbol{B_u}]d\boldsymbol{\Omega}\{\dot{\boldsymbol{U}}\}\\&+\int_{\Omega^{ele}}[\boldsymbol{\nabla N_u}]^{\mathrm{T}}\boldsymbol{m}[\boldsymbol{N_{u_w}}]d\boldsymbol{\Omega}\{\dot{\boldsymbol{U_w}}\}=\{\boldsymbol{0}\}\end{aligned} \tag{5-80}$$

where $[\boldsymbol{D}]$ is the reduced form of elastoplastic stiffness tensor as stated in Section 5.2.1. The matrix forms of $[\boldsymbol{N_u}]^{\mathrm{T}}$and $[\boldsymbol{\nabla N_u}]^{\mathrm{T}}$are illustrated in Appendix B-2.1 for deformation part and $[\boldsymbol{N_{u_w}}]$ are illustrated in Appendix B-2.2 for pressure part. $\{\dot{\boldsymbol{U}}\}$ is the nodal derivative displacement with time vector and $\{\dot{\boldsymbol{U_w}}\}$ is the nodal transient pore water pressure with time vector.

As proved in Appendix B-2, we could replace $[\boldsymbol{\nabla N_u}]$ and $[\boldsymbol{\nabla N_{u_w}}]$ into the Equation (5-80) by $[\boldsymbol{B_u}]$ and $[\boldsymbol{B_{u_w}}]$, respectively. We will get the first part of element equation which is the combination of the principal of static equilibrium in 2 – D and principal of effective stress for saturated soils as follows:

$$\int_{\Omega^{ele}}[\boldsymbol{B_u}]^{\mathrm{T}}[\boldsymbol{D}][\boldsymbol{B_u}]d\boldsymbol{\Omega}\{\dot{\boldsymbol{U}}\}+\int_{\Omega^{ele}}[\boldsymbol{B_u}]^{\mathrm{T}}\{\boldsymbol{m}\}[\boldsymbol{N_{u_w}}]d\boldsymbol{\Omega}\{\dot{\boldsymbol{U_w}}\}=\int_{\Gamma^{ele}}[\boldsymbol{N_u}]^{\mathrm{T}}\{\dot{\boldsymbol{t}}\}d\boldsymbol{\Gamma} \tag{5-81}$$

From Equation (5-81), the system equation is combined from many elements and it can be written in the compacting matrix form as expressed by:

$$[\boldsymbol{K_{ep}^{sat}}]\{\dot{\boldsymbol{U}}\}+[\boldsymbol{I}]\{\dot{\boldsymbol{U_w}}\}=\{\dot{\boldsymbol{F}}_{\boldsymbol{ext}}\} \tag{5-82}$$

where the summary of integration equation of the coefficient matrices and the nodal load vectors is shown in Table 5-4.

5.2.3.2 The combination of the volume change of soil relating with the inflows/outflows of water through the soil elements

In this part, the element equation is established from the combinations of 3 main governing equations which are shown in the following list:

1) Darcy's law
2) Continuity of flow
3) Volumetric behavior of soil

The equilibrium of net volume of water flow through the soil (ΔV_w) and the volume change of soil (ΔV) (Section 5.2.2) is the basic element for proving the element equation in this section. However, in the part of ΔV, the element equation could be continuously proved by replacing m_v with the increment of volumetric strain $\dot{\varepsilon}_v$. Doing this, the flow of water could be directly related to both the transient pore water pressure and the nodal derivative displacement with time $\{\dot{\boldsymbol{U}}\}$. In the transient condition, the volume change of soil in plane strain is considered with small increment of time t. It can be written as:

$$\frac{\partial V}{\partial t}=\dot{\varepsilon}_{xx}dxdydz+\dot{\varepsilon}_{yy}dydxdz \tag{5-83}$$

where the rate of volume change is always positive value in case of compression or outflows water. Equation (5-83) can be written in the matrix form of the derivative strain with time vector (as expressed in Equation (5-39)) as:

$$\frac{\partial V}{\partial t}=\lfloor 1 \quad 1 \quad 0\rfloor\begin{Bmatrix}\dot{\varepsilon_{xx}}\\ \dot{\varepsilon_{yy}}\\ \dot{\gamma_{xy}}\end{Bmatrix}dxdy=\{\boldsymbol{m}\}^{\mathrm{T}}\{\dot{\boldsymbol{\varepsilon}}_{\boldsymbol{x-y}}\}dxdydz \tag{5-84}$$

where $\{\boldsymbol{m}\}$ which denotes $\{1,1,0\}$ is multiplied with the strain vector $\{\dot{\boldsymbol{\varepsilon}}_{\boldsymbol{x-y}}\}$ to eliminate the deviatoric strain part for determining the volume change of soil for plane strain condition.

Substitute Equations (5-84) for the volume change of soil and Equation (5-56) for the net flow rate as stated in Section 5.2.2 into the same equilibrium equation as expressed by Equation (5-46), the differential equation for the formulation of coupled pressure-deformation by the considering the volumetric change of soil relating with the inflows/outflows of water can be written as:

$$-k_x \frac{\partial^2 h}{\partial x^2} dydzdx - k_y \frac{\partial^2 h}{\partial y^2} dxdzdy = \{\boldsymbol{m}\}^{\mathrm{T}} \{\dot{\boldsymbol{\varepsilon}}_{x-y}\} dxdydz \tag{5-85}$$

Finally, we will get:

$$-k_x \frac{\partial^2 h}{\partial x^2} - k_y \frac{\partial^2 h}{\partial y^2} = \{\boldsymbol{m}\}^{\mathrm{T}} \{\dot{\boldsymbol{\varepsilon}}_{x-y}\} \tag{5-86}$$

Then using the definition of pressure head h as stated in Equation (5-64), the Equation (5-86) can be rewritten in term of pore water pressure by:

$$-\frac{k_x}{\gamma_w} \frac{\partial^2 u_w}{\partial x^2} - \frac{k_y}{\gamma_w} \frac{\partial^2 u_w}{\partial y^2} = \{\boldsymbol{m}\}^{\mathrm{T}} \{\dot{\boldsymbol{\varepsilon}}_{x-y}\} \tag{5-87}$$

The compacted form of Equation (5-87) is written and rearranged by:

$$-\{\boldsymbol{\nabla}\}^{\mathrm{T}} [\mathbf{K_w}] \{\boldsymbol{\nabla} \mathrm{u_w}\} - \{\mathbf{m}\}^{\mathrm{T}} \{\dot{\boldsymbol{\varepsilon}}_{\mathrm{x-y}}\} = 0 \tag{5-88}$$

where the conductivity matrix $[\boldsymbol{K_w}]$ denotes $\frac{\begin{bmatrix} k_x & 0 \\ 0 & k_y \end{bmatrix}}{\gamma_w}$ and $\{\boldsymbol{\nabla}\}^{\mathrm{T}}$ denotes the transpose matrix of differential operator $\{\boldsymbol{\nabla}\}$ as shown in Equation (5-67).

From Equation (5-88), the weak form is generated using the weighted residuals Galerkin's method with the matrix of weighting function $\left[\boldsymbol{W_{u_w}}\right]$ for the pore water pressure approximation. Considering a body, the domain Ω^{ele} and boundary of the domain Γ^{ele}, the weak form can be written by:

$$-\int_{\Omega^{ele}} \left[\boldsymbol{W_{u_w}}\right] \{\boldsymbol{\nabla}\}^{\mathrm{T}} [\boldsymbol{K_w}] \{\boldsymbol{\nabla} u_w\} d\boldsymbol{\Omega} - \int_{\Omega^{ele}} \left[\boldsymbol{W_{u_w}}\right] \{\boldsymbol{m}\}^{\mathrm{T}} \{\dot{\boldsymbol{\varepsilon}}_{x-y}\} d\boldsymbol{\Omega} = \{\mathbf{0}\} \tag{5-89}$$

Integrating Equation (5-89) by parts using the Green theorem for the 2-D problem in the second derivative part results in the weak form as:

$$\begin{aligned} &\int_{\Omega^{ele}} \left[\boldsymbol{W_{u_w}}\right] \{\boldsymbol{\nabla}\}^{\mathrm{T}} [\boldsymbol{K_w}] \{\boldsymbol{\nabla} u_w\} d\boldsymbol{\Omega} - \int_{\Omega^{ele}} \left[\boldsymbol{W_{u_w}}\right] \{\boldsymbol{m}\}^{\mathrm{T}} \{\dot{\boldsymbol{\varepsilon}}_{x-y}\} d\boldsymbol{\Omega} \\ &= \int_{\Gamma^{ele}} \left[\boldsymbol{W_{u_w}}\right] \{\boldsymbol{\nabla}\}^{\mathrm{T}} [\boldsymbol{K_w}] (u_w \cdot \{\hat{\boldsymbol{n}}\}) d\boldsymbol{\Gamma} \end{aligned} \tag{5-90}$$

The matrix of weighting function $[\boldsymbol{W}]$ is assumed to be equal to the matrix of isoparametric interpolation function $[\boldsymbol{N}]$ using the Buffnode's Galerkin. Then, Equation (5-90) is written by:

$$\int_{\Omega^{ele}}\left[\boldsymbol{N_{u_w}}\right]^{\mathrm{T}}\{\boldsymbol{\nabla}\}^{\mathrm{T}}[\boldsymbol{K_w}]\{\boldsymbol{\nabla}u_w\}d\boldsymbol{\Omega}-\int_{\Omega^{ele}}\left[\boldsymbol{N_{u_w}}\right]^{\mathrm{T}}\{\boldsymbol{m}\}^{\mathrm{T}}\left\{\dot{\boldsymbol{\varepsilon}}_{x-y}\right\}d\boldsymbol{\Omega}$$
$$=\int_{\Gamma^{ele}}\left[\boldsymbol{N_{u_w}}\right]^{\mathrm{T}}\{\boldsymbol{\nabla}\}^{\mathrm{T}}[\boldsymbol{K_w}](u_w\cdot\{\hat{\boldsymbol{n}}\})d\boldsymbol{\Gamma} \tag{5-91}$$

where the matrix forms of $\left[\boldsymbol{N_{u_w}}\right]^{\mathrm{T}}$ are illustrated in Appendix B-2.

Substituting Equation (5-41) which is the strain-displacement equation (Section 5.2.1) and discretization of u_w Equation (5-71) (Section5.2.2) into Equation (5-91), we will get:

$$\int_{\Omega^{ele}}\left[\boldsymbol{\nabla N_{u_w}}\right]^{\mathrm{T}}[\boldsymbol{K_w}]\left[\boldsymbol{\nabla N_{u_w}}\right]d\boldsymbol{\Omega}\{\boldsymbol{U_w}\}-\int_{\Omega^{ele}}\left[\boldsymbol{N_{u_w}}\right]^{\mathrm{T}}\{\boldsymbol{m}\}^{\mathrm{T}}[\boldsymbol{B_u}]d\boldsymbol{\Omega}\{\dot{\boldsymbol{U}}\}$$
$$=\int_{\Gamma^{ele}}\left[\boldsymbol{N_{u_w}}\right]^{\mathrm{T}}\{\boldsymbol{\nabla}\}^{\mathrm{T}}[\boldsymbol{K_w}](u_w\cdot\{\hat{\boldsymbol{n}}\})d\boldsymbol{\Gamma} \tag{5-92}$$

where the matrix forms of $\left[\boldsymbol{N_{u_w}}\right]^{\mathrm{T}}$ and $\left[\boldsymbol{\nabla N_{u_w}}\right]^{\mathrm{T}}$ are illustrated in Appendix B-2.2 for pressure part and $[\boldsymbol{B_u}]$ are illustrated in Appendix B-2.1 for deformation part. $\{\boldsymbol{U_w}\}$ is the nodal pore water pressure vector and $\{\dot{\boldsymbol{U}}\}$ is the nodal derivative displacement with time vector.

As proved in Appendix B-2, we could replace $\left[\boldsymbol{\nabla N_{u_w}}\right]$ into the Equation (5-92) by $\left[\boldsymbol{B_{u_w}}\right]$, we will get the second part of element equation which is the combination of the volume change of soil relating with the inflows/outflows of water through the soil elements as follows:

$$\int_{\Omega^{ele}}\left[\boldsymbol{N_{u_w}}\right]^{\mathrm{T}}\{\boldsymbol{m}\}^{\mathrm{T}}[\boldsymbol{B_u}]d\boldsymbol{\Omega}\{\dot{\boldsymbol{U}}\}-\int_{\Omega^{ele}}\left[\boldsymbol{B_{u_w}}\right]^{\mathrm{T}}[\boldsymbol{K_w}]\left[\boldsymbol{B_{u_w}}\right]d\boldsymbol{\Omega}\{\boldsymbol{U_w}\}$$
$$=-\int_{\Gamma^{ele}}\left[\boldsymbol{N_{u_w}}\right]^{\mathrm{T}}\{\boldsymbol{\nabla}\}^{\mathrm{T}}[\boldsymbol{K_w}](u_w\cdot\{\hat{\boldsymbol{n}}\})d\boldsymbol{\Gamma} \tag{5-93}$$

From Equation (5-93), the system equation is combined from many elements and it can be written in the compacting matrix form as expressed by:

$$[\boldsymbol{I}^{\mathrm{T}}]\{\dot{\boldsymbol{U}}\}-[\boldsymbol{K_h}]\{\boldsymbol{U_w}\}=\{\boldsymbol{Q}\} \tag{5-94}$$

where the summary of integration equation of the coefficient matrices and the nodal load vectors is shown in Table 5-4.

Combining the element Equation (5-82) for the static equilibrium and Equation (5-94) for the continuity of flow, we could generate the formulation of soil – water two – phase seepage – deformation coupled FEM for saturated soil as shown below:

$$\begin{bmatrix}\boldsymbol{K_{ep}^{sat}} & \boldsymbol{I}\\ \boldsymbol{I}^{\mathrm{T}} & \boldsymbol{0}\end{bmatrix}\begin{Bmatrix}\dot{\boldsymbol{U}}\\ \dot{\boldsymbol{U}}_{\boldsymbol{w}}\end{Bmatrix}+\begin{bmatrix}\boldsymbol{0} & \boldsymbol{0}\\ \boldsymbol{0} & \boldsymbol{K_h}\end{bmatrix}\begin{Bmatrix}\boldsymbol{U}\\ \boldsymbol{U_w}\end{Bmatrix}=\begin{Bmatrix}\dot{\boldsymbol{F}}_{\boldsymbol{ext}}\\ \boldsymbol{Q}\end{Bmatrix} \tag{5-95}$$

For solving the nonlinear first order differential equation, discretizing Equation (5-95) with time (see Appendix B-6), we will get:

$$\begin{bmatrix} \boldsymbol{K_{ep}^{sat}} & \boldsymbol{I} \\ \boldsymbol{I}^{\mathrm{T}} & -\theta \boldsymbol{K_h} h_t \end{bmatrix} \begin{Bmatrix} \boldsymbol{\Delta U} \\ \boldsymbol{U_{w|t+h_t}} \end{Bmatrix} = \begin{Bmatrix} \boldsymbol{\Delta F_{ext}} + \boldsymbol{I U_{w|t}} \\ h_t \boldsymbol{Q} + (1-\theta) h_t \boldsymbol{K_h U_{w|t}} \end{Bmatrix} \tag{5-96}$$

where the summary of integration equation of the coefficient matrices and the nodal load vectors is shown in Table 5-4.

Table 5-4 Summary of integration equation for formulation of soil – water two – phase seepage – deformation coupled FEM for saturated condition

No.	Coefficient matrices or Nodal load vectors	Integration equation
1	Elastoplasticity element stiffness matrix (saturated soil)	$\left[\boldsymbol{K_{ep}^{sat}}\right] = \int_{\Omega} [\boldsymbol{B_u}]^{\mathrm{T}} [\boldsymbol{D}] [\boldsymbol{B_u}] d\boldsymbol{\Omega}$
2	Suction-independent permeability element matrix	$[\boldsymbol{K_h}] = \int_{\Omega} \left[\boldsymbol{B_{u_w}}\right]^{\mathrm{T}} [\boldsymbol{K_w}] \left[\boldsymbol{B_{u_w}}\right] d\boldsymbol{\Omega}$
3	Rectangular coupling pressure deformation element matrix (stress part)	$[\boldsymbol{I}] = \int_{\Omega} [\boldsymbol{B_u}]^{\mathrm{T}} \{\boldsymbol{m}\} \left[\boldsymbol{N_{u_w}}\right] d\boldsymbol{\Omega}$
4	Rectangular coupling pressure deformation element matrix (strain part)	$[\boldsymbol{I^T}] = \int_{\Omega} \left[\boldsymbol{N_{u_w}}\right]^{\mathrm{T}} \{\boldsymbol{m}\}^{\mathrm{T}} [\boldsymbol{B_u}] d\boldsymbol{\Omega}$
5	Nodal external force vector	$\{\dot{\boldsymbol{F}}_{\boldsymbol{ext}}\} = \int_{\Gamma} [\boldsymbol{N_u}]^{T} \{\dot{\boldsymbol{t}}\} d\boldsymbol{\Gamma}$
6	Nodal inflows/outflows vector	$\{\boldsymbol{Q}\} = -\int_{\Gamma} \left[\boldsymbol{N_{u_w}}\right]^{T} \{\boldsymbol{\nabla}\}^{\mathrm{T}} [\boldsymbol{K_w}] (u_w \cdot \{\hat{\boldsymbol{n}}\}) d\boldsymbol{\Gamma}$

Remarks: See Appendix B-5 for further details and formulas of the numerical integration.

5.2.4 Formulation of soil – water – air three – phase seepage – deformation coupled FEM for unsaturated soils (constant air pressure)

The mixed FEM formulation which incorporates displacement, pore water pressure and pore air pressure freedoms is used to generate the formulation of soil-water-air three-phase seepage-deformation coupled FEM for unsaturated soil. In this study, the air pressure is constant which is applicable in many practical situations including the soil compaction and fully drained shearing under low loading rate. The coupled element equation of the seepage – deformation analysis capturing the unsaturated soil behavior combines 2 groups of the governing equation as follows;

- The combination of the principal of static equilibrium in 2 – D and principal of effective stress for unsaturated soils
- Mass conservation for pore water

The detail of each part is further explained in this section.

5.2.4.1 The combination of the principal of static equilibrium in 2 – D and principal of effective stress for unsaturated soils

In this part, the element equation is established from the combinations of 4 main governing equations which are shown in the following list:

1) Principal of static equilibrium for 2 – D in a plane stress state
2) Principal of Bishop's effective stress for unsaturated condition
3) Constitutive model for unsaturated soil for 2 – D plane strain condition, $\dot{\varepsilon_{zz}} = 0$
4) Soil water characteristic curve, SWCC

The governing load – deflection equation for the solid deformation uncoupled FEM for saturated soil (Section 5.2.1) is the basic element for proving the element equation in this section. The element equation could be continuously proved by rewriting the total stress using the principle of Bishop's effective stress for unsaturated soil (Equation (A-1)) in order to couple the water and air phases with the deformation analysis. According to the main purposes of this study, the interpretation of the compaction behavior, the coupled FEM formulation is simplified by assuming the zero excess pore air pressure or $\dot{u}_a = 0$. With this assumption, this formulation is only applicable under the limit of the drainage condition which is the air must be completely drained out including the soil compaction and fully drained shearing. The Equation (A-1) can be written with the specified assumption in 2-D plane strain condition by:

$$\{\dot{\boldsymbol{\sigma}}\} = \{\dot{\boldsymbol{\sigma}}''\} + \{\boldsymbol{m}\}S_r\dot{u_w} - \{\boldsymbol{m}\}(u_a - u_w)\dot{S}_r \tag{5-97}$$

where $\{\dot{\boldsymbol{\sigma}}''\}$ are specifically defined for this chapter for the Bishop's effective stress vector in x-y plane for plane strain condition and $\{\boldsymbol{m}\}$ which denotes $\{1, 1, 0\}$ is multiplied to the excess pore pressure since the shearing stress is not affected by excess pore pressure.

Starting from the weak form (Equation (5-36)) of governing load – deflection equation for the solid deformation uncoupled FEM for saturated soil (Section 5.2.1), it is rewritten in this section in term of total stress vector $\{\dot{\boldsymbol{\sigma}}\}$ as:

$$-\int_{\Gamma^{ele}} [\boldsymbol{N_u}]^{\mathrm{T}}\{\dot{\boldsymbol{t}}\}d\boldsymbol{\Gamma} + \int_{\Omega^{ele}} [\boldsymbol{\nabla N_u}]^{\mathrm{T}}\{\dot{\boldsymbol{\sigma}}\}d\boldsymbol{\Omega} = \{\boldsymbol{0}\} \tag{5-98}$$

where the matrix forms of $[\boldsymbol{N_u}]^{\mathrm{T}}$ and $[\boldsymbol{\nabla N_u}]^{\mathrm{T}}$ are illustrated in Appendix B-2. Substituting Equation (5-97) into Equation (5-98), we will get:

$$\begin{aligned} -\int_{\Gamma^{ele}} [\boldsymbol{N_u}]^{\mathrm{T}}\{\dot{\boldsymbol{t}}\}d\boldsymbol{\Gamma} + \int_{\Omega^{ele}} [\boldsymbol{\nabla N_u}]^{\mathrm{T}}\{\dot{\boldsymbol{\sigma}}''\}d\boldsymbol{\Omega} + \int_{\Omega^{ele}} [\boldsymbol{\nabla N_u}]^{\mathrm{T}}\{\boldsymbol{m}\}S_r\dot{u}_w d\boldsymbol{\Omega} \\ - \int_{\Omega^{ele}} [\boldsymbol{\nabla N_u}]^{\mathrm{T}}\{\boldsymbol{m}\}(u_a - u_w)\dot{S}_r d\boldsymbol{\Omega} = \boldsymbol{0} \end{aligned} \tag{5-99}$$

Considering the load – displacement problem in FEM for solid mechanics, the constitutive model plays the important role to relate the increment of internal effective stress vector in the loading part and the increment of internal total strain vector in the displacement part including the effect of degree of saturation for unsaturated soils by:

$$\dot{\boldsymbol{\sigma}}'' = \boldsymbol{D^{ep}} : \dot{\boldsymbol{\varepsilon}} - \boldsymbol{D^{S_r}} \dot{S}_r \tag{5-100}$$

where $\dot{\boldsymbol{\sigma}}''$, $\dot{\boldsymbol{\varepsilon}}$, $\boldsymbol{D^{ep}}$ and $\boldsymbol{D^{S_r}}$ are specifically defined for the Bishop's effective stress vector, strain vector, elastoplastic stiffness tensor and the saturation stiffness tensor of the proposed constitutive model for unsaturated soil (Chapter 2).

In plane strain condition, the increment of normal strain in z-axis is zero or $\dot{\varepsilon}_{zz} = 0$, the reduced form of constitutive equation can be re-written as shown in the matrix form by:

$$\begin{Bmatrix} \dot{\sigma}''_{xx} \\ \dot{\sigma}''_{yy} \\ \dot{\tau}''_{xy} \end{Bmatrix} = \begin{bmatrix} D_{11}^{ep} & D_{12}^{ep} & D_{14}^{ep} \\ D_{21}^{ep} & D_{22}^{ep} & D_{24}^{ep} \\ D_{41}^{ep} & D_{42}^{ep} & D_{44}^{ep} \end{bmatrix} \begin{Bmatrix} \dot{\varepsilon}_{xx} \\ \dot{\varepsilon}_{yy} \\ \dot{\gamma}_{xy} \end{Bmatrix} + \begin{Bmatrix} D_1^{S_r} \\ D_2^{S_r} \\ D_4^{S_r} \end{Bmatrix} \dot{S}_r \tag{5-101}$$

or we can write in the compacted form as:

$$\{\dot{\boldsymbol{\sigma}}''\} = \left[\boldsymbol{D_{ij}^{ep}}\right]\{\dot{\boldsymbol{\varepsilon}}\} - \left[\boldsymbol{D_k^{S_r}}\right]\dot{S}_r = [\boldsymbol{D}]\{\dot{\boldsymbol{\varepsilon}}\} - [\boldsymbol{D^{sr}}]\dot{S}_r \tag{5-102}$$

where $\{\dot{\boldsymbol{\sigma}}''\}$ and $\{\dot{\boldsymbol{\varepsilon}}\}$ are specifically defined for the bishop's effective stress vector and total strain vector in x-y plane for plane strain condition. The subscription orders i and j of the plane strain elastoplastic stiffness matrix $\left[\boldsymbol{D_{ij}^{ep}}\right]$ refer to the stress part and the strain part, respectively. The subscription order *k* of the plane strain saturation stiffness matrix $\left[\boldsymbol{D_k^{S_r}}\right]$ refers to the stress part. The subscription indices of the matrices, 1, 2 and 4, denote the normal stress (σ_{xx}) or strain (ε_{xx}) in *x*-axis, the normal stress (σ_{yy}) or strain (ε_{yy}) in *y*-axis and shear stress (τ_{xy}) or strain (γ_{xy}) on the *x*-*y* plane, respectively. In addition, the rate of degree of saturation $\dot{S}_r$ is determined from the SWCC. For the constant air pressure condition, it could be written as:

$$\dot{S}_r = E^W \dot{u_w} + E^V \{\boldsymbol{m}\}^{\mathrm{T}} \{\dot{\boldsymbol{\varepsilon}}\} \tag{5-103}$$

where E^W and E^V are the variation parameters of the suction part and volumetric part as shown in Appendix B-7.

Substituting $\dot{\boldsymbol{\sigma}}''$ Equation (5-102), rate of degree of saturation Equation (5-103), discretization of $\dot{\boldsymbol{\varepsilon}}$ Equation (5-41) of Section 5.2.1 and discretization of $\dot{u}_w$ Equation (5-72) of Section 5.2.2 into the Equation (5-99), we will get:

$$\int_{\Omega^{ele}}[\boldsymbol{\nabla N_u}]^{\mathrm{T}}([\boldsymbol{D}][\boldsymbol{B_u}]-[\boldsymbol{D^{sr}}]E^{V}\{\boldsymbol{m}\}^{\mathrm{T}}[\boldsymbol{B_u}])d\boldsymbol{\Omega}\{\dot{\boldsymbol{U}}\}$$
$$-\int_{\Omega^{ele}}[\boldsymbol{\nabla N_u}]^{\mathrm{T}}[\boldsymbol{D^{sr}}]E^{W}\left[\boldsymbol{N_{u_w}}\right]d\boldsymbol{\Omega}\{\dot{\boldsymbol{U}}_{\boldsymbol{w}}\}$$
$$+\int_{\Omega^{ele}}[\boldsymbol{\nabla N_u}]^{\mathrm{T}}\{\boldsymbol{m}\}S_r\left[\boldsymbol{N_{u_w}}\right]d\boldsymbol{\Omega}\{\dot{\boldsymbol{U}}_{\boldsymbol{w}}\} \quad (5\text{-}104)$$
$$-\int_{\Omega^{ele}}[\boldsymbol{\nabla N_u}]^{\mathrm{T}}\{\boldsymbol{m}\}(u_a-u_w)E^{W}\left[\boldsymbol{N_{u_w}}\right]d\boldsymbol{\Omega}\{\dot{\boldsymbol{U}}_{\boldsymbol{w}}\}$$
$$-\int_{\Omega^{ele}}[\boldsymbol{\nabla N_u}]^{\mathrm{T}}\{\boldsymbol{m}\}(u_a-u_w)E^{V}\{\boldsymbol{m}\}^{\mathrm{T}}[\boldsymbol{B_u}]d\boldsymbol{\Omega}\{\dot{\boldsymbol{U}}\}=\int_{\Gamma^{ele}}[\boldsymbol{N_u}]^{\mathrm{T}}\{\dot{\boldsymbol{t}}\}d\boldsymbol{\Gamma}$$

Then, arranging the equation as the matrix coefficient of $\{\dot{\boldsymbol{U}}\}$, $\{\dot{\boldsymbol{U}}_{\boldsymbol{w}}\}$ by:

$$\int_{\Omega^{ele}}[\boldsymbol{\nabla N_u}]^{\mathrm{T}}([\boldsymbol{D}][\boldsymbol{B_u}]-[\boldsymbol{D^{sr}}]E^{V}\{\boldsymbol{m}\}^{\mathrm{T}}[\boldsymbol{B_u}]$$
$$-\{\boldsymbol{m}\}(u_a-u_w)E^{V}\{\boldsymbol{m}\}^{\mathrm{T}}[\boldsymbol{B_u}])d\boldsymbol{\Omega}\{\dot{\boldsymbol{U}}\}+\int_{\Omega^{ele}}[\boldsymbol{\nabla N_u}]^{\mathrm{T}}(-[\boldsymbol{D^{sr}}]E^{W}\left[\boldsymbol{N_{u_w}}\right] \quad (5\text{-}105)$$
$$+\{\boldsymbol{m}\}S_r\left[\boldsymbol{N_{u_w}}\right]-\boldsymbol{m}(u_a-u_w)E^{W}\left[\boldsymbol{N_{u_w}}\right])d\boldsymbol{\Omega}\{\dot{\boldsymbol{U}}_{\boldsymbol{w}}\}=\int_{\Gamma^{ele}}[\boldsymbol{N_u}]^{\mathrm{T}}\{\dot{\boldsymbol{t}}\}d\boldsymbol{\Gamma}$$

The matrix forms of$[\boldsymbol{N_u}]^{\mathrm{T}}$ and $[\boldsymbol{\nabla N_u}]^{\mathrm{T}}$ are illustrated in Appendix B-2.1 for deformation part and $\left[\boldsymbol{N_{u_w}}\right]$ are illustrated in Appendix B-2.2 for pressure part. $\{\boldsymbol{U}\}$ is the nodal displacement vector and $\left\{\dot{\boldsymbol{U}}_{\boldsymbol{w}}\right\}$ is the nodal transient pore water pressure with time vector.

As proved in Appendix B-2, we could replace $[\boldsymbol{\nabla N_u}]$ and $\left[\boldsymbol{\nabla N_{u_w}}\right]$ into the Equation (5-105) by $[\boldsymbol{B_u}]$ and $\left[\boldsymbol{B_{u_w}}\right]$, respectively, we will get the first part of element equation which is the combination of the principal of static equilibrium in 2 – D and principal of effective stress for saturated soils as follows:

$$\int_{\Omega^{ele}}[\boldsymbol{B_u}]^{\mathrm{T}}([\boldsymbol{D}][\boldsymbol{B_u}]-[\boldsymbol{D^{sr}}]E^{V}\{\boldsymbol{m}\}^{T}[\boldsymbol{B_u}]$$
$$-\{\boldsymbol{m}\}(u_a-u_w)E^{V}\{\boldsymbol{m}\}^{\mathrm{T}}[\boldsymbol{B_u}])d\boldsymbol{\Omega}\{\dot{\boldsymbol{U}}\}+\int_{\Omega^{ele}}[\boldsymbol{B_u}]^{\mathrm{T}}(-[\boldsymbol{D^{sr}}]E^{W}\left[\boldsymbol{N_{u_w}}\right] \quad (5\text{-}106)$$
$$+\{\boldsymbol{m}\}S_r\left[\boldsymbol{N_{u_w}}\right]-\{\boldsymbol{m}\}(u_a-u_w)E^{W}\left[\boldsymbol{N_{u_w}}\right])d\boldsymbol{\Omega}\{\dot{\boldsymbol{U}}_{\boldsymbol{w}}\}=\int_{\Gamma^{ele}}[\boldsymbol{N_u}]^{\mathrm{T}}\{\dot{\boldsymbol{t}}\}d\boldsymbol{\Gamma}$$

From Equation (5-106), the system equation of static equilibrium of unsaturated soil and movement of SBSs due to S_r is combined from many elements and it can be written in the compacting matrix form as expressed by:

$$\left[\boldsymbol{K_{ep}^{unsat}}\right]\{\dot{\boldsymbol{U}}\}+[\boldsymbol{L}]\{\dot{\boldsymbol{U}}_{\boldsymbol{w}}\}=\{\dot{\boldsymbol{F}}_{\boldsymbol{ext}}\} \quad (5\text{-}107)$$

where the summary of integration equation of the coefficient matrices and the nodal load vectors is shown in Table 5-5.

5.2.4.2 Mass conservation for pore water

In this part, the element equation is established from the combinations of 3 main governing equations which are shown in following list:

1) Darcy's law
2) Continuity of flow
3) Mass conservation law

Capturing the unsaturated soil behavior, the mass conservation law of each phase, solid-water-air, shall be considered. However, assuming here that the soil particles are incompressible, and the air pressure is constant. Therefore, the mass conservation for pore water is the sufficient way in order to capture the variations of pore water pressure and volumetric behavior that are resulted by the flow in unsaturated soil.

The FEM coupled pressure-deformation in this part is originated by the mass conservation for pore water. For a given closed surface in the domain, the change in time of the mass enclosed by surface is equal to the mass traverses the surface. Considering the mass balance of pore water and assuming that there is no mass is exchanged between the phases lead to the continuity equation of flow as shown in the followings:

$$\dot{\rho}_w + \rho^w \{\boldsymbol{\nabla}\}^{\mathrm{T}} \cdot \{\boldsymbol{v_w}\} = 0 \tag{5-108}$$

when $\{\boldsymbol{v_w}\}$ is the Darcy's velocity vector of water, ρ^w is the true density of pore water and ρ_w is the density of pore water in the soil element which can be determined by the following equation.

$$\rho_w = n_e S_r \rho^w \tag{5-109}$$

where n_e is the porosity which can be expressed as a function of specific volume v in small strain by:

$$n_e = (v-1)/v_o \tag{5-110}$$

First, the change in time of the pore water mass $\dot{\rho}_{\mathrm{w}}$ in Equation (5-108) could be determined by differentiating Equation (5-109) with time as:

$$\dot{\rho_w} = ((\rho^w \dot{n_e}) S_r) = \rho^w n_e \dot{S_r} + S_r(\rho^w \dot{n_e} + n\dot{\rho^w}) \tag{5-111}$$

Assuming here too that water is incompressible which is $\dot{\rho^w} \approx 0$, Equation (5-111) can be written as:

$$\dot{\rho_w} = \rho^w n_e \dot{S_r} + S_r \rho^w \dot{n_e} \tag{5-112}$$

The volumetric behavior is included in the part of $\dot{n_e}$ by:

$$\dot{n_e} = -\dot{\varepsilon}_v = -\{\boldsymbol{m}\}^{\mathrm{T}}\{\dot{\boldsymbol{\varepsilon}}\} \tag{5-113}$$

Substituting Equation (5-113) into Equation (5-112), we will get:

$$\dot{\rho_w} = \rho^w n_e \dot{S_r} - S_r \rho^w \{\boldsymbol{m}\}^{\mathrm{T}}\{\dot{\boldsymbol{\varepsilon}}\} \tag{5-114}$$

Second, in the part the traversing pore water mass through the surface $\rho^w\{\boldsymbol{\nabla}\}^{\mathrm{T}} \cdot \{\boldsymbol{v_w}\}$ in Equation (5-108). From the definition of the Darcy's law and the pressure head as stated in Section 5.2.2 $\rho^w\{\boldsymbol{\nabla}\}^{\mathrm{T}} \cdot \{\boldsymbol{v_w}\}$ can be written in another form by:

$$\rho^w\{\boldsymbol{\nabla}^{\mathrm{T}}\} \cdot \{\boldsymbol{v_w}\} = -\rho^w\{\boldsymbol{\nabla}\}^{\mathrm{T}}[\boldsymbol{K_w}]\{\boldsymbol{\nabla} u_w\} \tag{5-115}$$

Substituting Equations (5-114) and (5-115) into Equation (5-108), we will get:

$$\rho^w n_e \dot{S_r} - S_r \rho^w \{\boldsymbol{m}\}^{\mathrm{T}}\{\dot{\boldsymbol{\varepsilon}}\} - \rho^w\{\boldsymbol{\nabla}\}^{\mathrm{T}}[\boldsymbol{K_w}]\{\boldsymbol{\nabla} u_w\} = 0 \tag{5-116}$$

Since ρ^w is the constant, so the continuity equation of flow is written by:

$$S_r\{\boldsymbol{m}\}^{\mathrm{T}}\{\dot{\boldsymbol{\varepsilon}}\} - n_e \dot{S_r} + \{\boldsymbol{\nabla}\}^{\mathrm{T}}[\boldsymbol{K_w}]\{\boldsymbol{\nabla} u_w\} = 0 \tag{5-117}$$

From Equation (5-117), the weak form is generated using the weighted residuals Galerkin's method with the matrix of weighting function $[\boldsymbol{W_{u_w}}]$ for the pore water pressure approximation. Considering a body, the domain Ω_{ele} and boundary of the domain Γ_{ele}, the weak form can be written by:

$$\begin{aligned} &\int_{\Omega^{ele}} [\boldsymbol{W_{u_w}}] S_r \{\boldsymbol{m}\}^{\mathrm{T}}\{\dot{\boldsymbol{\varepsilon}}\} d\boldsymbol{\Omega} - \int_{\Omega^{ele}} [\boldsymbol{W_{u_w}}]\, n_e \dot{S_r}\, d\boldsymbol{\Omega} \\ &+ \int_{\Omega^{ele}} [\boldsymbol{W_{u_w}}]\{\boldsymbol{\nabla}\}^{\mathrm{T}}[\boldsymbol{K_w}]\{\boldsymbol{\nabla} u_w\}\, d\boldsymbol{\Omega} = \{\boldsymbol{0}\} \end{aligned} \tag{5-118}$$

The matrix of weighting function $[\boldsymbol{W}]$ is assumed to be equal to the matrix of isoparametric interpolation function $[\boldsymbol{N}]$ using the Buffnode's Galerkin. Then, Equation (5-118) is written by:

$$\begin{aligned} &\int_{\Omega^{ele}} [\boldsymbol{N_{u_w}}]^{\mathrm{T}} S_r \{\boldsymbol{m}\}^{\mathrm{T}}\{\dot{\boldsymbol{\varepsilon}}\} d\boldsymbol{\Omega} - \int_{\Omega^{ele}} [\boldsymbol{N_{u_w}}]^{\mathrm{T}}\, n_e \dot{S_r}\, d\boldsymbol{\Omega} \\ &+ \int_{\Omega^{ele}} [\boldsymbol{N_{u_w}}]^{\mathrm{T}}\{\boldsymbol{\nabla}\}^{\mathrm{T}}[\boldsymbol{K_w}]\,\{\boldsymbol{\nabla} u_w\} d\boldsymbol{\Omega} = \{\boldsymbol{0}\} \end{aligned} \tag{5-119}$$

Integrating Equation (5-119) by parts using the Green theorem for the 2-D problem in the second derivative part is separately shown as follows:

$$\begin{aligned} &\int_{\Omega^{ele}} [\boldsymbol{N_{u_w}}]^{\mathrm{T}} S_r \{\boldsymbol{m}\}^{\mathrm{T}}\{\dot{\boldsymbol{\varepsilon}}\} d\boldsymbol{\Omega} - \int_{\Omega^{ele}} [\boldsymbol{N_{u_w}}]^{\mathrm{T}}\, n_e \dot{S_r}\, d\boldsymbol{\Omega} \\ &+ \int_{\Gamma^{ele}} [\boldsymbol{N_{u_w}}]^{\mathrm{T}}\{\boldsymbol{\nabla}\}^{\mathrm{T}}[\boldsymbol{K_w}](u_w \cdot \{\hat{\boldsymbol{n}}\}) d\boldsymbol{\Gamma} - \int_{\Omega^{ele}} [\boldsymbol{N_{u_w}}]^{\mathrm{T}}\{\boldsymbol{\nabla}\}^{\mathrm{T}}[\boldsymbol{K_w}]\{\boldsymbol{\nabla} u_w\} d\boldsymbol{\Omega} \\ &= \boldsymbol{0} \end{aligned} \tag{5-120}$$

Substituting rate of degree of saturation Equation (5-103), discretization of $\dot{\boldsymbol{\varepsilon}}$ Equation (5-41) of Section 5.2.1 and discretization of u_w Equation (5-71) of Section 5.2.2 into the Equation (5-120) we will get:

$$\begin{aligned}
&\int_{\Omega^{ele}}\left[\boldsymbol{N_{u_w}}\right]^{\mathrm{T}} S_r\{\boldsymbol{m}\}^{\mathrm{T}}[\boldsymbol{B_u}]d\boldsymbol{\Omega}\{\dot{\boldsymbol{U}}\} - \int_{\Omega^{ele}}\left[\boldsymbol{N_{u_w}}\right]^{\mathrm{T}} n_e E^W\left[\boldsymbol{N_{u_w}}\right]d\boldsymbol{\Omega}\{\dot{\boldsymbol{U}}_{\boldsymbol{w}}\} \\
&- \int_{\Omega^{ele}}\left[\boldsymbol{N_{u_w}}\right]^{\mathrm{T}} n_e E^V\{\boldsymbol{m}\}^T[\boldsymbol{B_u}]d\boldsymbol{\Omega}\{\dot{\boldsymbol{U}}\} \\
&- \int_{\Omega^{ele}}\left[\boldsymbol{\nabla N_{u_w}}\right]^{\mathrm{T}}[\boldsymbol{K_w}]\left[\boldsymbol{\nabla N_{u_w}}\right]d\boldsymbol{\Omega}\{\boldsymbol{U_w}\} \\
&= -\int_{\Gamma^{ele}}\left[\boldsymbol{N_{u_w}}\right]^{\mathrm{T}}\{\boldsymbol{\nabla}\}^{\mathrm{T}}[\boldsymbol{K_w}](u_w\cdot\{\hat{\boldsymbol{n}}\})d\boldsymbol{\Gamma}
\end{aligned} \tag{5-121}$$

Then, arranging Equation (5-121) as the matrix coefficient of $\dot{\boldsymbol{U}}, \dot{\boldsymbol{U}}_{\boldsymbol{w}}$ and $\boldsymbol{U_w}$ by:

$$\begin{aligned}
&\int_{\Omega^{ele}}\left[\boldsymbol{N_{u_w}}\right]^{\mathrm{T}}(S_r\{\boldsymbol{m}\}^{\mathrm{T}}[\boldsymbol{B_u}] - n_e E^V\{\boldsymbol{m}\}^{\mathrm{T}}[\boldsymbol{B_u}])d\boldsymbol{\Omega}\{\dot{\boldsymbol{U}}\} \\
&- \int_{\Omega^{ele}}\left[\boldsymbol{N_{u_w}}\right]^{\mathrm{T}} n_e E^W\left[\boldsymbol{N_{u_w}}\right]d\boldsymbol{\Omega}\{\dot{\boldsymbol{U}}_{\boldsymbol{w}}\} - \int_{\Omega^{ele}}\left[\boldsymbol{\nabla N_{u_w}}\right]^{\mathrm{T}}[\boldsymbol{K_w}]\left[\boldsymbol{\nabla N_{u_w}}\right]d\boldsymbol{\Omega}\{\boldsymbol{U_w}\} \\
&= -\int_{\Gamma^{ele}}\left[\boldsymbol{N_{u_w}}\right]^{\mathrm{T}}\{\boldsymbol{\nabla}\}^{\mathrm{T}}[\boldsymbol{K_w}](u_w\cdot\{\hat{\boldsymbol{n}}\})d\boldsymbol{\Gamma}
\end{aligned} \tag{5-122}$$

From Equation (5-122), the system equation of continuity flow including effect of S_r is combined from many elements and it can be written in the compacting matrix form as:

$$[\boldsymbol{M}]\{\dot{\boldsymbol{U}}\} - [\boldsymbol{R}]\{\dot{\boldsymbol{U}}_{\boldsymbol{w}}\} - [\boldsymbol{P}]\{\boldsymbol{U_w}\} = \{\boldsymbol{Q}\} \tag{5-123}$$

where the summary of integration equation of the coefficient matrices and the nodal load vectors is shown in Table 5-5.

Combining Equations (5-107) and (5-123) which are the element equation for the static equilibrium and the element equation for the continuity of flow, we could generate the formulation of soil – water - air three – phase seepage – deformation coupled FEM for unsaturated soils as shown by:

$$\begin{bmatrix}\boldsymbol{K_{ep}^{unsat}} & \boldsymbol{L}\\ \boldsymbol{M} & \boldsymbol{-R}\end{bmatrix}\begin{Bmatrix}\dot{\boldsymbol{U}}\\ \dot{\boldsymbol{U}}_{\boldsymbol{w}}\end{Bmatrix} - \begin{bmatrix}\boldsymbol{0} & \boldsymbol{0}\\ \boldsymbol{0} & \boldsymbol{P}\end{bmatrix}\begin{Bmatrix}\boldsymbol{U}\\ \boldsymbol{U_w}\end{Bmatrix} = \begin{Bmatrix}\dot{\boldsymbol{F}}_{\boldsymbol{ext}}\\ \boldsymbol{Q}\end{Bmatrix} \tag{5-124}$$

For solving the nonlinear first order differential equation, discretizing Equation (5-124) with time (see Appendix B-6), we will get:

$$\begin{bmatrix}\boldsymbol{K_{ep}^{unsat}} & \boldsymbol{L}\\ \boldsymbol{M} & \boldsymbol{-(\theta P h_t + R)}\end{bmatrix}\begin{Bmatrix}\boldsymbol{\Delta U}\\ \boldsymbol{U_{w|t+h_t}}\end{Bmatrix} = \begin{Bmatrix}\boldsymbol{\Delta F_{ext}} + \boldsymbol{L U_{w|t}}\\ h_t\boldsymbol{Q} + ((1-\theta)h_t\boldsymbol{P} - \boldsymbol{R})\boldsymbol{U_{w|t}}\end{Bmatrix} \tag{5-125}$$

where the summary of integration equation of the coefficient matrices and the nodal load vectors is shown in Table 5-5.

Table 5-5 Summary of integration equation for formulation of soil – water – air three – phase seepage – deformation coupled FEM for unsaturated condition (constant air pressure)

No.	Coefficient matrices or Nodal load vectors	Integration equation
1	Elastoplastic stiffness element matrix (deformation part)	$\left[\boldsymbol{K_{ep}^{unsat}}\right] = \int_{\Omega} [\boldsymbol{B_u}]^{\mathrm{T}}([\boldsymbol{D}][\boldsymbol{B_u}] - [\boldsymbol{D^{sr}}]E^{V}\{\boldsymbol{m}\}^{\mathrm{T}}[\boldsymbol{B_u}] - \{\boldsymbol{m}\}(u_a - u_w)E^{V}\{\boldsymbol{m}\}^{\mathrm{T}}[\boldsymbol{B_u}])d\boldsymbol{\Omega}$
2	Elastoplastic stiffness element matrix (pressure part)	$[\boldsymbol{L}] = \int_{\Omega} [\boldsymbol{B_u}]^{\mathrm{T}}(-[\boldsymbol{D^{sr}}]E^{W}\left[\boldsymbol{N_{u_w}}\right] + \{\boldsymbol{m}\}S_r\left[\boldsymbol{N_{u_w}}\right] - \{\boldsymbol{m}\}(u_a - u_w)E^{W}\left[\boldsymbol{N_{u_w}}\right])d\boldsymbol{\Omega}$
3	Rectangular coupling pressure deformation element matrix (density-dependent degree of saturation)	$[\boldsymbol{M}] = \int_{\Omega} \left[\boldsymbol{N_{u_w}}\right]^{\mathrm{T}}(S_r\{\boldsymbol{m}\}^{\mathrm{T}}[\boldsymbol{B_u}] - n_e E^{V}\{\boldsymbol{m}\}^{\mathrm{T}}[\boldsymbol{B_u}])d\boldsymbol{\Omega}$
4	Suction-dependent degree of saturation element matrix	$[\boldsymbol{R}] = \int_{\Omega} \left[\boldsymbol{N_{u_w}}\right]^{\mathrm{T}} n_e E^{W}\left[\boldsymbol{N_{u_w}}\right]d\boldsymbol{\Omega}$
5	Permeability element matrix	$[\boldsymbol{P}] = \int_{\Omega} \left[\boldsymbol{B_{u_w}}\right]^{\mathrm{T}}[\boldsymbol{K_w}]\left[\boldsymbol{B_{u_w}}\right]d\boldsymbol{\Omega}$
6	Nodal external force vector	$\{\boldsymbol{\Delta F_{ext}}\} = \int_{\Gamma} [\mathbf{N_u}]^{\mathrm{T}}\{\dot{\boldsymbol{t}}\}d\boldsymbol{\Gamma}$
7	Nodal inflows/outflows vector	$\{\boldsymbol{Q}\} = -\int_{\Gamma} \left[\boldsymbol{N_{u_w}}\right]^{\mathrm{T}}\{\boldsymbol{\nabla}\}^{\mathrm{T}}[\boldsymbol{K_w}](u_w \cdot \{\hat{\boldsymbol{n}}\})d\boldsymbol{\Gamma}$

Remarks: See Appendix B-5 for further details and formulas of the numerical integration.

5.3 VALIDATION OF FEM FOR PREDICTING THE BEHAVIOR OF SATURATED AND UNSATURATED SOILS

Ensuring algorithm and accuracy of the in-house FEM programs for saturated and unsaturated soils which were generated in this study, all the FEM formulations in Section 5.2 were validated in this section through the exact solution or the proposed elastoplastic constitutive model. Calibrated constitutive model parameters for unsaturated soil and soil water characteristic curve (Table 3-3 and Table 3-4) of 5:5 mixed Toyoura sand and Fujinomori clay by weight were used to determine the internal stress – strain on each Gauss's point in Finite Element Analysis or FEA and the elementary simulation in all validations unless otherwise specified. For the behavior of water seepage, coefficient of water permeability in x and y directions are assumed to be constant equal to 10^{-8} m/s.

5.3.1 Validation of FEM for predicting the behavior of saturated soils

Two main validation parts were performed in this study in order to validate the FEM for predicting the behavior of saturated soils as described below;

- The uncoupled FEM pressure-only analysis (Section 5.2.2) and coupled FEM pressure – deformation analysis for saturated soils (Section 5.2.3) were validated through the exact solution of Terzaghi's theory of consolidation. By this, both approximations of elastic deformation and distribution of pore water pressure through the saturated soil elements during loading could be validated.
- The uncoupled FEM deformation-only analysis (Section 5.2.1) and coupled FEM pressure – deformation analysis for saturated soils (Section 5.2.3) were validated through the elementary simulation of elastoplastic constitutive model for saturated soil. By this, the stress-strain behavior of saturated soils when subjected to the considering plane strain condition tests could be validated.

5.3.1.1 FEM validation through the Terzaghi's theory of consolidation

Uncoupled FEM pressure – only analysis and coupled FEM pressure – deformation analysis for saturated soils could be validated through the Terzaghi's theory of consolidation, especially the approximations of water flows and elastic settlement during the consolidation process.

Validating with the Terzaghi's theory of consolidation, the recompression index κ, which controls the elastic volumetric behavior of soil in the constitutive model for FEA, must be adjusted to obtain the equivalent soil stiffness as the coefficient of volume compressibility m_v which controls the elastic volumetric behavior of soil in the Terzaghi's consolidation theory. As one of the theory's assumption is linear elastic soil skeleton, so the parameters κ and m_v shall be determined based on the constant Young's modulus E as shown below.

Assuming that constant E 1000.0 kPa (typically for very soft clay) and elastic poison's ratio v_e 0.25, m_v is determined by reciprocal of constrained modulus D_{1-d} or in term of E as:

$$m_v = \frac{(1+v_e)(1-2v_e)}{(1-v_e)\,E} = \frac{(1+0.25)\big(1-2(0.25)\big)}{(1-0.25)1000.0} = 8.33E^{-4}\ kPa^{-1} \qquad (5\text{-}126)$$

and by assuming an initial void ratio e_0 0.60 and a constant mean effective stress p' 10.0 kPa, κ is determined for the validation as:

$$\kappa = \frac{3(1-2v)p'v_0}{E} = \frac{3\big(1-2(0.25)\big)(10.0)(1.6)}{1000.0} = 0.024 \qquad (5\text{-}127)$$

For elementary simulation, in the oedometer, the soil element was immediately loaded by the constant external vertical pressure $\Delta\sigma_y$ 100 kPa at the initial stage which generated the initial uniform excess pore water Δu_{w0} 100 kPa in the soil element. Then, it was continuously consolidated until the end of primary (t = 8000 secs) or until there is no excess pore pressure.

Table 5-6 The constitutive linear elastic parameter for the coupled and uncoupled FEA of saturated soils

Parameters	
Young's Modulus, E [kPa]	1000.0
Coefficient of permeability, k [m/s]	$1E^{-8}$
Poisson's ratio, v_e	0.25
Mean effective stress, p'[kPa]	10.0
Initial void ratio, e_0	0.6
Recompression index, κ	0.024

Table 5-7 The constitutive linear elastic parameter for exact solution of Terzaghi's theory of consolidation

Parameters	
Young's Modulus, E [kPa]	1000.0
Coefficient of permeability, k [m/s]	$1E^{-8}$
Poisson's ratio, v_e	0.25
Coefficient of volume compressibility, m_v [kPa-1]	$8.33E^{-4}$

For numerical simulation, the soil sample, 0.10 m height and 0.10 m width, was meshed from many rectangular elements. The initial condition, boundary condition, element geometry and meshing corresponding with the elementary simulation for uncoupled and coupled FEM of saturated soils were applied as shown in Figure 5-8 and Figure 5-9. Total consolidation time was discretized to be a small time increment 0.025 secs per step in order to keep the accuracy of the non-linear approximation solution comparing with the exact solution.

Using the constitutive linear elastic parameter summarized in Table 5-6 and Table 5-7, the numerical analysis could be validated through the exact solution of Terzaghi's theory of consolidation. Both approximate excess pore water pressure from the uncoupled FEM pressure-only analysis and coupled FEM pressure-deformation analysis could be validated through the exact solution of pore water distribution using Equation D-6. Moreover, the approximate elastic settlement from the coupled-pressure deformation FEM could be validated through the exact solution of vertical settlement using Equation D-7.

Validating with the exact solution, the approximation of excess pore water pressure distribution and vertical settlement at top of the soil sample are plotted together with the exact solution in Figure C-1 and Figure C-2, respectively. They revealed that the proposed uncoupled FEM pressure-only analysis and coupled FEM pressure – deformation analysis for saturated soils provide the accurate approximation of pressure distribution and elastic settlement that conforming with the exact solution of Terzaghi's theory of consolidation (Appendix D-2).

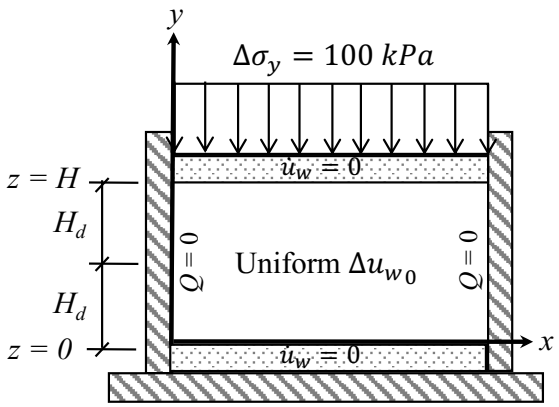

Figure 5-8 Initial condition and boundary condition of 1-D consolidations of saturated soils

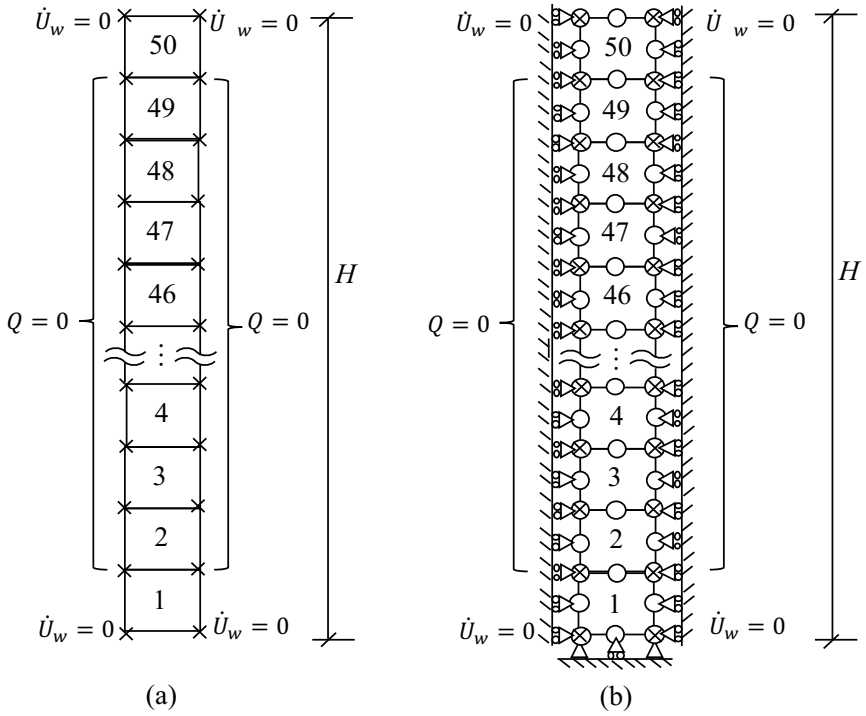

Figure 5-9 Element geometry and meshing of the 1-D consolidations (a) uncoupled FEM and (b) coupled FEM of saturated soils

5.3.1.2 FEM validation through the simulation of proposed elastoplastic constitutive model for saturated soil

Uncoupled FEM deformation - only analysis and coupled FEM pressure – deformation analysis for saturated soil could be validated through the simulation of proposed elastoplastic constitutive model for saturated soil, especially the approximations of load – displacement relation.

Both numerical simulation of the soil element using FEM and elementary simulation using the constitutive model were conducted. The initial states of soils were defined: initial void ratios

e_0 which represent dense and loose packing density (Table 5-8) under mean effective stress p' 98.0 kPa and initial pore water pressure u_{w0} 100.0 kPa. The soils were vertically compressed to 60% strain with the fully drained condition in oedometer compression test and biaxial radial constant shearing test, respectively. The simulation conditions for the validation are summarized in Table 5-8.

For numerical simulation, the soil samples were meshed by using a rectangular element, 1.0 m height and 1.0 m width, in order to validate with the elementary simulation under the continuum media condition. The initial condition, boundary condition, element geometry and meshing corresponding with the elementary simulation cases (Table 5-8) for uncoupled and coupled FEM of saturated soils were applied as shown in Figure 5-10 and Figure 5-11, respectively.

The set of comparison between the numerical simulation using both coupled and uncoupled FEMs and the elementary simulation results of each validation case is plotted in Figures C-3 through C-6 (Appendix C-2). They reveals that the generated uncoupled FEM deformation-only analysis and coupled FEM pressure – deformation analysis for saturated soils provide the accurate approximation of elastoplastic stress – strain relationship conforming with the proposed elastoplastic constitutive model for saturated soil which already validated through the experimental results.

In conclusion, the in-house FEM program for saturated soils is capable to predict the pressure – deformation behavior of saturated soils for the variation of packing density under plane strain and drained water condition based of the proposed constitutive model for saturated soil.

Table 5-8 Simulation condition for the validation of soil-water two-phase seepage-deformation coupled FEM for saturated soils

Packing densities	Testing	Case No.
Dense e_0=1.4	Oedometer compression	1DS
	Biaxial radial constant shearing	2DS
Loose e_0= 1.6	Oedometer compression	1LS
	Biaxial radial constant shearing	2LS

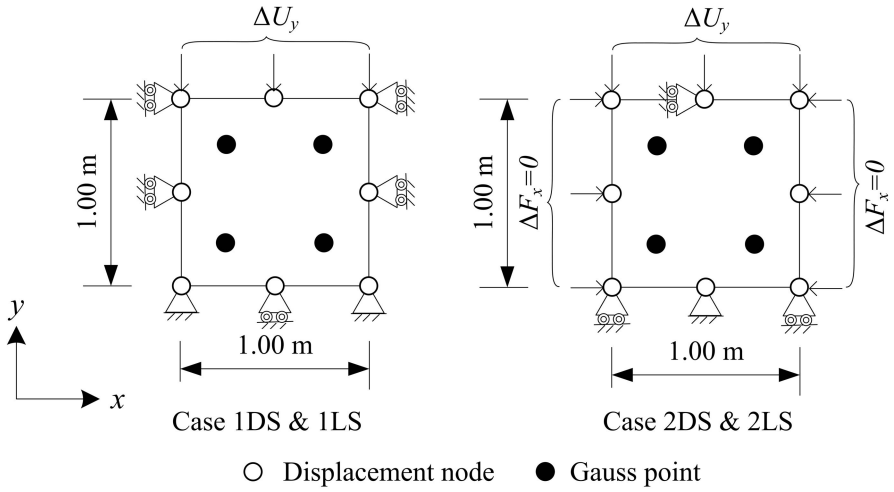

Figure 5-10 Geometry and boundary condition for the validation of uncoupled FEM for saturated soil for the validation case in Table 5-8

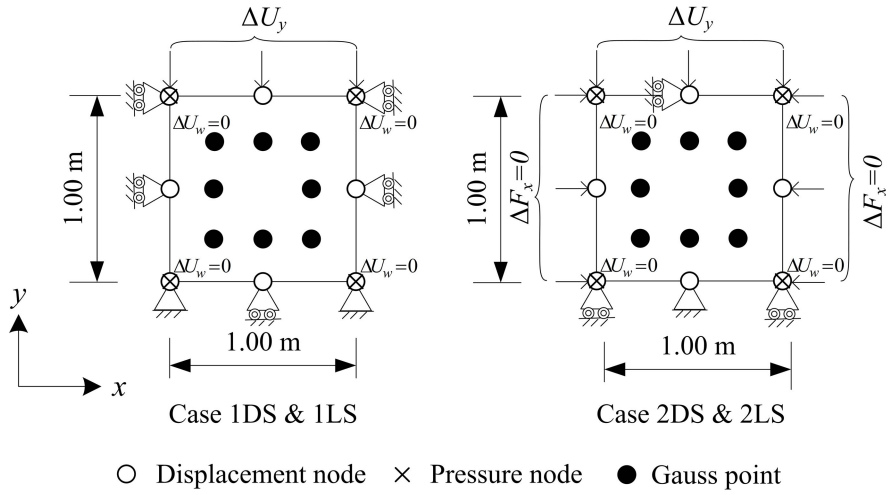

Figure 5-11 Geometry and boundary condition for the validation of coupled FEM for saturated soil for the validation case in Table 5-8

5.3.2 The validation of soil-water-air three-phase seepage-deformation coupled FEM for unsaturated soils

The soil-water-air three-phase seepage-deformation coupled FEM for unsaturated soils (Section 5.2.4) was validated through the simulation of constitutive model for unsaturated soil with the considering plane strain condition tests, especially the approximations of load – pore pressure - displacement relation.

Both the numerical simulation of a soil element using FEM and elementary simulation using the constitutive model were conducted with 8 cases of the simulation condition as summarized in Table 5-9. The initial states of soils, also using in elementary simulation of constitutive model were defined: initial void ratios e_0 which represent dense and loose packing

density (Table 5-9) under mean net stress p_{net} 20.0 kPa, pore air pressure u_a 98.0 kPa (assumed atmospheric pressure) and pore water pressure u_w 97.0 kPa.

Table 5-9 Simulation condition for the validation of soil-water-air three-phase seepage-deformation coupled FEM for unsaturated soils

Packing densities	Testing	Loading target (strain control)	Drainage conditions	Case No.
Loose e_0=1.226	Oedometer compression	Saturated state	Fully drained	1L
			Exhausted air - undrained water	2L
	Biaxial radial constant shearing	Critical state	Fully drained	3L
			Exhausted air - undrained water	4L
Dense e_0= 0.8	Oedometer compression	Saturated state	Fully drained	1D
			Exhausted air - undrained water	2D
	Biaxial radial constant shearing	Critical state	Fully drained	3D
			Exhausted air - undrained water	4D

For numerical simulation using FEM, the soil samples were meshed by using a rectangular element, 1.0 m height and 1.0 m width, in order to validate with the elementary simulation under the continuum media condition. For a soil element, the initial condition, boundary condition and geometry for each validation case (Table 5-9) are illustrated in Figure 5-12. In this study, the coefficient of water permeability is assumed to be constant equal to the saturated case since the total drainage time is not considered.

The set of comparison between the numerical simulation using the coupled FEM for unsaturated soils and the elementary simulation results of each case is plotted in Figures C-7 through C-22 (Appendix C-3). They reveals that the generated the coupled pressure – deformation analysis FEM for unsaturated soils provide the accurate approximation of elastoplastic stress – strain relationship that conforming with the proposed elastoplastic constitutive model for unsaturated soil that already validated through the experimental results.

In conclusion, coupled FEM for unsaturated soils is capable to predict the behavior of heterogenous media of unsaturated soil (variation in density and degree of saturation) under plane strain and exhausted air condition based of the proposed constitutive model for unsaturated soil.

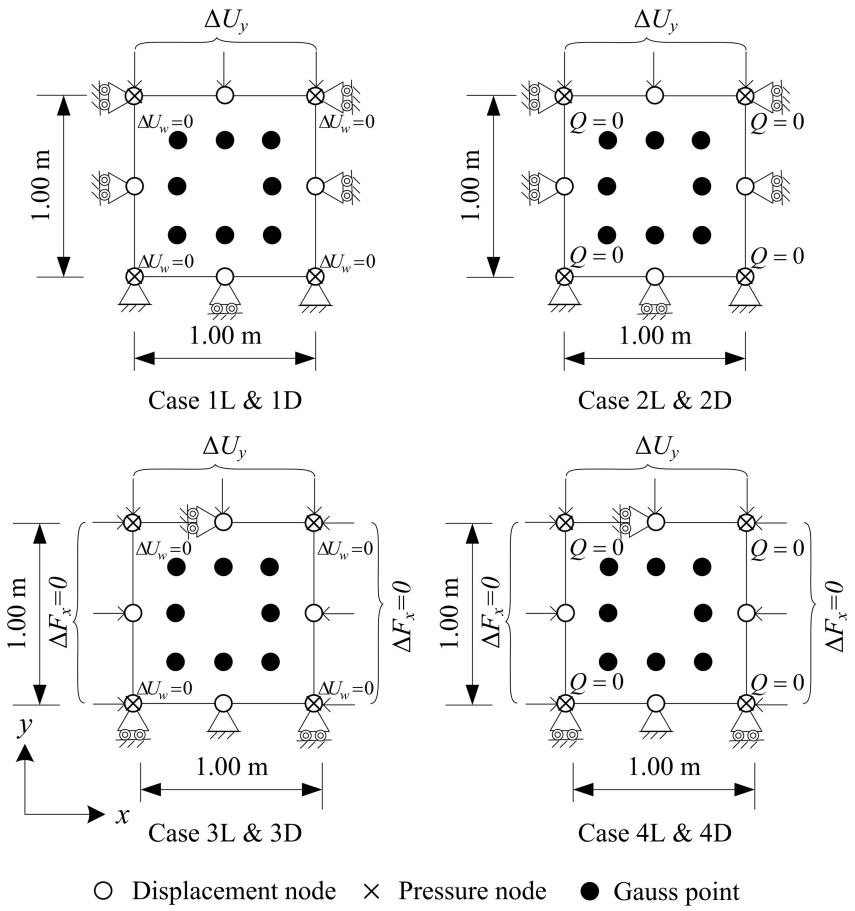

Figure 5-12 Geometry and boundary condition for the validation of coupled FEM for unsaturated soil

CHAPTER 6

EFFECT OF HETEROGENEITY IN 1-D STATIC COMPACTION

The interpretation of compaction mechanisms that was discussed in Chapter 4 is performed by the elementary analysis. The analysis is under the condition of continuum mechanics based on the assumption of very small domain; therefore, we infer that soil properties in the domain is homogenous. However, using only the constitutive model for unsaturated soils under the assumption of continuum mechanics could not be applied to investigate the real condition of geotechnical work. This is because, there are the heterogeneities of soil, water and air phases in the considering domain of unsaturated soils. Therefore, soil-water-air three-phases seepage-deformation coupled FEM for unsaturated soil is a tool to investigate the heterogeneity problem by sub-dividing the domain into the small elements. In each small element, a different set of soil properties could be applied.

Recently, coupled FEM for unsaturated soil has been applied as a tool in order to investigate the unsaturated soil behaviors by many researchers. For the compaction mechanism, using coupled FEM for unsaturated soil, Kawai, et al. (2012) and Kawai, et al. (2014) investigated 1-D static compaction mechanisms by considering pore water pressure and pore air pressure. Kawai, et al. (2016) investigated the distributions of dry density and degree of saturation after compaction. However, most of the studies, the initial states of soil were uniformly defined in the domain as the homogenous material. In another way, recent numerical investigations using coupled FEM for unsaturated soil, either the assumption of passive pore air pressure (Song, et al., 2012; Borja & Song, 2014; Song, 2014) or active pore air pressure (Song, et al., 2017), considering the material heterogeneity effect at the initial state have been performed by many researchers. They found that the material heterogeneities, such as density and degree of saturation, play an important role in triggering strain localization in unsaturated porous media (Song, et al., 2017 and Likos, et al., 2019). However, their main purpose is to interpret the inception of strain localization in unsaturated soils only.

In this study, using the proposed coupled FEM for unsaturated soil which is implemented by the proposed constitutive model for unsaturated soils, the interpretation of 1-D static compaction mechanisms considering the effect of heterogeneity in unsaturated porous media were performed. Considering the heterogeneities of dry density and degree of saturation, the numerical investigation results in this section proved that effect of heterogeneity shall be taken into account for the compaction control parameter specification in order to alleviate the localization failure (Song, et al., 2017). Moreover, the quality control of compaction test in the

laboratory is affected by the material heterogeneity and it is quite necessary to the compaction work starting from the sample preparation stage. Since the compaction control parameter for the field compaction and the strength for the engineering design are generated by the laboratory test, therefore the engineers should emphasize the quality control of compaction test in the laboratory.

Finally, we aim to indicate the recommendations for heterogeneity alleviation by the compaction control parameter specifications and the quality control of soil preparation for compaction test in the laboratory which affects the field compaction procedure, design process and cost and planning management of the embankment construction.

The numerical investigations were performed in this chapter for 1-D static compaction on unsaturated soil using 2-D soil-water-air three-phases seepage-deformation coupled FEM (passive pore air pressure) as proposed in Chapther 5. In this chapter, coefficient of water permeability in x and y directions were assumed to be constant equal to $5x10^{-7}$ m/s. The sets of validated parameters for 5:5 mixed Toyoura sand and Fujinomori clay by weight (Table 3-3 and 3-4) were used through the numerical investigation in the part of constitutive model for unsaturated soils implementation.

6.1 EFFECT OF MATERIAL HETEROGENEITY IN 1-D STATIC COMPACTION ON UNSATURATED SOILS

The numerical investigations were performed in this section to illustrate the effect of material heterogeneity in 1-D static compaction on unsaturated soils. The comparison of 1-D static compaction mechanism between homogenous and heterogenous soil samples are demonstrated as follows.

6.1.1 Geometry, meshing and boundary condition in the numerical investigation

In this study, for 2-D FEM, the dimensions of compaction mold were assumed to be 10 cm width and 10 cm height as shown in Figure 6-1. Considering volume of the mold per unit length (1 cm), the total volume of compaction mold V_{mold} was 100 cm^3. By the controlling of prescribed dry density ρ_d and compaction water content w_n in the compaction process, mass of dried soil M_s and mass of water M_w which were calculated by Equation (6-1), and Equation (6-2), respectively shall be uniquely prepared.

$$M_s = \rho_d V_{mold} \tag{6-1}$$

$$M_w = \frac{w_n}{100} M_s \tag{6-2}$$

In this numerical simulation, each soil sample was meshed by 100 square elements which the initial dimension of each element was 1 cm width by 1 cm height per unit length (1 cm).

The boundary conditions of displacement, external force and seepage of water and air (exhausted air – undrained water) of 1-D static compaction were set as shown in Figure 6-2.

6.1.2 Initial states of unsaturated soil samples

For ρ_d 1.5 g/cm^3 and w_n 22% of homogenous (U22) and random heterogenous (1R22) soil samples, M_s 150 g and M_w 33 g were prepared for the compaction. In this study, U22 denotes the homogenous soil sample with ρ_d 1.5 g/cm^3 and w_n 22%. While 1R22 denotes the 1st random arrangement of heterogenous soil sample with $\overline{\rho_d}$ 1.5 g/cm^3, w_n 22% and standard deviation SD 0.1. Initial states of unsaturated soils for U22 and 1R22 are described below.

6.1.2.1 Homogenous soil sample (U22)

Initial state of homogenous soil sample was assumed to be identical for all elements. By the prescribed dry density and compaction water content, initial void ratio e_0 0.782 and degree of saturation S_{r0} 75.20% were calculated by Equation (4-1) and Equation (4-2), respectively. Assuming that pore air pressure u_a 98.0 kPa (atmospheric pressure) and the soil was compacted on the main wetting curve (I_h = 0), pore water pressure u_w 96.43 kPa could be calculated by Equation (2-6). Initial isotropic total stress was 118.0 kPa in the simulation. The initial state of numerical simulation in form of meshed element including the prescribed specific volume, degree of saturation and pore water pressure are illustrated in Figure 6-6(a).

6.1.2.2 Heterogenous soil sample (1R22)

For the prescribed mean dry density $\overline{\rho_d}$ 1.5 g/cm^3, element initial dry densities were randomly distributed to 100 elements of the heterogenous soil sample based on the assumption of normal distribution with SD was 0.10 (Figure 6-3). Volume of each element V_{ele} and its geometry were similarly defined across the domain, then initial void ratio $e_{0,ele}$ and degree of saturation $S_{r0,ele}$ of each element were calculated by Equation (4-1) and Equation (4-2), respectively. Assuming that pore air pressure u_a 98.0 kPa (atmospheric pressure) and the soil was compacted on the main wetting curve (I_h = 0), the uniform distribution of an unique u_w 96.718 kPa across the domain which was calculated by Equation (2-6) could be solved by controlling the total mass of water in the domain M_w 33 g as specified in this section for w_n 22%. The random initial state of numerical simulation in form of meshed element including prescribed specific volume, degree of saturation and pore water pressure are illustrated in Figure 6-6(b).

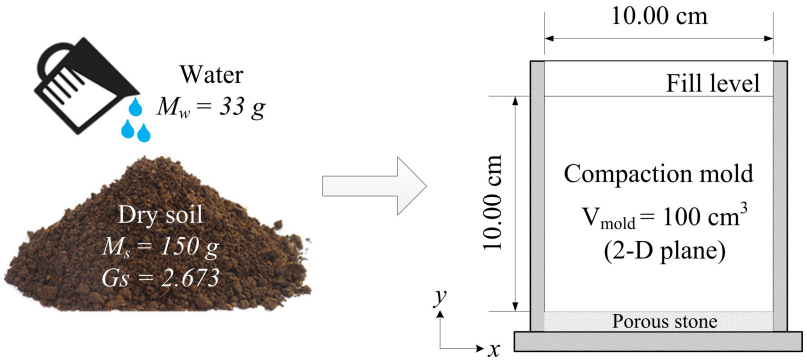

Note: Mass and volume are shown per unit length 1 cm

Figure 6-1 Geometry of compaction mold and soil sample

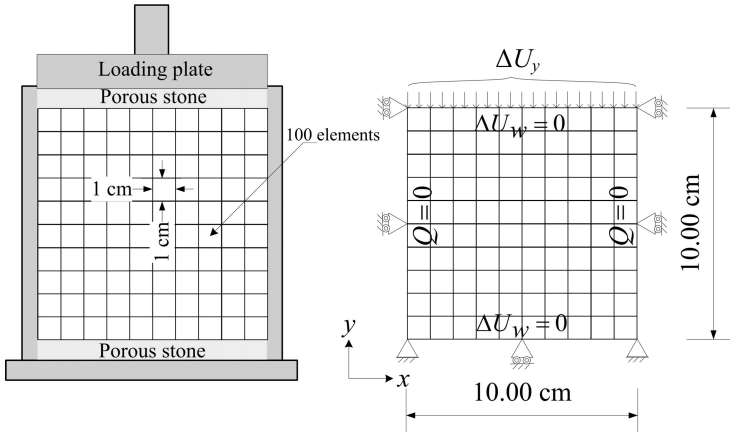

Figure 6-2 FEM boundary conditions of 1-D static compaction for soil samples

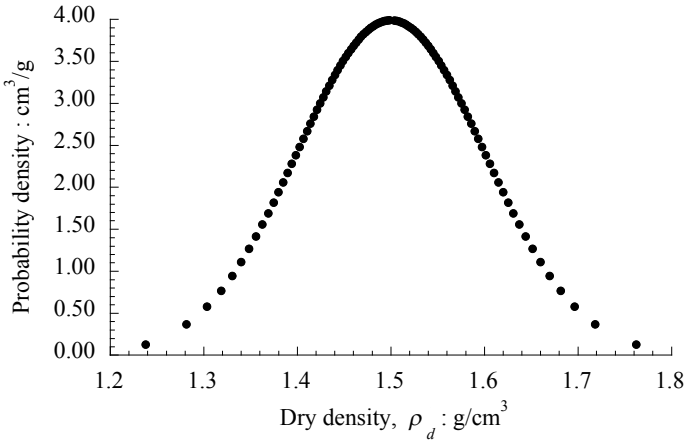

Figure 6-3 Normal distribution of dry density for heterogenous soil sample (SD = 0.1 and $\overline{\rho_d}$ = 1.5 g/cm^3)

6.1.3 Numerical results of compaction

6.1.3.1 Homogenous soil sample (U22)

6.1.3.1.1 Numerical investigation results

The homogenous soil sample (U22) was statically compacted by the uniform vertical pressure at the top surface of the sample until approaching the fully saturated state. The displacement rate was controlled at 0.001 mm/s to allow the local drainage of water in each element (Song, et al., 2017). By this condition, we could infer that air was also locally drained since the air permeability is higher than the water permeability. Stress – strain at the top surface of the sample and average dry density – applied vertical compaction stress are plotted in Figure 6-5(a) and Figure 6-5(b), respectively. In addition, the results of numerical simulation in form of meshed element including the specific volume, degree of saturation and pore water pressure at the applied vertical compaction stress 200 kPa and the saturated state are illustrated in Figure 6-6(a).

6.1.3.1.2 Validations of FEM through the elementary simulation

1-D static compaction results of homogenous soil sample (U22) which was performed by coupled FEM for unsaturated soils (Section 6.1.3.1.1) was validated through the elementary simulation under the same condition. Figure 6-4 reveals that compaction of homogenous soil sample by the numerical analysis, which is under the continuum mechanics and localized drainages conditions as the elementary analysis, provides the accurate approximation of stress-strain relationship conforming with the proposed elastoplastic constitutive model for unsaturated soils.

6.1.3.2 Heterogenous soil sample (1R22)

6.1.3.2.1 Numerical investigation results

The heterogenous soil sample (1R22) was statically compacted in 1-D by the displacement control at the top surface of the sample until approaching the fully saturated state. The displacement rate was controlled at 0.001 mm/s to allow the local drainages as previous described. Stress – strain at the top surface of the sample and average dry density – applied vertical compaction stress are plotted in Figure 6-5(a) and Figure 6-5(b), respectively. In addition, the results of numerical simulation in form of meshed element including the specific volume, degree of saturation and pore water pressure at the applied vertical compaction stress 200 kPa and the saturated state are illustrated in Figure 6-6(b).

6.1.4 Effect of material heterogeneity to the properties of compacted soils

In the comparison of the average dry density after compaction between the homogenous (U22) and heterogenous (1R22) soil samples (Figure 6-5(b)), we found that the average dry density of random heterogenous soil sample (1R22) is higher than the average dry density in the homogenous soil sample (U22) at a given applied vertical compaction stress. Higher compaction effort resulted in higher different dry density between the homogenous and heterogenous soil samples. While at the saturated state, the average dry densities are almost equal among the cases. Since they are limited by the incompressibility of water at the saturated state of 1-D compaction; therefore, the compaction effort did not affect the average dry density at this state. However, in the simulations, the average dry densities of heterogenous soil sample are a little lower than the homogenous soil sample. This is because fully saturated state for all elements could not be approached in the heterogenous soil sample under the same accuracy step in the simulation.

Considering the heterogenous soil sample (1R22), in addition to the increasing of compaction effort could cause the increasing of average dry density. Moreover, it also caused the decreasing of the variations of element dry density. During the compaction, low variation of the distribution curves of element dry density were observed and it continuously slid to the denser part by some limit of the maximum dry density (Figure 6-7). This is because, with increasing of compaction effort, the looser elements were highly deformed compare to the denser elements due to the high stiffness of the denser element and the limitation of minimum void ratio of each soil type. By these results, heterogeneity on materials which cause the localized failure under loadings (Song, et al., 2017) could be alleviated. Decreasing variation of element dry density after compaction (approaching the homogenous material) could be done by increasing the compaction effort in the compaction process.

In addition, the skewness of element dry density positively increased especially in the high compaction effort (Figure 6-7). Figure 6-7 shows that the number of lower dry density element is more than the denser dry density element with the small variation after compaction. This result implies that some looser elements could not be deformed due to the stress absorption of the denser element around their elements.

In conclusion, the material heterogeneities at the initial state including dry density and degree of saturation affect the average dry density at any considering stage of compaction excluding in the saturated state. Specified the appropriate compaction effort, the effect of heterogeneity after compaction on the localized behavior of compacted soil when subjected to loadings could be alleviated. After the effect of heterogeneity on the properties of compacted soils was confirmed in this section. Then, in the next section, for a given distribution of the dry

density (SD 0.1, $\overline{\rho_d}$ 1.5 g/cm^3), the significance of element dry density arrangement in the heterogeneity soil sample shall be investigated.

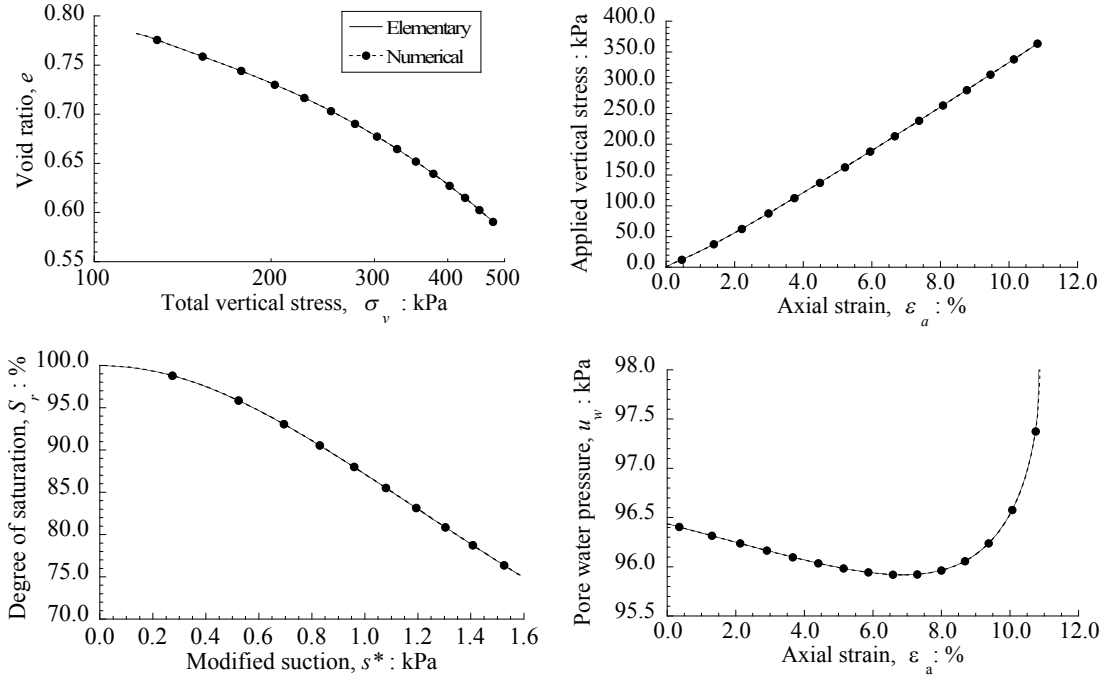

Figure 6-4 Validation of numerical analysis (U22) through the elementary analysis

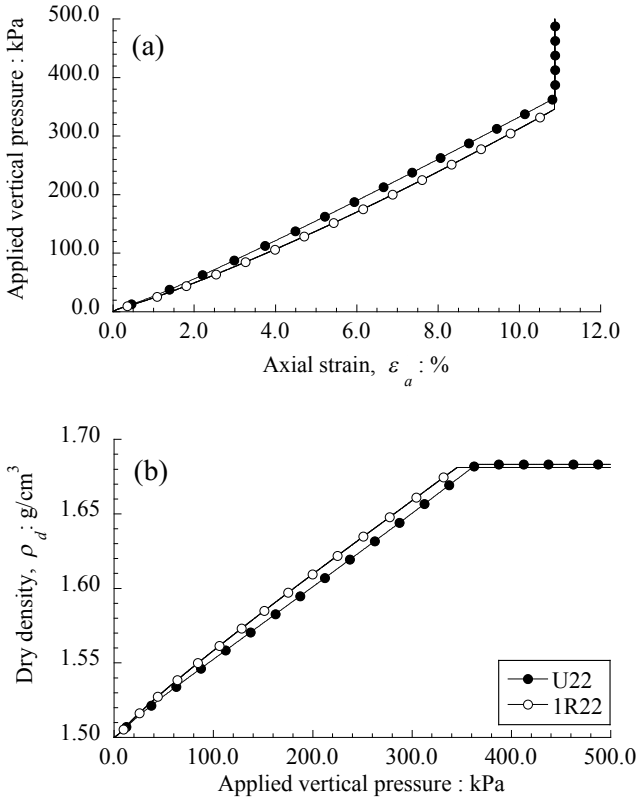

Figure 6-5 Comparisons of (a) stress – strain relationship at the top surface and (b) average dry density of compacted soil between homogenous and heterogenous soil samples

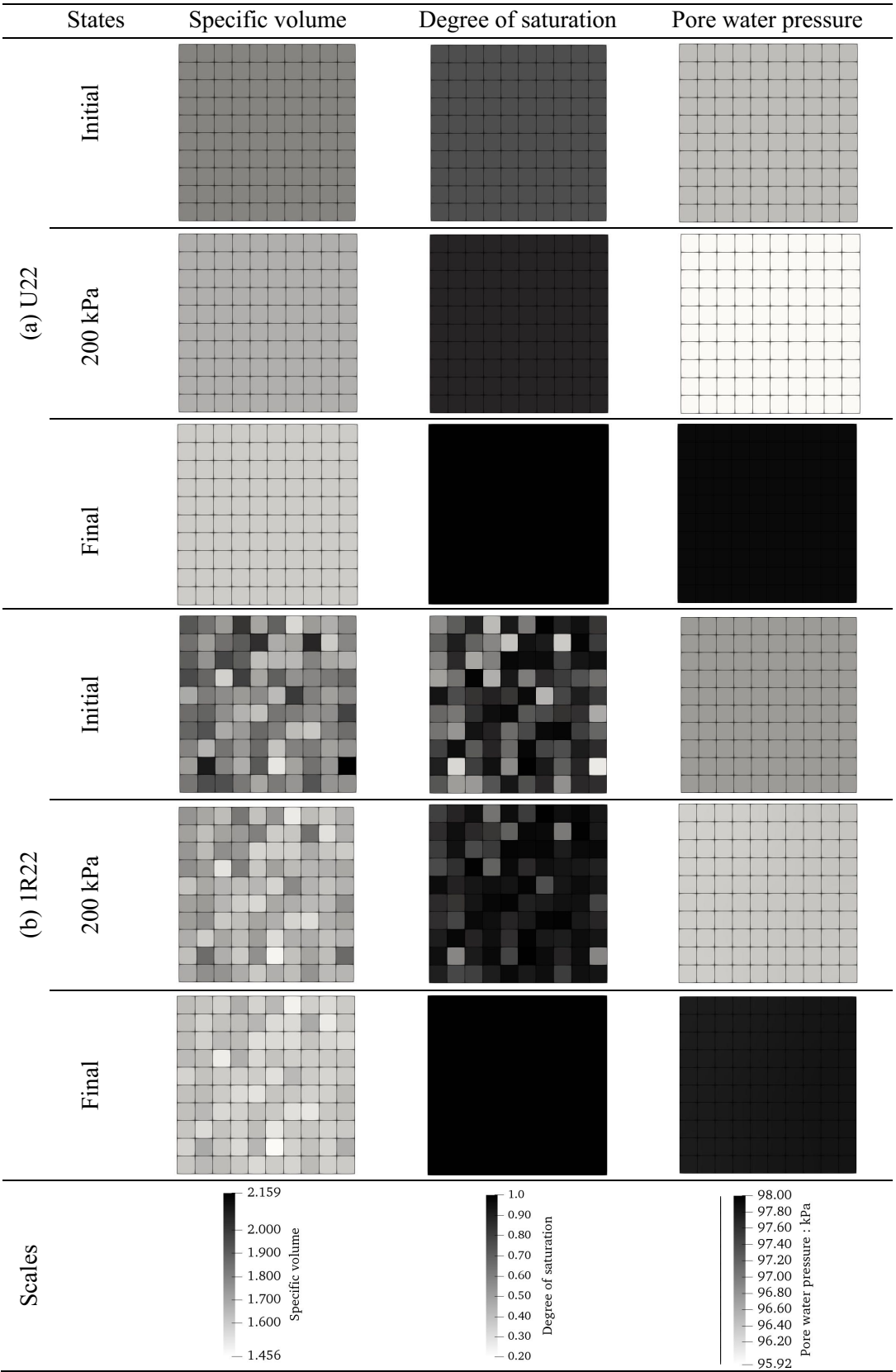

Figure 6-6 Numerical simulation results (meshed element) including v, S_r and u_w of the initial, applied vertical pressure 200 kPa and saturated states for cases (a) U22 and (b) 1R22

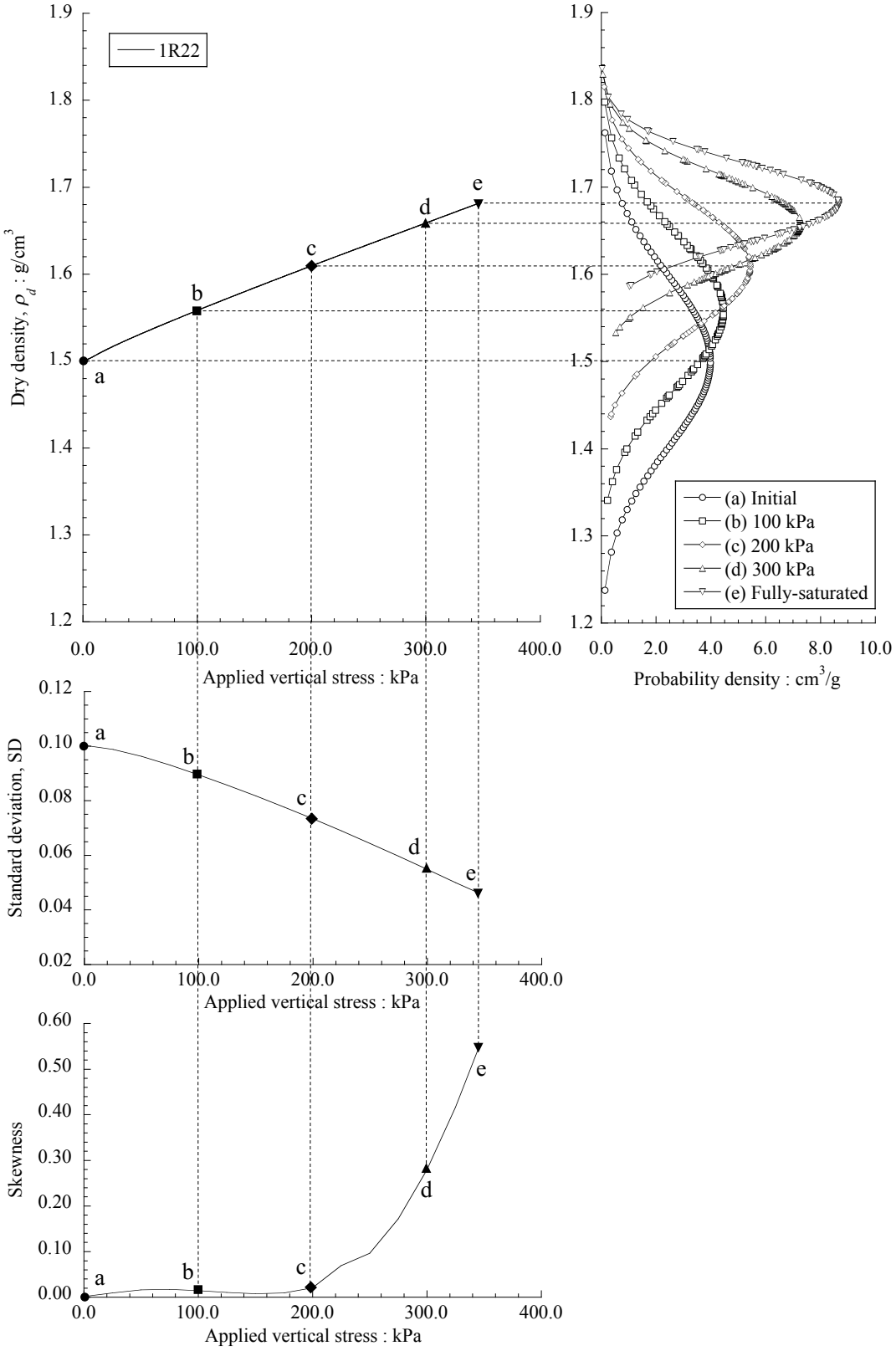

Figure 6-7 Variations of element dry density distributions during the compaction of 1R22

6.2 EFFECT OF INITIAL DRY DENSITY DISTRIBUTION ARRANGEMENT IN 1-D STATIC COMPACTION ON UNSATURATED SOILS

Refer to the numerical investigations in Section 6.1, the heterogeneities of initial dry density and degree of saturation of unsaturated soil affect the property of compacted soils. In this section, the effect of various initial dry density distribution arrangement in 1-D static compaction on unsaturated soils was investigated by keeping M_s 150 g, M_w 33 g, SD 0.1 and $\overline{\rho_d}$ 1.5 g/cm^3 as defined in Section 6.1.

6.2.1 Arrangements of initial dry density in the heterogenous soil sample

Following five arrangements of element dry density in heterogenous soil samples, including SV22; SH22; 1R22; 2R22 and 3R22 where $\overline{\rho_d}$ 1.5 g/cm^3 and SD 0.1, were set in order to investigate the effect of initial element dry density arrangement to the variation of dry density of compacted soil when the equivalent initial dry density was kept constant. In this study, SV22 and SH22 denote the segregated soil samples in vertical and horizontal directions, respectively, with w_n 22%. While 1R22, 2R22 and 3R22 denote the 1st, 2nd and 3rd random arrangement of heterogenous soil samples, respectively, with w_n 22%. SV22 and SH22 were extremely set in order to investigate the extremely effect of the arrangement. While 1R22, 2R22 and 3R22 were set to investigate the variation of dry density of compacted soil when the normal distribution of dry density (SD = 0.1 and $\overline{\rho_d}$ = 1.5 g/cm^3) was randomly mixed.

- SV22: The geometry domain was vertically segregated to two main parts, parallel arrangement, where dry density 1.4 g/cm^3 and 1.6 g/cm^3 were uniformly distributed in each part as shown in Figure 6-10(a).
- SH22: The geometry domain was horizontally segregated to two main parts, series arrangement, where dry density 1.4 g/cm^3 and 1.6 g/cm^3 were uniformly distributed in each part as shown in Figure 6-10(b).
- 1R22: Normal distribution of dry density (SD = 0.1, $\overline{\rho_d}$ = 1.5 g/cm^3, Figure 6-3) was randomly arranged in the heterogenous soil sample as shown in Figure 6-6(b). The arrangement was similar to the arrangement of heterogenous soil sample in Section 6.1.2.2
- 2R22 and 3R22: Normal distribution of dry density (SD = 0.1, $\overline{\rho_d}$ = 1.5 g/cm^3, Figure 6-3) was randomly arranged in the heterogenous soil samples, 2R22 and 3R22, as shown in Figure 6-11(a) and Figure 6-11(b), respectively.

6.2.2 Numerical results of compaction

The prescribed arrangements of dry density in the heterogenous soil samples were statically compacted by the displacement control at the top surface of the sample until approaching the fully saturated state. The displacement rate was controlled at 0.001 mm/s to allow the local drainages as previous described. Stress – strain at the top surface of the sample, average dry density – the applied vertical compaction stress and coefficient of variation (only 1R22, 2R22 and 3R22) – the applied vertical compaction stress are plotted in Figure 6-8(a), Figure 6-8(b) and Figure 6-9, respectively. In addition, the results of numerical simulation in form of meshed element including the specific volume, degree of saturation and pore water pressure at the applied vertical compaction stress 200 kPa and the saturated state for SV22 & SH22 and 2R22 & 3R22 are illustrated in Figure 6-10 and Figure 6-11, respectively.

6.2.3 Effect of initial dry density distribution arrangement to the properties of compacted soils

Refer to the comparison of the average dry density between the various arrangements of initial dry density distribution in heterogenous soil samples as shown in Figure 6-8, we found that average dry density of arrangement SH22, 1R22, 2R22 and 3R22 are significantly higher than the average dry density in the homogenous soil sample (U22) at a given applied vertical compaction stress. In addition, their sequence from highest to lowest dry density was SH > 1R22 ≈ 2R22 ≈ 3R22. Considering only the random arrangements, including 1R22; 2R22; 3R22, the random arrangement of initial element dry density insignificantly affected the average dry density of compacted soil among their group (Figure 6-9). While the average dry density of compacted soil of SV22 is lower than the U22 due to the parallel distribution. However, at the saturated state, average dry density was not affected by the arrangement as long as every element are uniformly approached the saturated state.

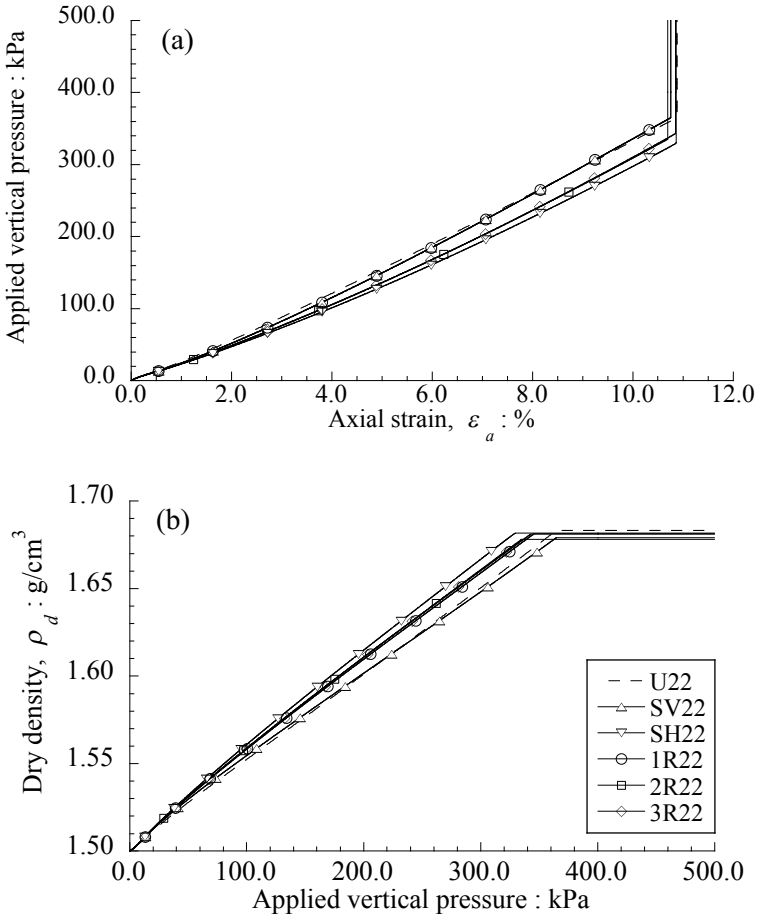

Figure 6-8 Comparisons of (a) stress – strain relationship at the top surface and (b) average dry density of compacted soil between homogenous and heterogenous soil samples (arrangement effect)

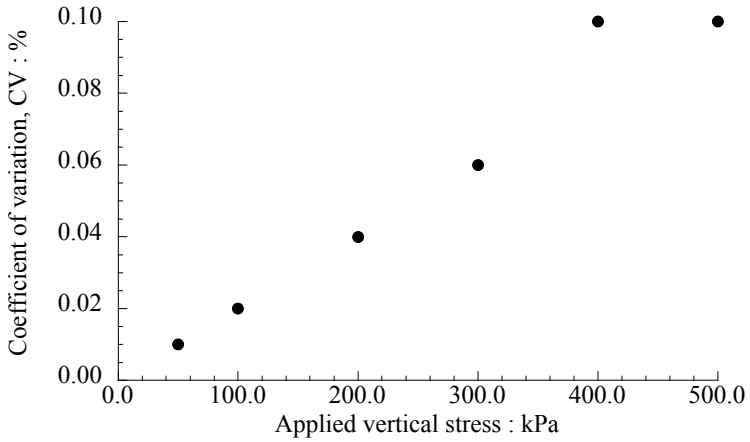

Figure 6-9 Coefficient of variation of random heterogeneity soil samples (only 1R22, 2R22 and 3R22) with applied vertical compaction stress

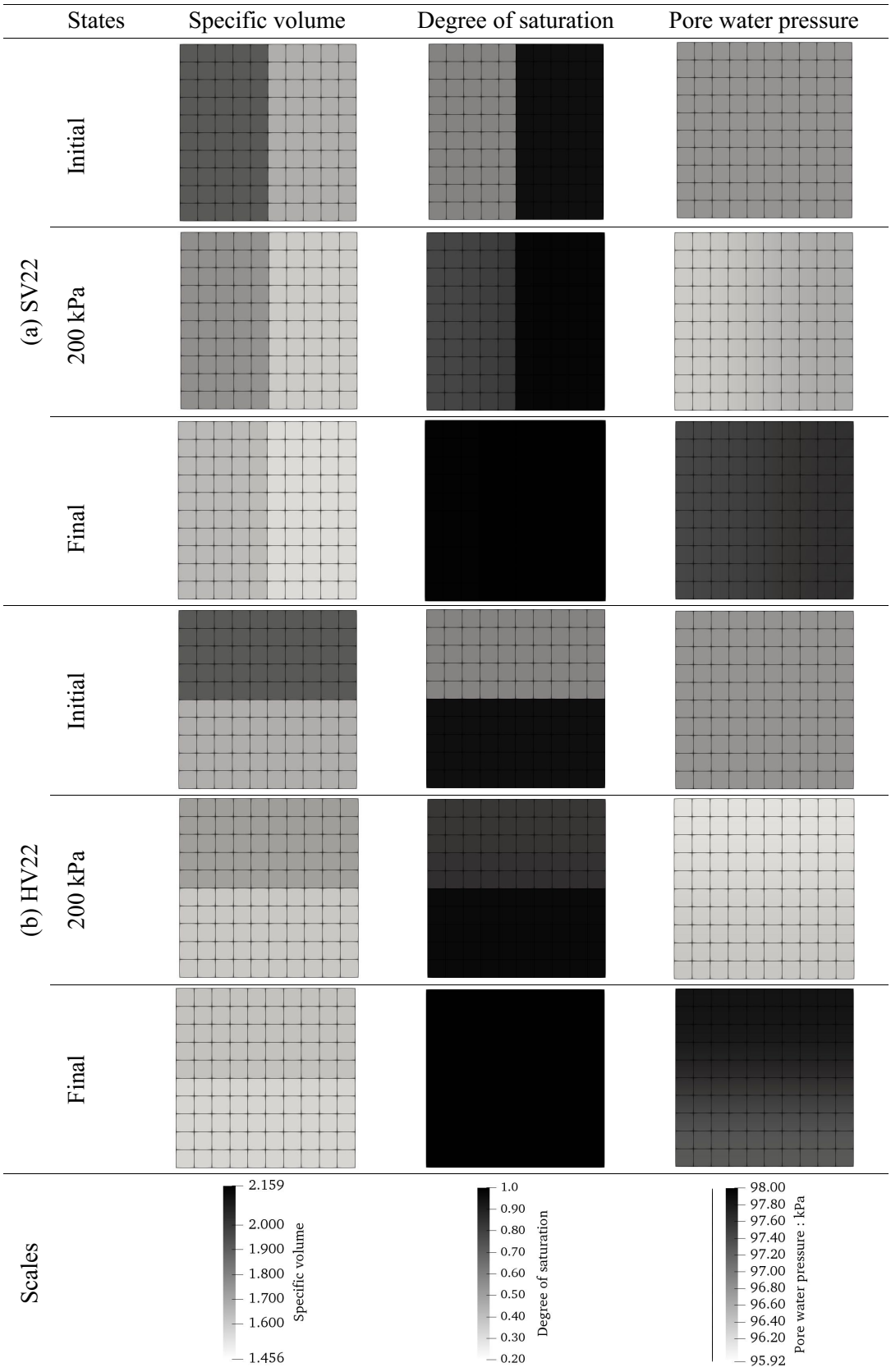

Figure 6-10 Numerical simulation results (meshed element) including v, S_r and u_w of the initial, applied vertical pressure 200 kPa and saturated states for cases (a) SV22 and (b) HV22

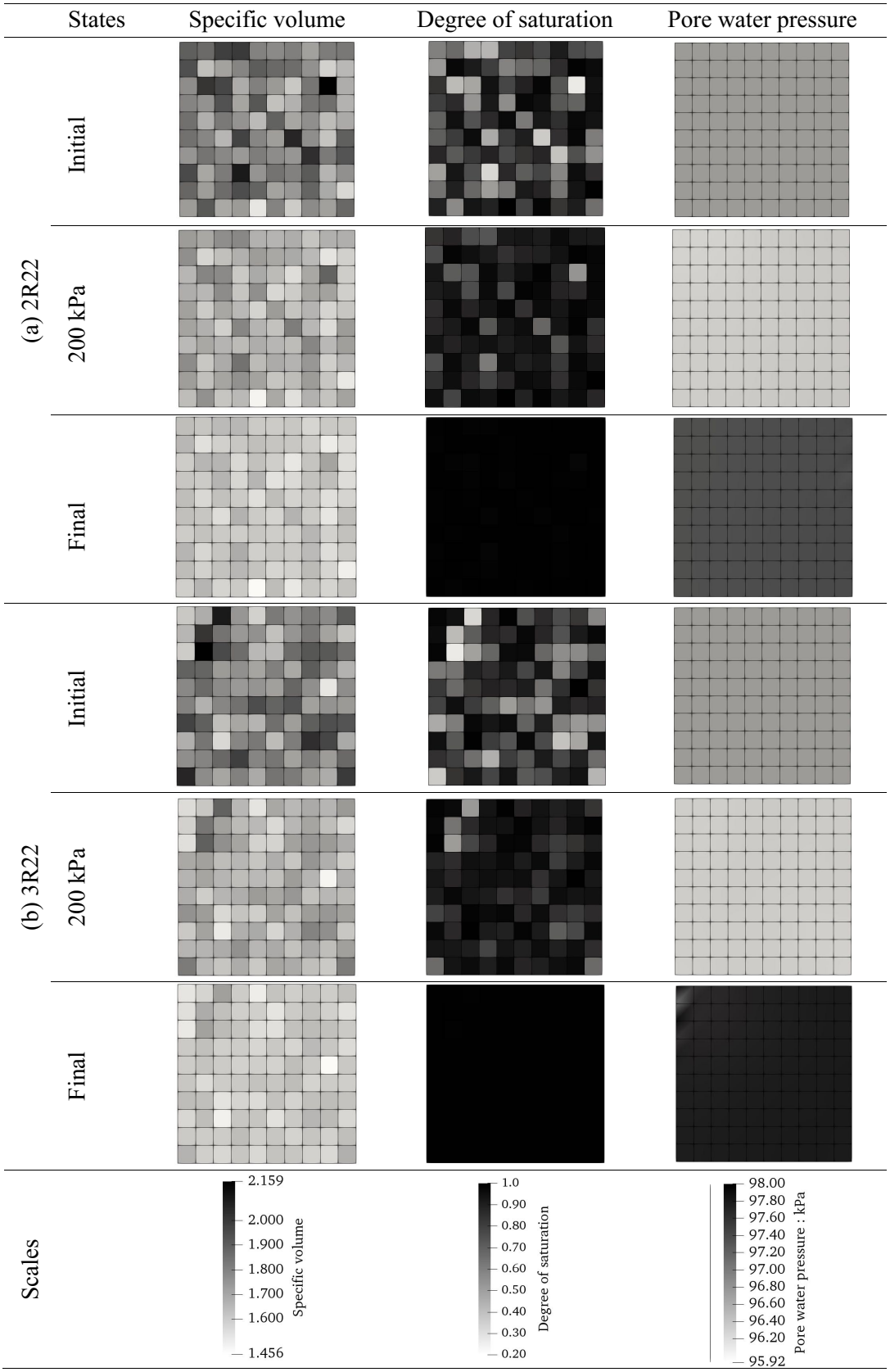

Figure 6-11 Numerical simulation results (meshed element) including v, S_r and u_w of the initial, applied vertical pressure 200 kPa and saturated states for cases (a) 2R22 and (b) 3R22

6.3 EFFECT OF INITIAL DRY DENSITY VARIATION IN 1-D STATIC COMPACTION ON UNSATURATED SOILS

Refer to the numerical investigations in Section 6.2, the random distribution arrangement of the dry density which is normally distributed with SD 0.1 and $\overline{\rho_d}$ 1.5 g/cm^3 results in insignificant variation of average dry density after compaction among their group. Therefore, in this section, the random arrangement of the dry density which was normally distributed with the prescribed SD (Figure 6-12) by keeping the same M_s 150 g, M_w 33 g and $\overline{\rho_d}$ 1.5 g/cm^3 for w_n 22%as defined in Section 6.1 were statically compacted in 1-D to investigate the effect of initial dry density variation in 1-D static compaction on unsaturated soils.

6.3.1 Variations of initial dry density in the heterogenous soil sample

The normal distribution of dry density in the heterogenous soil sample of SD 0.01, 0.05, 0.08, 0.10 and 0.117 were set in order to investigate the effect of variation of initial dry density to the compacted soil when the equivalent initial dry density, M_s and M_w were kept constant. The random arrangement of initial states of numerical simulation in form of meshed element including prescribed specific volume, degree of saturation and pore water pressure of SD 0.05 and 0.01 are illustrated in Figure 6-15(a) and Figure 6-15(b) respectively, as representatives. While, the meshing for numerical simulation with the random arrangement of SD 0.01 are illustrated in Figure 6-6(b).

6.3.2 Numerical results of compaction

The different variations of dry density in the heterogenous soil samples were statically compacted in 1-D by the displacement control at the top surface of the sample until approaching the fully saturated state. The displacement rate was controlled at 0.001 mm/s to allow the local drainages as previous described. Stress – strain at the top surface of the sample, average dry density – the applied vertical compaction stress and percent difference of compacted dry density – variation of initial dry density of vertical applied stress 200 kPa are plotted in Figure 6-13(a), Figure 6-13(b) and Figure 6-14, respectively. In addition, the results of numerical simulation in form of meshed element including the specific volume, degree of saturation and pore water pressure at applied vertical compaction stress 200 kPa and the saturated state of 1R22-SD0.05 and 1R22-SD0.01 are illustrated in Figure 6-15(a) and Figure 6-15(b) respectively. While, the results of numerical simulation in form of meshed element of 1R22-SD0.10 are illustrated in Figure 6-6(b).

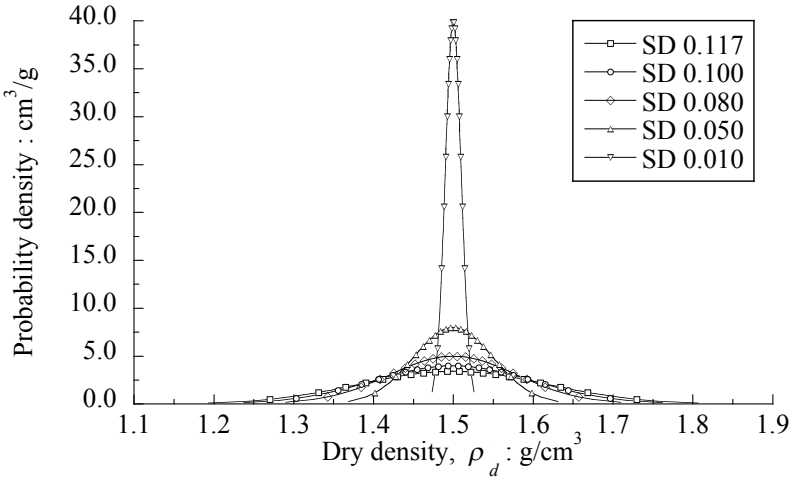

Figure 6-12 Variations of dry density in heterogenous soil samples

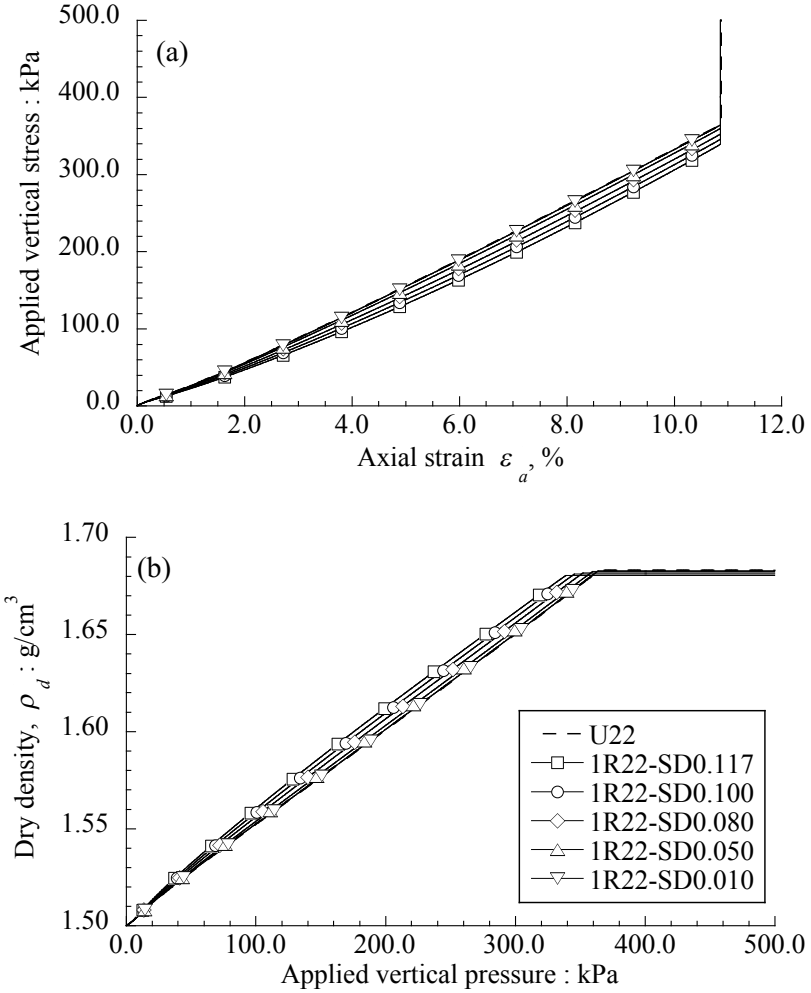

Figure 6-13 Comparisons of (a) stress – strain relationship at the top surface and (b) average dry density of compacted soil between homogenous soil sample and heterogenous soil samples (SD 0.1117, 0.100, 0.080, 0.050 and 0.010)

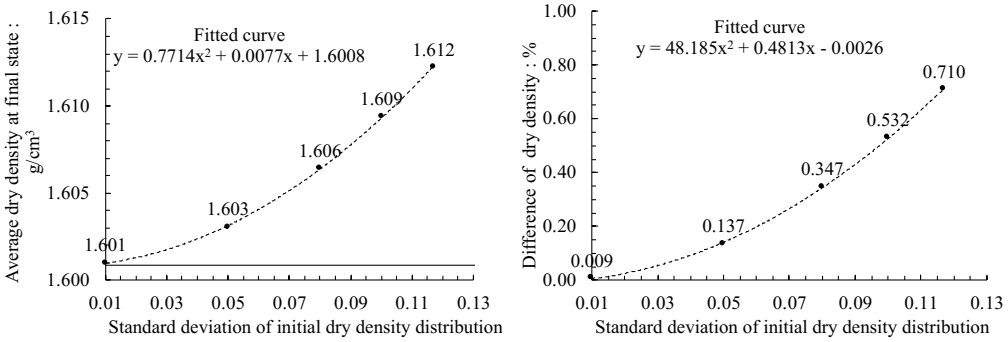

Figure 6-14 Difference of compacted dry density with variation of initial dry density for applied vertical stress 200 kPa

6.3.3 Effect of initial dry density variation distribution to the properties of compacted soils

In the comparison of the average dry density between the variations of initial dry density distribution in heterogenous soil samples as shown in Figure 6-13(b) and Figure 6-14, we found that the average dry density at a given applied vertical compaction stress of higher variation of initial dry density (or higher SD) significantly deviated from the homogenous case (U22) in the denser side. On the other hands, average dry density after compaction in the case of low variation of initial dry densities (e.g., 1R22-Sd0.01) closed to the dry density of homogenous soil sample (U22). However, at the saturated state, average dry density was not affected by the variation of dry density as long as every element were uniformly approached the saturated state.

6.4 CHARACTERISTICS OF COMPACTION CURVE OF HETEROGENOUS UNSATURATED SOIL

In this section, the effect of compaction water content along the compaction curve to the characteristic of compaction curve considering the effect of initial heterogeneity was investigated. Refer to the numerical investigations in Sections 6.2 and 6.3, in order to avoid the effect of arrangement and clarify the effect of the heterogeneity, the random arrangement of the dry density which was normally distributed with SD 0.1 and $\overline{\rho_d}$ 1.5 g/cm^3 was selected for the investigation of characteristics of the compaction curve in this section. By keeping, $\overline{\rho_d}$ 1.5 g/cm^3 and M_s 150 g, the variations of compaction water content w_n of the heterogenous soil sample along the compaction curve were controlled by the variation of M_w.

6.4.1 Variations of compaction water content along the compaction curve

First, the elementary compaction curves of homogenous soil sample were generated. The similar initial dry density 1.5 g/cm^3 was controlled by setting an identical initial void ratio e_0 0.782. Compaction water contents were varied in the prescribed range then the initial degree of saturations S_{r0} of each w_n in the range were calculated by Equation (4-2). Assuming that pore

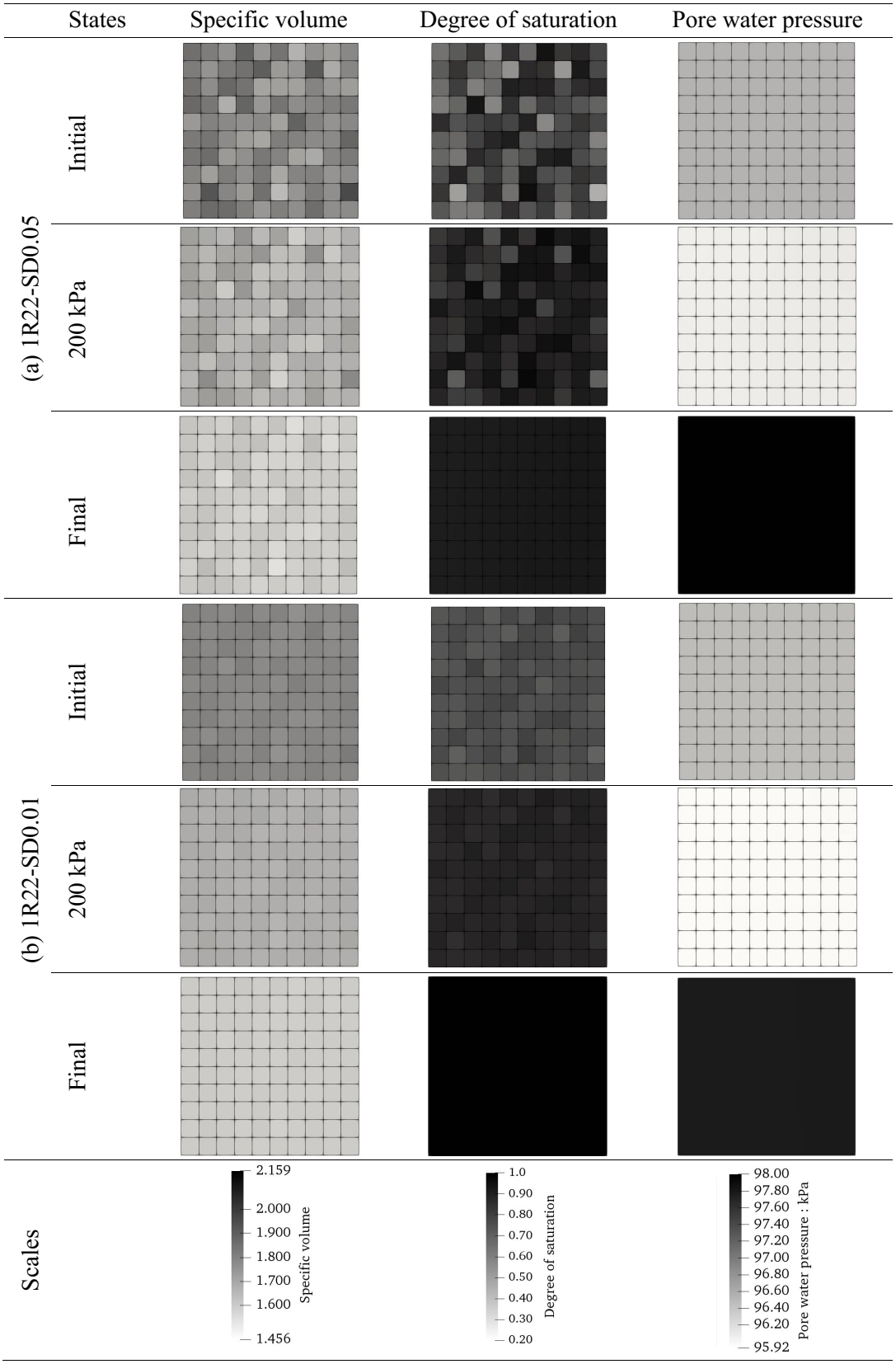

Figure 6-15 Numerical simulation results (meshed element) including v, S_r and u_w of the initial, applied vertical pressure 200 kPa and saturated states for cases (a) 1R22-SD0.05 and (b) 1R22-SD0.01

air pressure u_a 98.0 kPa (atmospheric pressure) and the soil was compacted on the main wetting curve (I_h = 0), pore water pressure u_w could be calculated by Equation (2-6) for each w_n. Initial isotopic total stress was 118.0 kPa in the simulation. The soil elements were statically compacted in 1-D by the vertical stress control to the applied vertical compaction stress 100 kPa, 200 kPa and 300 kPa. The convex-upward compaction curves with maximum dry densities and optimum water content were numerically generated, and their transition due to compaction stress were generated as shown in Figure 6-17.

From the compaction curve which was generated in the elementary simulation Figure 6-17, the compaction water content w_n 22%, 24% and 25% were selected as the representative of compacted soil on the dry side of optimum (1R22), optimum water content (1R24) and wet side of optimum (1R25) of the compaction curve at applied vertical compaction stress 200 kPa in the numerical investigation of the heterogenous soil samples (the random arrangement of the dry density which was normally distributed with SD 0.1 and $\overline{\rho_d}$ 1.5 g/cm^3). By keeping, $\overline{\rho_d}$ 1.5 g/cm^3 and M_s 150 g, the M_w were adjusted to be 33 g, 36 g and 37.5 g for w_n 22%, 24% and 25%, respectively. The random initial states of numerical simulation in form of meshed element including prescribed specific volume, degree of saturation and pore water pressure of 1R24 and 1R25 are illustrated in Figure 6-16(a) and Figure 6-16(c) respectively. While, the random initial state of numerical simulation in form of meshed element of 1R22 are illustrated in Figure 6-6(b).

6.4.2 Numerical results of compaction

With the same arrangement and variation of initial dry density, the variation of water content 22%, 24% and 25% in the heterogenous soil samples were investigated. They were statically compacted in 1-D by the displacement control at the top surface of sample until approaching the fully saturated state. The displacement rate was controlled at 0.001 mm/s to allow the local drainages as previous described. The average dry density after compaction of each compaction water content along the compaction curve at the vertical compaction stresses 100 kPa, 200 kPa and 300 kPa are illustrated in the Figure 6-17. Figure 6-16(a) and Figure 6-16(b) show the numerical investigation results when the heterogenous soil samples 1R24 and 1R25 were compacted to the saturated state, respectively. While, the numerical investigation results with the random arrangement of 1R22 are illustrated in Figure 6-6(b).

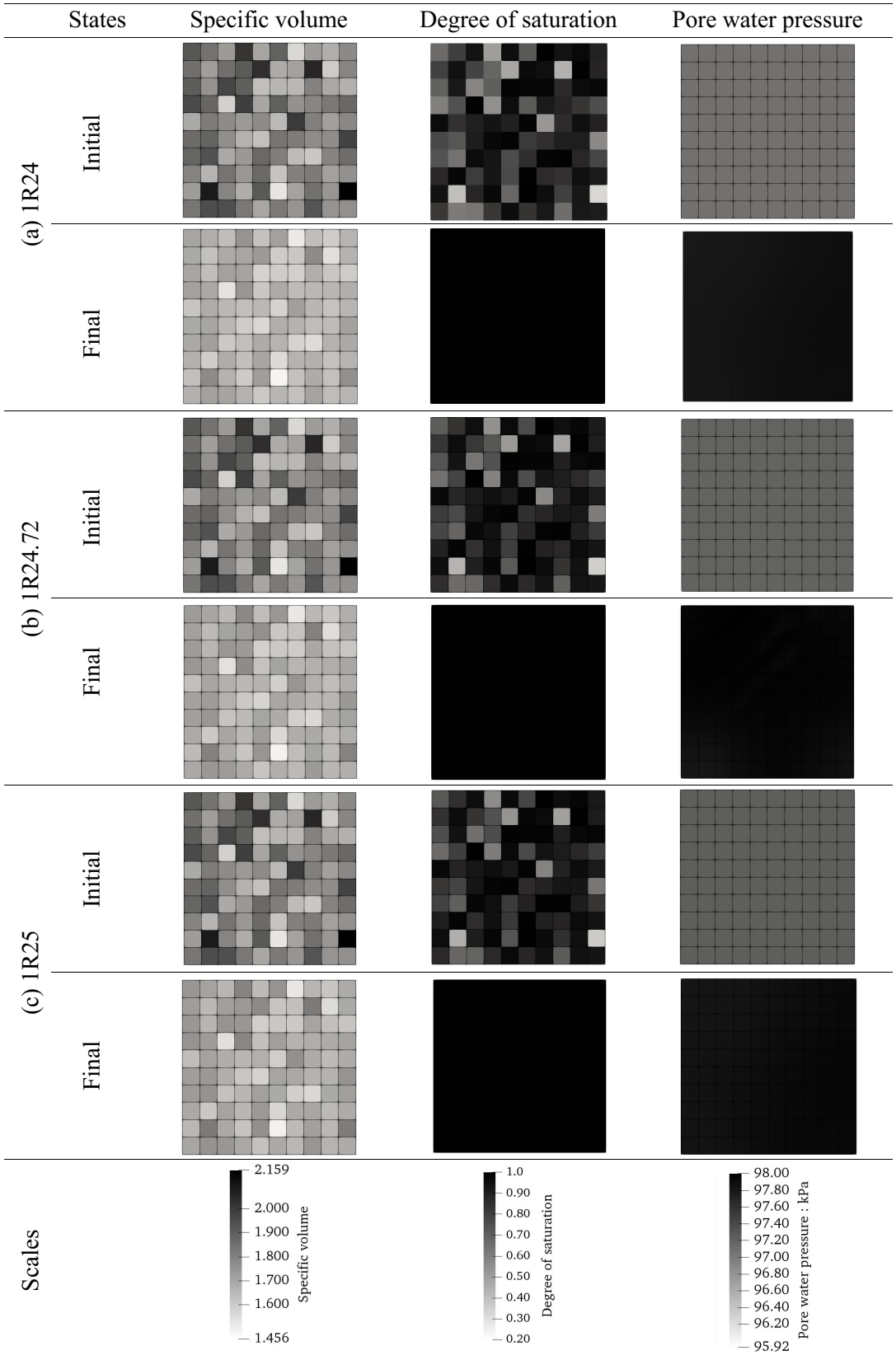

Figure 6-16 Numerical investigation results of heterogenous soil sample (a) w_n = 24% and (b) w_n = 24.72% and (c) w_n = 25% including the specific volume, degree of saturation and pore water pressure, at initial state and saturated state

6.4.3 Characteristics of compaction curve of heterogenous unsaturated soil

From Figure 6-17, at a given applied vertical compaction stress, the average dry density of heterogenous compacted soil is higher than the homogenous soil sample on the dry side of compaction. However, at the optimum water content and wet side of compaction, the dry densities were limited by the incompressibility of soils due to the approaching of saturated state. Consequently, considering the effect of the initial heterogenous dry density with the similar applied vertical compaction stress, the moving of typical compaction curves to the upper left was observed in the numerical investigation.

In addition, the effect of heterogeneity at the initial state to the behavior of compacted soil on the dry side and wet side at the same degree of compaction were also investigated in this section. Since the typical compaction curve moves to the upper left part, so we added the random arrangement case 1R24.72 on the wet side of compaction which provides the same degree of compaction as 1R22 on the dry side at the applied vertical stress 200 kPa. By keeping, $\overline{\rho_d}$ 1.5 g/cm^3 and M_s 150 g, the M_w was adjusted to be 37.08 g for w_n 24.72%. It was statically compacted in 1-D by the displacement control at the top surface of sample until 200 kPa or approaching the fully saturated state with the displacement rate 0.001 mm/s. The average dry density after compaction of 1R24.72 at the applied vertical compaction stresses 200 kPa is illustrated as point a in Figure 6-18. At the same degree of compaction, the effect of heterogeneity at the initial state to the behavior of compacted soils could be explained by the current variation of dry density of compaction as shown in Figure 6-18. The distribution curve and variation of SD of element dry density during compaction reveal that the soils compacted on the wet side provided lower variation of dry density than the dry side after compaction at the same degree of compaction. Since the initial element dry densities of cases 1R22 and 1R24.72 are similar, therefore the small variation and high magnitude of initial degree of saturation on the wet side results in the low heterogeneity of element dry density after compaction. The heterogenous soil on the wet side could compacted easily even under the low compaction effort as reflected by the skewness of element dry density during the compaction (Figure 6-18). Moreover, in Figure 6-18, at the final point of compaction point c and point b′ of the difference compaction water content 1R22 and 1R24.72, respectively, the optimum water content for each compaction effect was observed. It reveals that aiming to compact the initial heterogenous soil sample at the optimum water content, higher compaction effort results in low variation of final dry density after compaction.

In conclusion, the compaction water content affects the material heterogeneities of the compacted soil. At the same degree of compaction, the soil which is compacted on the wet side

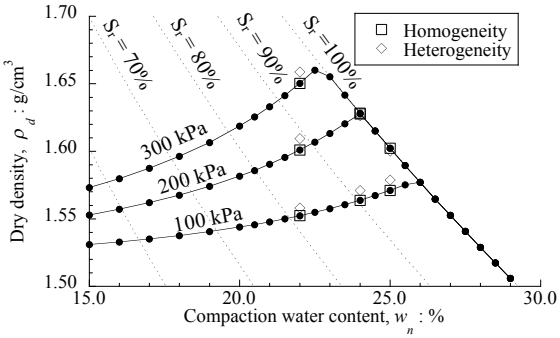

Figure 6-17 Effect of heterogeneities of dry density and degree of saturation to the characteristic of compaction curve

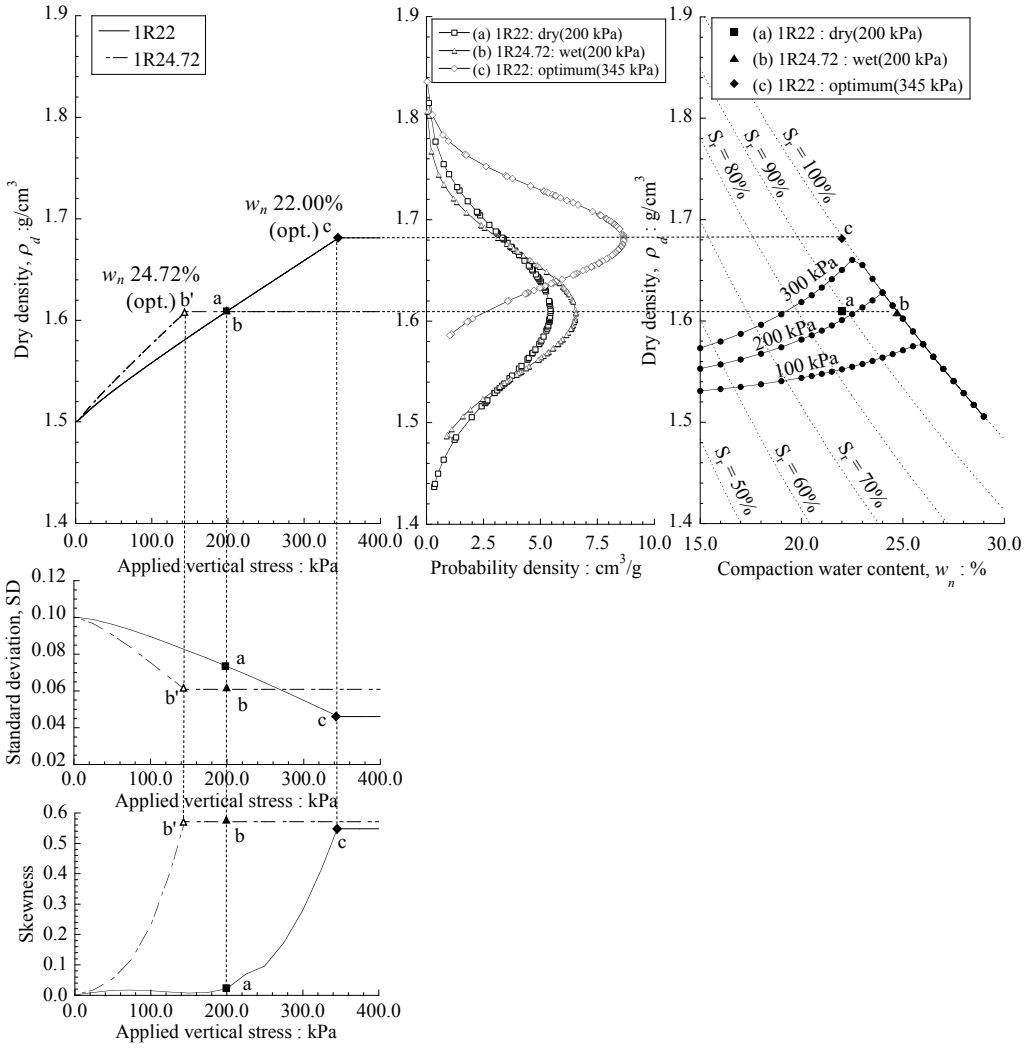

Figure 6-18 Variations of element dry density distributions of heterogenous soil samples considering the effect of compaction water content on 1R22 and 1R24.72

are numerically observed the low heterogeneity effect. In addition, at the optimum water content, higher compaction effort results in low variation of final dry density. Therefore, the appropriate specifications of compaction water content and compaction effort are the optimum

water content and high compaction effort. By this specification, the effect of heterogeneity after compaction to the strain localization behavior of compacted soil when subjected to loadings could be alleviated.

6.5 IMPLEMENTATION THE EFFECT OF HETEROGENEITY TO THE COMPACTION QUALITY CONTROL

Using the numerical investigation results from Sections 6.1 through 6.4, we could implement them in order to provide the recommendation of the quality control of soil preparation for compaction test which affects the field work procedure, design process and cost and planning management of the embankment construction.

Controlling the field work of soil compaction, the compaction control parameter including optimum water content, maximum dry density and compaction effort are generated for the fill material by performing the compaction test in the laboratory. From the numerical investigation, we found that the heterogeneity of initial dry density and degree saturation of the sample affect the average dry density of compacted soil. In this section, refer to the investigation result, we can conclude that controlling the quality of sample preparation before compaction could control the properties and strength of compaction in the construction and design process to be safe as following discussion.

6.5.1 Case A: Well preparing of the fill material for compaction test

In this section, following discussions about the effect of preparing fill material for compaction test in laboratory and field compaction are illustrated in Figure 6-19.

In the stage of sample preparing for compaction test in laboratory, the fill material is dried and pounded, then it is sieved to filter out the large soil sample and mixed well with water. By this process, the prepared sample has the small variation of initial dry density and degree of saturation in the compaction mold. For this case, in the theoretical thinking, the well-prepared sample is homogenous soil sample. From the numerical investigation result of homogenous sample (Figure 6-13), with the effect of variation of heterogeneity, the minimum dry density can be observed from the compaction test.

In the field compaction, using the compaction control parameter from the laboratory testing result, the initial proportions of dry soil mass and water mass is controlled. However, in the field, the small variation of soil sample is hardly prepared like in the laboratory (Case I: poor preparing). At the controlled optimum water content and compaction effort, in case of the well-prepared sample in laboratory test, similar average dry density and degree of saturation could be observed in the field compaction due to the approaching of saturated state. This statement is referred from the numerical investigation result considering the effect of

compaction water content on the heterogeneity (Figure 6-17). This result is on the assumptions that the compaction energy is completely transferred to any depth of the soil and the soils is compacted without unloading after compaction. By this result, refer to the parametric study of compacted soil in Chapter 4, the strength before and after soaking, magnitude of compression collapse and liquefaction resistant of field compaction are confirmed to be similar to the properties that used in the design process.

In conclusion, the coupled FEM for unsaturated soils could perform the numerical investigation considering the effect of heterogeneity in the initial stage of compaction. From the results, we can conclude that well preparing of the fill material for compaction test in laboratory could efficiently control the properties and strength of compacted soil in the construction design and management (cost and planning).

However, even the degree of saturation is uniformly distributed in the soil sample when the soil is compacted at the optimum water content, but the heterogeneity of the density is still remained. Refer to the study of Song (2017), they found that the heterogeneity of density causes the localization failure. Therefore, using the coupled FEM considering the effect of heterogeneity proposed in this study is still necessary to predict the strength of compacted soil with the effect of localization in the future study.

6.5.2 Case B: Poor preparing of the fill material for compaction test

In this section, following discussions about the effect of preparing fill material for compaction test in laboratory and field compaction are illustrated in Figure 6-20.

In the case of the fill material is poorly prepared in the stage of sample preparing for compaction test in laboratory. The prepared sample have the large variation of initial dry density and degree of saturation in the compaction mold. By the assumption that the soil is randomly mixed, from the numerical investigation result of heterogenous sample (for example SD 0.1 in Figure 6-13), with the effect of variation of heterogeneity, the higher dry density can be observed from the compaction test. Especially, the heterogenous compaction curves slide to the upper left.

In the field compaction, using the compaction control parameter from the laboratory testing result, the initial proportions of dry soil mass and water mass is controlled. Since the variation of prepared soil sample could not completely control in the field. Therefore, two extreme possibilities of heterogeneity variation could be occurred. If the variation of prepared sample in the field (random distribution) is higher than the laboratory (Case I, Figure 6-20), the result shows the same tendency as Case A (Section 6.5.1). However, if the variation of prepared

soil sample in the field is smaller than in the laboratory (Case II, Figure 6-20), uncertainty in the design and its effect to the construction management could be occurred.

6.5.2.1 Small variation of prepared soil sample in the field or similar to the laboratory preparing (Case II, Figure 6-20)

At the controlled optimum water content and compaction effort, in case of the poor-prepared sample in laboratory test, average dry density is lower than the expected dry density in the laboratory. Especially, the compacted soil is observed on the dry side of compaction when using the optimum compaction water content from the laboratory test. These statements are referred from the numerical investigation result considering the effect of compaction water content on the heterogeneity (Figure 6-17).

By this result, limiting the compaction effort and compaction water content by compaction control parameter, the designer engineer has to reduce the strength and liquefaction resistance in the design due to the lower compacted dry density. Moreover, the magnitude of compression collapse is higher than expectation of designer for the design at the optimum water content. Finally, even the strength after soaking of soil compacted in the dry side of optimum without unloading after compaction is insignificant but it is significantly reduced for unloading case. These statements are referred from the parametric study of compacted soil in Chapter 4.

In conclusion, the coupled FEM for unsaturated soil could perform the numerical investigation considering the effect of heterogeneity in the initial stage of compaction. From the results, we can conclude that engineer need to reduce the efficiency of compacted soil and overestimate the serviceability in the heavy rainfall case. The strength of the soil structure needs to be reduced just because the poor preparing of the fill material in the compaction laboratory test. This significantly affects to the construction management (cost and planning) in each project. However, followings discuss about the recommendation in order to achieve the required dry density using the coupled FEM for unsaturated soil considering the effect of heterogeneity.

6.5.2.1.1 Increasing compaction effort but keeping compaction water content as compaction control parameter

In order to achieve the target dry density as specified in the compaction control parameter, with the constant compaction water content, the compaction effort must be increased. By this process, although the strength and serviceability are not changed in the design, but it consumes higher cost and time in the construction.

6.5.2.1.2 Variation compaction water content and keeping compaction effort by compaction control parameter

By keeping the compaction effort, the 100% of target dry density could not be reached by the limit of incompressibility of soil in the saturated state. Using the numerical investigation result, we could recommend that adding compaction water content is the way to increase the dry density and there is no bad effect of the compaction on the dry side of optimum.

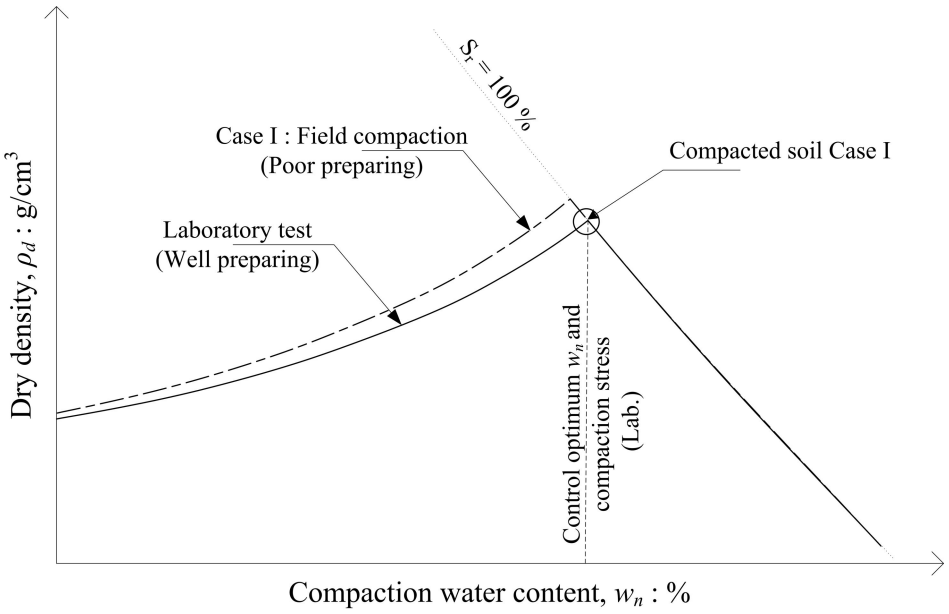

Figure 6-19 Implementation the effect of heterogeneity to the compaction quality control (Case A)

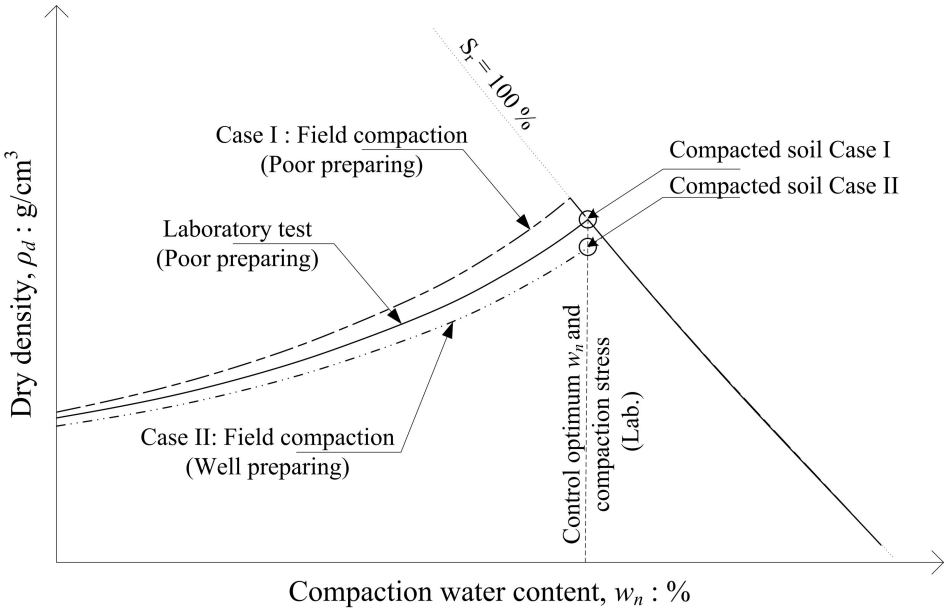

Figure 6-20 Implementation the effect of heterogeneity to the compaction quality control (Case B)

6.6 CONCLUSION

From the numerical investigations of 1-D static compaction considering effect of heterogeneity, the material heterogeneities at the initial state including dry density and degree of saturation affect the average dry density at any considering stage of compaction excluding in the saturated state. Specified the appropriate compaction control parameter, high compaction effort and wet side of compaction or optimum water content, the effect of heterogeneity after compaction to the strain localization behavior of compacted soil when subjected to loadings could be alleviated.

In addition, we could implement the effect of heterogeneity to the compaction quality control. Well preparing of the fill material for compaction test could reduce the risk of 1) strength reduction of compacted soil from the design planning; 2) increasing of cost and time in the compaction and 3) the increasing of collapse compression magnitude from the expectation in the design. This recommendation conforms with the specification in many standard methods of test for compaction, such as AASHTO T 180 and ASTM D 1557 for modified compaction test. In the testing standard, the well preparing of the fill material by filtering out of some large soil sample is also specified. In addition, from the numerical investigation, compaction on the wet side of optimum is recommend.

Although the recommendations are provided, using the coupled FEM for unsaturated soil considering the effect of heterogeneity proposed in this study is still necessary to predict the strength of compacted soil with the effect of localization in the future study. In the future, using the coupled FEM for unsaturated soil, we are able to utilize the full strength and serviceability of the compacted soils that the on-site fill material could be provided by control the variation of soil density in laboratory to be similar to the variation of soil density in the field. The effects of heterogeneity on 1-D static compaction mechanism could be investigated.

CHAPTER 7

CONCLUDING REMARKS AND FUTURE RESEARCH

7.1 SUMMARY OF CONCLUSION

In this study, the critical state constitutive model for unsaturated compacted soil was proposed and validated. By the proposed model, the behaviors of soil structure were predicted from compaction through a series of simulation from the beginning of compaction process through its failure. The effect of compaction water content and compaction effort on the characteristic behavior of unsaturated compacted soil were investigated. Then, the responses of unsaturated compacted soil under the considered loads which rely on its characteristic after compaction were also interpreted.

From the simulation result, we found that the proposed constitutive model for unsaturated soils could predict well the coupled hydro-mechanics behavior of compaction. The simulation results reveal that the compaction water content affects the behavior of compacted soil including characteristic of compaction curve, hydraulic collapse, shear strength and liquefaction resistance of compacted soil through the degree of saturation and dry density. Following typical behaviors of compacted soil could be properly generated by the proposed constitutive model for unsaturated soils. All the tendencies simulated by the proposed model are correspondence with the experimental results reported by many researchers.

1) Regarding the mechanism of compaction, the convex-upward curves with maximum dry density and optimum water content for various soil types and their transition due to compaction stress were properly predicted.
2) Regarding the shear behaviors under fully drained static monotonic shearing, compaction water content, compaction effort and remained confining pressure after compaction affect the peak strength of the compacted soil both before and after soakings. The difference between the strength of compacted soil before and after soaking of the compacted specimens along the compaction curve could be observed from the simulations. For the before soaking case, the peak strength of soils compacted dry of optimum is higher than the soils compacted wet of optimum. While at the same time, for the after soaking case, the peak strength of soils compacted dry of optimum is significantly decreased from the magnitude of before soaking. The tendency of the peak strength after soaking with the various compaction water content is similar to the tendency of compaction curve. At the optimum water

content, the maximum peak strength after soaking provides the small amount of volumetric change due to soaking.

3) Regarding the liquefaction behavior of compacted soil, the liquefaction resistance is very high in the dry side of compaction curve which is dominantly affected by degree of saturation. When the water contents are approached the optimum water content or higher, combined effect of degree of saturation and dry density on liquefaction resistance could be seen. The tendency of liquefaction resistance is independent of the compaction effort. Lastly, the compaction effort significantly affects the liquefaction resistance at low water content and the effect gradually decreases when water content increases.

In addition, the capability of the constitutive model was utilized for the soil-water-air three-phases seepage-deformation coupled FEM based on the assumptions of 2-D plain strain condition and passive air pressure for the unsaturated porous media. The in-house FEM program was used to investigate the behavior of soil structure from the compaction considering the non-uniformity of substance soil which certainly find in the real condition of geotechnical work.

From the numerical investigations of 1-D static compaction considering effect of heterogeneity, the material heterogeneities at the initial state including dry density and degree of saturation affect the average dry density at any considering stage of compaction excluding in the saturated state. By the appropriate specification of compaction control parameter, high compaction effort or wet side of compaction or optimum water content, the effect of heterogeneity after compaction to the strain localization behavior of compacted soil when subjected to loadings could be alleviated. In addition, we could implement the effect of heterogeneity to the compaction quality control. Well preparing of the fill material for compaction test could reduce the risk of 1) strength reduction of compacted soil from the design planning; 2) increasing of cost and time in the compaction and 3) the increasing of collapse compression magnitude from the expectation in the design. This recommendation conforms with the specification in many standard methods about the soil preparation for the compaction test.

All in all, we recommend that soil compacted at the optimum water content is suitable for the compacted soil confronted with the heavy rainfall and subjected to the static monotonic shearing. This is because the highest peak strength, the minimum volumetric changes and low coefficient of permeability after soaking are observed. In case of the optimum water content could not be reached in the compaction process, the soil shall be compacted on the wet side of

optimum to prevent the highly collapse compression due to soaking for the serviceability of the embankment. In addition, aiming to achieve the optimum water content is also the rational way to increase the liquefaction resistance of the unsaturated compacted soil. Moreover, specification of the appropriate compaction control parameter, selecting high compaction effort or compaction water content on the wet side or at the optimum, the effect of heterogeneity after compaction to the starin localization behavior of compacted soil when subjected to loadings could be alleviated. Importantly, engineer can specify the optimum compaction control parameters in the construction for the considered range by the simulation of the proposed model and the numerical analysis.

7.2 FUTURE RESEARCH

Although the recommendations for compaction are provided for alleviating the heterogeneity of compacted soil, using the coupled FEM for unsaturated soil considering the effect of heterogeneity proposed in this study is still necessary to predict the strength of compacted soil in order to improve the efficiency and quality of the construction of soil structures. Therefore, for the future research, the ideas of improvement are listed below;

1) Using the coupled FEM for unsaturated soil together with the soil gradation that related to the heterogeneity of substance soil in the field, we could utilize the full strength and serviceability of the compacted soils in the field by control the variation of soil density in laboratory to be similar to the variation of soil density in the field.
2) Prediction of the mechanical behaviors of compacted soil e.g., the shear behavior, the soaking behavior and the permeability of soil considering the effect of heterogeneity of soil from the initial state.
3) Development of the soil-water-air three-phases seepage-deformation coupled FEM with the assumption of active air pressure, the behavior of fully undrained condition, liquefaction resistance, of the compacted soil is going to be achieved by the numerical simulation.

REFERENCES

Alonso, E., Gens, A., & Hight, A. (1987). Special problems soils. *General Report, Proceedings 9th European Conference on Soil Mechanics and Foundation Engineering*, (pp. 1087-1146). Dublin 3, Balkema.

Alonso, E., Pinyol, N. M., & Gens, A. (2013). Compacted soil behaviour: initial state, structure and constitutive modelling. *Géotechnique*, 134.

Babuska, I. (1971). Error bounds for finite element methods. *Numer. Math. 16*, 322-333.

Babuska, I. (1973). The finite element method with Lagrangian multipliers. *Numer. Math. 20*, 179-192.

Barden, L., & Pavlakis, G. (1971). Air and water permeability of compacted unsaturated cohesive soil. *Soil Science Journal, 22*(3), 302-317.

Bell, J. R. (1956). Plastic moisture barriers for highway subgrade protection. *MSCE Thesis.* West Lafayette, Indiana: Purdue University.

Bishop, A. W. (1959). The principle of effective stress. *Tecnisk Ukeblad, 39*, 859-863.

Bishop, A. W., Alpan, I., Blight, G. E., & Donald, I. B. (1960). Factors controlling the strength of partly saturated cohesive soils. *Conference Shear Strength Cohesive Soils* (pp. 503-532). New York: American Society of Civil Engineers.

Bishop, A., & Donald, I. (1961). The experimental study of partly saturated soil in the triaxial apparatus. *Proceedings of 5th International Conference on Soil Mechanics and Foundation Engineering*, (pp. 13-21). Paris.

Borja, R., & Song, X. (2014). Strain localization in porous materials with spatially varying density and degree of saturation. *Computer Methods and Recent Advances in Geomechanics*, 13.

Brezzi, F. (1974). On the existence, uniqueness and approximation of saddle-point problems arising from Lagrange multipliers. *R.A.I.R.O. 8 (R-2)*, 129-151.

Cox, D. W. (1978). Volume change of compacted clay fill. *Clay fills* (pp. 79-86). London: Institution of Civil Engineers.

Dafalias, Y. F., & Popov, E. P. (1975). A model of nonlinearly hardening materials for complex loading. *Acta Mechanica, 21*(3), 173-192.

Essigmann, M. F. (1976). An examination of the variability resulting from soil compaction. *MSCE Thesis,.* West Lafayette, Indiana: Purdue university.

Fredlund, D. G. (2006). Unsaturated soil mechanics in engineering practice. *Journal of Geotechnical and Geoenvironmental Engineering, 132*(3), 286-321.

Gallipoli, D., Gens, A., Sharma, R., & Vaunat, J. (2003). An elasto-plastic model for unsaturated soil incorporating the effects of suction and degree of saturation on mechanical behavior. *Géotechnique, 53*(1), 123-135.

Gallipoli, D., Wheeler, S. J., & Karstunen, M. (2003). Modelling the variation of degree of saturation in a deformable unsaturated soil. *Géotechnique, 53*(1), 105-112.

Geiser, F., Laloui, L., & Vulliet, L. (2006). Elasto-plasticity of unsaturated soils: laboratory test results on a remoulded silt. *Soils and Foundations, 46*(4), 545-556.

Gibbs, H. J., Hilf, J. W., Holtz, W. G., & Walker, F. C. (1960). Shear Strength of Cohesive Soils. *Proceedings of the Research Conference on Shear Strength of Cohesive Soils* (pp. 819-836). Boulder: ASCE.

Griffiths, D. V. (1980). Finite element analyses of walls, footing and slopes. *PhD thesis.* Department of Engineering, University of Manchester.

Griffiths, D. V. (1982). Computation of bearing capacity factors using finite elements. *Geotechnique, 32*(3), 195-202.

Hashiguchi, K., & Ueno, M. (1977). Elastoplastic constitutive laws of granular material. *Proceedings of the 9th International Conference on Soil Mechanics and Foundation Engineering*, (pp. 73-82). Tokyo.

Holtz, W. G., & Gibbs, H. J. (1956). Engineering Properties of Expansive Clays. *Transactions of the American Society of Civil Engineers, 121*(1), 641-663.

Honda, M. (2000). *PhD Thesis.* Kobe, Japan. (in Japanese): Kobe university.

Hughes, T. J. (1980). Generalization of selective integration procedures to anisotropic and non-linear media. *International Journal for Numeriacal Methods in Engineering, 15*(9), 1413-1418.

Hughes, T. J. (1987). *The Finite Element Method Linear Static and Dynamic Finite Element Analysis.* New York: Dover.

Hughes, T. J., Cohen, M., & Haroun, M. (1978). Reduced and selective integration techniques in the finite element analysis of plates. *Nuclear Enginnering and Design 46*, 203-222.

Jennnings, J., & Burland, J. B. (1962). Limitations to the use of effective stresses in partly saturated soils. *Ge´otechnique, 12*, 125-144.

Johnson, A. W., & Sallberg, J. R. (1960). Factors that influence field compaction of soils. *Highway Research Board Bulletin*, 272.

Kawai, K., Phommachanh, V., Kawakatsu, T., & Iizuka, A. (2016). Explanation of dry density distribution induced by compaction through soil/water/air coupled simulation. *The 3rd International conference on Transportation Geotechnics* (pp. 276-283). Elsevier B.V.

Kawai, K., Phommachanh, V., Sakamoto, S., & Iizuka, A. (2014). Compaction simultion with soil/water/air coupled FEA code and parametric study. *Proceedings of the Sixth International conference on Unsaturated Soils* (pp. 545-552). London: Taylor & Francis Group.

Kawai, K., Shibata, M., Ohtsuki, T., Phommachanh, V., Kanazawa, S., & Iizuka, A. (2012). Simulations of static compaction with soil/water/air coupled F.E. analysis. *Proceedings of the Second European conference on Unsaturated Soils* (pp. 181-187). Napoli, Italy: Springer.

Khalili, N., Witt, R., Laloui, L., Vulliet, L., & Koliji, A. (2005). Effective stress in double porous media with two immiscible fluids. *Geophysical Research Letters, 32*(15), 15309.

Khun, H. W., & Tucker, A. W. (1951). Nonlinear programming. *Proceedings of 2nd Berkeley Symposium* (pp. 481-492). Berkeley: University of Califirnia Press.

Kikumoto, M., Kyokawa, H., Nakai, T., & Shahin, H. M. (2010). A simple elastro-plastic model for unsaturated soils and interpretations of collapse and compaction behaviours. In E. Alonso, & A. Gens (Ed.), *Proceeding of 5th International Conference on Unsaturated Soils*, (pp. 849-855). Barcelona.

Koga, K. (1991). *Soil compaction in agricultural land development.* Asian Institute of Technology.

Koike, M. (2010). *不飽和土の締固め特性と浸水挙動 (Compaction charateristic and soaking behavior of unsaturated soil, Master thesis).* Nagoya Institute of Technology.

Komolvilas, V. (2017). Fundamental study of liquefaction and hydraulic collapse of unsaturated soils. *Ph. D. Thesis.* Graduated School of Urban Innovation, Yokohama National University.

Komolvilas, V., & Kikumoto, M. (2017). Simulation of liquefaction of unsaturated soil using critical state soil model. *nternational Journal for Numerical and Analytical Methods in Geomechanics, 41*, 1217-1246.

Lambe, T. W. (1958). The structure of compacted clay. *Journal of the Soil Mechanics and Foundations Division, 84*(SM2), 1655-1 - 1655-35.

Lambe, T. W. (1960). A mechanistic picture of shear strength in clay. *Proceedings of the Research Conference on Shear Strength of Cohesive Soils.* Colorado: ASCE.

Lambe, T. W., & Whitman, R. V. (1969). *Soil Mechanics.* New York: Wiley.

Leonards, G. A. (1955). Strength characteristics of compacted clays. *Transaction of American Society of Civil Engineers, 120*, 1420-1454.

Likos, W. J., Song, X., Xiao, M., Cerato, A., & Lu, N. (2019). Fundamental challenges in unsaturated soil mechanics. *Geotechnical Fundamentals for Addressing New World Challenges*, 209-236.

Lu, N., & Khorshidi, M. (2015). Mechanisms for soil-water retention and hysteresis at high suction range. *Journal of Geotechnical & Geoenvironmental Engineering, 141*(8), 04015032.

Macneal, R. H. (1994). *Finite Element: their Deisgn and Performance.* New York: Marcel Dekker, Inc.

Marinho, F. A., Oliveira, O. M., Adem, H., & Vanapalli, S. (2013). Shear strength behavior of com- pacted unsaturated residual soil. *International Journal of Geotechnical Engineering, 7*(1), 1-9.

Marwick, A. (1945). *The basic principles of soil compaction and their application.* The Institution of Civil Engineers Engineering, Road Engineering Division.

Mesri, G., & Olson, R. E. (1971). Mechanisms controlling the permeability of clays. *Clays and Clay Minerals, 19*, 151-158.

Mountassir, G. E., Sanchez, M., & Romero, E. (2014). An experimental study on the compaction and collapsible behaviour of a flood defence embankment fill. *Engineering Geology, 179*, 132-145.

Nuth, M., & Laloui, L. (2008). Effective stress concept in unsaturated soils: Clarification and validation of a unified framework. *International Journal for Numerical and Aanlytical Methods in Geomechanics, 32*, 771-801.

Proctor , R. R. (1933). Fundamental principles of soil compaction. *Engineering News-Record, 111*(9), 286-289.

Rampino, C., Mancuso, C., & Vinale, F. (2011). Experimental behaviour and modelling of an unsaturated compacted soil. *Canadian Geotechnical Journal, 37*(4), 748-763.

Roscoe, K. H., & Burland, J. B. (1968). On the generalised stress-strain behaviour of "wet" clay. *Engineering plasticity* (pp. 535-609). Cambridge University Press.

Roscoe, K. H., Schofield, A. N., & Wroth, C. P. (1958). On the Yielding of Soils. *Géotechnique, 8*(1), 22-53.

Schrefler, B. A. (1984). The finite element method in soil consolidation (with applications to surface subsidence). *Ph. D. Thesis.* University Collage of Swansea.

Seed, H. B., & Chan, C. K. (1959). Structure and strength characteristics of compacted clays. *Journal of the Soil Mechanics and Foundations Division, 85*(SM5), 87-128.

Seed, H. B., & Monismith, C. L. (1954). Relationship between density and stability of subgrade soils. *Highway Research Board Bulletin, 93*, 16-32.

Seed, H. B., Mitchell, J. K., & Chan, C. K. (1960). The strength of compacted cohesive soils. *Proceedings of the Research Conference on Shear Strength of Cohesive Soils* (pp. 877-964). Reston, VA: ASCE.

Simo, J. C., & Rifai, M. S. (1990). A class of mixed assumed strain methods and the method of incompatible modes. *International Journal for Numerical Methods in Engineering, 29*, 1595-1638.

Sivakumar, V. (1993). A critical state framework for unsaturated soils. *Ph.D. Thesis.* Sheffield: University of Sheffield.

Sivakumar, V., & Wheeler, S. J. (2000). Influence of compaction procedure on the mechanical behaviour of an unsaturated compacted clay. Part 1: Wetting and isotropic compression. *Géotechnique, 50*(4), 359-368.

Smith, C. C., Cripps, J. C., & Wymer, M. J. (1999). Permeability of compacted colliery spoil - a parametric study. *Engineering Geology, 53*, 187-193.

Smith, I. M., Griffiths, D. V., & Margetts, L. (2014). *Programming the Finite Element Method.* West Sussex, United Kingdom: Wiley.

Song, X. (2014). Strain localization in unsaturated porous media. *Ph.D. Thesis.* Standford University.

Song, X., Idinger, G., Borja, R. I., & Wu, W. (2012). Finite element simulation of strain localization in unsaturated soils. *Proceedings of the Second European Conference on Unsaturated Soils, E-UNSAT*, (pp. 189-195). Napoli, Italy.

Song, X., Ye, M., & Wang, K. (2017). Strain locaization in a solid-water-air system with random heterogeneity via stabilized mixed finite elements. *International Journal for Numerical Methods in Engineering, 112*, 1926-1950.

Sun, D. A., Cui, H. B., Matsuoka, H., & Sheng, D. C. (2007a). A three-dimensional elastoplastic model for unsaturated compacted soil with hydraulic hysteresis. *Soils and Foundations, 47*(2), 253-264.

Sun, D. A., Sheng, D. C., Cui, H. B., & Sloan , S. W. (2007b). A density-dependent elastoplastic hydro-mechanical model for unsaturated compacted soils. *International Journal for Numerical and Analytical Methods in Geomechanics, 31*, 1257-1279.

Sun, D. A., Sheng, D., & Xu, Y. (2007c). Collapse behaviour of unsaturated compacted soil with different initial densities. *Canadian Geotechnical Journal, 44*, 673-686.

Tadepalli, R., & Fredlund, D. G. (1991). The collapse behavior of a comapcted soil during inundation. *Canadian Geotechnical Journal, 28*, 477-488.

Taibi, S., Fleureau, J. M., Abou-Bekr, N., Zerhouni, M. I., Benchouk, A., Lachgueur, K., & Souli, H. (2011). Some aspects of the behaviour of compacted soils along wetting paths. *Géotechnique, 61*(5), 431-437.

Tarantino, A., & De Col, E. (2008). Compaction behaviour of clay. *Géotechnique, 58*(3), 199-213.

Tarantino, A., & Tombolato, S. (2005). Coupling of hydraulic and mechanical behavious in unsaturated compacted clay. *Géotechnique, 55*(4), 307-317.

Tatsuoka, F., & Shibuya, S. (2014). Several issues in the compaction of residential embankments. *Monthly Journal, the Foundation Engineering & Equipment (Kisoko), 42*(9), 17-23 (in Japanese).

Taylor, D. W. (1948). *Fundamentals of soil mechanics.* New York: Wiley.

Terzaghi, K., Peck, R. B., & Mesri, G. (1996). *Soil mechanics in engineering practice.* New York: Wiley.

Tsiampousi, A., Zdravkovic', L., & Potts, D. M. (2013). A three-dimensional hysteristic soil-water retention curve. *Ge´otechnique, 63*(2), 155-164.

Turnbull, W. J., & Foster, C. R. (1956). Stabilization of Materials by Compaction. *Journal of the Soil Mechanics and Foundation Division, 82*(SM2), 934-1 -1 934-23.

Unno, T., Kazama, M., Uzuoka, R., & Sento, N. (2008). Liquefaction of unsaturated sand considering the pore air pressure and volume compressibility of the soil particle skeleton. *Soils and Foundations, 48*(1), 87-99.

van Genuchten, M. T. (1980). A closed-form equation for predicting the hydraulic conductivity of unsaturated soils. *Soil Science Society of America Journal, 44*, 892-898.

Wheeler, S. J., & Sivakumar, V. (2000). Influence of compaction procedure on the mechanical behaviour of an unsaturated compacted clay. Part 2: shearing and constitutive modelling. *Géotechnique, 50*(4), 369-376.

Wilson, S. D. (1952). Effect of compaction on soil properties. *Proceedings of the Conference on Soil Sta- bilization* (pp. 148-161). M.I.T.

Yoder, E. J., & Witczak, M. W. (1975). *Principles of pavement design. 2nd Edition.* New York: John Wiley and Sons.

Zhang, B., Muraleetharan, K. K., & Liu, C. (2016). Liquefaction of unsaturated sand. *In ternational Journal of Geomechanics, 16*(6), D4015002.

Zhou, A., & Sheng, D. (2015). An advanced hydro-mechanical constitutive model for unsaturated soils with different initial densities. *Computers and Geotechnics., 63*, 46-66.

Zienkiewicz, O. C., Humpheson, C., & Lewis, R. W. (1975). Associated and non-associated viscoplasticity and plasticity in soil mechanics. *Ge'otechnique, 25*(4), 671-689.

Zienkiewicz, O. C., Taylor, R. C., & Zhu, J. Z. (2005). *The Finite Element Method : Its Basis and Fundamentals.* Oxford: Elsevier.

Zienkiewicz, O. C., Taylor, R. L., & Too, J. M. (1971). Reduced integration technique in general analysis of plates and shells. *International Journal for Numeriacal Methods in Engineering, 3*, 275-290.

RESEARCH PUBLICATIONS

Srinil, C., Kimumoto, M., & Komolvilas, V. (2019). Simulation on liquefaction of unsaturated compacted soils – effect of compaction degree –. *Proceedings of the 7th International Conference on Earthquake Geotechnical Engineering (ICEGE 2019),*(pp. 5095-5103). Rome, Italy. DOI: https://doi.org/10.1201/9780429031274

APPENDIX A

RATE FORM OF STRESS – STRAIN RELATIONSHIP FOR CONDUCTING THE ELEMENTARY TEST

A - 1 GENERAL FORM OF STRESS – STRAIN RELATIONSHIP FOR CONDUCTING THE ELEMENTARY TEST

The elastoplastic effective stress – strain relationship for unsaturated soil Equation (2-55) which is generated by the yield function is utilized for conducting the elementary analysis under the specified drainage condition for each application.

From Equation (2-4), the time derivative of Bishop's effective stress $\dot{\boldsymbol{\sigma}}''$ can be written as:

$$\dot{\boldsymbol{\sigma}}'' = \dot{\boldsymbol{\sigma}}^{net} + S_r \mathbf{1}\dot{s} + s\mathbf{1}\dot{S}_r \tag{A-1}$$

where $\dot{\boldsymbol{\sigma}}^{net}$ and $\dot{s}$ are the time derivatives of Cauchy's net stress tensor and suction, respectively.

Substituting Equation (A-1) into Equation (2-55) in order to incorporate the Bishop's effective stress into the stress – strain relationship as written by:

$$\dot{\boldsymbol{\sigma}}^{net} + S_r \mathbf{1}\dot{s} + s\mathbf{1}\dot{S}_r = \boldsymbol{D}^{ep} : \dot{\boldsymbol{\varepsilon}} - \boldsymbol{D}^{S_r}\dot{S}_r \tag{A-2}$$

From Equation (2-16), the time derivation of degree of saturation $\dot{S}_r$ derived from SWCC is rewritten by Equation (A-3), when $\dot{v} = -v_0 \mathbf{1} : \dot{\boldsymbol{\varepsilon}}$.

$$\dot{S}_r = \frac{\frac{\partial S_r}{\partial s}\dot{s} - \frac{\partial S_r}{\partial v} v_0 \mathbf{1} : \dot{\boldsymbol{\varepsilon}}}{1 - \frac{\partial S_r}{\partial I_h}\frac{dI_h}{dS_r}} \tag{A-3}$$

Then, the variation of degree of saturation by suction, including effect of density and hysteresis, are also included in the stress – strain relationship by substituting the time derivation of degree of saturation $\dot{S}_r$ (Equation (A-3)) into Equation (A-2) as written by:

$$\dot{\boldsymbol{\sigma}}^{net} + S_r \mathbf{1}\dot{s} + s\mathbf{1}\dot{S}_r = \boldsymbol{D}^{ep} : \dot{\boldsymbol{\varepsilon}} - \boldsymbol{D}^{S_r} \frac{\frac{\partial S_r}{\partial s}\dot{s} - \frac{\partial S_r}{\partial v} v_0 \mathbf{1} : \dot{\boldsymbol{\varepsilon}}}{1 - \frac{\partial S_r}{\partial I_h}\frac{dI_h}{dS_r}} \tag{A-4}$$

Then, Equation (A-4) can be rearranged as written by:

$$\dot{\boldsymbol{\sigma}}^{net} = \underbrace{\left\{ \boldsymbol{D}^{ep} + (\boldsymbol{D}^{S_r} + s\mathbf{1}) \otimes \frac{\frac{\partial S_r}{\partial v} v_0 \mathbf{1}}{1 - \frac{\partial S_r}{\partial I_h}\frac{dI_h}{dS_r}} \right\}}_{\boldsymbol{D}^{net}} : \dot{\boldsymbol{\varepsilon}} - \underbrace{\left\{ S_r \mathbf{1} + (\boldsymbol{D}^{S_r} + s\mathbf{1}) \frac{\frac{\partial S_r}{\partial s}}{1 - \frac{\partial S_r}{\partial I_h}\frac{dI_h}{dS_r}} \right\}}_{\boldsymbol{D}^{s}} \dot{s} \tag{A-5}$$

From Equation (A-5), the net stress – strain relationship for unsaturated soil can be written in the compacted form as:

$$\dot{\boldsymbol{\sigma}}^{net} = \boldsymbol{D}^{net} : \dot{\boldsymbol{\varepsilon}} - \boldsymbol{D}^{s}\dot{s} \tag{A-6}$$

Finally, substituting $\dot{\boldsymbol{\sigma}}^{net} = \dot{\boldsymbol{\sigma}} - \dot{u_a}\mathbf{1}$ and $\dot{s} = \dot{u_a} - \dot{u_w}$ into Equation (A-6), the total stress – strain relationship for unsaturated soil for control the testing condition can be written in the compacted form by:

$$\dot{\boldsymbol{\sigma}} = \boldsymbol{D}^{net} : \dot{\boldsymbol{\varepsilon}} + (\mathbf{1} - \boldsymbol{D}^{s})\dot{u_a} + \boldsymbol{D}^{s}\dot{u_w} \tag{A-7}$$

where $\dot{u_a}$ and $\dot{u_w}$ are the time derivatives of pore air pressure and pore water pressure.

A - 2 DRAINAGE CONDITION

Drainage conditions of void air and void water need to be selected and applied properly for simulating compaction, soaking and shearing behavior of unsaturated soils as summarized in Table A-1. Pore air pressure rate $\dot{u_a}$ and pore water pressure rate $\dot{u_w}$ in the simulation shall be controlled for particular drainage condition. Finally, in the simulation, the combination of total stress (Equation (A-7)) and drainage conditions (Equations (A-8), (A-9), (A-13) and (A-21)) will be applied to constitutive equations of each testing condition.

A - 2.1 Drained water condition

The drained water condition is the condition that water is allowed to escape from the soil. By this, we keep the pore water pressure rate constant in the simulation as given by:

$$\dot{u_w} = 0 \tag{A-8}$$

A - 2.2 Exhausted air condition

The exhausted air condition is the condition that air is allowed to escape from the soil. By this, we keep the pore air pressure rate constant in the simulation as given by:

$$\dot{u_a} = 0 \tag{A-9}$$

A - 2.3 Undrained water condition

The undrained water condition is the condition that water is not allowed to escape from the soil. By this, the pore water pressure rate is always changed in the simulation as given by:

$$\dot{u_w} \neq 0 \tag{A-10}$$

In other direction, for undrained water condition, we control the mass of water in the closed system instead of pore water pressure rate. Regarding the basic volume mass equation for unsaturated soil as given in Equation (4-2), the water content w_n is kept constant as given by

$$\dot{w_n} = \frac{e\dot{S_r} + S_r\dot{e}}{G_s} = 0 \tag{A-11}$$

so

$$\dot{S_r} = \frac{-S_r\dot{e}}{e} \tag{A-12}$$

where $\dot{e} = \dot{v} = -v_0\mathbf{1}:\dot{\boldsymbol{\varepsilon}}$.

By substituting Equation (A-12) into Equation (A-3), the equation of variation of degree of saturation by suction, including effect of density and hysteresis under the water mass constant condition can be written as:

$$\left(\frac{S_r}{e} + \frac{\frac{\partial S_r}{\partial v}}{1 - \frac{\partial S_r}{\partial I_h}\frac{dI_h}{dS_r}}\right) v_0\mathbf{1}:\dot{\boldsymbol{\varepsilon}} - \frac{\frac{\partial S_r}{\partial s}}{1 - \frac{\partial S_r}{\partial I_h}\frac{dI_h}{dS_r}}\dot{u_a} + \frac{\frac{\partial S_r}{\partial s}}{1 - \frac{\partial S_r}{\partial I_h}\frac{dI_h}{dS_r}}\dot{u_w} = 0 \tag{A-13}$$

A - 2.4 Unexhausted air condition

The unexhausted air condition is the condition that air is not allowed to escape from the soil. By this, the pore air pressure rate is always changed in the simulation as given by:

$$\dot{u_a} \neq 0 \tag{A-14}$$

In other direction, for unexhausted air condition, we control the mass of air in the closed system instead of pore air pressure rate. Regarding the ideal gas law which the empirical equation can be written as:

$$p_aV_a = molR_aT \tag{A-15}$$

where p_a is the pressure of ideal gas, V_a is the volume of ideal gas, mol is air mole or amount of substance, R_a is gas constant and T is absolute temperature of gas. In this study, the temperature T is kept constant under the Boyle's law, therefore the mass of air can be kept constant by control the variation of pore air pressure u_a and air volume V_a as given by:

$$\dot{p_aV_a} = \dot{u_aV_a} = 0 \tag{A-16}$$

Volume of air is related to the degree of saturation S_r and density of soil (or void ratio e) by assume constant volume of soil $V_s = 1$ as given by:

$$V_a = e(1 - S_r) \tag{A-17}$$

So, the mass of air rate can be written in term of degree of saturation S_r, density of soil (or void ratio e) and pore air pressure as written by:

$$(\dot{u_aV_a}) = ((u_ae)(\dot{1 - S_r})) = 0 \tag{A-18}$$

so

$$u_a\dot{S_r} = u_a(1-S_r)\frac{\dot{e}}{e} + (1-S_r)\dot{u_a} \tag{A-19}$$

where $\dot{e} = \dot{v} = -v_0\mathbf{1}\colon\dot{\boldsymbol{\varepsilon}}$.

By substituting Equation (A-19) into Equation (A-3), the equation of variation of degree of saturation by suction, including effect of density and hysteresis under the air mass constant condition can be written as:

$$\left(\frac{\frac{\partial S_r}{\partial v}u_a}{1-\frac{\partial S_r}{\partial I_h}\frac{dI_h}{dS_r}} + \frac{S_r-1}{e}\right)u_a v_0\mathbf{1}\colon\dot{\boldsymbol{\varepsilon}} - \left(\frac{\frac{\partial S_r}{\partial s}u_a}{1-\frac{\partial S_r}{\partial I_h}\frac{dI_h}{dS_r}} + S_r - 1\right)\dot{u}_a + \left(\frac{\frac{\partial S_r}{\partial s}u_a}{1-\frac{\partial S_r}{\partial I_h}\frac{dI_h}{dS_r}}\right)\dot{u}_w = 0 \tag{A-20}$$

The form of air mass constant equation is reduced by multiply Equation (A-13) with u_a and subtract it by Equation (A-20) as written by:

$$\frac{u_a}{e}v_0\mathbf{1}\colon\dot{\boldsymbol{\varepsilon}} + (S_r-1)\dot{u_a} = 0 \tag{A-21}$$

A - 3 APPLICATIONS

A - 3.1 Compaction mechanism

Compaction mechanism is investigated through static loading condition. As compaction primality occurs by exhaustion of void air without any change in water content, this testing condition is applied under exhausted air, undrained water condition. The constitutive equations are the combination of Equations (A-7), (A-9) and (A-13) in the elementary simulation as summarized by:

$$\begin{cases} \dot{\boldsymbol{\sigma}} = \boldsymbol{D}^{net}\colon\dot{\boldsymbol{\varepsilon}} + \boldsymbol{D}^{s}\dot{u_w} \\ \left(\frac{S_r}{e} + \frac{\frac{\partial S_r}{\partial v}}{1-\frac{\partial S_r}{\partial I_h}\frac{dI_h}{dS_r}}\right)v_0\mathbf{1}\colon\dot{\boldsymbol{\varepsilon}} + \frac{\frac{\partial S_r}{\partial s}}{1-\frac{\partial S_r}{\partial I_h}\frac{dI_h}{dS_r}}\dot{u_w} = 0 \end{cases} \tag{A-22}$$

A - 3.2 Monotonic static shearing

Static shearing under fully drained condition is used in considering the long-term stability analysis of soil. In the elementary test, shearing load will be applied slowly and pore pressure is not allowed to build up. So, this testing condition allow the air and water to escape from the soil. In other words, both increment of pore air pressure and pore water pressure are always zero. The constitutive equations are the combination of Equations (A-7), (A-8) and (A-9) in the elementary simulation as summarized by:

$$\dot{\boldsymbol{\sigma}} = \boldsymbol{D}^{net}\colon\dot{\boldsymbol{\varepsilon}} \tag{A-23}$$

A - 3.3 Soaking and adjusting water content

Suction varying under constant mean net stress is applied in the simulation to focus only its effect for soaking mechanism and adjusting water content (or water absorption) before performing compaction simulation. The suction is controlled under the fully drained condition where void air and water are freely exhausted and drained, respectively. For this testing condition, the constitutive equations are the combination of Equations (A-7) with keeping the total stress and pore air pressure constant ($\dot{\sigma} = 0$ and $\dot{u_a} = 0$) in order to keep $\dot{p_{net}} = 0$. While pore water pressure is controlled to be increased ($\dot{u_w} > 0$) for wetting in the elementary simulation as written by:

$$\boldsymbol{D}^{net}\!:\dot{\boldsymbol{\varepsilon}} = -\boldsymbol{D}^{s}\dot{u_w} \tag{A-24}$$

A - 3.4 Fully undrained static shearing

Liquefaction during an earthquake is usually occurred by cyclic shearing within a very short time period. This condition is considered by cyclic shearing under the unexhausted air and undrained water drainage condition. It is applied by keeping the mass of air and that of water constant ($\left(V_a\dot{u}_a\right) = 0$; $\left(e\dot{S}_r\right) = 0$), respectively. In this condition, both pore air pressure and pore water pressure can vary. The constitutive equations are the combination of Equations (A-7), (A-13) and (A-21) in the elementary simulation as summarized by:

$$\begin{cases} \dot{\boldsymbol{\sigma}} = \boldsymbol{D}^{net} : \dot{\boldsymbol{\varepsilon}} + (\mathbf{1} - \boldsymbol{D}^{s})\dot{u_a} + \boldsymbol{D}^{s}\dot{u_w} \\ \dfrac{u_a}{e} v_0 \mathbf{1}\!:\dot{\boldsymbol{\varepsilon}} + (S_r - 1)\dot{u_a} = 0 \end{cases} \tag{A-25}$$

Table A-1 Drainage conditions and their applications

Air	Water	Drainage conditions	Applications
Drained $\dot{u_a} = 0$	Drained $\dot{u_w} = 0$	Fully drained	A – 3.2 Monotonic static shearing A – 3.3 Soaking and adjusting water content
	Undrained $\dot{w_n} = 0$	Exhausted - Undrained	A – 3.1 Compaction mechanism
Undrained $u_a\dot{V_a} = 0$		Fully undrained	A – 3.4 Fully undrained static shearing (assume earthquake)

APPENDIX B

SUPPLEMENTARY INFORMATION FOR FEM FORMULATIONS

For APPENDIX B, defining $i = 1, 2, ..., n$ and n is the number of nodes in 2-D element, unless otherwise specified.

B - 1 SHAPE FUNCTION AND ELEMENT NODE NUMBERING OF 2D ELEMENTS

- Bilinear Quadrilateral (4 nodes)

$$N_1 = \frac{1}{4}(1-\xi)(1-\eta)$$

$$N_2 = \frac{1}{4}(1+\xi)(1-\eta)$$

$$N_3 = \frac{1}{4}(1+\xi)(1+\eta)$$

$$N_4 = \frac{1}{4}(1-\xi)(1+\eta)$$

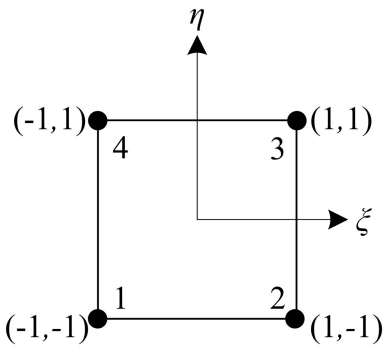

- Serendipity Quadrilateral (8 nodes)

$$N_1 = \frac{1}{4}(1-\xi)(1-\eta)(-\xi-\eta-1)$$

$$N_2 = \frac{1}{2}(1-\xi^2)(1-\eta)$$

$$N_3 = \frac{1}{4}(1+\xi)(1-\eta)(\xi-\eta-1)$$

$$N_4 = \frac{1}{2}(1+\xi)(1-\eta^2)$$

$$N_5 = \frac{1}{4}(1+\xi)(1+\eta)(\xi+\eta-1)$$

$$N_6 = \frac{1}{2}(1-\xi^2)(1+\eta)$$

$$N_7 = \frac{1}{4}(1-\xi)(1+\eta)(-\xi+\eta-1)$$

$$N_8 = \frac{1}{2}(1-\xi)(1-\eta^2)$$

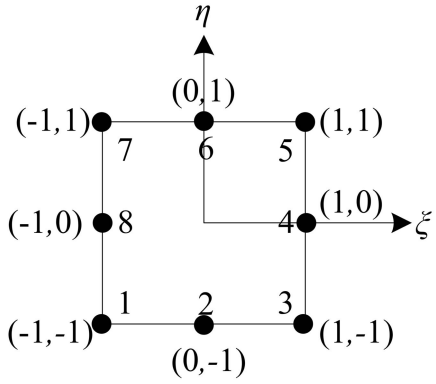

B - 2 SPATIAL DISCRETIZATION

B - 2.1 Details of vector and matrix forms for the discretization of displacement and strain

Approximation solutions of the displacement in x-axis ($\dot{u_x}$) and y-axis ($\dot{u_y}$) for n-node element are written as Equations (B-1) and (B-2), respectively.

$$\dot{u}_x = N_{u_1}\dot{U}_{x_1} + N_{u_2}\dot{U}_{x_2} + \cdots + N_{u_{n-1}}\dot{U}_{x_{n-1}} + N_{u_n}\dot{U}_{x_n} \tag{B-1}$$

$$\dot{u}_y = N_{u_1}\dot{U}_{y_1} + N_{u_2}\dot{U}_{y_2} + \cdots + N_{u_{n-1}}\dot{U}_{y_{n-1}} + N_{u_n}\dot{U}_{y_n} \tag{B-2}$$

We can express Equations (B-1) and (B-2) in the matrix from as:

$$\begin{Bmatrix}\dot{u}_x\\ \dot{u}_y\end{Bmatrix}_{2\times 1} = \begin{bmatrix}N_{u_1} & 0 & N_{u_2} & 0 & \ldots\ldots N_{u_{n-1}} & 0 & N_{u_n} & 0\\ 0 & N_{u_1} & 0 & N_{u_2} \ldots\ldots & 0 & N_{u_{n-1}} & 0 & N_{u_n}\end{bmatrix}_{2\times 2n} \begin{Bmatrix}\dot{U}_{x_1}\\ \dot{U}_{y_1}\\ \dot{U}_{x_2}\\ \dot{U}_{y_2}\\ \vdots\\ \vdots\\ \dot{U}_{x_{n-1}}\\ \dot{U}_{y_{n-1}}\\ \dot{U}_{x_n}\\ \dot{U}_{y}\end{Bmatrix}_{2n\times 1} \tag{B-3}$$

or writing in the compacting form as

$$\{\dot{\boldsymbol{u}}\} = [\boldsymbol{N_u}]\{\dot{\boldsymbol{U}}\} \tag{B-4}$$

where $\dot{\boldsymbol{u}}$ denotes the approximate displacement vector of the element, $[\boldsymbol{N_u}]$ denotes the matrix of isoparametric interpolation function N and $\{\dot{\boldsymbol{U}}\}$ is the nodal derivative displacement with time vector.

From Equations (B-1) and (B-2), strain vector in x-y plane for plain strain condition $\{\dot{\boldsymbol{\varepsilon}}\}$ can be written as following set of equation.

$$\begin{aligned}
\frac{\partial \dot{u}_x}{\partial x} &= \frac{\partial N_{u_1}}{\partial x}\dot{U}_{x_1} + \frac{\partial N_{u_2}}{\partial x}\dot{U}_{x_2} + \cdots + \frac{\partial N_{u_{n-1}}}{\partial x}\dot{U}_{x_{n-1}} + \frac{\partial N_{u_n}}{\partial x}\dot{U}_{x_n}\\
\frac{\partial \dot{u}_x}{\partial y} &= \frac{\partial N_{u_1}}{\partial y}\dot{U}_{x_1} + \frac{\partial N_{u_2}}{\partial y}\dot{U}_{x_2} + \cdots + \frac{\partial N_{u_{n-1}}}{\partial y}\dot{U}_{x_{n-1}} + \frac{\partial N_{u_n}}{\partial y}\dot{U}_{x_n}\\
\frac{\partial \dot{u}_y}{\partial y} &= \frac{\partial N_{u_1}}{\partial y}\dot{U}_{y_1} + \frac{\partial N_{u_2}}{\partial y}\dot{U}_{y_2} + \cdots + \frac{\partial N_{u_{n-1}}}{\partial y}\dot{U}_{y_{n-1}} + \frac{\partial N_{u_n}}{\partial y}\dot{U}_{y_n}\\
\frac{\partial \dot{u}_y}{\partial x} &= \frac{\partial N_{u_1}}{\partial x}\dot{U}_{y_1} + \frac{\partial N_{u_2}}{\partial x}\dot{U}_{y_2} + \cdots + \frac{\partial N_{u_{n-1}}}{\partial x}\dot{U}_{y_{n-1}} + \frac{\partial N_{u_n}}{\partial x}\dot{U}_{y_n}
\end{aligned} \tag{B-5}$$

Equation (B-5) can be written in the matrix form as:

$$\begin{Bmatrix} \dot{\varepsilon_{xx}} \\ \dot{\varepsilon_{yy}} \\ \dot{\gamma_{xy}} \end{Bmatrix}_{3\times1} = \begin{Bmatrix} \dfrac{\partial \dot{u_x}}{\partial x} \\ \dfrac{\partial \dot{u_y}}{\partial y} \\ \dfrac{\partial \dot{u_x}}{\partial y} + \dfrac{\partial \dot{u_y}}{\partial x} \end{Bmatrix}_{3\times1}$$

$$= \begin{bmatrix} \dfrac{\partial N_{u_1}}{\partial x} & 0 & \dfrac{\partial N_{u_2}}{\partial x} & 0 & \dots & \dfrac{\partial N_{u_{n-1}}}{\partial x} & 0 & \dfrac{\partial N_{u_n}}{\partial x} & 0 \\ 0 & \dfrac{\partial N_{u_1}}{\partial y} & 0 & \dfrac{\partial N_{u_2}}{\partial y} & \dots & 0 & \dfrac{\partial N_{u_{n-1}}}{\partial y} & 0 & \dfrac{\partial N_{u_n}}{\partial y} \\ \dfrac{\partial N_{u_1}}{\partial y} & \dfrac{\partial N_{u_1}}{\partial x} & \dfrac{\partial N_{u_2}}{\partial y} & \dfrac{\partial N_{u_2}}{\partial x} & \dots & \dfrac{\partial N_{u_{n-1}}}{\partial y} & \dfrac{\partial N_{u_{n-1}}}{\partial x} & \dfrac{\partial N_{u_n}}{\partial y} & \dfrac{\partial N_{u_n}}{\partial x} \end{bmatrix}_{3\times2n} \begin{Bmatrix} \dot{U_{x1}} \\ \dot{U_{y1}} \\ \dot{U_{x2}} \\ \dot{U_{y2}} \\ \vdots \\ \dot{U_{xn}} \\ \dot{U_{yn}} \end{Bmatrix}_{2n\times1} \quad \text{(B-6)}$$

or it could be written in the compacting form as:

$$\{\dot{\boldsymbol{\varepsilon}}\} = [\boldsymbol{B_u}]\{\dot{\boldsymbol{U}}\} \quad \text{(B-7)}$$

where $[\boldsymbol{B_u}]$ denotes the element strain – displacement matrix.

The differential operator $[\boldsymbol{\nabla}] = \begin{bmatrix} \frac{\partial}{\partial x} & 0 \\ 0 & \frac{\partial}{\partial y} \\ \frac{\partial}{\partial y} & \frac{\partial}{\partial x} \end{bmatrix}$ is specified in this section and $[\boldsymbol{\nabla}]^T = \begin{bmatrix} \frac{\partial}{\partial x} & 0 & \frac{\partial}{\partial y} \\ 0 & \frac{\partial}{\partial y} & \frac{\partial}{\partial x} \end{bmatrix}$ denotes the transpose matric of $[\boldsymbol{\nabla}]$. Then, $[\boldsymbol{\nabla N_u}]$ can be written as Equation (B-8) which is equal to $[\boldsymbol{B_u}]$.

$$[\boldsymbol{\nabla N_u}] = \begin{bmatrix} \frac{\partial}{\partial x} & 0 \\ 0 & \frac{\partial}{\partial y} \\ \frac{\partial}{\partial y} & \frac{\partial}{\partial x} \end{bmatrix}_{3\times2} \begin{bmatrix} N_{u_1} & 0 & N_{u_2} & 0 & \dots & N_{u_{n-1}} & 0 & N_{u_n} & 0 \\ 0 & N_{u_1} & 0 & N_{u_2} & \dots & 0 & N_{u_{n-1}} & 0 & N_{u_n} \end{bmatrix}_{2\times2n}$$

$$[\boldsymbol{\nabla N_u}] = \begin{bmatrix} \dfrac{\partial N_{u_1}}{\partial x} & 0 & \dfrac{\partial N_{u_2}}{\partial x} & 0 & \dots & \dots & \dfrac{\partial N_{u_{n-1}}}{\partial x} & 0 & \dfrac{\partial N_{u_n}}{\partial x} & 0 \\ 0 & \dfrac{\partial N_{u_1}}{\partial y} & 0 & \dfrac{\partial N_{u_2}}{\partial y} & \dots & \dots & 0 & \dfrac{\partial N_{u_{n-1}}}{\partial y} & 0 & \dfrac{\partial N_{u_n}}{\partial y} \\ \dfrac{\partial N_{u_1}}{\partial y} & \dfrac{\partial N_{u_1}}{\partial x} & \dfrac{\partial N_{u_2}}{\partial y} & \dfrac{\partial N_{u_2}}{\partial x} & \dots & \dots & \dfrac{\partial N_{u_{n-1}}}{\partial y} & \dfrac{\partial N_{u_{n-1}}}{\partial x} & \dfrac{\partial N_{u_n}}{\partial y} & \dfrac{\partial N_{u_n}}{\partial x} \end{bmatrix}_{3x2n} \quad \text{(B-8)}$$

$$[\boldsymbol{\nabla N_u}] = [\boldsymbol{B_u}]$$

In addition, $[\boldsymbol{\nabla N_u}]^{\mathbf{T}}$ denotes the transpose matric of $[\boldsymbol{\nabla N_u}]$ as shown below which is equal to $[\boldsymbol{B_u}]^T$.

$$[\boldsymbol{\nabla N_u}]^T = \begin{bmatrix} \frac{\partial N_{u_1}}{\partial x} & 0 & \frac{\partial N_{u_1}}{\partial y} \\ 0 & \frac{\partial N_{u_1}}{\partial y} & \frac{\partial N_{u_1}}{\partial x} \\ \frac{\partial N_{u_2}}{\partial x} & 0 & \frac{\partial N_{u_2}}{\partial y} \\ 0 & \frac{\partial N_{u_2}}{\partial y} & \frac{\partial N_{u_2}}{\partial x} \\ \vdots & \vdots & \vdots \\ \vdots & \vdots & \vdots \\ \frac{\partial N_{u_{n-1}}}{\partial x} & 0 & \frac{\partial N_{u_{n-1}}}{\partial y} \\ 0 & \frac{\partial N_{u_{n-1}}}{\partial y} & \frac{\partial N_{u_{n-1}}}{\partial x} \\ \frac{\partial N_{u_n}}{\partial x} & 0 & \frac{\partial N_{u_n}}{\partial y} \\ 0 & \frac{\partial N_{u_n}}{\partial y} & \frac{\partial N_{u_n}}{\partial x} \end{bmatrix}_{2n\times 3} = [\boldsymbol{B_u}]^T \quad \text{(B-9)}$$

B - 2.2 Details of vector and matrix forms for the discretization of pore water pressure and distribution of pore water pressure

The approximation of the pore water pressure u_w can be written as Equation (B-10) for n-nodes element.

$$\dot{u}_w = N_{u_{w_1}}\dot{U}_{w_1} + N_{u_{w_2}}\dot{U}_{w_2} + \cdots + N_{u_{w_{n-1}}}\dot{U}_{w_{n-1}} + N_{u_{w_n}}\dot{U}_{w_n} \quad \text{(B-10)}$$

We can express Equation (B-10) in the matrix from as:

$$\dot{u}_w = \begin{bmatrix} N_{u_{w_1}} & N_{u_{w_2}} & \dots & N_{u_{w_{n-1}}} & N_{u_{w_n}} \end{bmatrix}_{1xn} \begin{Bmatrix} \dot{U}_{w_1} \\ \dot{U}_{w_2} \\ \vdots \\ \dot{U}_{w_{n-1}} \\ \dot{U}_{w_n} \end{Bmatrix}_{nx1} = [\boldsymbol{N_{u_w}}]\{\dot{\boldsymbol{U}}_{\boldsymbol{w}}\} \quad \text{(B-11)}$$

The approximation of the transient pore water pressure with time $\dot{u_w}$ can be written as Equation (B-12) for n-nodes element.

$$u_w = N_{u_{w_1}}U_{w_1} + N_{u_{w_2}}U_{w_2} + \cdots + N_{u_{w_{n-1}}}U_{w_{n-1}} + N_{u_{w_n}}U_{w_n} \quad \text{(B-12)}$$

We can express Equation (B-12) in the matrix from as:

$$u_w = \begin{bmatrix} N_{u_{w_1}} & N_{u_{w_2}} & \dots & N_{u_{w_{n-1}}} & N_{u_{w_n}} \end{bmatrix}_{1xn} \begin{Bmatrix} U_{w_1} \\ U_{w_2} \\ \vdots \\ U_{w_{n-1}} \\ U_{w_n} \end{Bmatrix}_{nx1} = [\boldsymbol{N_{u_w}}]\{\boldsymbol{U_w}\} \quad \text{(B-13)}$$

where $[\boldsymbol{N_{u_w}}]$ is the matrix of isoparametric interpolation function *N*, $\{\dot{\boldsymbol{U}}_{\boldsymbol{w}}\}$ is the nodal transient pore water pressure vector and $\{\boldsymbol{U_w}\}$ is the nodal transient pore water pressure vector.

From Equation (B-10), distribution of pore water pressure in x and y directions can be written as following set of equation.

$$\begin{aligned}\frac{\partial u_w}{\partial x} &= \frac{\partial N_{u_{w_1}}}{\partial x} U_{w_1} + \frac{\partial N_{u_{w_2}}}{\partial x} U_{w_2} + \cdots + \frac{\partial N_{u_{w_{n-1}}}}{\partial x} U_{w_{n-1}} + \frac{\partial N_{u_{w_n}}}{\partial x} U_{w_n} \\ \frac{\partial u_w}{\partial y} &= \frac{\partial N_{u_{w_1}}}{\partial y} U_{w_1} + \frac{\partial N_{u_{w_2}}}{\partial y} U_{w_2} + \cdots + \frac{\partial N_{u_{w_{n-1}}}}{\partial y} U_{w_{n-1}} + \frac{\partial N_{u_{w_n}}}{\partial y} U_{w_n}\end{aligned} \tag{B-14}$$

Equation (B-14) can be written in the matrix form as

$$\begin{Bmatrix} \frac{\partial u_w}{\partial x} \\ \frac{\partial u_w}{\partial y} \end{Bmatrix} = \begin{bmatrix} \frac{\partial N_{u_{w_1}}}{\partial x} & \frac{\partial N_{u_{w_2}}}{\partial x} & \cdots & \frac{\partial N_{u_{w_{n-1}}}}{\partial x} & \frac{\partial N_{u_{w_n}}}{\partial x} \\ \frac{\partial N_{u_{w_1}}}{\partial y} & \frac{\partial N_{u_{w_2}}}{\partial y} & \cdots & \frac{\partial N_{u_{w_{n-1}}}}{\partial y} & \frac{\partial N_{u_{w_n}}}{\partial y} \end{bmatrix}_{2\times n} \begin{Bmatrix} U_{w_1} \\ U_{w_2} \\ \vdots \\ U_{w_{n-1}} \\ U_{w_n} \end{Bmatrix}_{nx1} \tag{B-15}$$

or it could be written in the compacting form as

$$\{\boldsymbol{\nabla} u_w\} = [\boldsymbol{B_{u_w}}]\{\boldsymbol{U_w}\} \tag{B-16}$$

where $[\boldsymbol{B_{u_w}}]$ denotes the element pressure distribution – pressure matrix.

The differential operator $\{\boldsymbol{\nabla}\}$ is specified in this section as $\{\boldsymbol{\nabla}\} = \begin{Bmatrix} \frac{\partial}{\partial x} \\ \frac{\partial}{\partial y} \end{Bmatrix}$ and $\{\boldsymbol{\nabla}\}^T$ denotes the transpose matric of $\{\boldsymbol{\nabla}\}$ as $\{\boldsymbol{\nabla}\}^T = \begin{bmatrix} \frac{\partial}{\partial x} & \frac{\partial}{\partial y} \end{bmatrix}$. Then, $[\boldsymbol{\nabla N_{u_w}}]$ can be written as Equation (B-17) which is equal to $[\boldsymbol{B_{u_w}}]$.

$$[\boldsymbol{\nabla N_{u_w}}] = \begin{Bmatrix} \frac{\partial}{\partial x} \\ \frac{\partial}{\partial y} \end{Bmatrix}_{2\times 1} \begin{bmatrix} N_{u_{w_1}} & N_{u_{w_2}} & \cdots & N_{u_{w_{n-1}}} & N_{u_{w_n}} \end{bmatrix}_{1\times n}$$

$$[\boldsymbol{\nabla N_{u_w}}] = \begin{bmatrix} \frac{\partial N_{u_{w_1}}}{\partial x} & \frac{\partial N_{u_{w_2}}}{\partial x} & \cdots & \frac{\partial N_{u_{w_{n-1}}}}{\partial x} & \frac{\partial N_{u_{w_n}}}{\partial x} \\ \frac{\partial N_{u_{w_1}}}{\partial y} & \frac{\partial N_{u_{w_2}}}{\partial y} & \cdots & \frac{\partial N_{u_{w_{n-1}}}}{\partial y} & \frac{\partial N_{u_{w_n}}}{\partial y} \end{bmatrix}_{2\times n} \tag{B-17}$$

$$[\boldsymbol{\nabla N_{u_w}}] = [\boldsymbol{B_{u_w}}]$$

In addition, $\left[\boldsymbol{\nabla N_{u_w}}\right]^T$ denotes the transpose matrix of $\left[\boldsymbol{\nabla N_{u_w}}\right]$ as shown below which is equal to $\left[\boldsymbol{B_{u_w}}\right]^T$.

$$\left[\boldsymbol{\nabla N_{u_w}}\right]^T = \begin{bmatrix} \frac{\partial N_{u_{w_1}}}{\partial x} & \frac{\partial N_{u_{w_1}}}{\partial y} \\ \frac{\partial N_{u_{w_2}}}{\partial x} & \frac{\partial N_{u_{w_2}}}{\partial y} \\ \vdots & \vdots \\ \frac{\partial N_{u_{w_{n-1}}}}{\partial x} & \frac{\partial N_{u_{w_{n-1}}}}{\partial y} \\ \frac{\partial N_{u_{w_n}}}{\partial x} & \frac{\partial N_{u_{w_n}}}{\partial y} \end{bmatrix}_{n\times 2} = \left[\boldsymbol{B_{u_w}}\right]^T. \tag{B-18}$$

B - 3 CALCULATION DETAILS OF B - MATRIX

B - 3.1 B - Matrix Calculation (Including $\boldsymbol{B_u}$ and $\boldsymbol{B_{u_w}}$ for strain – displacement and rate of pressure change – pressure, respectively)

From Equation (B-6), the approximate solution of internal strain is written in the matrix form in term of nodal derivative displacement with time vector and B - matrix (or strain-displacement element matrix) which is established from the local derivative, $\boldsymbol{\nabla}(x, y)$, of the shape function in natural coordinate $\boldsymbol{N_i}(\xi, \eta)$ (isoparametric element). Therefore, the local derivative $\boldsymbol{\nabla}(x, y)$ shall be replaced by the natural derivative $\boldsymbol{\nabla}(\xi, \eta)$ using the chain rule.

The normal strain $(\frac{\partial \dot{u_x}}{\partial x}, \frac{\partial \dot{u_y}}{\partial y})$ and deviatoric strain $(\frac{\partial \dot{u_x}}{\partial y} + \frac{\partial \dot{u_y}}{\partial x})$ shall be written is the natural coordinates form as shown below:

- The derivative of $\dot{u_x}$ along the natural axis

The derivative of $\dot{u_x}$ along the natural axis can be written as:

$$\begin{aligned} \frac{\partial \dot{u_x}}{\partial \xi} &= \frac{\partial \dot{u_x}}{\partial x}\frac{\partial x}{\partial \xi} + \frac{\partial \dot{u_x}}{\partial y}\frac{\partial y}{\partial \xi} \\ \frac{\partial \dot{u_x}}{\partial \eta} &= \frac{\partial \dot{u_x}}{\partial x}\frac{\partial x}{\partial \eta} + \frac{\partial \dot{u_x}}{\partial y}\frac{\partial y}{\partial \eta} \end{aligned} \tag{B-19}$$

or we can write in the matric form as:

$$\begin{Bmatrix} \frac{\partial \dot{u_x}}{\partial \xi} \\ \frac{\partial \dot{u_x}}{\partial \eta} \end{Bmatrix} = \begin{bmatrix} \frac{\partial x}{\partial \xi} & \frac{\partial y}{\partial \xi} \\ \frac{\partial x}{\partial \eta} & \frac{\partial y}{\partial \eta} \end{bmatrix} \begin{Bmatrix} \frac{\partial \dot{u_x}}{\partial x} \\ \frac{\partial \dot{u_x}}{\partial y} \end{Bmatrix} \tag{B-20}$$

where $\begin{bmatrix} \frac{\partial x}{\partial \xi} & \frac{\partial y}{\partial \xi} \\ \frac{\partial x}{\partial \eta} & \frac{\partial y}{\partial \eta} \end{bmatrix}$ is the Jacobian matrix $[\boldsymbol{J}]$. See Appendix B - 3.3 for the calculation details.

Then, using Equation (B-20), the normal strain in x-axis $\frac{\partial \dot{u_x}}{\partial x}$ and the deviatoric part along the y-axis $\frac{\partial \dot{u_x}}{\partial y}$ can be expressed in the natural coordinates as:

$$\begin{Bmatrix} \frac{\partial \dot{u_x}}{\partial x} \\ \frac{\partial \dot{u}}{\partial y} \end{Bmatrix} = \begin{bmatrix} \frac{\partial x}{\partial \xi} & \frac{\partial y}{\partial \xi} \\ \frac{\partial x}{\partial \eta} & \frac{\partial y}{\partial \eta} \end{bmatrix}^{-1} \begin{Bmatrix} \frac{\partial \dot{u_x}}{\partial \xi} \\ \frac{\partial \dot{u_x}}{\partial \eta} \end{Bmatrix} \tag{B-21}$$

Finally, substitute the vector $\left\{\frac{\partial \dot{u_x}}{\partial \xi}, \frac{\partial \dot{u_x}}{\partial \eta}\right\}$ in Equation (B-21) with the general form of the distribution of approximate solution, we will get:

$$\begin{Bmatrix} \frac{\partial \dot{u_x}}{\partial x} \\ \frac{\partial \dot{u_x}}{\partial y} \end{Bmatrix} = \begin{bmatrix} \frac{\partial x}{\partial \xi} & \frac{\partial y}{\partial \xi} \\ \frac{\partial x}{\partial \eta} & \frac{\partial y}{\partial \eta} \end{bmatrix}^{-1} \begin{bmatrix} \frac{\partial N_1}{\partial \xi} & \frac{\partial N_2}{\partial \xi} & \cdots & \frac{\partial N_n}{\partial \xi} \\ \frac{\partial N_1}{\partial \eta} & \frac{\partial N_2}{\partial \eta} & \cdots & \frac{\partial N_n}{\partial \eta} \end{bmatrix} \begin{Bmatrix} \dot{U}_{x1} \\ \dot{U}_{x2} \\ \vdots \\ \dot{U}_{xn} \end{Bmatrix} \tag{B-22}$$

where the calculation details of $\frac{\partial N_i}{\partial \xi}$ and $\frac{\partial N_i}{\partial \eta}$ are shown in Appendix B - 3.2.

- The derivative of $\dot{u_y}$ along the natural axis

The derivative of $\dot{u_y}$ along the natural axis can be written as:

$$\begin{aligned} \frac{\partial \dot{u_y}}{\partial \xi} &= \frac{\partial \dot{u_y}}{\partial x}\frac{\partial x}{\partial \xi} + \frac{\partial \dot{u_y}}{\partial y}\frac{\partial y}{\partial \xi} \\ \frac{\partial \dot{u_y}}{\partial \eta} &= \frac{\partial \dot{u_y}}{\partial x}\frac{\partial x}{\partial \eta} + \frac{\partial \dot{u_y}}{\partial y}\frac{\partial y}{\partial \eta} \end{aligned} \tag{B-23}$$

or we can write in the matric form as:

$$\begin{Bmatrix} \frac{\partial \dot{u_y}}{\partial \xi} \\ \frac{\partial \dot{u_y}}{\partial \eta} \end{Bmatrix} = \begin{bmatrix} \frac{\partial x}{\partial \xi} & \frac{\partial y}{\partial \xi} \\ \frac{\partial x}{\partial \eta} & \frac{\partial y}{\partial \eta} \end{bmatrix} \begin{Bmatrix} \frac{\partial \dot{u_y}}{\partial x} \\ \frac{\partial \dot{u_y}}{\partial y} \end{Bmatrix} \tag{B-24}$$

where $\begin{bmatrix} \frac{\partial x}{\partial \xi} & \frac{\partial y}{\partial \xi} \\ \frac{\partial x}{\partial \eta} & \frac{\partial y}{\partial \eta} \end{bmatrix}$ is the Jacobian matrix $[\boldsymbol{J}]$. See Appendix B - 3.3 for the calculation details.

Then, using Equation (B-24) the normal strain in x-axis $\frac{\partial \dot{u_y}}{\partial x}$ and the deviatoric part along the y-axis $\frac{\partial \dot{u_y}}{\partial y}$ can be expressed in the natural coordinates as:

$$\begin{Bmatrix} \frac{\partial \dot{u}_y}{\partial x} \\ \frac{\partial \dot{u}_y}{\partial y} \end{Bmatrix} = \begin{bmatrix} \frac{\partial x}{\partial \xi} & \frac{\partial y}{\partial \xi} \\ \frac{\partial x}{\partial \eta} & \frac{\partial y}{\partial \eta} \end{bmatrix}^{-1} \begin{Bmatrix} \frac{\partial \dot{u}_y}{\partial \xi} \\ \frac{\partial \dot{u}_y}{\partial \eta} \end{Bmatrix} \tag{B-25}$$

Finally, substitute the vector $\begin{Bmatrix} \frac{\partial \dot{u}_y}{\partial \xi} & \frac{\partial \dot{u}_y}{\partial \eta} \end{Bmatrix}$ in Equation (B-25) with the general form of the distribution of approximate solution, we will get

$$\begin{Bmatrix} \frac{\partial \dot{u}_y}{\partial x} \\ \frac{\partial \dot{u}_y}{\partial y} \end{Bmatrix} = \begin{bmatrix} \frac{\partial x}{\partial \xi} & \frac{\partial y}{\partial \xi} \\ \frac{\partial x}{\partial \eta} & \frac{\partial y}{\partial \eta} \end{bmatrix}^{-1} \begin{bmatrix} \frac{\partial N_1}{\partial \xi} & \frac{\partial N_2}{\partial \xi} & \cdots & \frac{\partial N_n}{\partial \xi} \\ \frac{\partial N_1}{\partial \eta} & \frac{\partial N_2}{\partial \eta} & \cdots & \frac{\partial N_n}{\partial \eta} \end{bmatrix} \begin{Bmatrix} \dot{U}_{y1} \\ \dot{U}_{y2} \\ \vdots \\ \dot{U}_{yn} \end{Bmatrix} \tag{B-26}$$

where the calculation details of $\frac{\partial N_i}{\partial \xi}$ and $\frac{\partial N_i}{\partial \eta}$ are shown in Appendix B - 3.2.

- Categorizing the derivative of $\dot{u}_x$ and $\dot{u}_y$ along the natural axis as the normal part and the deviatoric part

From Equations (B-22) and (B-26), considering the part of the normal strain in x and y axis, we will get

$$\begin{Bmatrix} \frac{\partial \dot{u}_x}{\partial x} \\ \frac{\partial \dot{u}_y}{\partial y} \end{Bmatrix} = \begin{bmatrix} \frac{\partial x}{\partial \xi} & \frac{\partial y}{\partial \xi} \\ \frac{\partial x}{\partial \eta} & \frac{\partial y}{\partial \eta} \end{bmatrix}^{-1} \begin{bmatrix} \frac{\partial N_1}{\partial \xi} & 0 & \frac{\partial N_2}{\partial \xi} & 0 & \cdots & \frac{\partial N_n}{\partial \xi} & 0 \\ 0 & \frac{\partial N_1}{\partial \eta} & 0 & \frac{\partial N_2}{\partial \eta} & \cdots & 0 & \frac{\partial N_n}{\partial \eta} \end{bmatrix} \begin{Bmatrix} \dot{U}_{x1} \\ \dot{U}_{y1} \\ \dot{U}_{x2} \\ \dot{U}_{y2} \\ \vdots \\ \vdots \\ \dot{U}_{xn} \\ \dot{U}_{yn} \end{Bmatrix} \tag{B-27}$$

and the part of deviatoric strain in x and y axis, we will get

$$\begin{Bmatrix} \frac{\partial \dot{u}_y}{\partial x} \\ \frac{\partial \dot{u}}{\partial y} \end{Bmatrix} = \begin{bmatrix} \frac{\partial x}{\partial \xi} & \frac{\partial y}{\partial \xi} \\ \frac{\partial x}{\partial \eta} & \frac{\partial y}{\partial \eta} \end{bmatrix}^{-1} \begin{bmatrix} 0 & \frac{\partial N_1}{\partial \xi} & 0 & \frac{\partial N_2}{\partial \xi} & \cdots & 0 & \frac{\partial N_n}{\partial \xi} \\ \frac{\partial N_1}{\partial \eta} & 0 & \frac{\partial N_2}{\partial \eta} & 0 & \cdots & \frac{\partial N_n}{\partial \eta} & 0 \end{bmatrix} \begin{Bmatrix} \dot{U}_{x1} \\ \dot{U}_{y1} \\ \dot{U}_{x2} \\ \dot{U}_{y2} \\ \vdots \\ \vdots \\ \dot{U}_{xn} \\ \dot{U}_{yn} \end{Bmatrix} \tag{B-28}$$

Therefore, the B-matrix for the calculation of normal part $[\boldsymbol{B_n}]$ and deviatoric part $[\boldsymbol{B}_d]$ can be simply determined by the natural coordination as shown in Equation (B-29) and (B-30), respectively.

$$[\boldsymbol{B_n}] = \begin{bmatrix} \frac{\partial N_1}{\partial x} & 0 & \frac{\partial N_2}{\partial x} & 0 & \dots & \dots & \frac{\partial N_n}{\partial x} & 0 \\ 0 & \frac{\partial N_1}{\partial y} & 0 & \frac{\partial N_2}{\partial y} & \dots & \dots & 0 & \frac{\partial N_n}{\partial y} \end{bmatrix}$$
$$= \begin{bmatrix} \frac{\partial x}{\partial \xi} & \frac{\partial y}{\partial \xi} \\ \frac{\partial x}{\partial \eta} & \frac{\partial y}{\partial \eta} \end{bmatrix}^{-1} \begin{bmatrix} \frac{\partial N_1}{\partial \xi} & 0 & \frac{\partial N_2}{\partial \xi} & 0 & \dots & \dots & \frac{\partial N_n}{\partial \xi} & 0 \\ 0 & \frac{\partial N_1}{\partial \eta} & 0 & \frac{\partial N_2}{\partial \eta} & \dots & \dots & 0 & \frac{\partial N_n}{\partial \eta} \end{bmatrix} \quad \text{(B-29)}$$

$$[\boldsymbol{B_d}] = \begin{bmatrix} 0 & \frac{\partial N_1}{\partial x} & 0 & \frac{\partial N_2}{\partial x} & \dots & \dots & 0 & \frac{\partial N_n}{\partial x} \\ \frac{\partial N_1}{\partial y} & 0 & \frac{\partial N_2}{\partial y} & 0 & \dots & \dots & \frac{\partial N_n}{\partial y} & 0 \end{bmatrix}$$
$$= \begin{bmatrix} \frac{\partial x}{\partial \xi} & \frac{\partial y}{\partial \xi} \\ \frac{\partial x}{\partial \eta} & \frac{\partial y}{\partial \eta} \end{bmatrix}^{-1} \begin{bmatrix} 0 & \frac{\partial N_1}{\partial \xi} & 0 & \frac{\partial N_2}{\partial \xi} & \dots & \dots & 0 & \frac{\partial N_n}{\partial \xi} \\ \frac{\partial N_1}{\partial \eta} & 0 & \frac{\partial N_2}{\partial \eta} & 0 & \dots & \dots & \frac{\partial N_n}{\partial \eta} & 0 \end{bmatrix} \quad \text{(B-30)}$$

By this calculation procedure, the element strain – displacement matrix $\boldsymbol{B}_u$ as shown in Equation (B-6) can be determined by the simple calculation in term of natural coordination as:

$$[\boldsymbol{B_u}] = \begin{bmatrix} [\boldsymbol{B_n}][1,:] \\ [\boldsymbol{B_n}][2,:] \\ [\boldsymbol{B_d}][1,:] + [\boldsymbol{B_d}][2,:] \end{bmatrix} \quad \text{(B-31)}$$

In addition, using the same calculation procedure, the element pressure distribution – pressure matrix $\left[\boldsymbol{B_{u_w}}\right]$ as shown in Equation (B-15) could be determined by the simple calculation in term of natural coordination as:

$$\left[\boldsymbol{B_{u_w}}\right] = \begin{bmatrix} [\boldsymbol{B_n}][1\,, 2n-1] \\ [\boldsymbol{B_n}][2\,, 2n] \end{bmatrix} \quad \text{(B-32)}$$

B - 3.2 Determination of $\frac{\partial N_i}{\partial \xi}$ and $\frac{\partial N_i}{\partial \eta}$ for the shape function of 2-D elements in natural coordinates

- Bilinear Quadrilateral (4 nodes)

$$\frac{\partial N_1}{\partial \xi} = -\frac{1}{4}(1-\eta) \qquad \frac{\partial N_1}{\partial \eta} = -\frac{1}{4}(1-\xi)$$
$$\frac{\partial N_2}{\partial \xi} = +\frac{1}{4}(1-\eta) \qquad \frac{\partial N_2}{\partial \eta} = -\frac{1}{4}(1+\xi)$$
$$\frac{\partial N_3}{\partial \xi} = +\frac{1}{4}(1+\eta) \qquad \frac{\partial N_3}{\partial \eta} = +\frac{1}{4}(1+\xi)$$
$$\frac{\partial N_4}{\partial \xi} = -\frac{1}{4}(1+\eta) \qquad \frac{\partial N_4}{\partial \eta} = +\frac{1}{4}(1-\xi)$$

- Serendipity Quadrilateral (8 nodes)

$$\frac{\partial N_1}{\partial \xi} = +\frac{1}{4}(1-\eta)(2\xi+\eta) \qquad \frac{\partial N_1}{\partial \eta} = +\frac{1}{4}(1-\xi)(2\eta+\xi)$$
$$\frac{\partial N_2}{\partial \xi} = +\frac{1}{2}(1-\eta)(-2\xi) \qquad \frac{\partial N_2}{\partial \eta} = +\frac{1}{2}(1-\eta^2)(-1)$$
$$\frac{\partial N_3}{\partial \xi} = +\frac{1}{4}(1-\eta)(2\xi-\eta) \qquad \frac{\partial N_3}{\partial \eta} = +\frac{1}{4}(1+\xi)(2\eta-\xi)$$
$$\frac{\partial N_4}{\partial \xi} = +\frac{1}{2}(1)(1-\eta^2) \qquad \frac{\partial N_4}{\partial \eta} = +\frac{1}{2}(1+\xi)(-2\eta)$$
$$\frac{\partial N_5}{\partial \xi} = +\frac{1}{4}(1+\eta)(2\xi+\eta) \qquad \frac{\partial N_5}{\partial \eta} = +\frac{1}{4}(1+\xi)(2\eta+\xi)$$
$$\frac{\partial N_6}{\partial \xi} = +\frac{1}{2}(1+\eta)(-2\xi) \qquad \frac{\partial N_6}{\partial \eta} = +\frac{1}{2}(1-\xi^2)(1)$$
$$\frac{\partial N_7}{\partial \xi} = +\frac{1}{4}(1+\eta)(2\xi-\eta) \qquad \frac{\partial N_7}{\partial \eta} = +\frac{1}{4}(1-\xi)(2\eta-\xi)$$
$$\frac{\partial N_8}{\partial \xi} = +\frac{1}{2}(-1)(1-\eta^2) \qquad \frac{\partial N_8}{\partial \eta} = +\frac{1}{2}(1-\xi)(-2\eta)$$

Remarks: Please refer to Appendix B - 1 for shape function and node numbering

B - 3.3 Jacobian matrix $[\boldsymbol{J}]$ determination

$$[\boldsymbol{J}] = \begin{bmatrix} \frac{\partial x}{\partial \xi} & \frac{\partial y}{\partial \xi} \\ \frac{\partial x}{\partial \eta} & \frac{\partial y}{\partial \eta} \end{bmatrix} \tag{B-33}$$

From Equation (B-33), Jacobian matrix $[\boldsymbol{J}]$ shall be substituted by any *x*-*y* coordinates of the trapezium element (Equation (5-1)) which is written in the relation of local trapezium element node (x_i, y_i) and the shape function (or equivalent to interpolation function) in term of

natural coordinates, $N(\xi_i, \eta_i)$. Therefore, each member in the $[\boldsymbol{J}]$ matrix can be re-written in term of the summation equation as:

$$[\boldsymbol{J}] = \begin{bmatrix} \sum_{i=1}^{n} \frac{\partial N_i}{\partial \xi} x_i & \sum_{i=1}^{n} \frac{\partial N_i}{\partial \xi} y_i \\ \sum_{i=1}^{n} \frac{\partial N_i}{\partial \eta} x_i & \sum_{i=1}^{n} \frac{\partial N_i}{\partial \eta} y_i \end{bmatrix} \tag{B-34}$$

Finally, the J matrix can be defined in the calculation code in this study as:

$$[\boldsymbol{J}] = \begin{bmatrix} \frac{\partial N_1}{\partial \xi} & \frac{\partial N_2}{\partial \xi} & \cdots & \frac{\partial N_n}{\partial \xi} \\ \frac{\partial N_1}{\partial \eta} & \frac{\partial N_2}{\partial \eta} & \cdots & \frac{\partial N_n}{\partial \eta} \end{bmatrix} \begin{bmatrix} x_1 & y_1 \\ x_2 & y_2 \\ \vdots & \vdots \\ x_n & y_n \end{bmatrix} \tag{B-35}$$

where $\frac{\partial N_i}{\partial \xi}$ and $\frac{\partial N_i}{\partial \eta}$ of each shape function of 2-D elements are shown in Appendix B - 3.2 and x_i and y_i is the initial local coordinate of the elements.

B - 4 GAUSS - LEGENDRE INTEGRATION FORMULAS

Gauss - Legendre integration formulas are applicable to the numerical integration in order to generate the finite element matrix when the boundary of the element is in between -1 to 1 in each direction. The selecting shape function in the boundary of element is integrated over the element by the summation of weights and the function at the Gauss point locations for all specified Gauss points.

Gauss-Legendre integration formulas in 1-D problem for function $f(x)$ can be written as

$$\int_{-1}^{1} f(x)dx \cong \sum_{i=1}^{NG} w_i f(x_i) \tag{B-36}$$

where

NG denotes number of Gauss points.

i denotes the subscription index represents the Gauss point order in x coordinate.

w_i denotes weights in x coordinates.

x_i denotes Gauss point locations in x coordinates.

$f(x)$ denotes function in 1-D in the coordinate x that is required to do the integration.

Gauss-Legendre integration formulas in 2-D problem for function $f(\xi, \eta)$ can be written as follow by integrating using the integration formulas in 1-D problem for each direction.

$$\int_{-1}^{1}\int_{-1}^{1} f(\xi,\eta)d\xi d\eta = \int_{-1}^{1}\left[\sum_{j=1}^{NG} w_j f(\xi,\eta_j)\right]d\xi = \sum_{i=1}^{NG}\sum_{j=1}^{NG} w_i w_j f(\xi_i,\eta_j) \qquad \text{(B-37)}$$

where

NG denotes number of Gauss points.

i,j denote the subscription index represents the Gauss point order in ξ,η coordinates, respectively.

w_i, w_j denote weights in ξ,η coordinates, respectively.

ξ_i, η_j denote Gauss point locations in ξ,η coordinates, respectively.

$f(\xi,\eta)$ denote the function in 2-D in the coordinate ξ,η that is required to do the integration.

After selecting the shape function that can be properly predicted the considered behaviors, the number of Gauss points that appropriate with the characteristic of the shape function is also important in order to maintain the full rate of convergence of the exactly integrated formulation. In general, integrating the function which is the polynomial function order m, $(m+1)/2$ is the proper number of Gauss points that results in the exact solution from the integration. Weights and Gauss point locations depends on number of gauss points in Table B-1shall be used.

Table B-1 Weights and Gauss point locations for specific function and number of Gauss points

Order of function	Function characteristics	Number of Gauss points, NG	Gauss point locations, x_i	Weights, w_i
1	linear	1	0	2
3	cubic	2	$-1/\sqrt{3}$	1
			$+1/\sqrt{3}$	1
5	5th order	3	0	$8/9$
			$-\sqrt{0.6}$	$5/9$
			$+\sqrt{0.6}$	$5/9$

B - 5 DETERMINING THE ELEMENT MATRIX USING NUMERICAL INTEGRATION: EXPLANATION AND FORMULATION

B - 5.1 Explanation of the calculation procedure of the element matrix

Determining the coefficient matrix for uncoupled FEM deformation – only analysis for saturated soil, $[\boldsymbol{K_{ep}}]$ (Table 5-2) is selected as an example in order to explain the procedure of calculation in detail as follows. Beginning with,

$$[\boldsymbol{K_{ep}^{sat}}] = \int_{\Omega} [\boldsymbol{B_u}]^T [\boldsymbol{D}][\boldsymbol{B_u}] d\boldsymbol{\Omega} \qquad \text{(B-38)}$$

Considering Equation (B-38) in 2-D problem for local coordinate x-y, it can be written as

$$\begin{aligned}\left[\boldsymbol{K_{ep}^{sat}}\right] &= \iint_A [\boldsymbol{B_u}(x,y)]^T[\boldsymbol{D}][\boldsymbol{B_u}(x,y)]tdA \\ &= \int_y \int_x [\boldsymbol{B_u}(x,y)]^T[\boldsymbol{D}][\boldsymbol{B_u}(x,y)]tdxdy\end{aligned} \tag{B-39}$$

where domain Ω is considered in the area A with the thickness t where $\Omega = tdA = tdxdy$.

To simplify the numerical integration on the trapezium element as stated before. The Equation (B-39) shall be transformed into the natural coordinate $(\xi - \eta)$ square element with the distance from -1 to 1 in each direction as

$$\left[\boldsymbol{K_{ep}^{sat}}\right] = \int_{-1}^{1}\int_{-1}^{1} [\boldsymbol{B_u}(\xi,\eta)]^T[\boldsymbol{D}][\boldsymbol{B_u}(\xi,\eta)]t|[\boldsymbol{J}(\xi,\eta)]|d\xi d\eta \tag{B-40}$$

where $|[\boldsymbol{J}(\xi,\eta)]|d\xi d\eta = dxdy = A$ and $[\boldsymbol{B_u}(\xi,\eta)]$ can be calculated follow the calculation procedure in Appendix B - 3.

Gauss-Legendre integration formulas (Appendix B - 4) shall be applied to the Equation (B-40) in order to do the numerical integration of the finite element matrix when the boundary of the element is in between -1 to 1 in each direction as shown the final equation used in the in-house FEM program by

$$\left[\boldsymbol{K_{ep}^{sat}}\right] = \sum_{i=1}^{NG}\sum_{j=1}^{NG} w_i w_j \left[\boldsymbol{B_u}(\xi_i,\eta_j)\right]^T [\boldsymbol{D}]\left[\boldsymbol{B_u}(\xi_i,\eta_j)\right]t\left|\left[\boldsymbol{J}(\xi_i,\eta_j)\right]\right| \tag{B-41}$$

B - 5.2 Summary of element matrix formulas

B.5.2.1 Formulation of solid deformation uncoupled FEM for saturated soils

$$\left[\boldsymbol{K_{ep}^{sat}}\right] = \sum_{i=1}^{NG}\sum_{j=1}^{NG} w_i w_j \left[\boldsymbol{B_u}(\xi_i,\eta_j)\right]^T [\boldsymbol{D}]\left[\boldsymbol{B_u}(\xi_i,\eta_j)\right]t\left|\left[\boldsymbol{J}(\xi_i,\eta_j)\right]\right| \tag{B-42}$$

Remarks: For nodal external load vector $\{\boldsymbol{F_{ext}^{\cdot}}\}$ shall be manually defined by the boundary condition which conform to each simulation problems for matrix solving.

B.5.2.2 Formulation of transient state of water seepage uncoupled FEM for saturated soils

$$[\boldsymbol{K_h}] = \sum_{i=1}^{NG}\sum_{j=1}^{NG} w_i w_j \left[\boldsymbol{B_{u_w}}(\xi_i,\eta_j)\right]^T [\boldsymbol{K_w}]\left[\boldsymbol{B_{u_w}}(\xi_i,\eta_j)\right]t\left|\left[\boldsymbol{J}(\xi_i,\eta_j)\right]\right| \tag{B-43}$$

$$[\boldsymbol{M_m}] = \sum_{i=1}^{NG}\sum_{j=1}^{NG} w_i w_j \left[\boldsymbol{N_{u_w}}(\xi_i,\eta_j)\right]^T \left[\boldsymbol{N_{u_w}}(\xi_i,\eta_j)\right]^T t\left|\left[\boldsymbol{J}(\xi_i,\eta_j)\right]\right| \tag{B-44}$$

Remarks: The inflows or outflows nodal vector $\{\boldsymbol{Q}\}$ shall be manually defined by the boundary condition which conform to each simulation problems for matrix solving.

B.5.2.3 Formulation of soil – water two – phase seepage – deformation coupled FEM for saturated soils

See Equation (B-42) and (B-43) for the calculation of $\left[\boldsymbol{K_{ep}^{sat}}\right]$ and $[\boldsymbol{K_h}]$, respectively. Addition coefficient matrix are shown as follow;

$$[\boldsymbol{I}] = \sum_{i=1}^{NG}\sum_{j=1}^{NG} w_i w_j \left[\boldsymbol{B_u}(\xi_i,\eta_j)\right]^T \{\boldsymbol{m}\}\left[\boldsymbol{N_{u_w}}(\xi_i,\eta_j)\right] t \left|\left[\boldsymbol{J}(\xi_i,\eta_j)\right]\right| \tag{B-45}$$

$$[\boldsymbol{I^T}] = \sum_{i=1}^{NG}\sum_{j=1}^{NG} w_i w_j \left[\boldsymbol{N_{u_w}}(\xi_i,\eta_j)\right]^T \{\boldsymbol{m}\}^T\left[\boldsymbol{B_u}(\xi_i,\eta_j)\right] t \left|\left[\boldsymbol{J}(\xi_i,\eta_j)\right]\right| \tag{B-46}$$

Remarks: Nodal external load vector $\left\{\dot{\boldsymbol{F_{ext}}}\right\}$ and inflows or outflows nodal vector $\{\boldsymbol{Q}\}$ shall be manually defined by the boundary condition which conform to each simulation problems for matrix solving.

B.5.2.4 Formulation of soil – water – air three – phase seepage – deformation coupled FEM for unsaturated soils (constant air pressure)

$$\begin{aligned}\left[\boldsymbol{K_{ep}^{unsat}}\right] = \sum_{i=1}^{NG}\sum_{j=1}^{NG} w_i w_j \ &\left[\boldsymbol{B_u}(\xi_i,\eta_j)\right]^T \big([\boldsymbol{D}]\left[\boldsymbol{B_u}(\xi_i,\eta_j)\right] \\ &- [\boldsymbol{D^{sr}}]E^V\{\boldsymbol{m}\}^T\left[\boldsymbol{B_u}(\xi_i,\eta_j)\right] \\ &- \{\boldsymbol{m}\}(u_a-u_w)E^V\{\boldsymbol{m}\}^T\left[\boldsymbol{B_u}(\xi_i,\eta_j)\right]\big)\, t\left|\left[\boldsymbol{J}(\xi_i,\eta_j)\right]\right|\end{aligned} \tag{B-47}$$

$$\begin{aligned}[\boldsymbol{L}] = \sum_{i=1}^{NG}\sum_{j=1}^{NG} w_i w_j \ &\left[\boldsymbol{B_u}(\xi_i,\eta_j)\right]^T \left(-[\boldsymbol{D^{sr}}]E^W\left[\boldsymbol{N_{u_w}}(\xi_i,\eta_j)\right]\right. \\ &+ \{\boldsymbol{m}\}S_r\left[\boldsymbol{N_{u_w}}(\xi_i,\eta_j)\right] \\ &\left.- \{\boldsymbol{m}\}(u_a-u_w)E^W\left[\boldsymbol{N_{u_w}}(\xi_i,\eta_j)\right]\right) t\left|\left[\boldsymbol{J}(\xi_i,\eta_j)\right]\right|\end{aligned} \tag{B-48}$$

$$\begin{aligned}[\boldsymbol{M}] = \sum_{i=1}^{NG}\sum_{j=1}^{NG} w_i w_j \ &\left[\boldsymbol{N_{u_w}}(\xi_i,\eta_j)\right]^T \left(S_r\{\boldsymbol{m}\}^T\left[\boldsymbol{B_u}(\xi_i,\eta_j)\right]\right. \\ &\left.- n_e E^V\{\boldsymbol{m}\}^T\left[\boldsymbol{B_u}(\xi_i,\eta_j)\right]\right) t\left|\left[\boldsymbol{J}(\xi_i,\eta_j)\right]\right|\end{aligned} \tag{B-49}$$

$$[\boldsymbol{R}] = \sum_{i=1}^{NG}\sum_{j=1}^{NG} w_i w_j \left[\boldsymbol{N_{u_w}}(\xi_i,\eta_j)\right]^T n_e E^W\left[\boldsymbol{N_{u_w}}(\xi_i,\eta_j)\right] t\left|\left[\boldsymbol{J}(\xi_i,\eta_j)\right]\right| \tag{B-50}$$

$$[\boldsymbol{P}] = \sum_{i=1}^{NG}\sum_{j=1}^{NG} w_i w_j \left[\boldsymbol{B_{u_w}}(\xi_i,\eta_j)\right]^T [\boldsymbol{K_w}]\left[\boldsymbol{B_{u_w}}(\xi_i,\eta_j)\right] t\left|\left[\boldsymbol{J}(\xi_i,\eta_j)\right]\right| \tag{B-51}$$

Remarks: Nodal external load vector $\{\dot{\boldsymbol{F}}_{\boldsymbol{ext}}\}$ and inflows or outflows nodal vector $\{\boldsymbol{Q}\}$ shall be manually defined by the boundary condition which conform to each simulation problems for matrix solving.

B - 6 TIME DISCRETIZATION

Considering the ordinary differential equation with the small increment of time h_t and Euler's method, we will get the approximation of pore pressure and displacement for nonlinear problem as following equations.

For nodal pore water pressure and distribution of pore water pressure vectors:

$$\{\dot{\boldsymbol{U}}_{\boldsymbol{w}}\} = \frac{\{\boldsymbol{\Delta U}_{\boldsymbol{w}}\}}{h_t} = \frac{\{\boldsymbol{U}_{\boldsymbol{w|t+h_t}}\} - \{\boldsymbol{U}_{\boldsymbol{w|t}}\}}{h_t} \tag{B-52}$$

$$\{\boldsymbol{U}_{\boldsymbol{w}}\} = \theta\{\boldsymbol{U}_{\boldsymbol{w|t+h_t}}\} + (1-\theta)\{\boldsymbol{U}_{\boldsymbol{w|t}}\} \tag{B-53}$$

For nodal displacement and strain vectors:

$$\{\dot{\boldsymbol{U}}\} = \frac{\{\boldsymbol{\Delta U}\}}{h_t} = \frac{\{\boldsymbol{U}_{\boldsymbol{|t+h_t}}\} - \{\boldsymbol{U}_{\boldsymbol{|t}}\}}{h_t} \tag{B-54}$$

$$\{\boldsymbol{U}\} = \theta\{\boldsymbol{U}_{\boldsymbol{|t+h_t}}\} + (1-\theta)\{\boldsymbol{U}_{\boldsymbol{|t}}\} \tag{B-55}$$

For nodal external force vector:

$$\{\dot{\boldsymbol{F}}_{\boldsymbol{ext}}\} = \frac{\{\boldsymbol{\Delta F}_{\boldsymbol{ext}}\}}{h_t} \tag{B-56}$$

B - 6.1 Formulation of transient state of water seepage uncoupled FEM for saturated soils

From Equation (5-75), in the matrix form, the element equation can be written as

$$[\boldsymbol{K_h}]\{\boldsymbol{U}_{\boldsymbol{w}}\} + [\boldsymbol{M_m}]\{\dot{\boldsymbol{U}}_{\boldsymbol{w}}\} = \{\boldsymbol{Q}\}$$

Substituting Equation (B-52) and (B-53) into the element equation, we will get

$$\theta[\boldsymbol{K_h}]\{\boldsymbol{U}_{\boldsymbol{w|t+h_t}}\} + (1-\theta)[\boldsymbol{K_h}]\{\boldsymbol{U}_{\boldsymbol{w|t}}\} + [\boldsymbol{M_m}]\frac{\{\boldsymbol{U}_{\boldsymbol{w|t+h_t}}\}}{h_t} + [\boldsymbol{M_m}]\frac{\{\boldsymbol{U}_{\boldsymbol{w|t}}\}}{h_t} = \{\boldsymbol{Q}\} \tag{B-57}$$

$$\theta h_t[\boldsymbol{K_h}]\{\boldsymbol{U}_{\boldsymbol{w|t+h_t}}\} + (1-\theta)h_t[\boldsymbol{K_h}]\{\boldsymbol{U}_{\boldsymbol{w|t}}\} + [\boldsymbol{M_m}]\{\boldsymbol{U}_{\boldsymbol{w|t+h_t}}\} + [\boldsymbol{M_m}]\{\boldsymbol{U}_{\boldsymbol{w|t}}\} = h_t\{\boldsymbol{Q}\} \tag{B-58}$$

Finally, arranging the Equation (B-58), we will get the time discretization of the global equation system as shown below.

$$(\theta h_t[\boldsymbol{K_h}] + [\boldsymbol{M_m}])\{\boldsymbol{U}_{\boldsymbol{w|t+h_t}}\} = h_t\{\boldsymbol{Q}\} + ([\boldsymbol{M_m}] - (1-\theta)h_t[\boldsymbol{K_h}])\{\boldsymbol{U}_{\boldsymbol{w|t}}\} \tag{B-59}$$

B - 6.2 Formulation of soil – water two – phase seepage – deformation coupled FEM for saturated soils

From Equation (5-82), in the matrix form, the element equation can be written as

$$\left[\boldsymbol{K_{ep}^{sat}}\right]\{\dot{\boldsymbol{U}}\} + [\boldsymbol{I}]\{\dot{\boldsymbol{U}_w}\} = \{\dot{\boldsymbol{F}}_{\boldsymbol{ext}}\}$$

Substituting Equation (B-52) and (B-54) into the element equation, we will get

$$\left[\boldsymbol{K_{ep}^{sat}}\right]\frac{\{\boldsymbol{\Delta U}\}}{h_t} + [\boldsymbol{I}]\frac{\left\{\boldsymbol{U}_{\boldsymbol{w}|\boldsymbol{t}+\boldsymbol{h_t}}\right\} - \left\{\boldsymbol{U}_{\boldsymbol{w}|\boldsymbol{t}}\right\}}{h_t} = \frac{\{\boldsymbol{\Delta F}_{\boldsymbol{ext}}\}}{h_t} \tag{B-60}$$

$$\left[\boldsymbol{K_{ep}^{sat}}\right]\{\boldsymbol{\Delta U}\} + [\boldsymbol{I}]\left\{\boldsymbol{U}_{\boldsymbol{w}|\boldsymbol{t}+\boldsymbol{h_t}}\right\} = \{\boldsymbol{\Delta F}_{\boldsymbol{ext}}\} + [\boldsymbol{I}]\left\{\boldsymbol{U}_{\boldsymbol{w}|\boldsymbol{t}}\right\} \tag{B-61}$$

From Equation (5-94), in the matrix form, the element equation can be written as

$$[\boldsymbol{I^T}]\{\dot{\boldsymbol{U}}\} - [\boldsymbol{K_h}]\{\boldsymbol{U_w}\} = \{\boldsymbol{Q}\}$$

Substituting Equation (B-53) and (B-54) into the element equation, we will get

$$[\boldsymbol{I^T}]\frac{\{\boldsymbol{\Delta U}\}}{h_t} - [\boldsymbol{K_h}](\theta\left\{\boldsymbol{U}_{\boldsymbol{w}|\boldsymbol{t}+\boldsymbol{h_t}}\right\} + (1-\theta)\left\{\boldsymbol{U}_{\boldsymbol{w}|\boldsymbol{t}}\right\}) = \{\boldsymbol{Q}\} \tag{B-62}$$

$$[\boldsymbol{I^T}]\{\boldsymbol{\Delta U}\} - \theta[\boldsymbol{K_h}]h_t\left[\boldsymbol{U}_{\boldsymbol{w}|\boldsymbol{t}+\boldsymbol{h_t}}\right] = h_t\{\boldsymbol{Q}\} + (1-\theta)h_t[\boldsymbol{K_h}]\left\{\boldsymbol{U}_{\boldsymbol{w}|\boldsymbol{t}}\right\} \tag{B-63}$$

Rewriting Equation (B-61) and (B-63) in the matrix form, coupled time discretization equation is shown below.

$$\begin{bmatrix} \boldsymbol{K_{ep}^{sat}} & \boldsymbol{I} \\ \boldsymbol{I}^T & -\theta\boldsymbol{K_h}h_t \end{bmatrix}\begin{Bmatrix} \boldsymbol{\Delta U} \\ \boldsymbol{U}_{\boldsymbol{w}|\boldsymbol{t}+\boldsymbol{h_t}} \end{Bmatrix} = \begin{Bmatrix} \boldsymbol{\Delta F_{ext}} + \boldsymbol{I U_{w|t}} \\ h_t\boldsymbol{Q} + (1-\theta)h_t\boldsymbol{K_h U_{w|t}} \end{Bmatrix} \tag{B-64}$$

B - 6.3 Formulation of soil – water – Air Three – Phase Seepage – Deformation Coupled Finite Element Method (Constant air pressure) for Unsaturated Condition

From Equation (5-107), in the matrix form, the element equation can be written as

$$\left[\boldsymbol{K_{ep}^{unsat}}\right]\{\dot{\boldsymbol{U}}\} + [\boldsymbol{L}]\{\dot{\boldsymbol{U}_w}\} = \{\dot{\boldsymbol{F}}_{\boldsymbol{ext}}\}$$

Substituting Equation (B-52) and (B-54) into the element equation, we will get

$$\left[\boldsymbol{K_{ep}^{unsat}}\right]\frac{\{\boldsymbol{\Delta U}\}}{h_t} + [\boldsymbol{L}]\frac{\left\{\boldsymbol{U}_{\boldsymbol{w}|\boldsymbol{t}+\boldsymbol{h_t}}\right\} - \left\{\boldsymbol{U}_{\boldsymbol{w}|\boldsymbol{t}}\right\}}{h_t} = \frac{\{\boldsymbol{\Delta F}_{\boldsymbol{ext}}\}}{h_t} \tag{B-65}$$

$$\left[\boldsymbol{K_{ep}^{unsat}}\right]\{\boldsymbol{\Delta U}\} + [\boldsymbol{L}]\left\{\boldsymbol{U}_{\boldsymbol{w}|\boldsymbol{t}+\boldsymbol{h_t}}\right\} = \{\boldsymbol{\Delta F}_{\boldsymbol{ext}}\} + [\boldsymbol{L}]\left\{\boldsymbol{U}_{\boldsymbol{w}|\boldsymbol{t}}\right\} \tag{B-66}$$

From Equation (5-123), in the matrix form, the element equation can be written as

$$[\boldsymbol{M}]\{\dot{\boldsymbol{U}}\} - [\boldsymbol{R}]\{\dot{\boldsymbol{U}}_{\boldsymbol{w}}\} - [\boldsymbol{P}]\{\boldsymbol{U_w}\} = \{\boldsymbol{Q}\}$$

$$[\boldsymbol{M}]\frac{\{\boldsymbol{\Delta U}\}}{h_t} - [\boldsymbol{R}]\frac{\{\boldsymbol{U_{w|t+h_t}}\} - \{\boldsymbol{U_{w|t}}\}}{h_t} - [\boldsymbol{P}](\theta\{\boldsymbol{U_{w|t+h_t}}\} + (1-\theta)\{\boldsymbol{U_{w|t}}\}) = \{\boldsymbol{Q}\} \quad \text{(B-67)}$$

$$[\boldsymbol{M}]\{\boldsymbol{\Delta U}\} - ([\boldsymbol{R}] + \theta[\boldsymbol{P}]h_t)\{\boldsymbol{U_{w|t+h_t}}\} = h_t\{\boldsymbol{Q}\} + ((1-\theta)h_t[\boldsymbol{P}] - [\boldsymbol{R}])\{\boldsymbol{U_{w|t}}\} \quad \text{(B-68)}$$

Rewriting Equation (B-66) and (B-68) in the matrix form, coupled time discretization equation is shown below.

$$\begin{bmatrix} \boldsymbol{K_{ep}^{unsat}} & \boldsymbol{L} \\ \boldsymbol{M} & -(\theta \boldsymbol{P} h_t + \boldsymbol{R}) \end{bmatrix} \begin{Bmatrix} \boldsymbol{\Delta U} \\ \boldsymbol{U_{w|t+h_t}} \end{Bmatrix} = \begin{Bmatrix} \boldsymbol{\Delta F_{ext}} + \boldsymbol{L U_{w|t}} \\ h_t \boldsymbol{Q} + ((1-\theta)h_t \boldsymbol{P} - \boldsymbol{R})\boldsymbol{U_{w|t}} \end{Bmatrix} \quad \text{(B-69)}$$

B - 7 DETERMINATIONS OF E^W AND E^V

From time derivation of degree of saturation $\dot{S}_r$ in Equation (A-3), E^W and E^V could be determined by substituting $\dot{s} = -\dot{u_w}$ based on the assumption of $\dot{u_a} = 0$ as

$$\dot{S}_r = \frac{-\frac{\partial S_r}{\partial s}\dot{u_w} - \frac{\partial S_r}{\partial v}v_0\dot{\varepsilon_v}}{1 - \frac{\partial S_r}{\partial I_h}\frac{dI_h}{dS_r}} \quad \text{(B-70)}$$

Equation (B-70) can be written in the compacted form as shown in Equation (5-103) where

$$E^W = \frac{-\frac{\partial S_r}{\partial s}}{1 - \frac{\partial S_r}{\partial I_h}\frac{dI_h}{dS_r}} \quad \text{(B-71)}$$

$$E^V = \frac{-\frac{\partial S_r}{\partial v}v_0}{1 - \frac{\partial S_r}{\partial I_h}\frac{dI_h}{dS_r}} \quad \text{(B-72)}$$

APPENDIX C

FEM VALIDATION RESULTS

C - 1 FEM VALIDATION RESULTS THROUGH THE TERZAGHI'S THEORY OF CONSOLIDATION

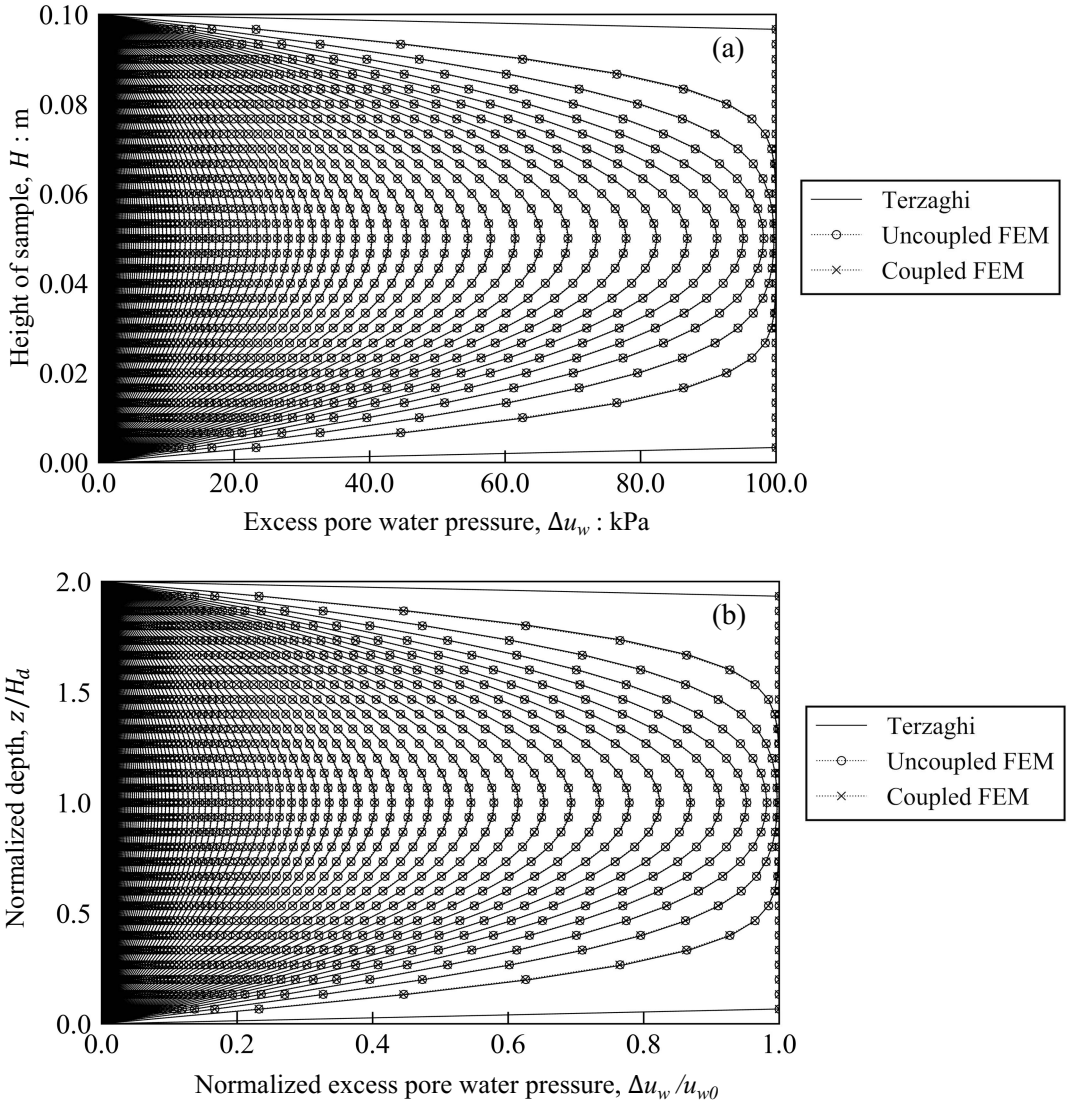

Figure C-1 FEM validation: a) excess pore water pressure distribution and b) normalized excess pore water pressure of 1-D consolidation test

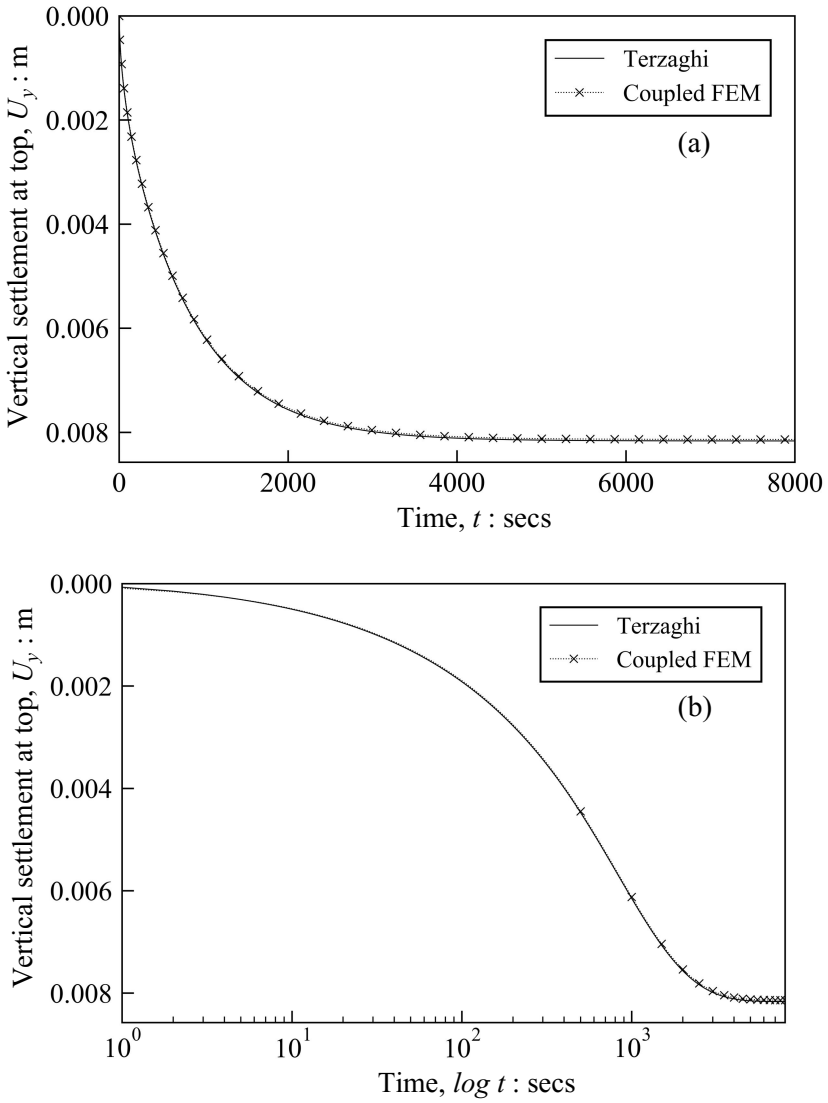

Figure C-2 FEM validation: vertical settlement at top of the sample of 1-D consolidation test a) t-plot and b) $log\ t$ - plot

C - 2 FEM VALIDATION RESULTS THROUGH THE SIMULATION OF PROPOSED ELASTOPLASTIC CONSTITUTIVE MODEL FOR SATURATED SOIL

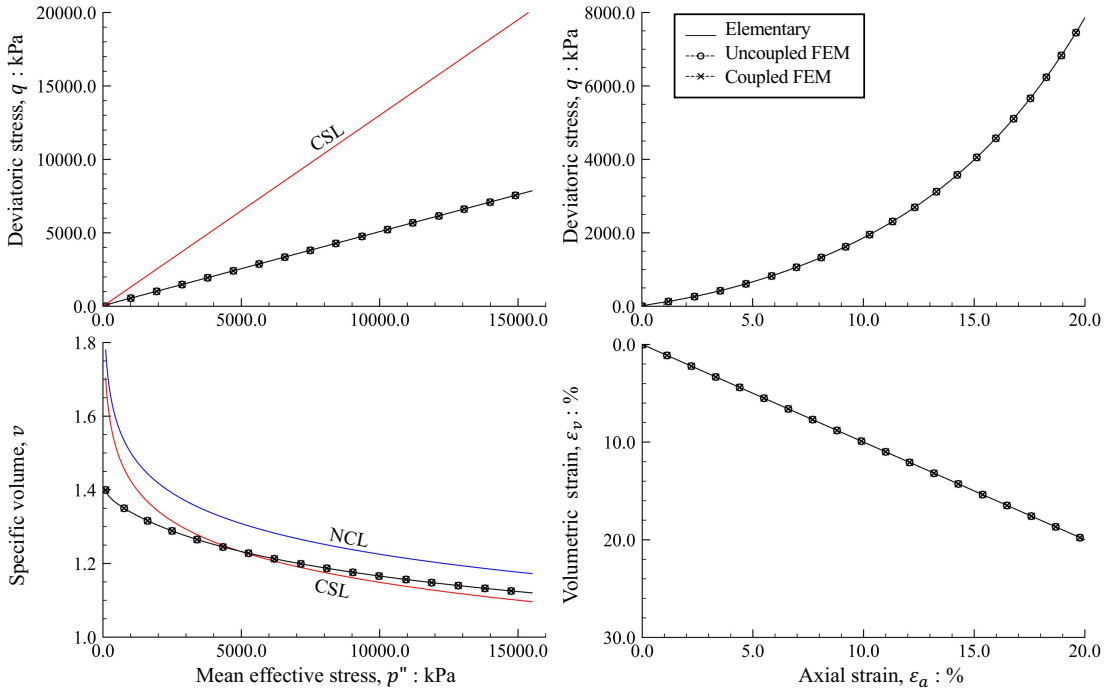

Figure C-3 1-D compression test of saturated soil under water drained condition (Case 1DS)

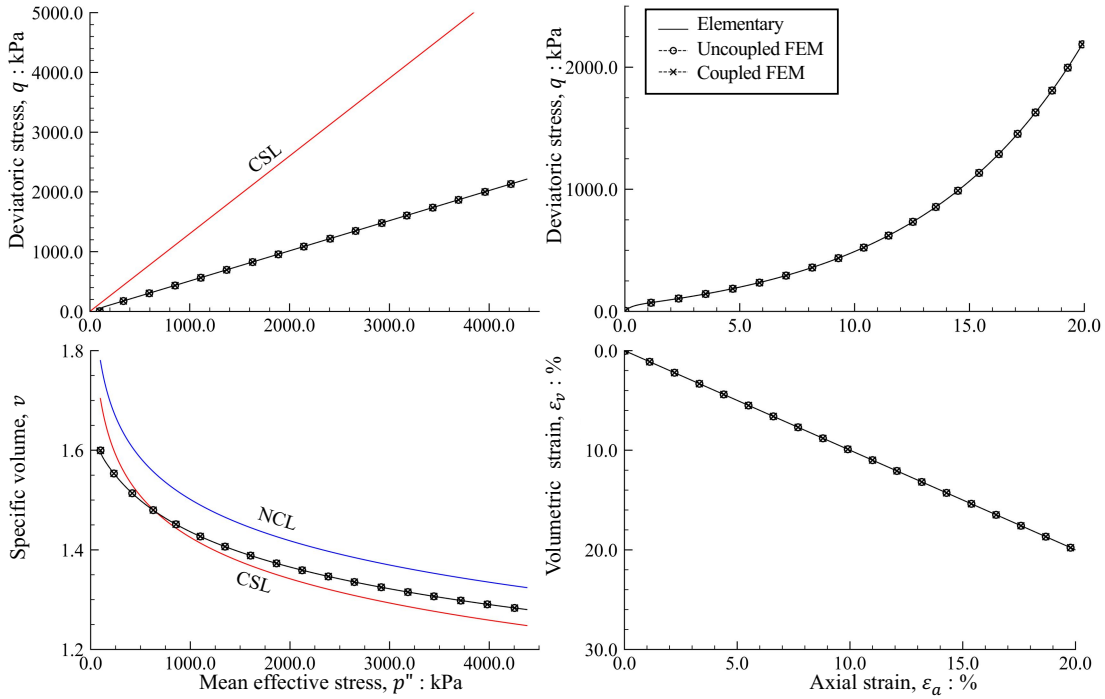

Figure C-4 1-D compression test of saturated soil under water drained condition (Case 1LS)

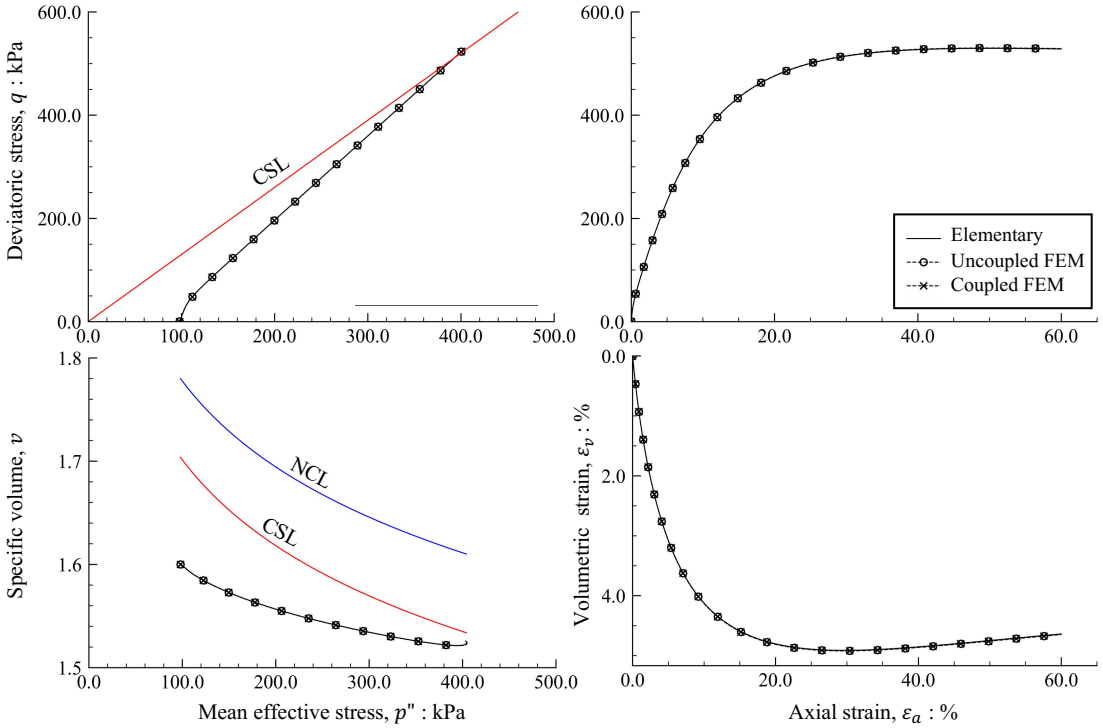

Figure C-5 Biaxial radial constant shearing test of saturated soil under water drained condition (Case 2LS)

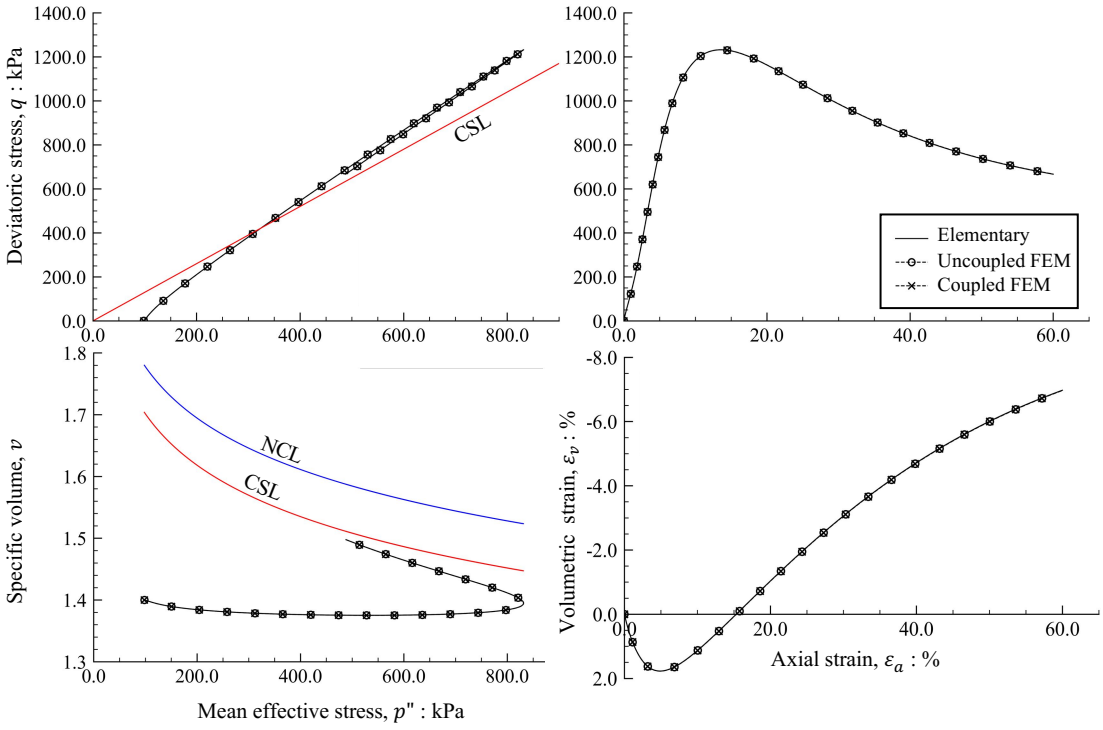

Figure C-6 Biaxial radial constant shearing test of saturated soil under water drained condition (Case 2DS)

C - 3 FEM VALIDATION RESULTS OF SOIL-WATER-AIR THREE-PHASE SEEPAGE-DEFORMATION COUPLED FEM FOR UNSATURATED SOILS

C - 3.1 Stress – strain behaviors

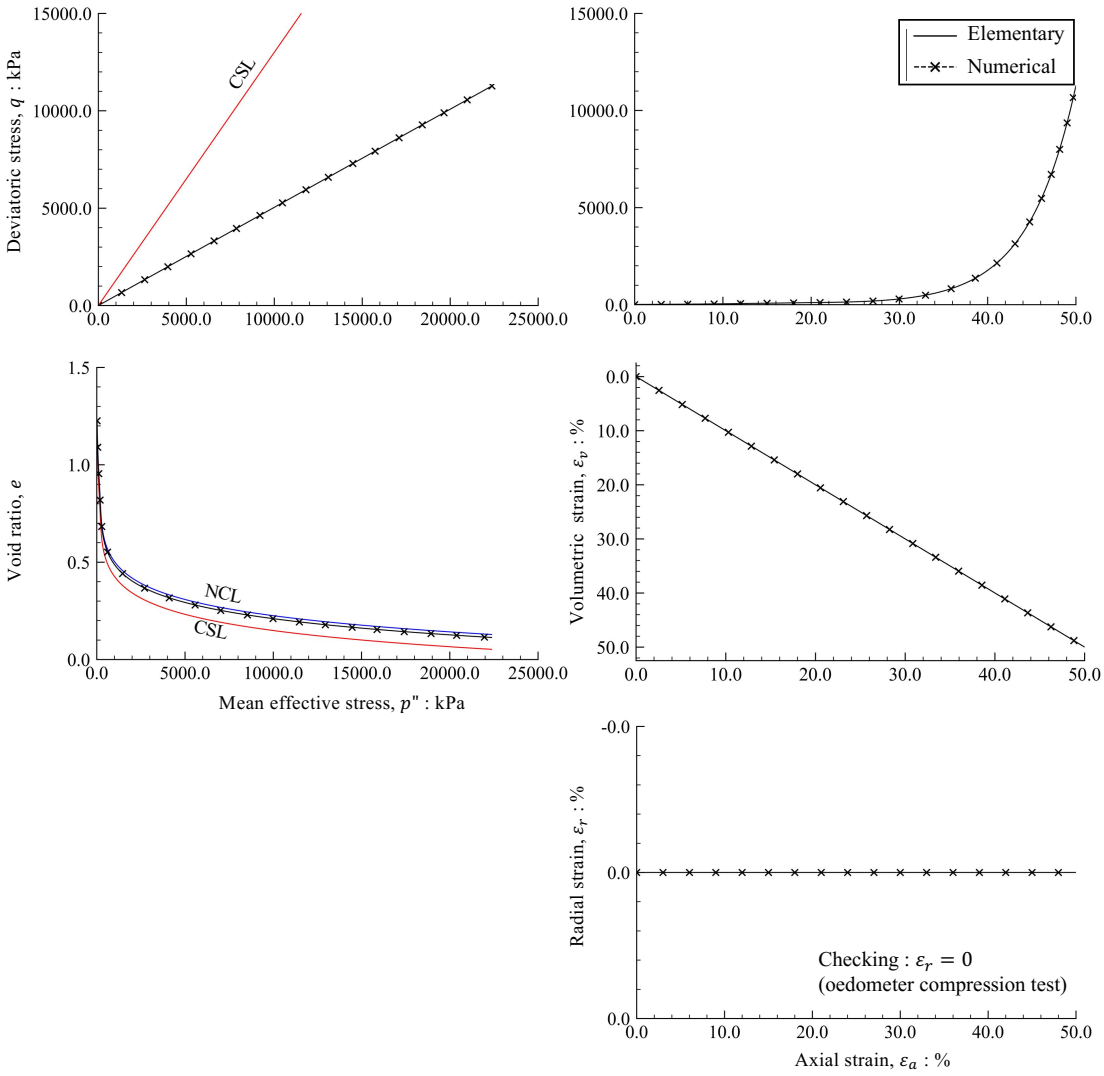

Figure C-7 Stress – strain behaviors of validation Case 1L for unsaturated soil

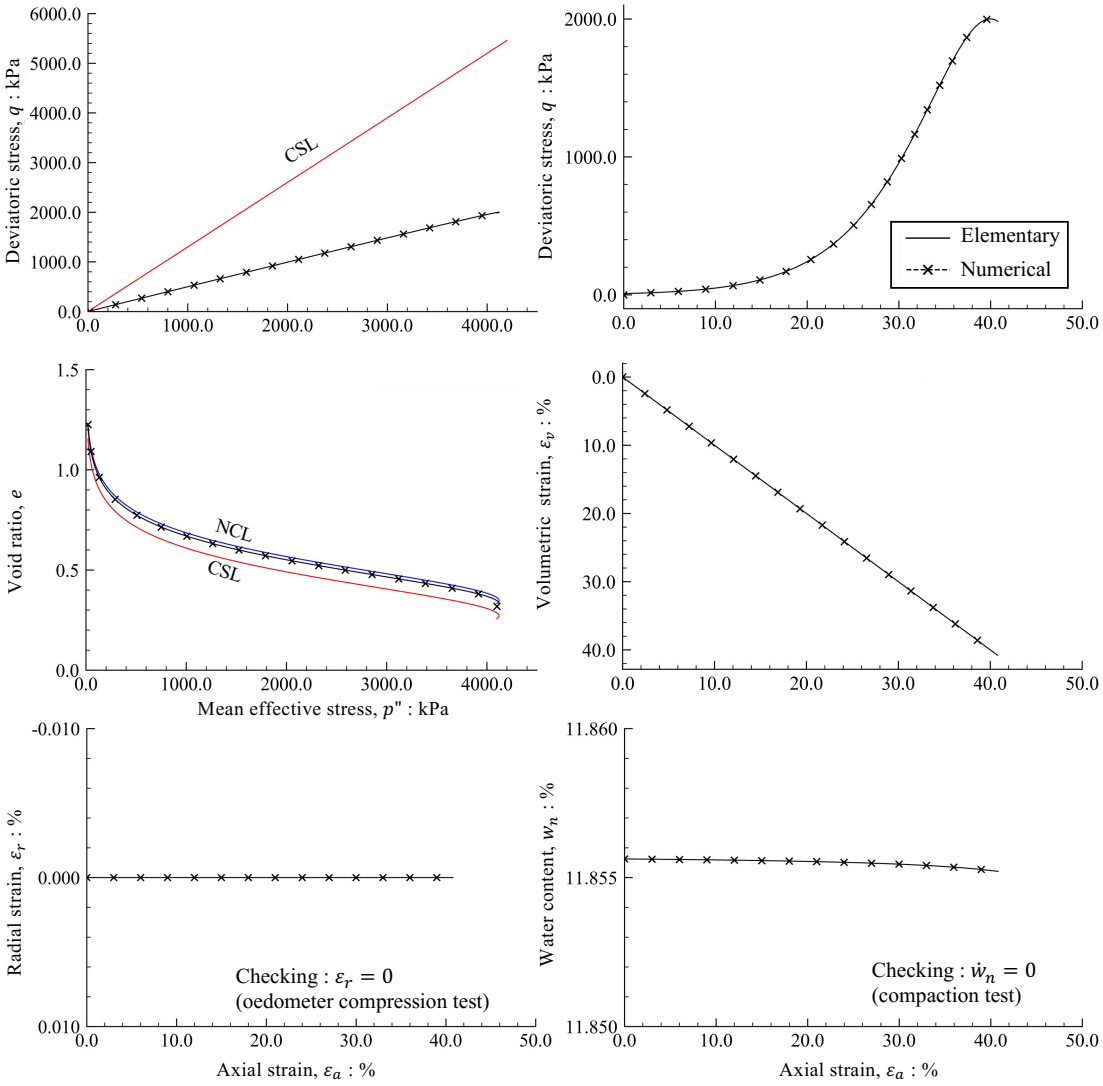

Figure C-8 Stress – strain behaviors of validation Case 2L for unsaturated soil

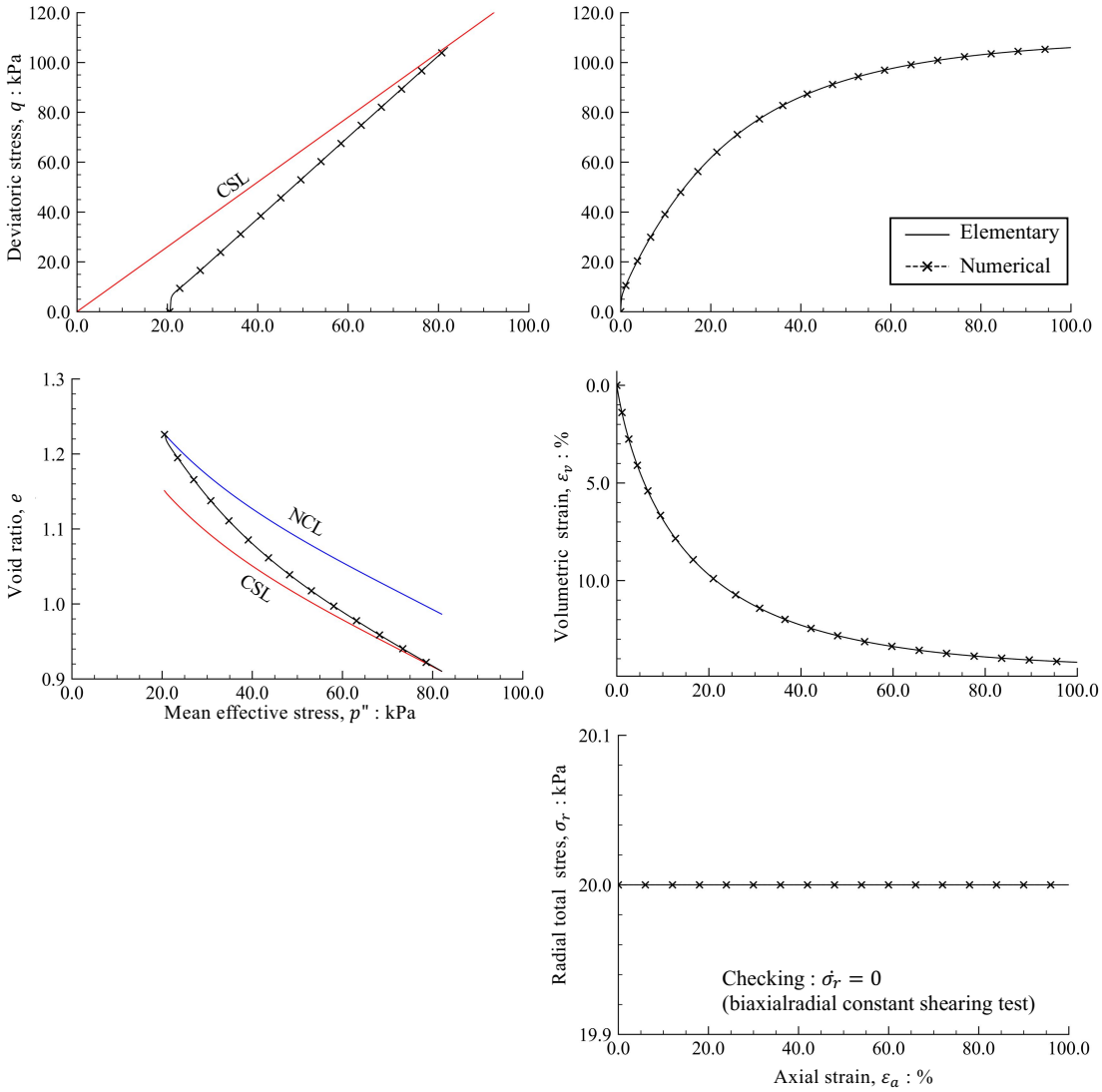

Figure C-9 Stress – strain behaviors of validation case 3L for unsaturated soil

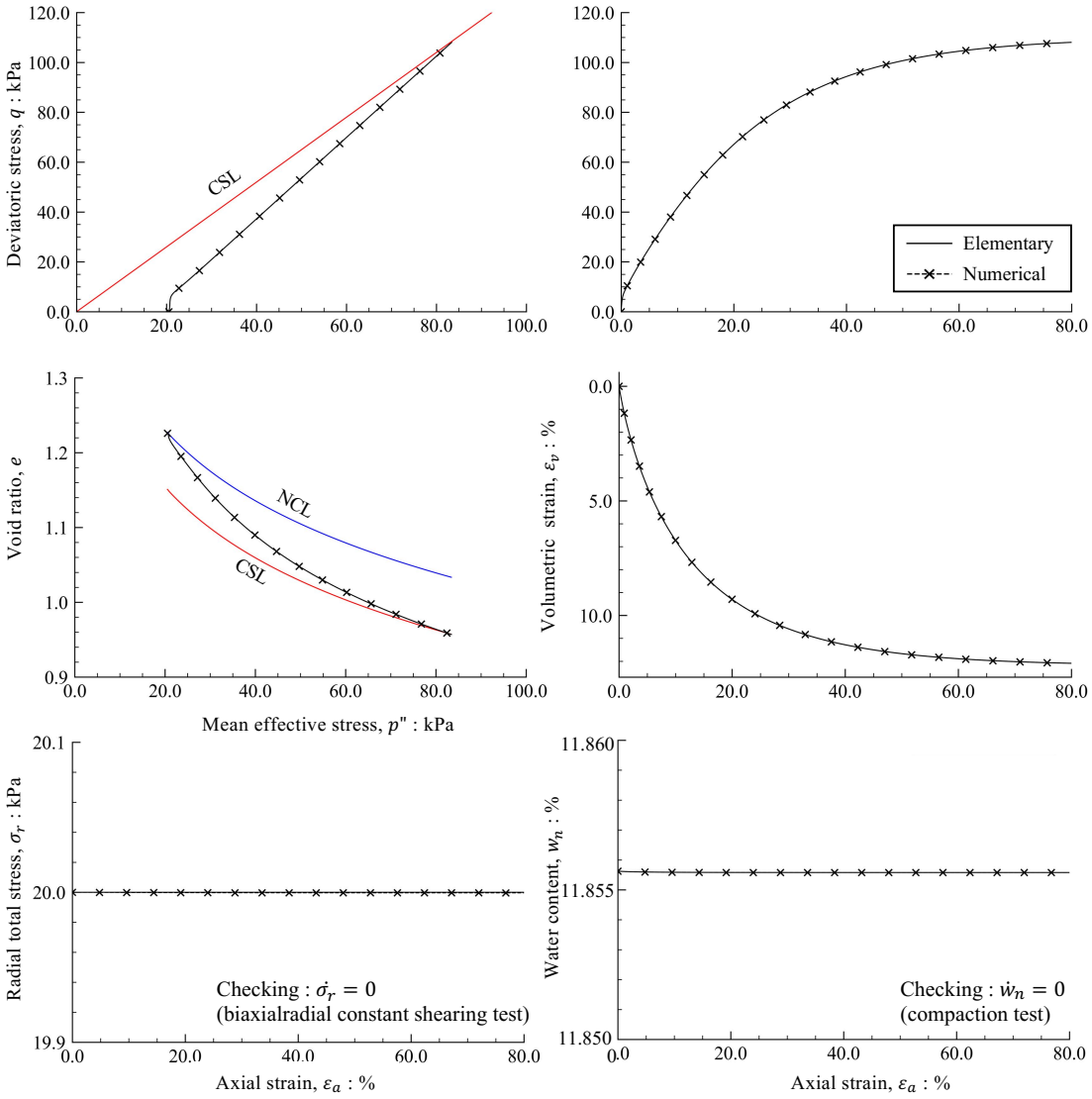

Figure C-10 Stress – strain behaviors of validation Case 4L for unsaturated soil

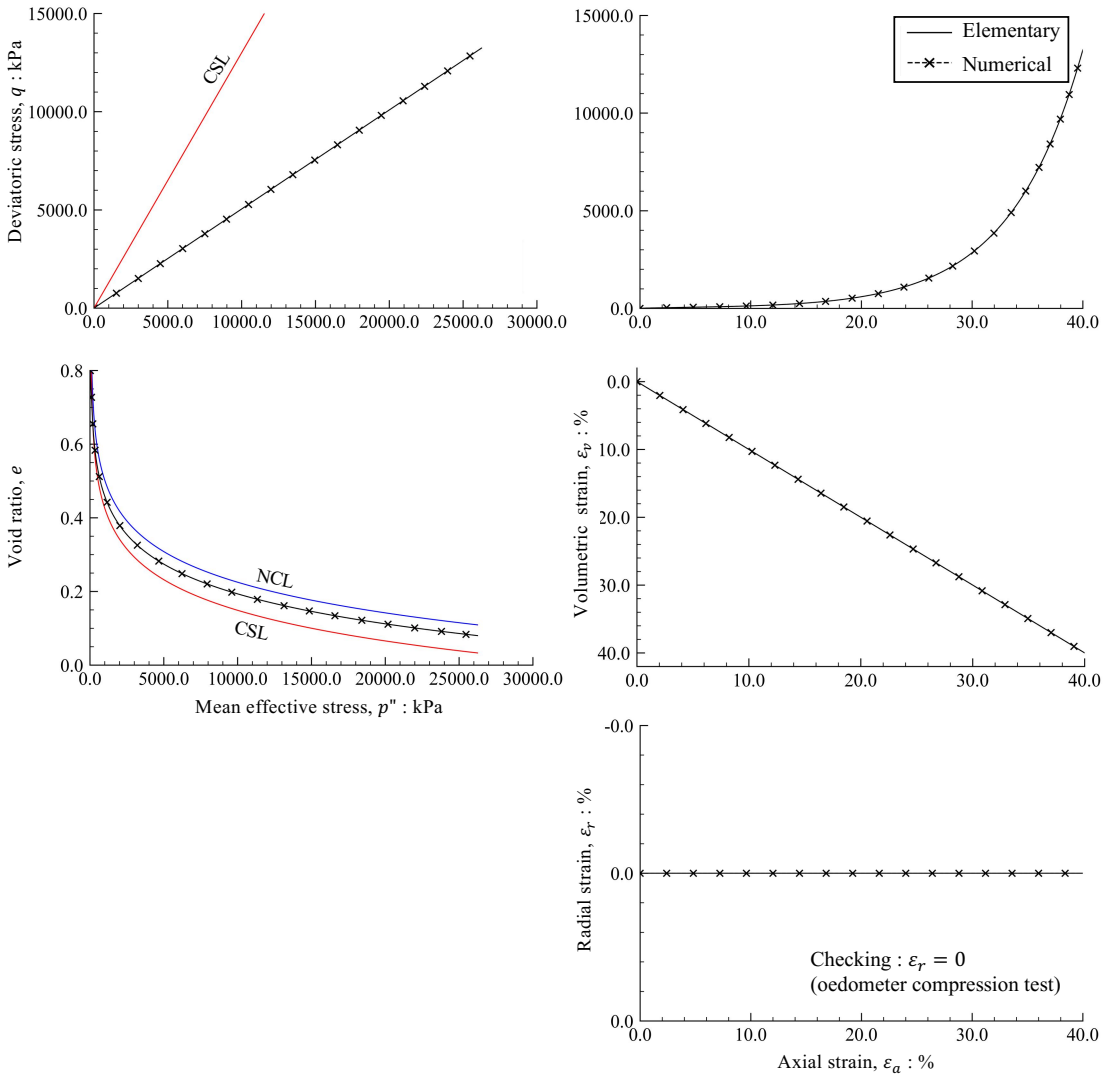

Figure C-11 Stress – strain behaviors of validation Case 1D for unsaturated soil

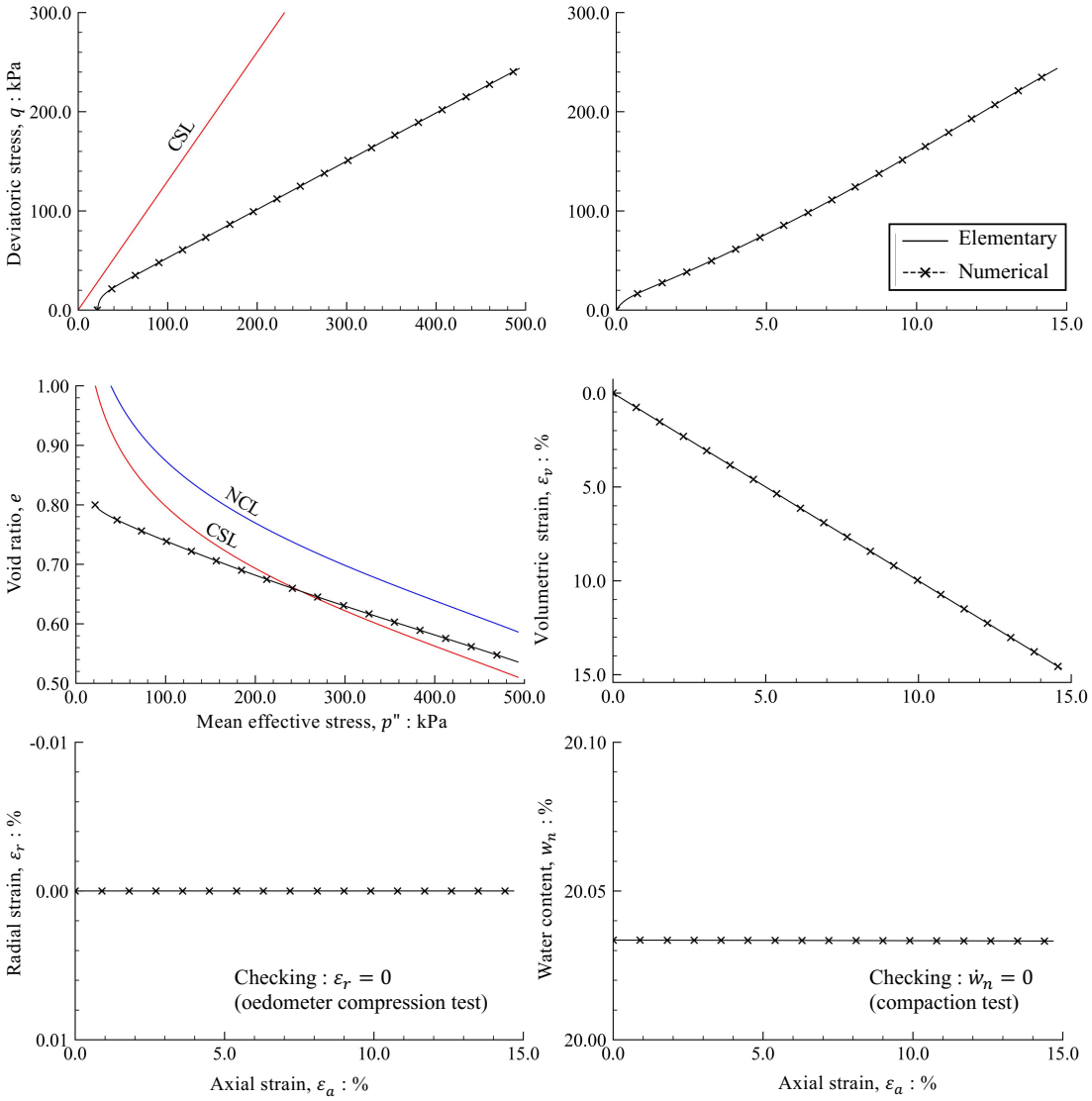

Figure C-12 Stress – strain behaviors of validation Case 2D for unsaturated soil

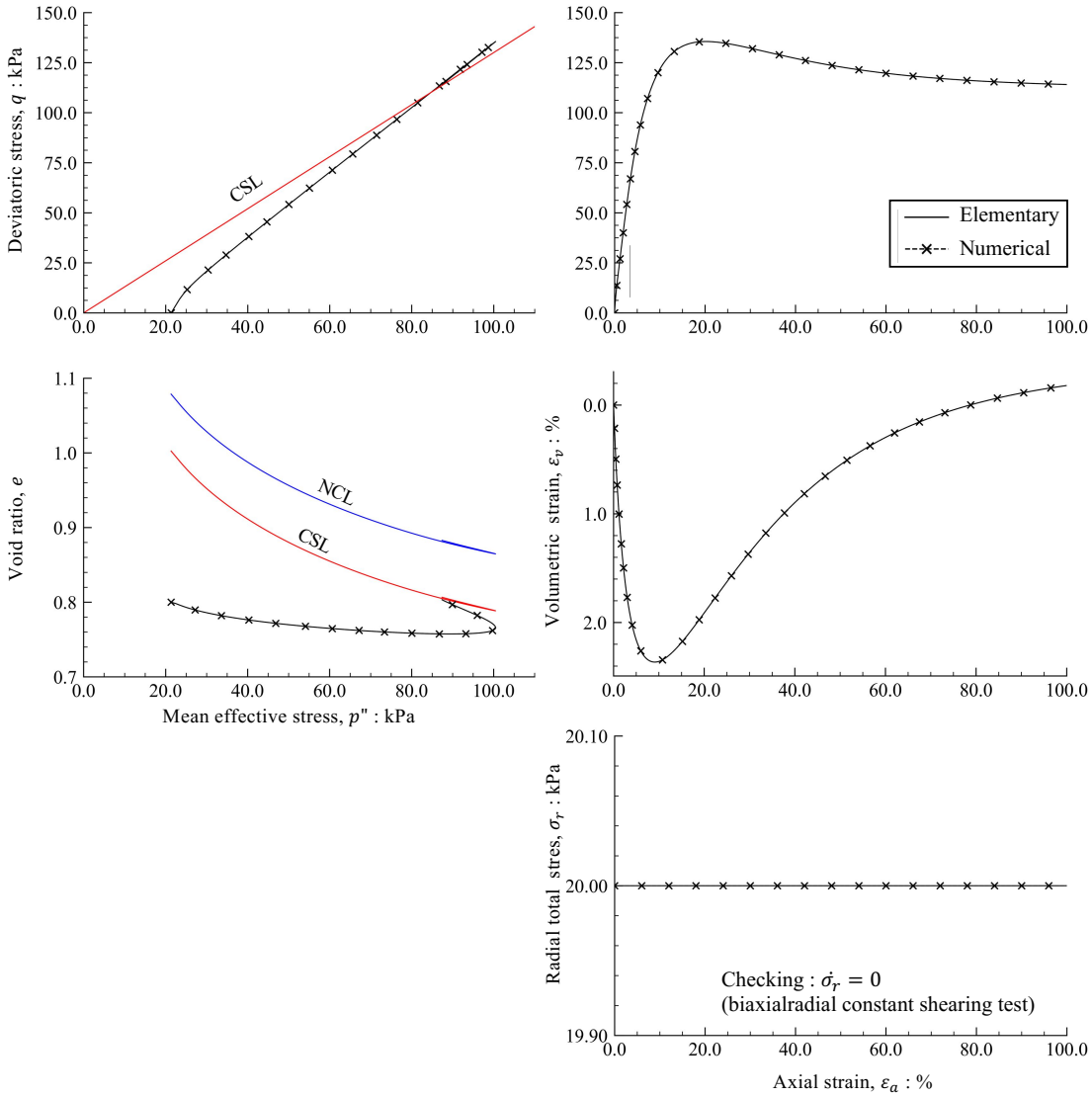

Figure C-13 Stress – strain behaviors of validation Case 3D for unsaturated soil

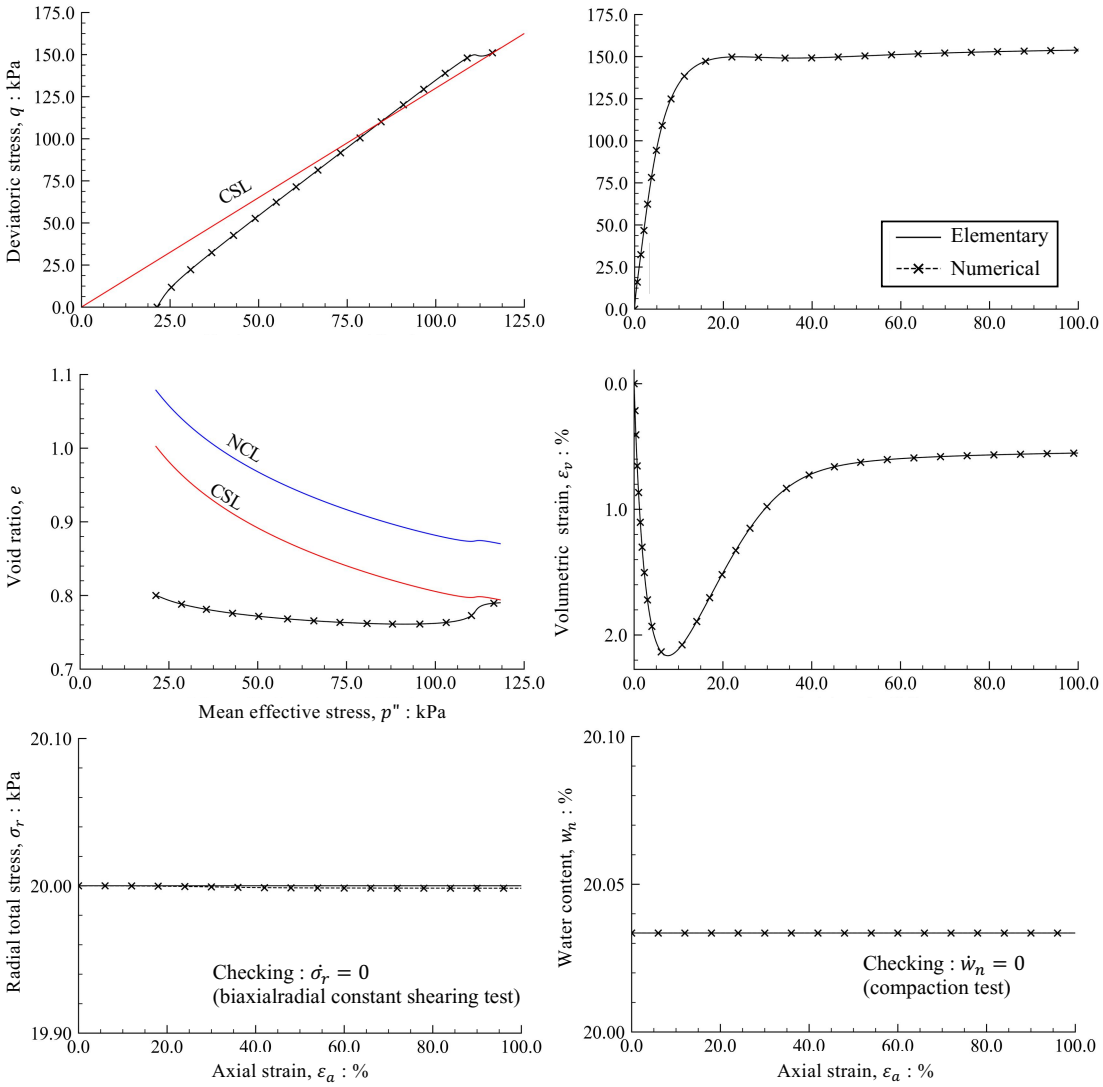

Figure C-14 Stress – strain behaviors of validation Case 3D for unsaturated soil

C - 3.2 Degree of saturation variations

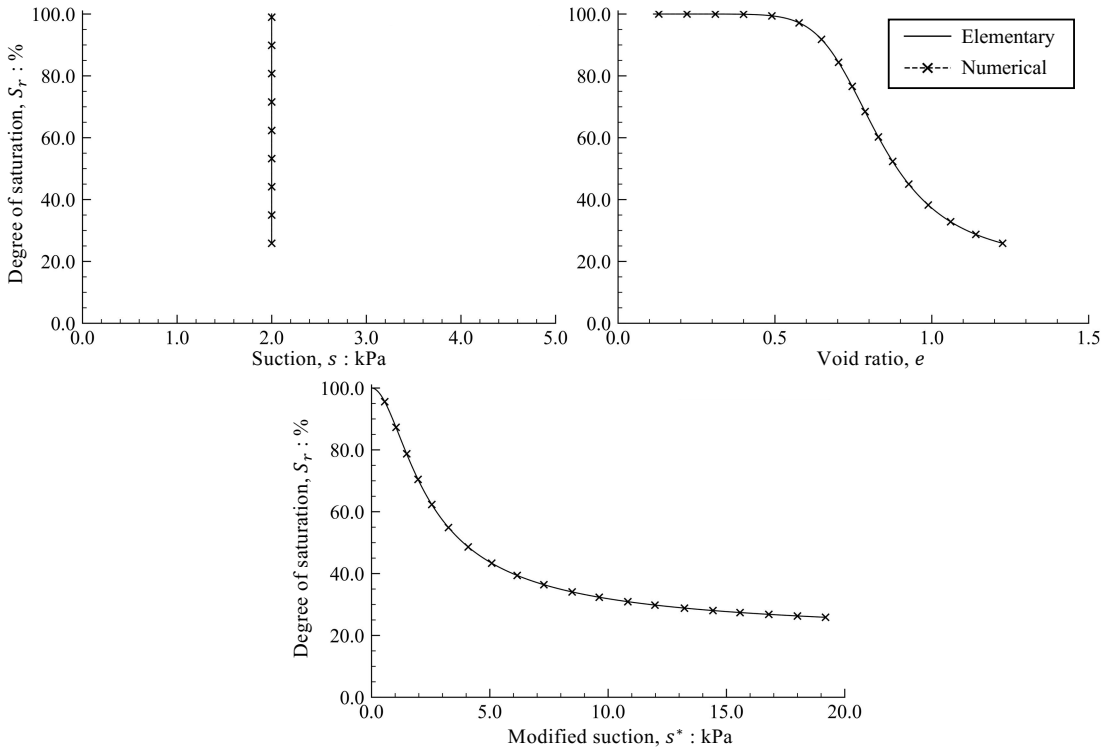

Figure C-15 S_r variation of valdation Case 1L for unsaturated soil

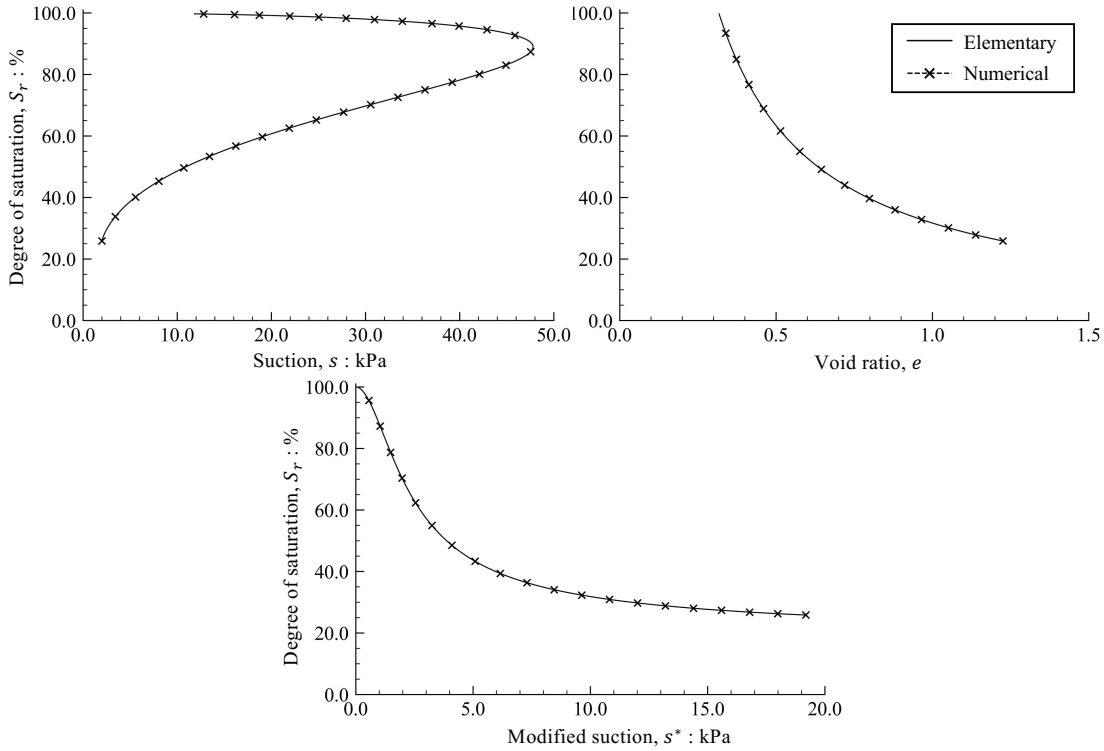

Figure C-16 S_r variation of validation Case 2L for unsaturated soil

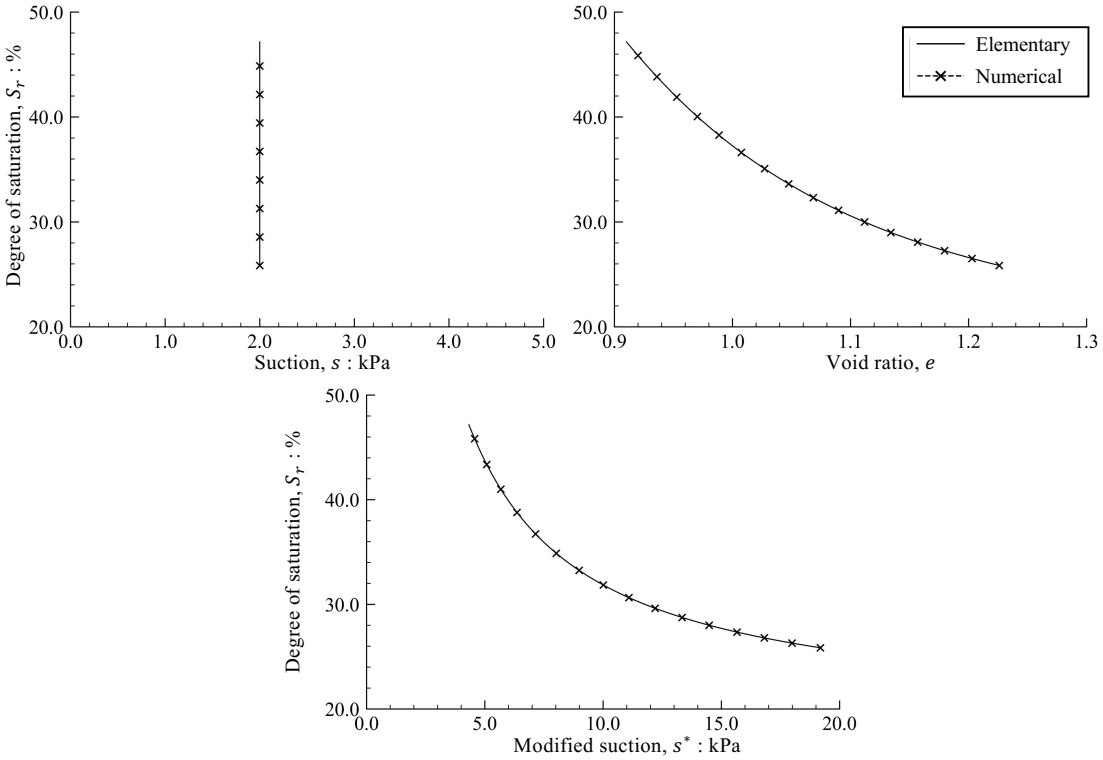

Figure C-17 S_r variation of validation Case 3L for unsaturated soil

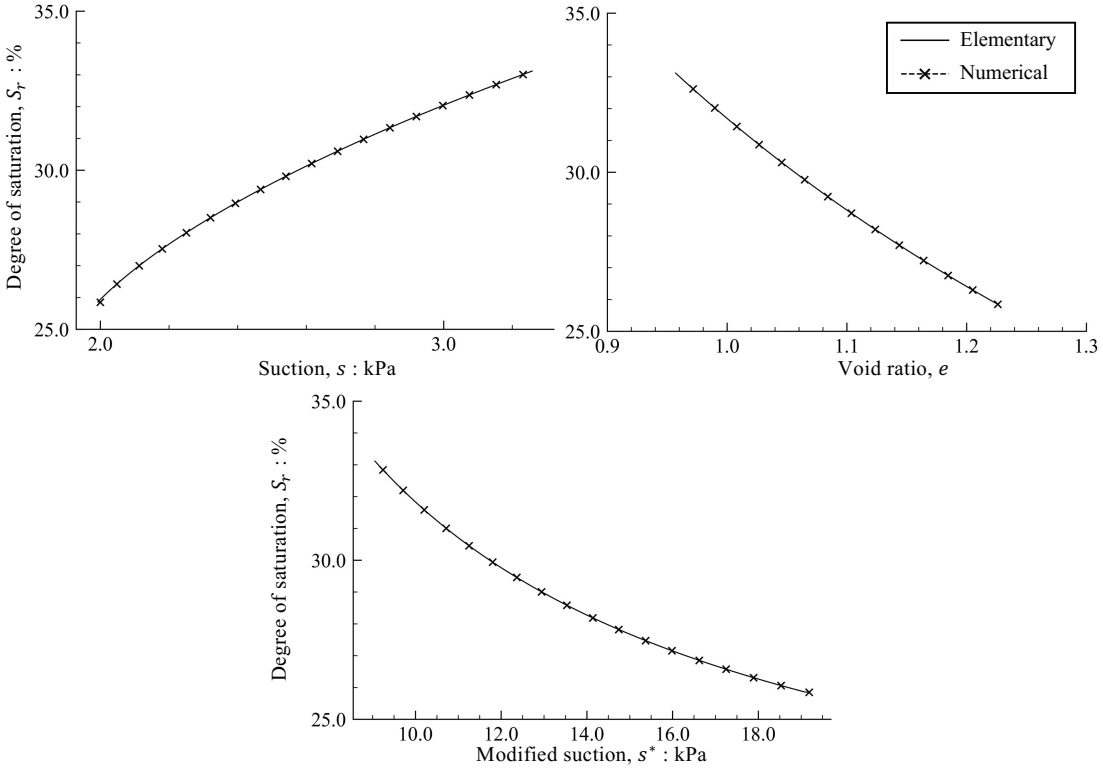

Figure C-18 S_r variation of validation Case 4L for unsaturated soil

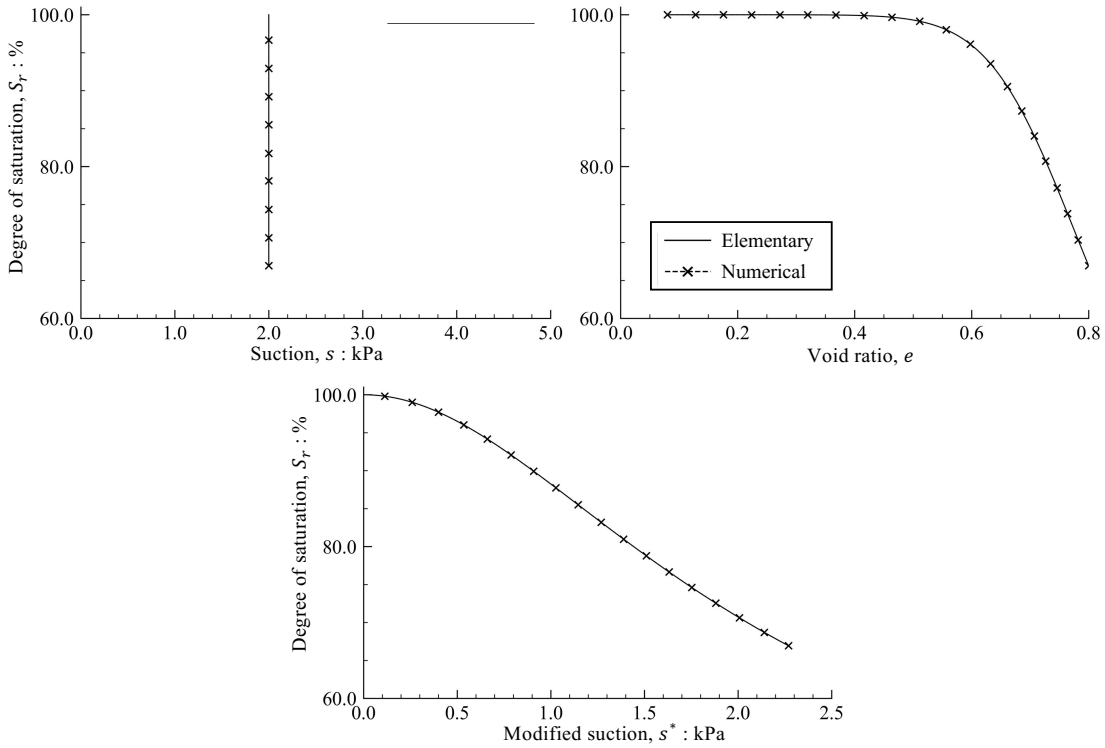

Figure C-19 S_r variation of validation Case 1D for unsaturated soil

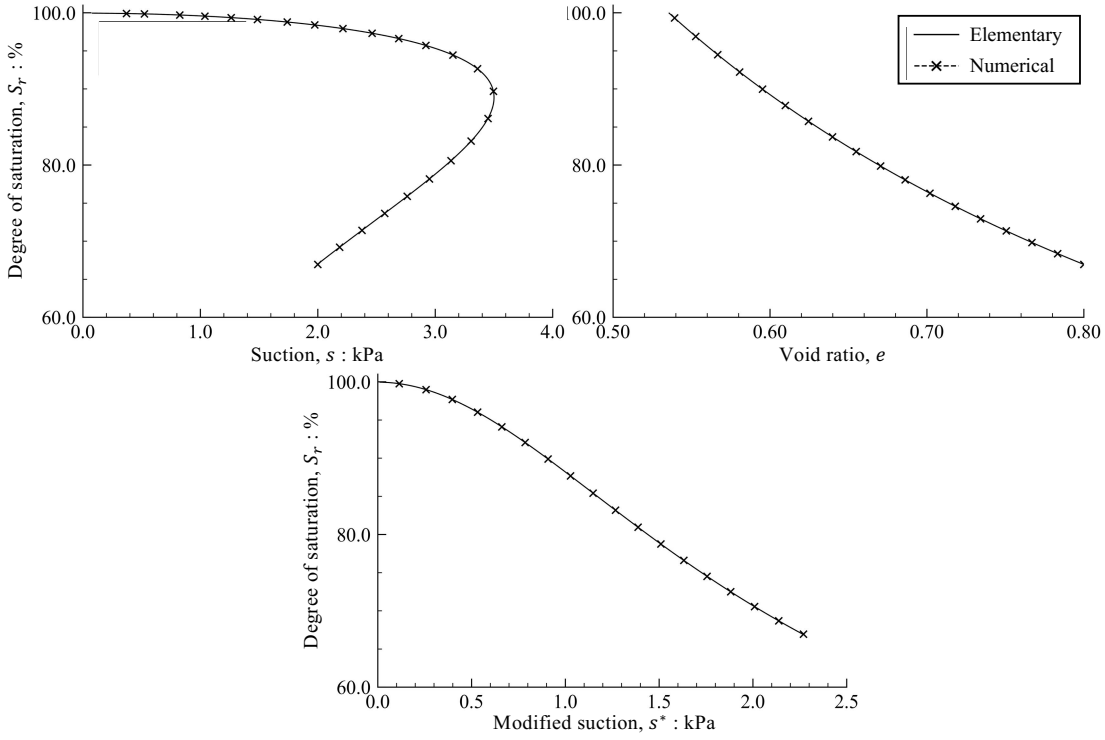

Figure C-20 S_r variation of validation Case 2D for unsaturated soil

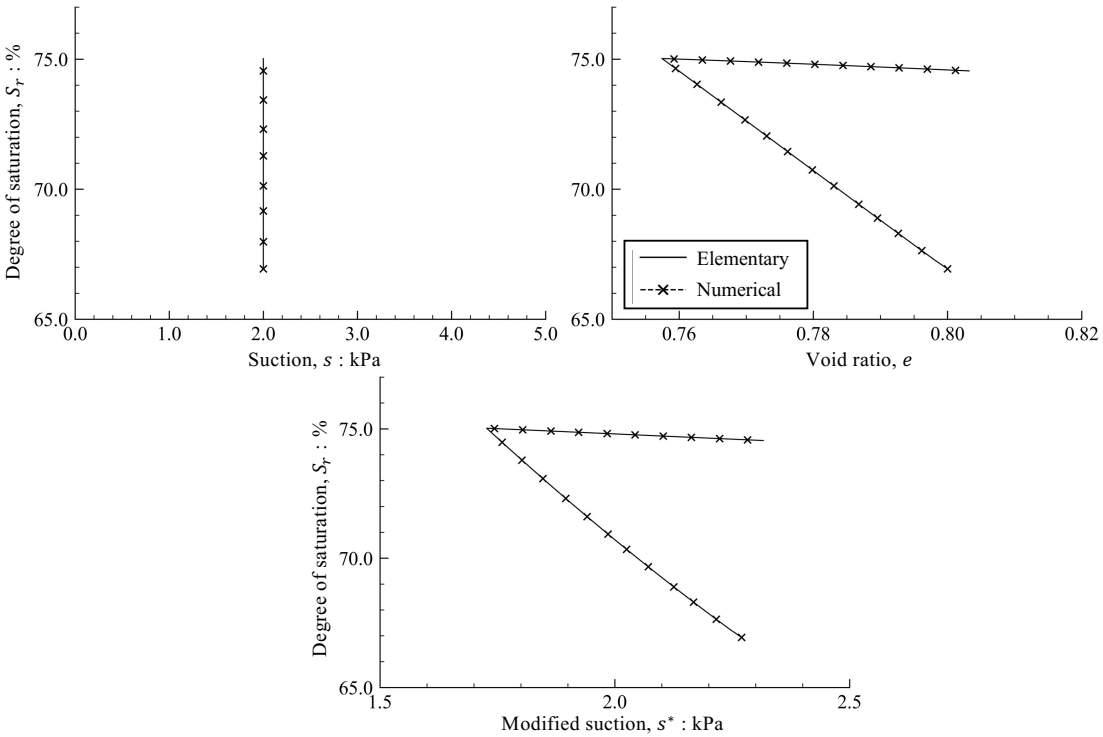

Figure C-21 S_r variation of validation Case 3D for unsaturated soil

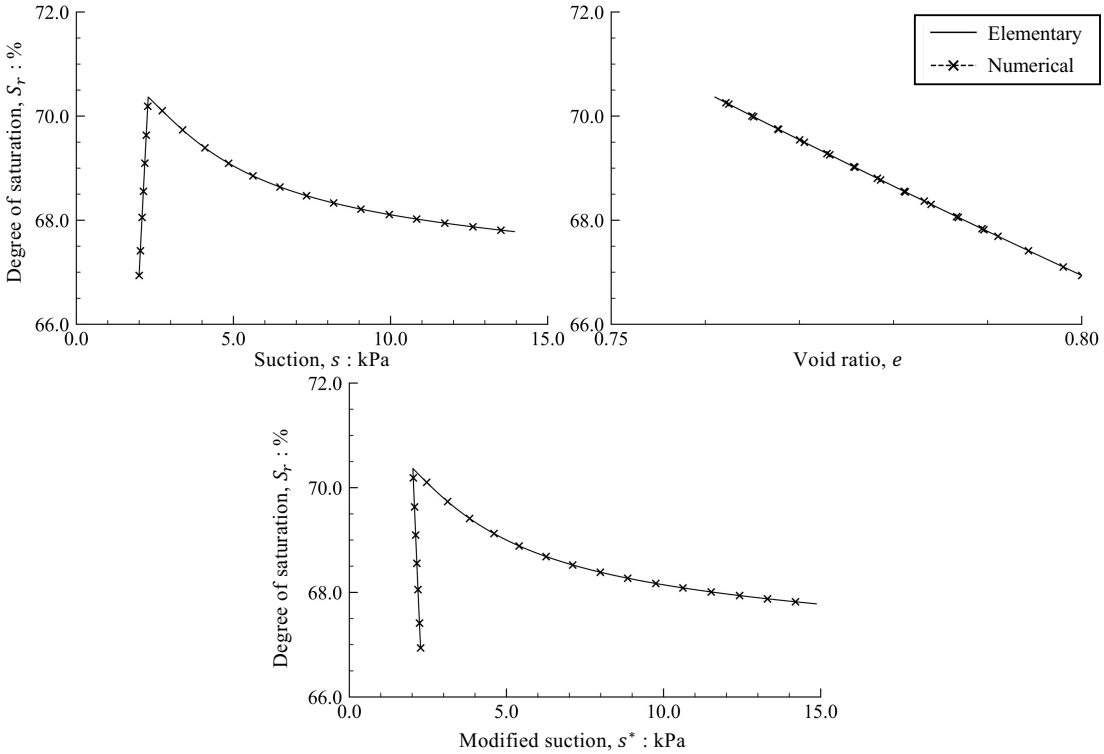

Figure C-22 S_r variation of validation Case 4D for unsaturated soil

APPENDIX D

SUPPLEMENTARY THEORIES

D - 1 DARCY'S LAW

Water flows under pressure condition through the soil element is explained by head. The total head is the summation of elevation head H_z, velocity head H_v and pressure head H_p as show in the equation of total head H_T by

$$H_T = H_z + H_v + H_p \tag{D-1}$$

In this study, the total head is dominant by the pressure head only. The elevation head is assumed to be zero since the datum is set at the reference level equal to zero and assuming that there is no effect of elevation. Besides, the velocity head will be ignored for simplicity in the study because flow in the soil is very slow. Therefore, the Equation (D-1) can be written as

$$H_T = H_p = \frac{u_w}{\gamma_w} \tag{D-2}$$

where u_w is the pore water pressure and γ_w is the unit weight of water. By this reason, total head is always positive value in the saturated condition (u_w is always positive).

Darcy's law is the empirical relationship. From the experiments, they found that "velocity of water flow (V) is proportional to the hydraulic gradient (i) as

$$V = ki \tag{D-3}$$

In this study, due to the fact that water flows from high pressure to low pressure, the hydraulic gradient value i is positive. Since, increasing of flow distance ($dl(+)$) while total head decrease ($dH(-)$) , therefore the negative sign is applied by

$$i = -\frac{dH}{dl} \tag{D-4}$$

then

$$V = -k\frac{dH}{dl} \tag{D-5}$$

D - 2 TERZAGHI'S THEORY OF CONSOLIDATION

Terzaghi's theory of consolidation is a one-dimensional consolidation theory based on the following assumptions;

1) Soil is homogenous and isotropic.

2) Soil is fully saturated with water.
3) Solid particles are incompressible.
4) Water in the pores of the soil is incompressible.
5) Compression and flow are one-dimensional.
6) Strains in the soil are relatively small.
7) Darcy's law is valid for all hydraulic gradients.
8) k_v and m_v are constant throughout the process.
9) The soil skeleton is linear elastic and independent of time.

The exact solution of the distribution of excess pore water pressure of the open layer, water is free to drain through both its upper and lower surfaces (Figure 5-8) can be written as

$$\Delta u_w = \sum_{m=0}^{\infty} \frac{2\Delta u_{w0}}{M} sin\left(\frac{Mz}{H_d}\right) exp\ (-M^2 T_v) \tag{D-6}$$

and vertical settlement S in the unit of [m] can be determined by

$$S = \int_0^H m_v(\Delta u_{w0} - \Delta u_w)dz \tag{D-7}$$

where

Δu_w denotes excess pore water pressure at time t (sec) in the unit of [kPa]
Δu_{w0} denotes initial excess pore water pressure at t = 0 sec in the unit of [kPa]
H_d denotes maximum drainage height in the unit of [m] (open layer, $H_d = 0.5H$)
H denotes total height
z denotes any depth of sample in the unit of [m]
T_v denotes time factor which is calculated by $c_v t/H_d^2$
c_v denotes coefficient of consolidation; $c_v = \frac{k_v}{m_v \gamma_w} = k_v/m_v\gamma_w$
k_v denotes coefficient of vertical permeability [m/s]
m_v denotes coefficient of volume compressibility [MPa^{-1}]

D - 3 UNSATURATED COEFFICIENT OF PERMEABILITY

Considering the mixed Toyoura sand and Fujinomori clay 5:5 by weight in the simulation, calculation method of unsaturated coefficient of permeability of sand-clay mixture are described herein (Terzaghi et al., 1996).

First, with clay to sand ratios of about 10%, the saturated coefficient of permeability of sand-clay mixture (k_{sm}) which is controlled by the coefficient permeability of clay can be calculated by;

$$k_{sm} = \frac{k_{sc}(V_{total} - V_{sand})}{V_{total}} \tag{D-8}$$

where V_{total} denotes the total volume of sand-clay mixture in the unit of [m^3], V_{sand} denotes the sand volume in the unit of [m^3] and k_{sc} denotes the saturated coefficient permeability of clay in the unit of [m/s]. Calculating k_{sc}, first, void ratio of clay e_c in an ideal saturated sand-clay mixture depends on the amount of dry clay in the mixture and on the volume between sand particles can be determined by;

$$e_c = \frac{\left(1 + \frac{1}{r_m}\right) G_{clay}\gamma_w}{\gamma_{dm}} - \frac{G_{clay}}{r_m G_{sand}} - 1 \tag{D-9}$$

where r_m denotes the ratio of dry mass of clay and sand. G_{clay}, G_{sand} denotes the specific gravity of clay and sand, respectively and γ_{dm} denotes the dry unit weight of the mixture [kN/m^3]. Then, k_{sc} can be calculated by using the empirical relations for coefficient of permeability in clayey soils (Taylor, 1948) as written by;

$$k_{sc} = k_{sc,0}\, exp\big((e_c - e_{c,0})/\lambda_k\big) \tag{D-10}$$

where the initial saturated coefficient permeability of clay ($k_{sc,0}$) respects with the prescribed initial void ratio of clay $e_{c,0}$ are provide by the experimental result of the permeability test as shown in Figure D-1 and λ_k denotes the permeability change index.

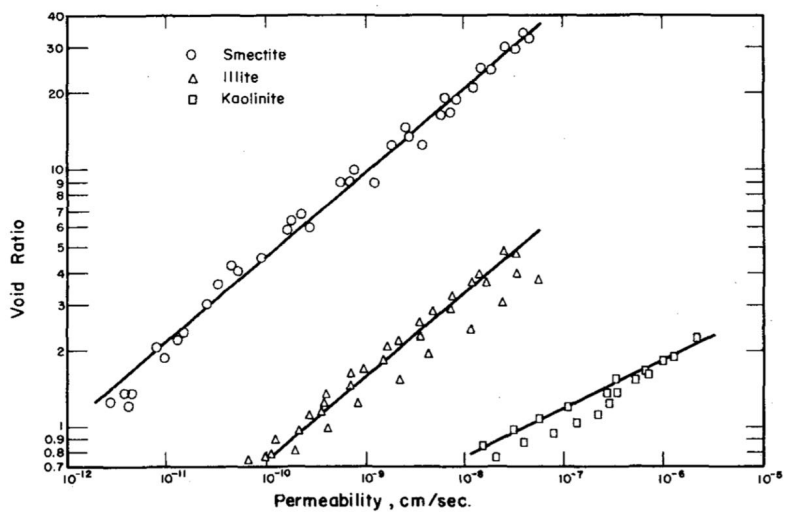

Figure D-1 Coefficient of permeability of clays (Mesri and Olson, 1971)

Finally, the unsaturated coefficient of permeability (k) can be calculated by;

$$k = k_r k_{sc} \tag{D-11}$$

where k_r denotes the relative coefficient of permeability which can be determined in the function of degree of saturation (van Genuchten, 1980) as;

$$k_r(S_r) = S_r^{\frac{1}{2}}\left(1-\left(1-S_r^{\frac{1}{m}}\right)^m\right)^2 ; m = 1-\frac{1}{n}\ and\ 0 < m < 1 \quad \text{(D-12)}$$

where m and n is the parameter for the shape of main SWCC's curve.